UAB

Universitat Autònoma
de Barcelona

Supercritical CO_2 assisted preparation of mesoporous composites for emerging applications

Márta Kubovics

Doctoral Thesis

Ph.D. in Chemistry

Supervisors: Prof. Concepción Domingo Pascual
Dr. Ana M. López-Periago

Departament de Química – Facultat de Ciéncies
2023

Thesis presented by

Márta Kubovics

to aspire to the Doctorate in Chemistry

Supervisor and tutor: Supervisor:

Prof. Concepción Domingo Pascual   Dr. Ana M. López-Periago

Bellaterra, February 2023

Acknowledgments

It is almost unbelievable that I started this journey more than three years ago, and now it comes to a certain end. Surely, all this work would not have been done without the support of many people, and I would not have so many memories if you were not the ones accompanying me along the way. Thanks for all of you for making these years some of the bests!

First of all, I would like to start with our little ICMAB group, and my supervisors of the thesis. Thank you, Concha, for giving me the opportunity to work in this group, having your doors always open to enter without hesitation, and mostly for always putting us first, whether it is about following our ideas, publishing papers, or any doubts we have. Ana, thank you for all the help that you gave me in the lab, your enthusiasm for science, and for navigating me in the labyrinth of Spanish bureaucracy. Julio, agradezco toda tu ayuda y quiero darte las gracias por estar siempre allí para arreglar todas las fugas de los reactores, mientras me contabas un nuevo capítulo de la historia de España. Alex and Albert, you never let me have any boring moment in the lab in the last three years. Alex, thanks for being curious about all my questions, and have the answer for everything. Albert, it is a pleasure to share all the tonterías, you are always ready to laugh. Laura, you always keep surprising me, thanks for your infinite energy. Núria, we only coincided for a few months in ICMAB, but you are still up for any route or squash match. Albert petit, thanks for being curious and motivated to help me in many experiments. Sandra and Ona, thanks for sharing some time with us. I couldn't ask for better groupmates!

I am also grateful to all the collaborators and colleagues from ICMAB and outside, who were involved in some ways to have all the results, and taught many things through the process.

Abstract

Among porous materials, those that possess mesopores (2-50 nm) have recently come into prominence due to their exceptional structural and surface properties. Their pores are large enough to be functionalized with complex molecules, or even with nanoparticles, are accessible for a wide variety of substances and, still, they possess sufficiently high surface area even after loading. Such features give these materials great potential in numerous applications, like in drug delivery, catalysis, pollutant removal, among many others. Infinite possibilities regarding building components, their interaction, the established structure and the consequent physicochemical properties offer the development of a huge number of new mesoporous systems, able to face the increasing economic, environmental and healthcare demands. To reach the targeted properties, often functional composites are preferred *vs.* single materials, the former involving various constituents, that are synergically contributing to the properties. The synthesis of these composite functional porous materials is challenging, requiring novel preparation methods. In particular, there is a need for replacing synthesis procedures involving harsh conditions and harmful solvents to those applying milder conditions and minimizing the environmental impact. Supercritical CO_2 (scCO$_2$) technology fulfils these requirements. Additionally, frequently the obtained products using this technology possess unique characteristics, related to the morphology, chemical composition and purity. The role of this medium in the synthesis of materials can be diverse, serving for particles precipitation, as a reaction solvent or drying agent or taking part in gelation, impregnation of guest molecules and foaming processes. The goal of this thesis was to synthesize novel porous composites using supercritical CO_2 assisted procedures and to demonstrate their usability in emerging applications. In particular, composites based on two classes of mesoporous solids, metal-organic frameworks (MOFs) and graphene-oxide (GO) aerogels, were the focus of this work. All materials prepared in this thesis are characterized by possessing a significant amount of pores in the mesosize range, although they are distinct regarding their structural and pore arrangement. Analysis of the composite properties and structural changes occurring throughout the processing was carried out with the aim of understanding their role and behavior in certain applications.

The thesis is divided to the following sections:

The ***General introduction*** aims to give a brief overview of the most important properties of porous, and, specifically, of mesoporous materials. Categorization regarding the arrangement

of the pores (ordered/disordered) and overviewing of preparation methods are presented in this section. Considerable attention is given to graphene-based aerogels and mesoporous MOFs. Finally, general properties of supercritical fluids, and, in particular, of supercritical CO_2 are defined, followed by the precedents of using $scCO_2$ for the fabrication of porous composites.

Then, the ***Objectives*** of this thesis are described.

In the ***Equipment and methods*** section, the main steps in the preparation of the composites fabricated in this work are detailed. Special emphasis is placed on the high-pressure equipment used for performing the $scCO_2$ processes, the main parts and the operation of the system. Finally, an overview of the applied characterization techniques and their basic principles are given.

In the ***Summary of the results*** section the most important findings of each performed study are introduced. Detailed discussion is given in the corresponding Chapters I to V. Four chapters correspond to already published (Chapters I, II, III and V) manuscripts, while results presented in Chapter IV are still being optimized before to be considered for publication. The first two chapters addressed the preparation and characterization of graphene-based composite aerogels with deposited metal nanoparticles, and their application as catalysts. The following two chapters present the synthesis of composites based on the Fe(BTC) MOF using $scCO_2$-assisted methods. The products are further used in biomedical or catalytic applications. The last chapter describes the preparation of porphyrin-based MOFs in $scCO_2$ and their utilization in a biomedical application.

- In ***Chapter I,*** reduced graphene-oxide aerogel supporting CuZnO nanoparticles composite was designed to be applied in the CO_2 hydrogenation reaction to selectively produce methanol. The role of the GO support, the catalyst design and the reaction conditions were investigated regarding the catalytic performance and reaction mechanism. This Chapter is based on the following published article:

Márta Kubovics, Albert Trigo, Antoni Sánchez, Gregorio Marbán, Alejandro Borrás, Javier Moral-Vico, Ana M. López-Periago, Concepción Domingo, Role of Graphene Oxide Aerogel Support on the CuZnO Catalytic Activity: Enhancing Methanol Selectivity in the Hydrogenation Reaction of CO_2, *ChemCatChem* **2022**, *14*, e202200607. https://doi.org/10.1002/cctc.202200607

- In ***Chapter II,*** Pt/TiO$_2$ nanoparticles were deposited on mildly reduced graphene-oxide based aerogel, and the thus obtained 3D porous composites were tested in the photocatalytic H$_2$ production reaction from an aqueous methanol solution. A systematic study on the optimization of the catalyst composition, architecture and reaction conditions was performed with the aim of maximizing H$_2$ production. All these factors had strong influence on the reactant/product diffusion, the permeability in the porous structure and the light-harvesting characteristics. This Chapter is based on the following published article:

Márta Kubovics, Cláudia G. Silva, Ana M. López-Periago, Joaquim L. Faria, Concepción Domingo, Photocatalytic hydrogen production using porous 3D graphene-based aerogels supporting Pt/TiO$_2$ nanoparticles, *Gels* **2022**, *8*, 719.
https://doi.org/10.3390/gels8110719

- In ***Chapter III,*** a cutaneous polymeric formulation (patch) is prepared based on drug impregnated into iron trimesate MOFs, following a multistep scCO$_2$-assisted procedure. The MOF preparation, the drug impregnation and polymeric patch formation is stepwisely contrasted with conventional liquid techniques. The drug delivery and permeation profile of the patches were studied with i*n vitro* and *ex vivo* tests. This chapter is based on the following published article:

Márta Kubovics, Sara Rojas, Ana M. López-Periago, Julio Fraile, Patricia Horcajada, Concepción Domingo, Fully supercritical CO$_2$ preparation of a nanostructured MOF composite with application in cutaneous drug delivery, *The Journal of Supercritical Fluids* **2021,** *178*, 105379.
https://doi.org/10.1016/j.supflu.2021.105379

- In ***Chapter IV,*** a novel method to encapsulate copper nanoparticles in Fe(BTC) MOF *via* scCO$_2$-assisted impregnation of copper-acetylacetonate (Cu(acac)$_2$) is described. The process is followed by reduction step. The effect of the MOF properties and the Cu-loading is investigated in the CO$_2$ hydrogenation reaction towards the formation of methanol and methane.

- In ***Chapter V,*** a series of metalloporphyrine frameworks were prepared from flourinated metal complexes (M(hfac)$_2$ M = Cu, Zn, Co, Ni) and a porphyrin-based linker (5,10,15,21-tetra(4-pyridyl)porphyrin) using scCO$_2$ as the reaction solvent. The metal-coordination in

the pyrrole ring and on the exocyclic pyridine moieties, and the amorphization of the structure due to structure defects were studied. The Zn-based MOF was selected for analyzing the photodynamic properties in a tumorigenic human cell line. This chapter is based on the following published manuscript:

Márta Kubovics, Oriol Careta, Oriol Vallcorba, Guillermo Romo-Islas, Laura Rodríguez, Concepción Domingo, Jose A. Ayllón, Carme Nogués, Ana M. López-Periago, Supercritical CO_2 synthesis of porous metalloporphyrine frameworks: application in photodynamic therapy, *Chemistry of Materials* **2023**.
https://doi.org/10.1021/acs.chemmater.2c03018

Finally, in the ***Conclusions*** section the main findings of this thesis are summarized.

Resumen

Entre los materiales porosos, aquellos que tienen mesoporos (2-50 nm) han cobrado importancia recientemente, debido a sus excepcionales propiedades estructurales y superficiales. Sus poros son suficientemente grandes para ser funcionalizados con moléculas complejas, o incluso con nanopartículas, son accesibles por varias sustancias, y, aun así, tienen un área superficial suficientemente alta después de la carga. Estas características conceden a estos materiales un gran potencial en numerosas aplicaciones, como en la administración de fármacos, catálisis, eliminación de contaminantes, entre muchas otras. Actualmente se contempla el desarrollo de un gran número de nuevos sistemas mesoporosos con posibilidades infinitas respecto a sus constituyentes, sus interacciones, la estructura y sus consecuentes propiedades fisicoquímicas. Estos sistemas son capaces de enfrentarse a las crecientes demandas económicas, ambientales y sanitarias. Para obtener las propiedades deseadas, a menudo se prefieren los compuestos funcionales frente a los materiales individuales. En el primer grupo, los materiales están formados por varios componentes, que contribuyen sinérgicamente a las propiedades. La síntesis de estos compuestos porosos funcionales es desafiante y requiere nuevos métodos de preparación. En particular, se necesita reemplazar los procedimientos de síntesis que implican condiciones severas y disolventes tóxicos, por otros que requieren de condiciones más suaves y además minimizan el impacto ambiental. La tecnología de CO_2 supercrítico (scCO$_2$) cumple con estos requisitos. Además, frecuentemente los productos que se obtienen con esta tecnología tienen características únicas, relacionadas con la morfología, la composición química y la pureza. La función de este medio en la síntesis de los materiales es diversa, por ejemplo, como: agente para el aumento de la precipitación de las partículas; disolvente en la reacción; agente secante; factor en procesos de gelificación, impregnación de moléculas huésped y procesos de espumado. El objetivo de esta tesis ha sido sintetizar nuevos compuestos porosos utilizando tecnología de CO_2 supercrítico y demostrar su utilidad en aplicaciones emergentes. En particular, los compuestos basados en dos clases de sólidos mesoporosos: las estructuras metalorgánicas (MOF) y los aerogeles de óxido de grafeno (GO). Todos los materiales presentados en esta tesis se caracterizan por tener una cantidad significativa de poros en el rango de tamaño meso, aunque son distintos en cuanto a las estructuras y la organización de los poros. Se ha realizado el análisis de las propiedades de los compuestos y los cambios estructurales que se producen a lo largo del proceso con el objetivo de entender la función y comportamiento en ciertas aplicaciones.

Absztrakt

A pórusos anyagok közül az utóbbi időben előtérbe kerültek azok, amelyek pórusmérete a „mezo" mérettartományba esik. Ennek oka elsősorban a kivételes szerkezeti és felületi tulajdonságaikban rejlik. A mezopórusos anyagok jellemzője, hogy a pórusok mérete elegendően nagy ahhoz, hogy hozzáférhetőek legyenek komplex molekulák, akár nanorészecskék számára, valamint a funkcionalizálás után is elegendő felülettel rendelkeznek. Ezen tulajdonságokból eredő potenciál számos területen kihasználható, többek között gyógyszer-adagolás, katalízis vagy szennyezőanyag eltávolítás során. Kimeríthetetlen lehetőség rejlik az alkotó elemek, a közöttük kialakuló kölcsönhatások, a szerkezet, és az ebből eredő fizikokémiai tulajdonságok terén, ennek megfelelően számos új mezopórusos anyag fejleszthető, amely képes lehet megfelelni a gazdasági, környezetvédelmi és egészségügyi igényeknek. A kívánt cél eléréséhez, az egyszerű anyagokkal szemben gyakran funkcionális kompozitok szükségesek, amelyekben az alkotó elemek együttesen alakítják ki a végső tulajdonságokat. A funkcionális pórusos kompozitok előállítása kihívást jelent, ehhez új gyártási módszerekre van szükség. Különösen fontos az erélyes körülmények és az ártalmas oldószerek kiváltása enyhébb folyamatokra, ezzel csökkentve a környezetre gyakorolt hatást. A szuperkritikus szén-dioxidos technológiák amellett, hogy megfelelnek ezen követelményeknek, az így gyártott termékek egyedi jellemzőkkel bírnak, mind a morfológiát, mind a kémiai összetételt és a tisztaságot tekintve. A szuperkritikus közeg szerepe a szintézis során sokféle lehet, többek között részt vehet a részecskék kicsapásában, a gél képzésben és szárításában, az impregnálási folyamatokban, valamint a habképzésben.

A dolgozat célja új, pórusos kompozitok előállítása szuperkritikus szén-dioxidos technikákkal, és a termékek felhasználásának bemutatása aktuális alkalmazásokban. Az előállított mezopórusos kompozitok két kategóriába sorolhatók, a fémorganikus vegyület-, illetve a grafén-oxid aerogél alapú kompozitok közé. Minden termék jelentős mennyiségű mezopórussal rendelkezik, ugyanakkor a pórusok szerkezetében és azok elrendezésében különböznek. Ahhoz, hogy megértsük az egyes anyagok funkcióját és viselkedését a választott alkalmazásokban, a kompozitok tulajdonságinak és a feldolgozás során fellépő szerkezetbeli változásoknak az elemzésére volt szükség.

Acronyms

acac	acetylacetonate
ANOVA	analysis of variance
API	active pharmaceutical agent
ATR	attenuated total reflectance
AzA	azelaic acid
BASF	Badische Anilin und Soda Fabrik
BDC	1,4-benzenedicarboxylate
BET	Brunauer, Emmett and Teller
BJH	Barret, Joyner and Halenda
BSE	Back scattered electrons
BTC	1,3,5-benzenetricarboxylate
CFC	chlorofluorocarbon
CMP	conjugated microporous polymers
CNT	carbon nanotubes
COF	covalent organic framework
CP	coordination polymer
CuCs	copper clusters
DFT	density functional theory
DLS	dynamic light scattering
DMF	dimethylformamide
DMSO	dimethyl sulfoxide
DNA	deoxyribonucleic acid
EA	elemental analysis
EDA	ethylenediamine
EDS	energy-dispersive X-ray spectroscopy
EtOH	ethanol
FDA	United States Food and Drug Administration
Fe(BTC)	iron trimesate MOF
FID	flame ionization detector
FTIR	Fourier transform infrared
GC	gas chromatography
GHSV	gas hourly space velocity

GO	graphene oxide
GOa	graphene oxide aerogel
GRAS	generally recognized as safe
H_2TPyP	5,10,15,20-Tetra(4-pyridyl)-21H,23H-porphine
HBSS	Hank's balanced salt solution
HKUST	Hong Kong University of Science and Technology
HOF	hydrogen-bonded organic frameworks
HPLC	high performance liquid chromatography
ICP-MS	inductively coupled plasma - mass spectrometry
IL	ionic liquid
IR	infrared spectroscopy
IRMOF	isoreticular metal-organic frameworks
IUPAC	International Union of Pure and Applied chemistry
JCPDS	Joint committee on powder diffraction standards
LED	light emitting diode
MCs	metal clusters
MeOH	methanol
MIL	Materials of Institut Lavoisier
MOF	metal-organic framework
MW	microwave
NASA	National Aeronautics and Space Administration
NP	nanoparticle
PBS	phosphate-buffered saline
Pcrit	critical pressure
PCC	porous coordination cages
PDT	photodynamic therapy
PL	photoluminescence spectroscopy
PLA	polylactic acid
PPN	porous polymer networks
PVA	poly(vinyl-alcohol)
PXRD	powder X-ray diffraction
RF	resorcinol-formaldehyde
rGO	reduced graphene oxide
rGOa	reduced graphene oxide aerogel
ROS	reactive oxygen species

S_a	surface area
SBU	secondary building unit
$scCO_2$	supercritical carbon dioxide
SCXRD	single crystal X-ray diffraction
SE	secondary electrons
SEM	scanning electron microscopy
SKBR-3	a human breast cancer cell line
STEM	scanning transmission electron microscopy
STY	space-time yield
Tcrit	critical temperature
TCD	thermal conductivity detector
TEM	transmission electron microscopy
TGA	thermogravimetric analysis
UiO	Universitetet i Oslo
UV-vis DRS	UV-vis diffuse reflectance spectroscopy
V_p	pore volume
WGA	wheat germ agglutinin
XPS	X-ray photoelectron spectroscopy
XRD	X-ray diffraction
ZIF	zeolitic imidazole framework

Table of contents

Chapter II. Photocatalytic hydrogen production using porous 3D graphene-based aerogels supporting Pt/TiO$_2$ nanoparticles

Chapter III. Fully supercritical CO$_2$ preparation of a nanostructured MOF composite with application in cutaneous drug delivery

Chapter IV. scCO$_2$ assisted Cu-loading on Fe(BTC) semiamorphous MOF: application in catalytic CO$_2$ hydrogenation

Chapter V. Supercritical CO$_2$ synthesis of porous metalloporphyrin frameworks: application in photodynamic therapy

General introduction

The general introduction summarizes the background of the main topics that are providing the basis of this thesis. The first part focuses on the general description of porous materials, both single components and composites. Then, the attention is turned towards mesoporous solids with ordered or disordered pores, as all materials synthesized in this work belong to these categories. Later, two specific categories of porous solids, aerogels and metal-organic frameworks, are discussed in terms of their structure, composition, preparation methods and applications. Extensive attention is placed on graphene aerogels and amorphous, mesoporous metal organic frameworks, again highlighting the structures that are synthesized in this work. Finally, supercritical CO_2, the media that was used for the preparation and processing of all the samples, is described.

1. Introduction to porous materials

1.1. Definition

Any solid, containing significant void space that is not occupied by atoms of the main framework is called a porous material.[1] In these materials, the continuous phase that forms the framework is a solid, while a fluid phase (gaseous or liquid) fill the pores.[2] Only very recently, porous liquids have been described as a novel class of porous materials, possessing intrinsic porosity and fluidity at the same time.[3] From a structural point of view, intraparticle and interparticle voids must be distinguished. Intraparticle, intrinsic pores in a material can be generated during synthesis by chemical reaction, foaming and template approaches. Secondary processes, such as aggregation, self-assembly or sintering of primary particles, which can be porous or dense, generate the extrinsic, interparticle void.[4,5]

1.2. Historical evolution

The concept of pores and porous structures dates back to ancient times, surrounding the humankind from the beginning and accompanying it through thousands of years. Clay minerals, zeolites, wood, plants, bones, lungs are all containing regions of empty spaces.[6] Even butterfly wings exhibit unique porous micro/nanostructures.[7] Often, natural creations inspired the fabrication of advanced porous structures by replicating their unique arrangement.[8] The scientific and technological evolution brought numerous significant breakthroughs in understanding, constructing and manipulating porous materials designed to satisfy necessities of high-tech emerging applications. A brief overview about the evolution of porous materials in chronological order, starting from the first remains of scientific literature up until recent discoveries, is depicted in (Figure 1).[9] This collection cannot be complete or exhaustive due to the tremendous period elapsed since ancient time, lack of archeological remains from pre-historic time and steep acceleration of the created novel structures in modern time.

Charcoal was the first porous material widely used by human beings since the ancient period. Prehistoric people used to live in tight connection with the nature, utilizing parts of plants, animals and surrounding objects for their everyday lives and, at the same time, making and intense observation of their environment. Their curiosity and positive experiences led to the first practical use of charcoal to treat indigestion.[10] Actually, the first written record about this material dates back to the ancient Egypt. Another crucial use of charcoal, found in ancient Hindu sources, was to provide potable water.[11] Several centuries later, the British navy was using the same concept, although the stains remaining from the carbon might brought up

hygiene related issues.[12] Until the 18th century, applications of porous materials were relying on good experience and legends arising from the positive practice. However, right before the industrial revolution, scientists started to have the desire of building theories and understand the adsorptive properties of porous materials. One of the first recorded investigation was that of C. Scheel, a Swedish chemist. In his experiment, published in 1780,[13] a piece of charcoal was placed in a closed vessel, that was attached to a rubbery bladder. He observed that upon heating, the bladder was largely expanded, and assigned this phenomenon to the release of the adsorbed gas within the porous structure of the charcoal. Around the same time, the appearance of new products, together with certain necessities towards advanced purification systems, boosted the scientific development of adsorptive materials. Adsorbents for sugar refining, beverage purification and masks used in World Wars are some representative examples of new applications that gave rise to develop systems involving porous charcoal.[9]
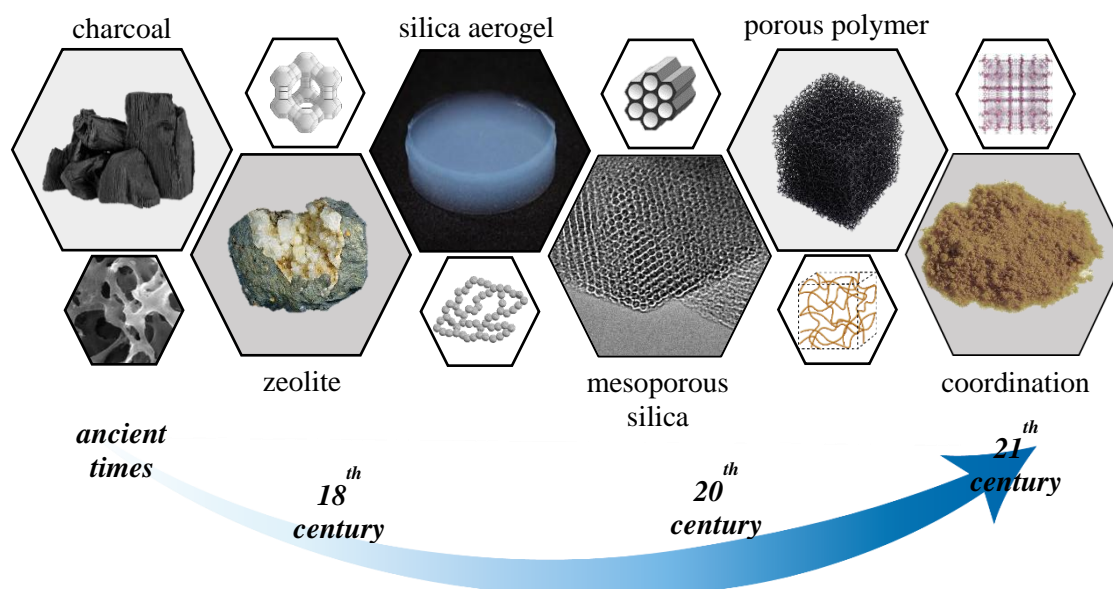
Figure 1. Some of the major milestones in the evolution of porous materials in chronological order.

After charcoal, the next rising star in porous materials was the family of zeolites, derived from aluminosilicate minerals and possessing ordered porous structures. These materials were first described by another Swedish scientist, A.F. Cronstedt, in the mid 18th century.[14] A century later the first synthetic zeolites, the levynite, was fabricated by a French chemist, M.H. Sainte-Claire-Deville.[15] It took almost hundred years until the possible benefits of high scale production of zeolites was realized. Particularly, the Union Carbide company started the research on developing processes for the industrial synthesis of zeolites, primarily to be used

as catalysts in hydrocarbon valorization.[16] The early successes of zeolites as catalysts accelerated the research in the field of porous materials. Thus, a new family of amorphous mesoporous silica was developed by Mobil Oil Corporation in the 20th century, synthesizing materials with highly ordered pores (*e.g*., SBA, MCM).[17] By this time, silica aerogels have already been conceived at the NASA's Glenn Research Center by S. Kistler around the 1930s.[18] In the late 20th century, with the invention of new techniques in chemical preparation and characterization, controlling the synthesis of materials at the molecular level became possible. The idea of associating a crystalline structure with the porous character of a particular material gave birth to the metal-organic frameworks (MOFs) chemistry, a subdivision of the coordination polymers chemistry. The first crystalline MOF with permanent porosity and rigidity, was a material based on Zn(II) created by O. Yaghi just before the end of the second millennium.[19] Following the same principles, new porous materials emerged, such as porous coordination cages (PCCs) and hydrogen-bonded organic frameworks (HOFs). On the other end of the organic-inorganic spectrum, porous polymers and all-organic materials are generally cheaper to synthesize and easier to process into a variety of porous morphologies. For instance, covalent organic frameworks (COFs),[20] conjugated microporous polymers (CMPs)[21] and porous polymer networks (PPNs),[22] are incorporating intrinsic porosity through hypercrosslinking.

In summary, the improvement of already existing porous structures, as well as the creation of new applicable porous systems, has been and still is highly necessary to face serious economic and environmental challenges. Some of these materials are currently targeted to offer solutions related to adsorption, separation and filtration in environmental commitment, such as gas separation, liquid purification, energy storage and catalysis.

1.3. Characteristics defining the pores

Many properties of porous materials arising from their pore characteristics. The IUPAC extensive report on physisorption methods and practices classifies pores in categories, with the final objective of properly analyzing gas adsorption isotherms.[23] A large variety of different pores can be distinguished in natural and artificial porous materials, each type possessing unique shape, size, origin, accessibility, *etc*. (Figure 2).
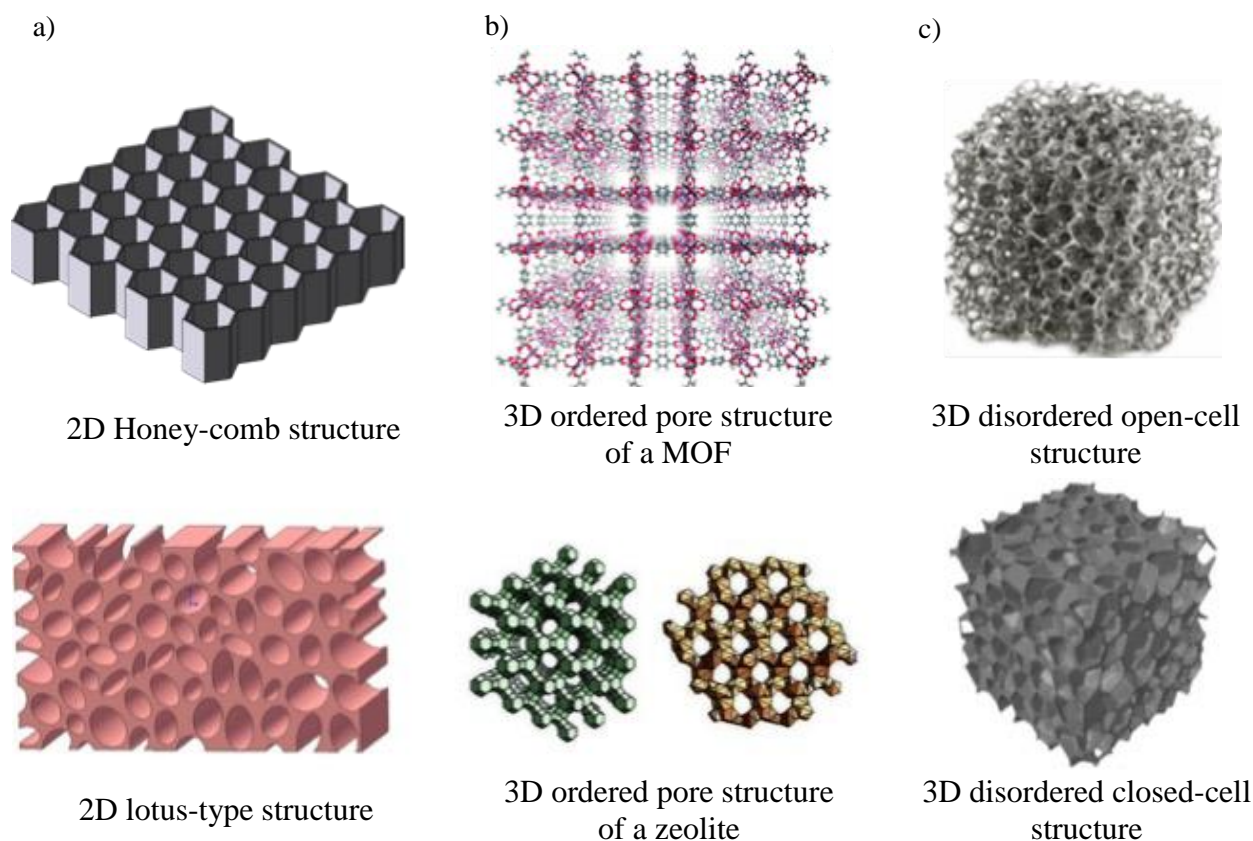
Figure 2. Classification of porous materials based on the structure of the continuous solid phase. Images are adapted.[2]

First, the continuous network surrounding the empty pores defines the 2D or 3D structure of the voids.[4] Honey-comb and lotus-type materials have 1D directional channels within a network with a 2D polygonal or circular/elliptic shape, respectively (Figure 2a). Representative materials with a honey-comb intrinsic structure are several mesoporous silicas (*e.g.,* MCM-41 and SBA-15) and zeolites (*e.g.,* VPI-5). Extrinsic lotus type pores are observed in sintered metallic structures. A 3D arrangement of the pore network can lead to materials with ordered and disordered pores.[2] Representative examples of the first are most zeolites and MOFs with interconnected pores (Figure 2b). On the contrary, aerogels and foamed polymeric materials possess 3D structures with disordered pores (Figure 2c). Aerogels, with an interconnected network of pores, form an open-cell structure built by continuous channels with open endings in both sides. Polymers are often bubblelike foamed, which implies the presence of closed-cell pores isolated from their neighbors and blind pores open only at one end. Such pores are inactive in adsorption/permeation processes, but they can significantly modify the bulk properties of the material, such as the thermal conductivity, density or mechanical strength.

The most common types of intraparticle and interparticle pores are schematized in Figure 3a. The geometry of the pores influences the permeability and distribution of the fluid inside the solid and the fluid-solid interactions, as well. The pore bodies are described with geometrical shapes, being the most common funnel, ink-bottle, cylindrical and slit-shaped pores (Figure 3b).[23] However, due to the huge variety and irregularity in geometry, pores are described with network models by considering the void space as a network of bodies connected through pore throats with different cross sections.[24]
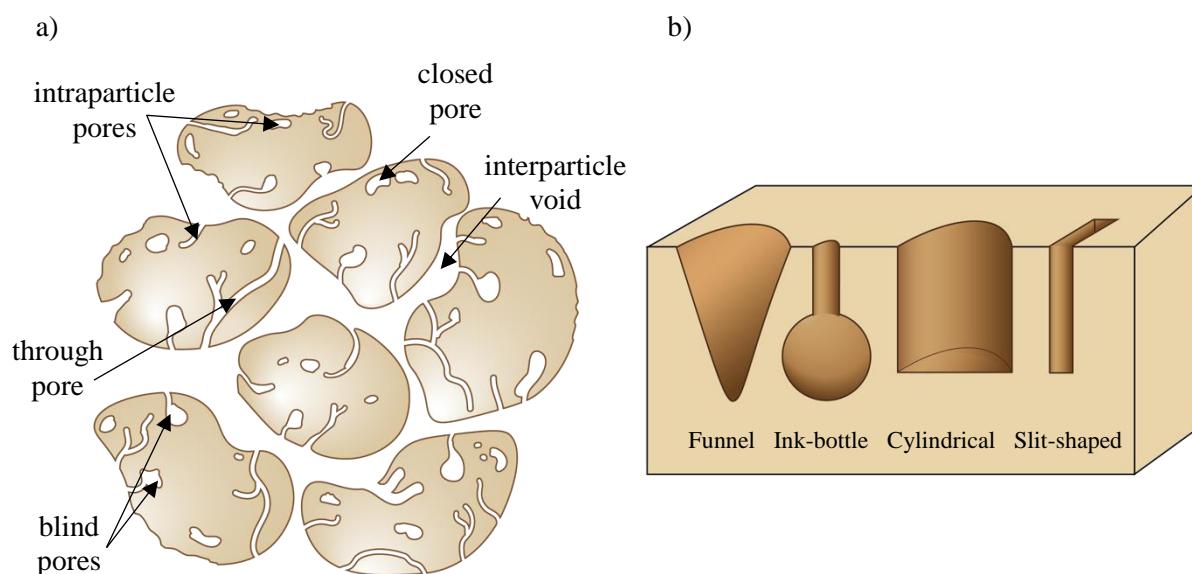
Figure 3. Schematic representation of IUPAC pore classification: (a) most common intraparticle and interparticle pores, and (b) pore geometries.

The term nanopore (pores between 1 and 100 nm) includes micro-, meso- and macroporous architectures. Hence, it covers a large array of different porous products, ranging from classical inorganic zeolites or hybrid metal organic frameworks to aerogels.

1.4. Porous composites

Materials composed of two or more constituents are called composites. The unique properties of these materials arise not only from the contribution of the individual components, but also from the synergistic effect due to the interaction of the components. Composing materials with several constituents gives the possibility of flexible design of the end products, with characteristics not attainable with a single component. In a composite, usually a primary and secondary phase are found. The primary phase is the matrix and has a continuous structural character. The second phase or phases are generally dispersed in the matrix in a discontinuous

form, thus reinforcing the properties of the bulk. Based on matrix material, the composites are classified into metal (dispersed metal/ceramic), ceramic (dispersed ceramic) and polymer (dispersed polymer or inorganic) matrix composites. Based on the reinforcing dispersed material, the classification involves particulate or fibrous, with dispersed particles or fibers, respectively, and laminates with several layers of fibers.[25] By tailoring the parameters of the dispersed substances (size, geometry, ratio, distribution, orientation, *etc.*) precisely targeted properties can be reached. For instance, a frequently searched feature is the combination of robustness and low weight, which requires components with different nature and could not be achieved without composing them.[26] Actually, in a composite material the matrix phase is usually more ductile than the dispersed phase. The matrix, besides providing surface for the dispersed entities, also gives stability to the structure and can influence other properties, such as the conductivity or thermal stability. The interaction between the matrix and the dispersed phase plays an important role in the structural integrity of the composite, influencing the final properties, as well. In some cases, chemical bonds are established between the composite components, but the cohesion of the material can be based just on weaker, physical intermolecular interactions, such as hydrogen bonds and π-π or van der Waals interactions.[27]

In the broad term of composite materials, nanocomposites, in which at least one constituent is at the nanoscale, are of extraordinary importance, since the nanosize entails homogenous distribution and finer microstructures. The nanoscale dimension of the dispersed phase is a crucial requirement for many applications, in which the high surface/volume ratio of the dispersed phase induce a high number of attractive interactions with the matrix. Nevertheless, nanoparticles (NPs) have a great tendency to aggregate, which difficulted the homogeneous dispersion of the second phase in the composite. In the subclass of porous composites, the matrix is the skeletal portion of the material with a significant amount of empty void. Composite materials designed to retain porosity usually have applications specific to their pore-structure. Typical advantageous characteristics given by the pores are enhanced mass transfer and liquid retention, improved opacity, lighter weight, enhanced gloss, controlled spread and control of heat conduction. Porosity also has the drawback of reducing mechanical strength and stiffness. The use of porous composites has advantages to prepare high quality nanocomposites, since they fulfill the essential demand of providing large surface area able to keep the NPs dispersed.

2. Mesoporous materials

2.1. Particular characteristics due to the pore size

As mentioned in the Introduction, this thesis is dealing with different types of composite mesoporous materials, involving a porous matrix (*e.g.,* graphene aerogel, iron(III) trimesate and metal-porphyrin MOFs) loaded with dispersed substances (*e.g.,* metals and oxide nanoparticles), forming engineered composites with advanced physicochemical properties specialized for medicine and energy applications. Among porous materials, those that possess mesopores (2-50 nm) are of great interest, due to particular advantages over micro- (< 2 nm) and macroporous (> 50 nm) substances. To the contrary of microporous materials, their pores are large enough to be functionalized with complex molecules or NPs. In the same time, mesoporous materials exhibit high values of surface area, which further facilitate the stable functionalization. Mesoporous materials can be classified with respect to crystallinity and the structural order of the pores. Historically, much of the research effort on porous materials was focused on developing crystalline products, with an array of ordered pores (zeolites). However, with the development of amorphous porous solids, such as mesoporous silicas, foams and aerogels, the potential processing advantages of materials (crystalline or amorphous) with ordered and disordered pores are being highlighted. The materialization of the specific properties of mesoporous materials is the result of the used preparation methods, which are described in the following sections.

2.2. Synthesis

2.2.1. Mesoporous materials with ordered pores

- ***Amorphous structures:*** obtained by using a template, allowing to control the porosity of the solid. Soft-templating (endotemplate) and hard-templating (exotemplate) routes can be distinguished.[28] In soft-templating, organic molecules are used as structure-directing agents (surfactants), and the inorganic precursors condense around them. After the formation of the mesoporous phase, the organic template is removed by calcination or solvent extraction. Several amorphous mesoporous silicas (MCM-41, SBA-15, *etc.*) were synthesized using this method. In the hard-templating route, the template is a porous solid (mesoporous silica, carbon, polymer beads, *etc.*), in which the void space is loaded with the precursors of the end-product and then transformed under certain experimental conditions. Finally, the template is removed by high temperature or chemical dissolution (*e.g.,* using NaOH or HF). Thus, the negative structure of the porous template remains. First mesoporous carbons were synthesized using this method.[29]

- ***Crystalline structures:*** mesoporous metal-oxides (Cr_2O_3, Co_3O_4, Fe_2O_3, MnO_2, *etc.*) and non-oxides (carbides, nitrides, sulfides, selenides, fluorides) with crystalline structure have been synthesized using the above mentioned hard-templating method.[30,31] The use of surfactants as templates to obtain crystalline structures is, generally, not applicable, due to the high temperature required for the crystallization of the end-compound, which would cause the early decomposition of the template. Recently, a template free-method for obtaining mesoporous transition metal-oxides with crystalline walls has been developed, using basic carbonates as precursors. The mesopores are generated by the diffusion of gasses (CO_2, H_2O) generated by the thermal transformation of the carbonate to oxide.[32] Crystalline mesoporous structures with ordered pores are also obtained by direct synthesis through a chemical reaction. An important representative of this category is the mesoporous MOFs family. Currently, most MOFs are microporous, and only few of them exhibit cages in the meso range. Micro and mesoporous materials are mainly obtained by solvothermal synthesis, by mixing the two building blocks, the metal precursor and the organic ligand, in an organic solvent. Less frequently, surfactants have also been used to direct the formation of mesopores in MOFs.[33] It is worth mentioning that, although traditionally MOFs are crystalline frameworks, recently their amorphous and semiamorphous counterparts have gained interest due to their rapid synthesis and the potential applications arising from the structural irregularities.[34]

2.2.2. Mesoporous materials with disordered pores

The family of porous materials with disordered pores is huge, involving all different types of materials, from metals to polymers and to organic and inorganic structures. Sintering of metal powders, results in a porous structure, where the individual particles are connected through the sintered necks of the particles. Melt foaming, electrical deposition or infiltration are further techniques to prepare porous metals.[2] Mesoporous polymer frameworks, a class of porous materials with nano-truss-like morphology constructed from rigid macromolecular interconnectors and directional connectivity, can be obtained by chemical cross-linking, amphiphilic surfactant templating and foaming techniques. Foams are highly porous materials, involving beside the mesopores, a large amount of macropores (50 – 500 µm, or even bigger). Most cellular foamed plastics contain closed pores. They are prepared by foaming, in which a fluid is dissolved through the melt material to be swelled (Figure 4a). Foaming can be instigated by either a physical processing (boiling by heating or depressurization) or chemical reaction. Upon the elimination of the solvent, a solid foam is recovered.

Aerogels, xerogels and cryogels are the most studied highly porous 3D materials involving irregular porosity. They are fabricated without any sacrificial template. In these materials, the method of synthesis and the attained porosity, together with the average pore size, define the term used to differentiate them. The three sub-classes are prepared by gelation of a solid in a solvent, and subsequent drying of the formed gel (Figure 4b). The aim of the gelation is to link the dispersed substances in a solvent by establishing interactions among them, thus constructing an assembled structure. Often the assembly of the network is induced by the modification of the reaction conditions (temperature pH), or by adding reducing agents or cross linkers.

a)
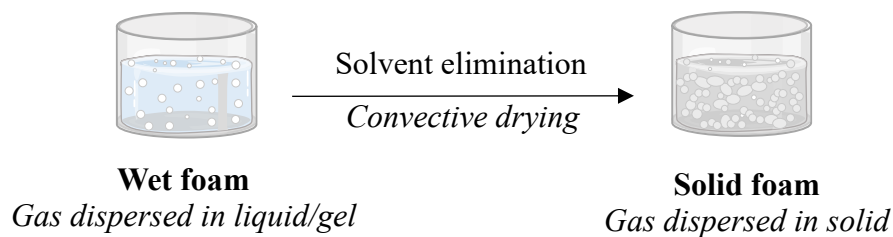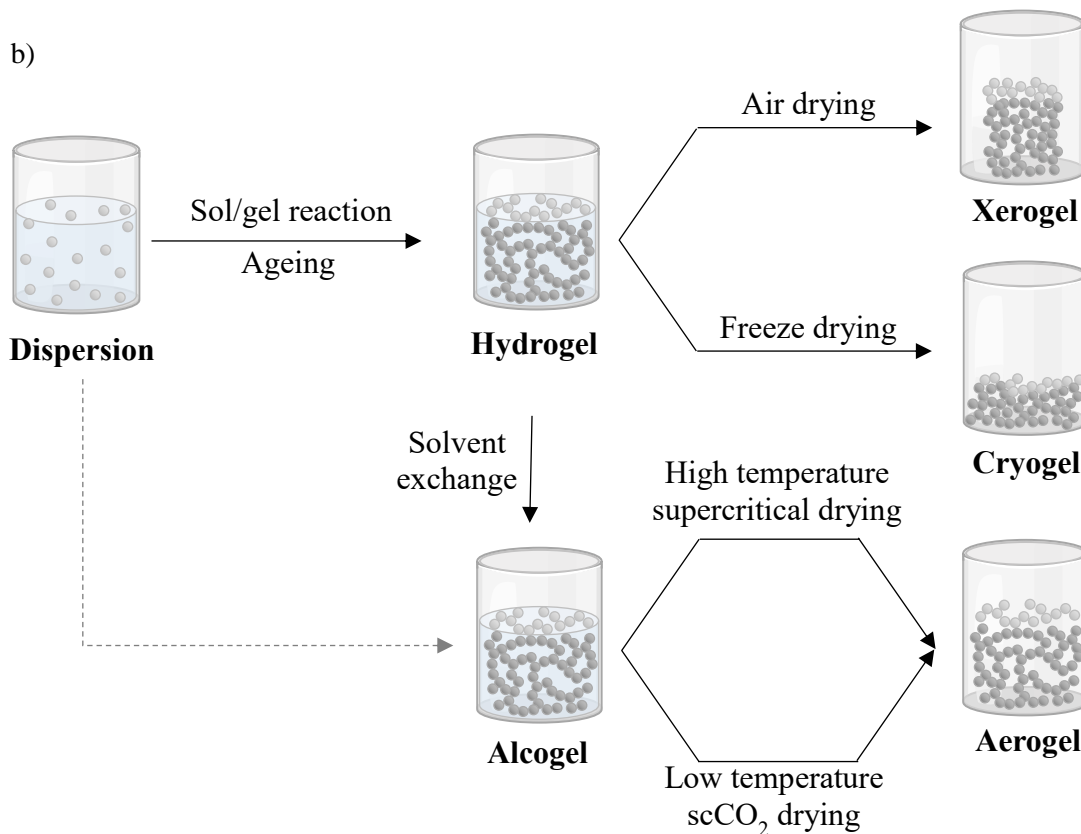
Figure 4. Preparation steps to obtain: (a) solid foam and (b) different types of dry gels.

The wet gel possesses a 3D interconnected framework, but filled with a solvent that often has residual precursors of the gel. To obtain dry aerogels, the fluid from the voids must be removed and replaced with air, while maintaining the structure. The method used for the extraction of the liquid defines the characteristics of the final material. The most applied techniques are:

- ***Air drying:*** The liquid phase in the gel is removed by evaporation. To avoid the collapse of the structure the reinforcement of the structure with cross-linking agents is necessary. Still significant shrinkage (>30 v%) occurs which causes the formation of high-density products that are named as **xerogels**.[35]

- ***Lyophilization or freeze-drying:*** the hydrogel is frozen at around 223 K / 193 K. Then, mild temperature is applied to provide enough energy to induce the phase transition of the frozen water molecules. The heat is applied under high vacuum to favor the solid to gas transformation. Solvent sublimation is performed slowly, in a lasting-time process, to avoid the damage of the structure. By reducing the sublimation temperature and extending the time, the forces exerted towards the walls of the pores are minimized, reducing the shrinkage (<10 v%) with respect to air drying. The porosity of the aerogel is strongly related with the shape and size of the generated ice crystals. Typically elongated, large mesopores and mostly macropores are generated, thus the materials present low values of surface area.[36] The growth of ice crystals during freezing is accompanied of a volumetric expansion, which induces stress on the pore walls, thus triggering the formation of cracks in the monolithic piece, leading, eventually, to the formation of dried gel powder.[37] Products prepared by this technique are called **cryogels**.

- ***High temperature supercritical drying:*** the temperature and the pressure of the gel are raised above the critical point of the applied solvent. Hydrogels cannot be used in this method for practical reasons, since supercritical water has the critical point at 647 K and 21.8 MPa, presenting extremely high acidity. The water in the gel must be first interchanged with a low molecular weight organic solvent, such as methanol (512 K, 8.1 MPa), ethanol (516 K, 6.4 MPa) or acetone (508 K, 4.8 MPa). The appearance of surface tension and destructive capillary forces created upon air drying is here eliminated, allowing to maintain the 3D framework of the gel, with only slight shrinkage (<10-15 v%). These products are called **aerogels**, are highly porous (even values of 99.7 v% can be reached), with high values of surface area, and an interconnected pore structure.[38] Despite of the

superior properties, the application of harsh conditions brings up environmental and economic concerns.

- Low temperature supercritical CO$_2$ drying: To overcome the problems encountered with using high temperature supercritical drying, alternatively, supercritical CO$_2$ (scCO$_2$) can be used to produce **aerogels**. In this case, scCO$_2$ is replacing the gel solvent present in the pores. Again, the lack of liquid-vapor transition upon the elimination of the mixture prevents pore collapse. This methodology has been applied for various types of aerogels (*e.g.,* cellulose,[39] silica or starch[37]), and in all cases a separated gelling step preceded the drying procedure. Similar to high temperature supercritical drying, high porosity and surface area and open pore structure characterize the aerogel.

3. Aerogels

Comprehensively defining aerogels is rather challenging due to the large diversity regarding the preparation methods and the properties of these materials. The name "aerogel" refers to the network constituting the solid framework (gel) and the air filling the pores (aer). The definition stablished by IUPAC in 2007 stablished that "aerogel is a gel comprised of a microporous solid in which the dispersed phase is a gas".[40] The same publication gives microporous silica, microporous glass and zeolites as examples of aerogels. However, this definition does not describe accurately most materials that are already assigned as aerogels, many of them possessing multiscale porosity in the micro-/meso-/macropore range. Several intents have been made recently to propose a more comprehensive description that discern aerogels from other porous and cellular solids. Some of them are focusing on the preparation method, describing aerogels as those fabricated by methods involving sol-gel chemistry.[18,41] This definition excludes aerogels originated by self-assembly, like some polymers or graphene derivatives. Other terminologies emphasized some unique properties as the requirement to be named aerogels,[42] for instance, the maintenance of the pore structure upon drying. In this definition the controversy arises from the determination of the shrinkage, unavoidable to a certain extent during the synthetic procedure, that can be accepted. The definition chosen in this thesis was suggested in 2019: "aerogels are light solids, with an open-porous network of loosely packed, bonded particles or nano-scale fibers, obtained from a gel after the removal of the fluid from the pores without significant structural modification".[43] This definition describes adequately the materials prepared in this thesis.

Aerogels can be classified on the basis of appearance, composition and microstructure (Figure 5). Based on their appearance aerogels can be classified, as monoliths, powders or films. Often their solid structures involve a mixture of micro-, meso- and macropores. Numerous aerogel structures, made of a large variety of organic and inorganic species, have been fabricated throughout the almost 100 years of aerogel history. Following, the most remarkable, and those that were prepared in this thesis, are detailed.
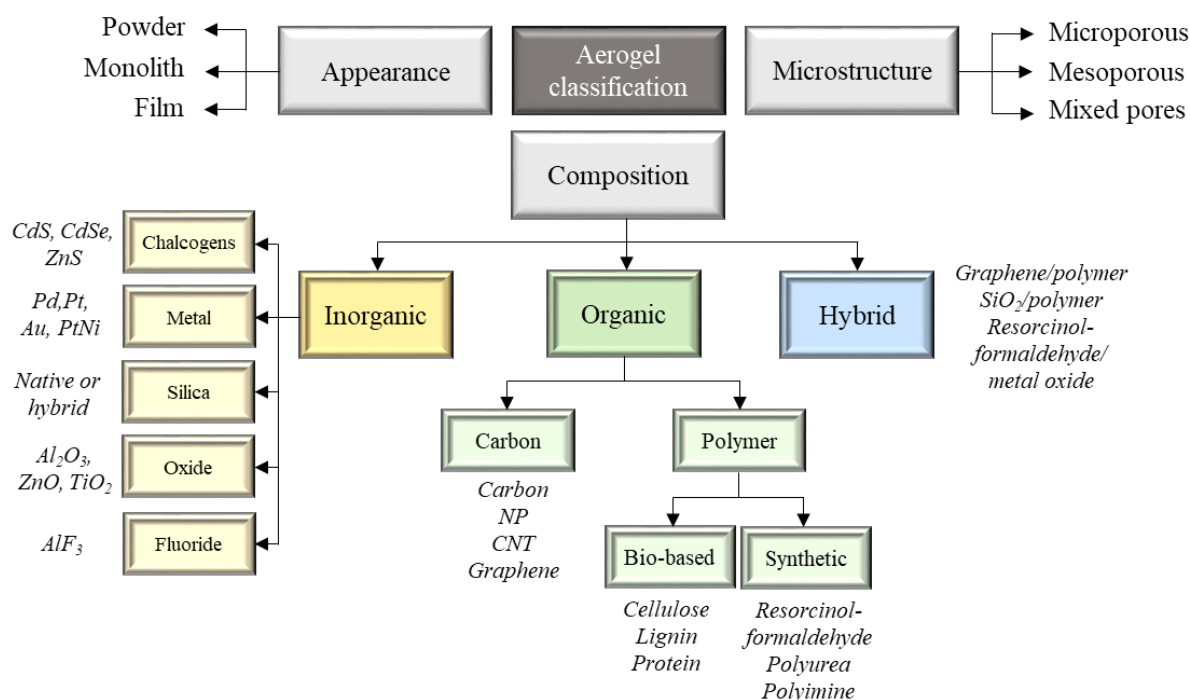
Figure 5. Aerogel classification based on appearance, composition and microstructure.[44,45]

3.1. Silica

Undeniably, the most well-known and frequently seen in commercial applications are silica aerogels. For these aerogels, the solid matrix is composed of a sol of silica particles, in which the arrangement and interconnection of the NPs determines the main properties of the macroscopic structure. The preparation procedure was established by S. Kistler, using sodium silicate to form silicic acid, which further polymerizes to silica gel (Figure 6a).[18] The hydrolysis reaction is driven by acid or base catalysis, and the pH of the media determines the gel quality. At low pH long polymer chains are formed, with few crosslinks, while in a basic environment branched polymeric structure is formed.[46] In a different procedure, silica gels are formed by hydrolyzing silicon alkoxide precursors in an acid or based catalyzed reaction.[47] Simultaneously, alcohol and water condensation reactions take place forming siloxane bonds

(Si-O-Si) (Figure 6b). During aging, the silica gel network is strengthened by further condensation.

a)

$$Na_2SiO_3 + 2\ HCl + H_2O \xrightarrow{\underset{catalyst}{Acid\,/\,base}} Si(OH)_4 + 2NaCl$$

$$[Si(OH)_4]n \xrightarrow{\underset{catalyst}{Acid\,/\,base}} n\left[\begin{matrix} & OH & & OH & \\ & | & & | & \\ OH-&Si&-O-&Si&-OH \\ & | & & | & \\ & OH & & OH & \end{matrix}\right]\cdot + 2n\ H_2O$$

b)

$$[Si(OR)_4] + 4\ H_2O \longrightarrow Si(OH)_4 + 4\ ROH$$

Water condensation

$$-\,Si-OH + HO-Si- \longrightarrow\ -\,Si-O-Si-\ +H_2O$$

Alcohol condensation

$$-\,Si-OH + CH_3O-Si- \longrightarrow\ -\,Si-O-Si-\ +CH_3OH$$

Hydrogel

drying
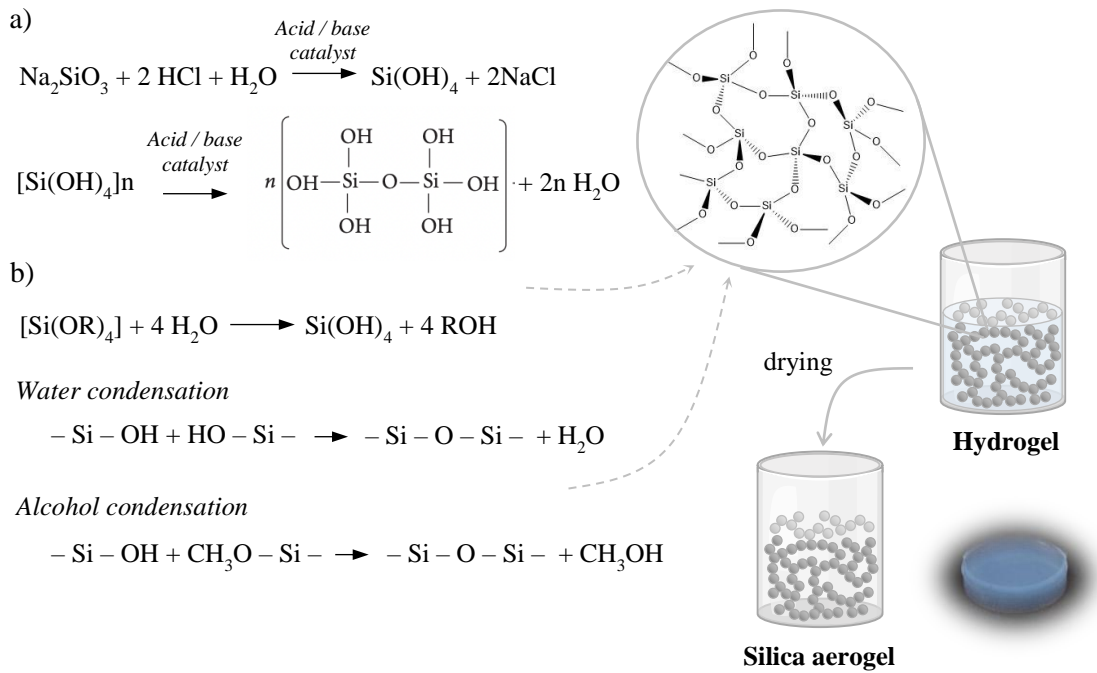
Silica aerogel

Figure 6. Preparation procedures to obtain silica aerogels: (a) starting from sodium-silicate and (b) silicon alkoxide precursors.

In both described procedures, to dry the wet gels, supercritical and freeze-drying methods have been established, resulting in aerogel and cryogel end-products, respectively.[46] In contrast to other aerogels, silica aerogels can be obtained with proper surface properties by using ambient pressure drying. This is usually achieved after the modification of the surface by replacing the hydrogen on the surface silanol groups (Si-OH) by hydrophobic alkyl or aryl functional groups. Thus, condensation reactions are prevented, which decreases the shrinkage of the gel during the drying procedure.[46]
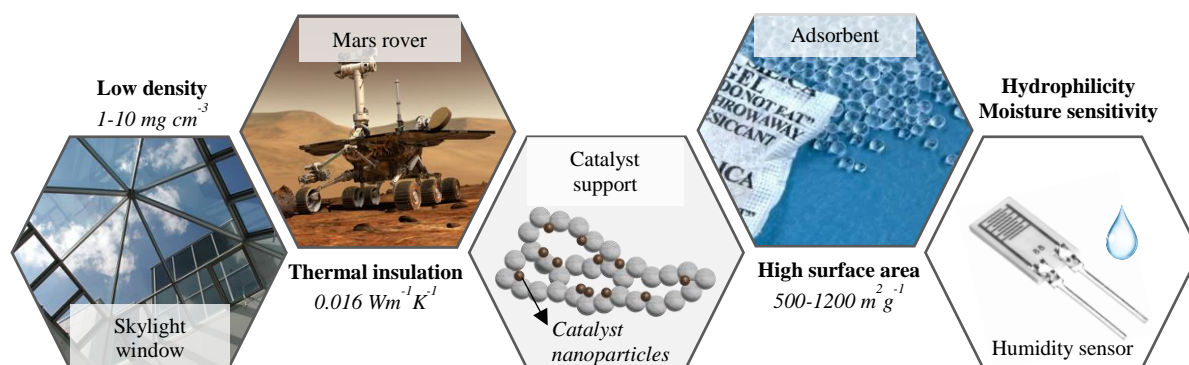
Figure 7. Properties and some applications of silica aerogels.

In most silica aerogels about 80 v% of their body is composed of pores, but this value can reach up to 99.8 v%.[48] Described surface area values are within the 500-1200 m^2g^{-1} range, making them excellent adsorbents for environmental clean-up or as catalyst supports, among other applications.[49] Due to their extremely low thermal conductivity, they are used as thermal insulation materials for skylight windows or heat storage devices.[50] These features, together with their low density, made them an attractive candidate for the aerospace industry. For instance, it was used in the Mars missions for the insulation of the battery packs in the Mars Rover. Moreover, particulated silica aerogels are added as a filler in spacesuits or dresses for Antarctic missions, since they provide protection against any extreme thermal condition.[51] Another representative property, beneficial only in certain applications, is their hydrophilicity, sourcing from the high amount of unreacted silanol groups (Si-OH) on the surface of the skeleton. Taking advantage of the high moisture sensitivity, humidity sensors have been fabricated based on silica aerogels.[52] Nevertheless, this property can also be a weakness for this type of materials, as small amounts of water, or even the humidity of the air, force the collapse of the solid network. For this reason, often the hygroscopic character is tuned by functionalization of the silanol groups with hydrophobic moieties. One important drawback of these aerogels is their significant fragility and poor mechanical properties arising from the rigid Si-O-Si bonds in the solid framework.[53] For practical applications, the framework can be reinforced by establishing carbon bonds between the silica NPs through the incorporation of polymeric system in the matrix. Other methods, such as the aging of the wet gel or hybridization by co-gelation with organic matter, are also used for strengthening purposes.[54] Nevertheless, it should be taken into account, that along with the increase in the mechanical robustness, usually other properties, such as the thermal conductivity or low density, change in an unfavored way.

3.2. Polymeric

The methodology to form polymer aerogels is similar to those previously described.[55] Gel formation typically starts with the dissolution of the monomers in a solvent, which is followed by the formation of solid colloidal particles through the establishment of chemical bonds between the monomers. Most frequently, hydrolysis and polycondensation of the precursors induces the generation of colloidal clusters. Then, as the polymerization follows, the colloidal particles link to each other, forming a 3D network of the polymeric chains (gel). During the ageing period, the structure is reinforced due to the still ongoing polycondensation, thus increasing the connectivity. Finally, the solvent in the pores of the wet gel is removed by any of the typical drying procedures. Polymer aerogels can be produced with very little shrinkage and possess better mechanical stability in comparison to silica aerogels, due to the robust network and strong chemical bonds.

Polymer-based aerogels can be divided to those prepared from synthetic and from biobased polymers (Figure 5). Synthetic polymer aerogels are synthesized via sol-gel polymerization of phenolic resins (*e.g.,* resorcinol-formaldehyde RF), polyureas, polyimides, polyamides, *etc.*[56] The most famous representative is the RF aerogel, prepared by series of aqueous polycondensation reactions between formaldehyde and resorcinol.[57] Initially, the addition of formaldehyde to resorcinol occurs in the presence of a mild base catalyst (Figure 8a). Then, at elevated temperature, the polycondensation occurring between the aromatic and aliphatic hydroxyl groups form a 3D crosslinked network, composed of the aromatic rings linked by ether and methylene bridges (Figure 8b). The cross-linking reaction and chain growth take place before gelation, which is later followed by gel drying.[58] The structure of the RF aerogels is influenced by the size and the number of the resorcinol-formaldehyde clusters, formed during the polymerization step, which is primarily influenced by the reaction parameters. Generally, RF aerogels are mesoporous, presenting high surface area values (*ca.* 1000 m^2g^{-1}).[59] Synthetic polymer aerogels have found widespread commercial application uses, *e.g.,* adsorption, catalysis, ion-exchange resins, chromatographic separation, *etc.*, but their insufficient biodegradability, and often toxic precursors/degradation products raise concerns regarding their sustainable use.[58]

a) Addition:

b) Condensation:

Cross-linked polymer
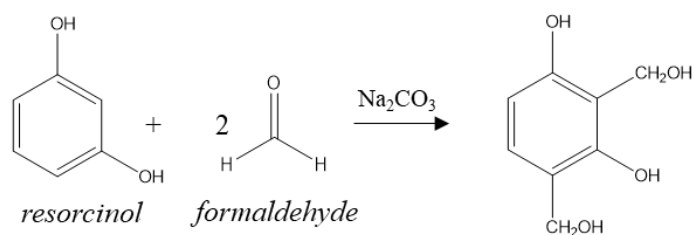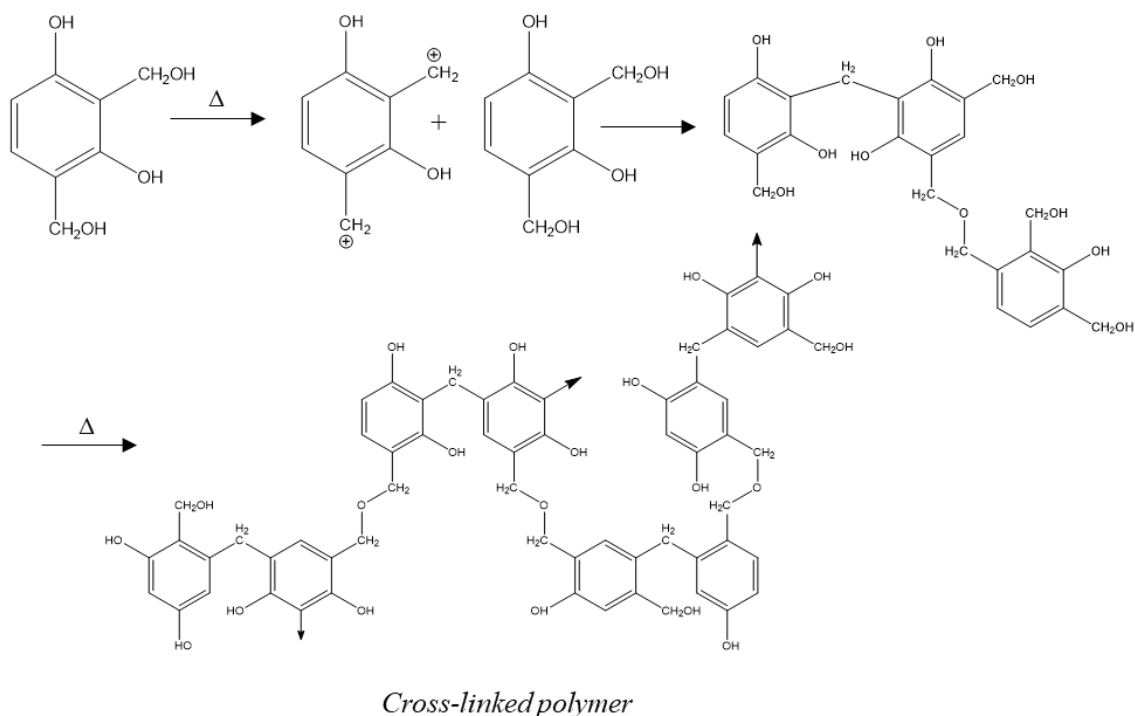
Figure 8. Preparation of resorcinol-formaldehyde polymer involving: (a) addition and (b) polycondensation reactions.[57]

Nowadays, biopolymer-based aerogels are receiving enhanced attention due to their cytocompatiblity and biodegradablity.[45] They are prepared from renewable sources (sugar cane, protein or starches) or from certain biopolymers (chitosan, alginate, cellulose, lignin). Among these, cellulose aerogels were first prepared, and are characterized by their high impact resistance and capacity to be cross-linked.[18] The second most abundant biopolymer after cellulose is lignin, but with only very little utilization worldwide as a resource.[60] This fact, together with the rigidity of the macromolecules presenting numerous functional groups, make lignin aerogels an attractive option. The obtained structures show strong mechanical performance with still significant compressibility. Owing to their biocompatibility, these

aerogels are primarily applied in the biomedical field, such as in tissue engineering, drug delivery, implantable devices or wound dressings.[45]

Polymer-based hybrid aerogels

Polymers in aerogel structures are often used to improve their robustness and avoid cracking and shrinkage during drying, with the aim of providing sufficient mechanical stability for further application. Hybrid aerogels have been built using polymers and an inorganic phase, such as silica NPs, carbon nanotubes (CNT), graphene flakes, *etc*.[55] the preparation method, the polymer can be added directly to the dispersion of the inorganic phase, or the polymerization can be triggered from suitable monomers after gelation.[61]

3.3. Carbon-based

Carbon aerogels have been constructed with elements as diverse as amorphous carbon NPs, CNTs, carbides, carbonitrides, graphene flakes or even nanoparticles of diamond.[62–65] These aerogels display very low density values, close to that of air. Actually, a carbon-based aerogel has been described as the lightest material known on Earth, with a density of 0.16 mg cm^{-3}.[66] Moreover, some of these aerogels possess extremely high surface area, up to 3000 m^{2}g^{-1}, and are electrically conductive.[67] By customizing the preparation methodology, the bulk and surface properties of carbon aerogels can be conveniently tuned, satisfying the demand for diverse applications in the areas of energy, such as fuel cells and supercapacitors or the design thermal and sound insulators, catalytic supports and chemical adsorbents.[68,69] The most relevant carbon-based aerogels, classified on the basis of the nature of the carbon precursor used for their preparation, are described in the followings.

3.3.1. Amorphous carbon

Amorphous carbon aerogels are made of amorphous carbon NPs. This type of materials was initially prepared by the pyrolysis or carbonization of organic polymeric aerogels.[63] As a precursor, beside the traditional RF aerogel, aromatic-aldehyde pairs, or biomass derivatives, such as saccharides, have been recently used.[68,70] The carbonization step is carried out in a range of 773 - 2773 K in an inert atmosphere. Applying these high temperatures, some densification of the structure is observed, but compensated by the outstanding electrical conductivity that can be obtained. The interconnected polymeric clusters provide the skeletal network in the amorphous carbon aerogels, involving a large amount of micropores formed within the primary particles and by the agglomeration of those, while abundant mesopores are simultaneously

generated by clusters aggregation.[71] In fact, the micropore characteristics are influenced primarily by the carbonization procedure, while the meso- and macropores are determined mostly by the gelation/drying conditions of the precursor.[68] Although the pyrolysis of organic aerogels continues to be a widespread technique for obtaining carbon-based aerogels, for more than a decade now highly sp^2-hybridized carbon species (*e.g.*, CNT or graphene) are used as precursors. These aerogels, contrarily to those derived from organic species, are composed of primary carbon units with certain crystallinity, and have improved transport and mechanical properties.[63]

3.3.2. Carbon nanotube

CNTs are empty cylinders composed of either one-layer (single-wall) or multiple concentric layers (multi-wall) of hexagonally arranged carbon atoms. Due to their unique arrangement, CNTs already possess extraordinary properties in their 0D individual form, such as strong rigidity and high electrical conductivity. CNT aerogels can be fabricated by the self-assemble of CNT nanoentities, usually using surfactant (*e.g.,* sodium dodecylbenzene sulfonate) to improve their dispersibility in the solvent. The drying of the gel is carried out with freeze-drying or supercritical drying.[72] The establishment of electronic interactions among the separated nanotubes makes possible the fabrication of porous aerogels using exclusively CNTs, although the van der Waals forces often do not result in sufficiently robust structures. To stiffen the aerogel, binders, often made of carbonaceous materials, and polymers can be incorporated within the framework. These additives cross-linked the CNTs in the aerogels, while maintaining the porous character. Some described CNT aerogels reinforced with polyvinyl-alcohol can support weights three orders of magnitude higher than their own mass.[72] Nevertheless, the incorporation of organic additives compromises other properties, such as conductivity, which could affect some of the intended applications. Electrodes, catalysts or sensors have been fabricated from these structures.[63,72]

3.3.3. Graphene and graphene oxide

First of all, the discrimination between reduced graphene species and the oxidized forms should be always taken into account, as their physicochemical properties, processing methods and applicability are different. Individual graphene sheets, reduced and oxidized, are two-dimensional structures, formed by the in-plane hexagonal arrangement of carbon atoms. Structural defects in the form of both in-plane and out-of-plane displacements, and/or oxygenated functional groups, enrich the planar structure (Figure 9a).

a)

b)   carboxyl group

c)

epoxy group   hydroxyl group   thermal / chemical reduction
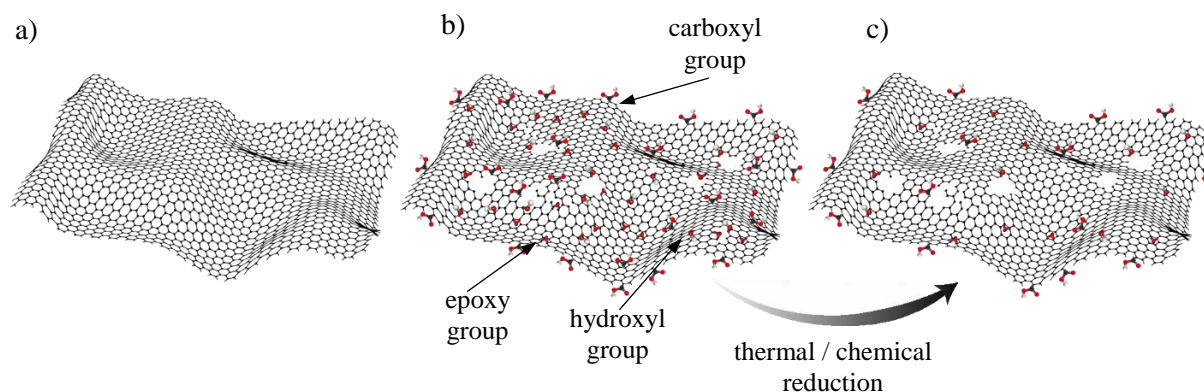
Figure 9. Illustration of: (a) 2D graphene, (b) graphene oxide and (c) reduced graphene oxide (GO) sheets.

The high theoretical surface area of single-graphite layers (>2500 m^{2}g^{-1}), electrical conductivity and chemical, mechanical and thermal stability are some of the characteristics that provide the basis for several potential applications of this material.[73] For ensuring such outstanding properties, a 2D planar lattice structure needs to be achieved in the graphene structure, which is concomitant with the absence of any oxygenated functional group distributed over the surface. One of the most interesting attribute of the oxygen-rich form, the graphene oxide, is that oxygen containing functional groups are decorating the basal plane (mainly hydroxyl and epoxide) and the edges of the GO sheets (mainly carboxyl) (Figure 9b).[74] The oxygenated surface chemistry provides the possibility of establishing an increased number of electrostatic, or, in specific cases, covalent interactions, with a wide variety of substances, making GO a multipurpose material able to modify and enhance the properties of designed hybrid or composite materials. An important feature of the oxygenated graphene is their convenient dispersibility in polar liquids. However, other characteristics, such as the electrical conductivity, are compromised by the oxygenation of the graphene sheets.[75] To acquire the desired oxygenated character, GO can be reduced in a post-synthetic treatment, in which by choosing the reduction method and experimental conditions fine tuning of the final oxygen content is possible (Figure 9c).

An important drawback common to graphene derivatives, *e.g.,* graphene, graphene oxide and reduced graphene oxide, is the significant loss of surface area occurring due to the stacking of the flakes during processing. This typical behavior is the result of the high number of π-π interactions established between the layers. Keeping the 2D layers exfoliated by forming a 3D aerogel structure is a suitable way to hinder this detrimental phenomenon.[74,76] Apart from

reducing the stacking, extended functionalization with organic or inorganic entities becomes feasible in the 3D porous structure (Figure 10). These aspects, together with the generated pores within the structure, are especially beneficial in adsorption and catalytic applications, allowing appropriate contacts between the reactants and the surface. Finally, 3D monolithic structures can be created with the desired shape, since the starting precursor is a liquid gel. Thus, personalized aerogels for specific application can be fabricated.
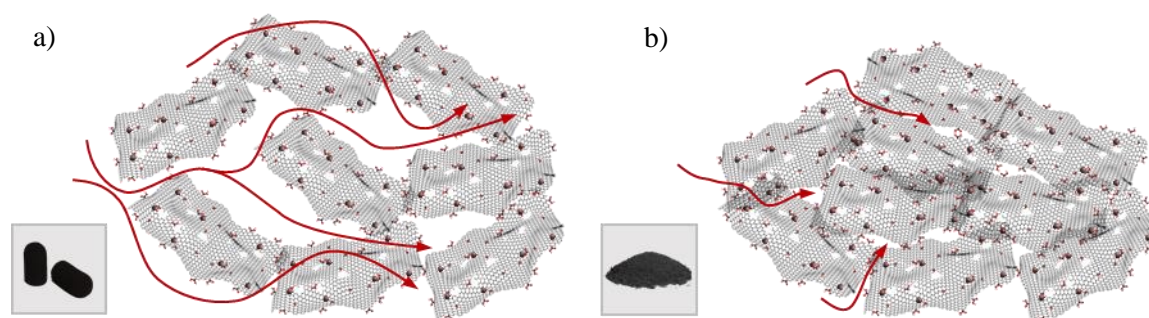
Figure 10. Accessibility of the internal structure for: (a) 3D aerogel with exfoliated GO flakes, and (b) GO stacked flakes.

3.4. Synthesis of graphene derivatives aerogels

GO is traditionally fabricated from graphite, an abundant mineral, following the Hummers' method.[77] In this process, typically strong oxidizing agents ($NaNO_3$, $KMnO_4$, H_2O_2) are used to obtain graphite oxide by the generation of oxygen species, mainly epoxides, carboxyls, carbonyls and hydroxyls, on both sides of the graphitic layers. Aqueous acidic conditions (H_2SO_4, H_3PO_4, HCl) and sonication are used to exfoliate graphite oxide, obtaining a graphene oxide dispersion. The incorporation of the oxygenated functionalities induces a significant increase in the interlayer spacing by overcoming the van der Waals forces. Indeed, the interlayer separation becomes approximately double, from 0.3 to 0.6 nm. It is worth to mention that total exfoliation cannot be achieved, and the system is often constituted by GO clusters of few-layers width. During the oxidation of graphite, the aromatic lattice is partially distorted generating defects along the flakes. Most research regarding GO preparation usually focuses on the type of functional groups added to the surface and the amount of those, tuned by using different oxidizing agents and processing conditions. Moreover, the process must be scalable and environmentally sustainable.[78–80]

Aerogels can be formed from stable suspensions of GO by gelation and drying in a multistep procedure.

The most common gelation mechanisms are:

- ***Hydrothermal reduction:*** the gelation of water dispersed GO flakes is carried out in an autoclave at high temperature (373-473 K) and pressures higher than the atmospheric. During the hydrothermal treatment, the reduction of the GO flakes occurs, since the oxygenated groups are mainly eliminated from the structure. The reduction promotes the assembly of the flakes into a 3D framework. The hydrogel properties can be well-controlled by choosing the applied experimental conditions, or even with the addition of cross-linking agents.[81]

- ***Chemical reduction:*** a chemical agent induces the reduction of the GO sheets and their self-assembly in a gel. Reducing agents, such as vitamin C, ammonia, ethylenediamine (EDA) or hydrazine, are applied. Gels prepared with different reducing agents possess different properties. For instance, EDA, besides the reducing ability, also functions as a cross-linker agent between the formed rGO sheets, providing stable aerogels with enhanced conductivity after the drying.[82] Vitamin C, being a relatively strong reducing agent, facilitates the formation of highly hydrophobic gels.[83–85]

- ***Cross linking methods:*** The aim of these methods is to enhance the interactions between GO flakes. An easy way of achieving this effect is by acidifying the medium, thus increasing the number of protonated oxygen moieties and hydrogen bonding. Incorporating additives, containing hydroxyl, oxygen or nitrogen functionalities to establish more H-bonds between the GO sheets, is also a feasible way to facilitate gelation. Besides, metallic ions, small organic molecules or even biomacromolecules (polysaccharides, proteins, DNA) have been also used for increasing the number of chemical/physical interactions in the gel.[83,86]

- ***Polymer incorporation:*** The gelation of GO can be supported by polymers able to chemically bind to the GO layers, thus generating steric hindrance and avoiding stacking of the flakes.[87] Additionally, by using conductive polymers, charge transfer properties can be largely augmented.[88]

All typical drying procedures (detailed in section 2.2.2.) have been applied to obtain dry gels of graphene/graphene oxide from hydrogels/alcogels. From them, air-drying requires the previous reinforcement of the structure, usually achieved by polymer addition.[89] Robust structures have been built by vacuum-drying, but with high aerogel density in the order of 0.6-1.2 g cm^{-3} (Figure 11).[90] Nonetheless, it is worth to mention that no extensive research on pure graphene xerogels can be found in the literature.
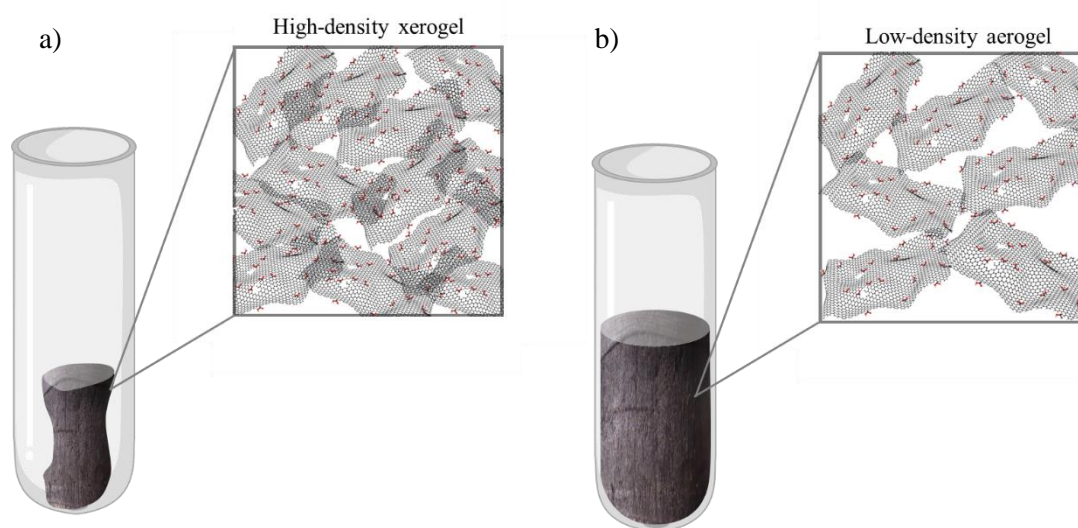
Figure 11. Structures of graphene: (a) xerogel and (b) aerogel.

Freeze-drying causes lower damage in the graphene cryogel structure due to their relatively larger mean pore size (meso/macro) in comparison to the silica aerogels with smaller mesopores. Thus, the former is more resistant to volume expansion when ice crystals are formed. These cryogels usually have relatively low surface area resulting from the lack of microporosity and small mesopores.[91] Graphene cryogels can be obtained directly from GO dispersions, by slightly acidifying the liquid medium to induce gel formation. This method has been used because it was the only procedure where most of the oxygen functionalities on the GO sheets were preserved. However, the obtained products are brittle without sufficient mechanical stability for most applications.[61] In case freeze drying is preceded by hydrothermal gelation, stable graphene cryogels are obtained. However, the high-temperature used in the hydrothermal procedure leads to the formation of cryogels of reduced graphene oxide. Graphene aerogels can be obtained by simultaneous gelation and drying at high temperature and pressure, *e.g.,* above the critical temperature and pressure of the dispersing fluid. This supercritical drying provides graphene aerogels in which the oxygenated groups have been

eliminated, but with fine and uniform pore morphology (Figure 12).[38] Due to the harsh conditions, the reduction of the oxygen functionalities on the GO sheets always take place.
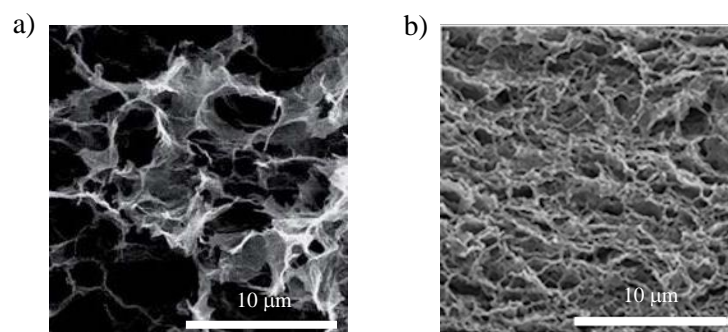
Figure 12. Electron microscopy images of graphene aerogels showing the different pore morphology obtained by: (a) freeze-drying[85] and (b) high temperature supercritical drying using ethanol. Images are adapted.[38]

In the previously mentioned preparation methods, either the GO flakes were reduced throughout the process (high temperature, reducing agent), or extremely brittle monoliths were obtained (one-step freeze-drying). Maintaining the oxygenated character of the aerogel, while providing reasonable robustness, was a problem solved by defining a specific preparation procedure based on supercritical CO_2, established in the group in which this thesis was performed (SFFM group, ICMAB-CSIC).[92] As an additional advantage, and in contrast to most previously mentioned procedures, in the scCO$_2$ process the gelation and drying occurs in one-step inside the same high-pressure reactor.

In the general scCO$_2$ procedure, the dispersion of GO in a convenient solvent (usually a short-chain alcohol, such as ethanol or methanol) is treated with supercritical CO_2 at high pressure (20 MPa) and mild temperatures (313-333 K) (Figure 13). Due to the addition of CO_2, the alcoholic suspension is acidified diminishing the electrostatic repulsion between the oxygenated functionalities on the flakes surface. Consequently, the flexible oxidized graphene layers can partially overlap with each other, opening the possibility for the establishment of an increased number of contact points, which finally results in a self-assembled GO framework. The macroscopic 3D structure is stabilized by both π-π interactions between the basal planes of the carbon atoms and hydrogen bonds established by the functional groups. During gel aging (*ca.* 48 h), the alcohol in the pores is replaced by scCO$_2$ in a continuous, relatively slow procedure, until the concentration of the alcohol is equal within and surrounding the gel. The solvent interchange is favored by the high diffusivity of the supercritical fluid and the specific solubilizing capability of scCO$_2$ for short-chain alcohols. However, the shaping of the 3D

network is slow, since aerogels recovered under the used experimental conditions at a shorter reaction time (*e.g.*, 24 h), are often collapsed structures. Finally, the solvent is slowly (*ca.* 0.5 mL min^{-1}) released from the reactor under isothermal conditions, avoiding the materialization of capillary forces. During pressure release, the temperature is maintained above the critical point of the media, thus the scCO$_2$ transforms directly to gas without the realization of a liquid-gas interphase in the fluid. The recovered product is a light-weight aerogel, able to withstand further manipulation. Its composition is unique in the literature, due to the applied low temperature and the lack of reducing agents, which results in the oxygen functional groups preserved on the surface of the graphene layers.
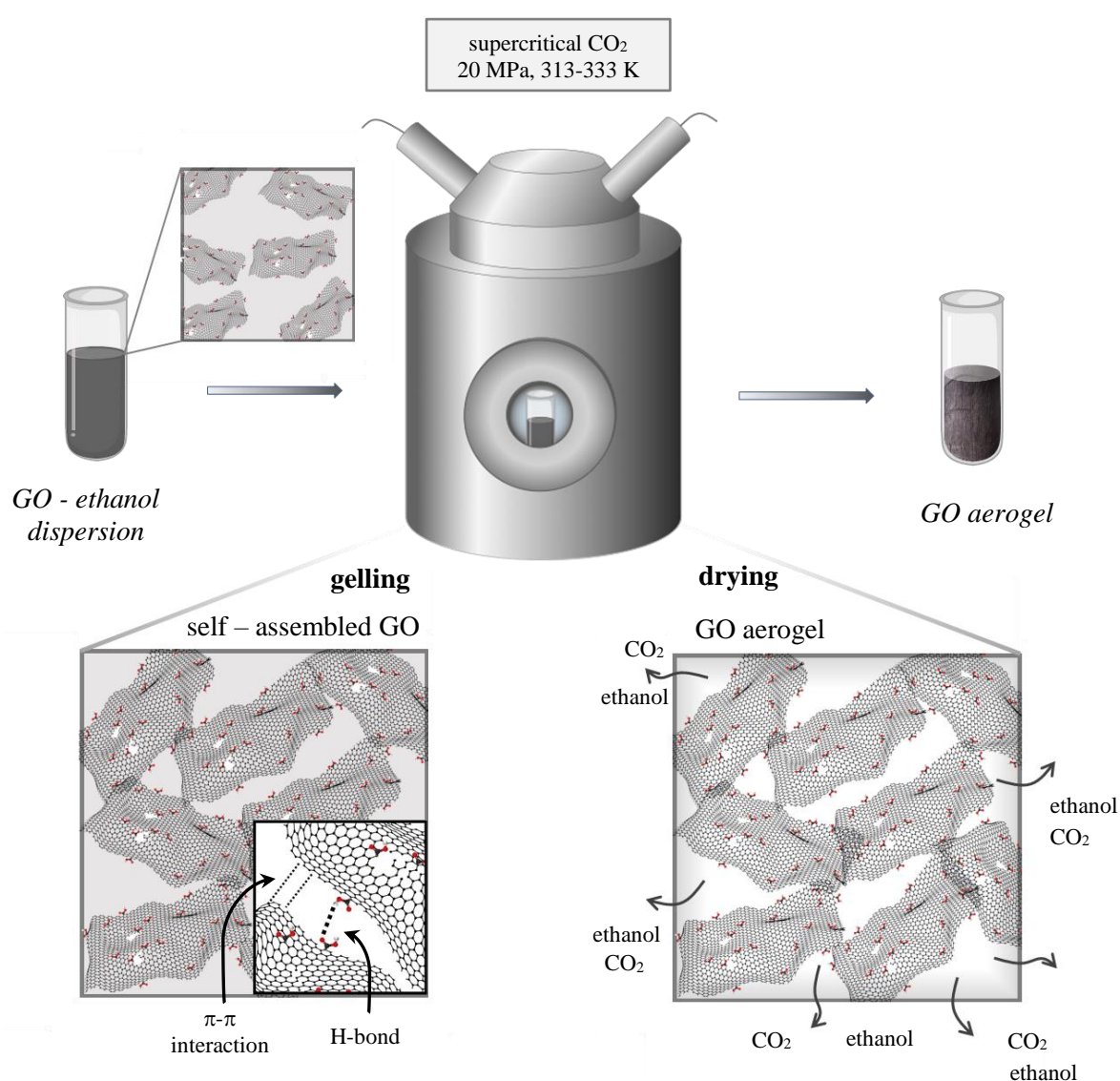
Figure 13. GO aerogel preparation in the one-pot scCO$_2$ procedure, involving gel formation and drying.

Properties and applications of graphene-based aerogels

Due to their unique properties, graphene-based aerogels are excellent candidates for application in emerging fields, such as energy storage, energy conversion and environmental protection. One of the most important uses of graphene-based aerogels is on efficient energy storage, probably one of the biggest challenges that humanity is facing in the next years. Supercapacitors have been proposed as potential solutions for energy storage due to their high specific power and long lifetime.[93] In this respect, graphene-based aerogels, with high surface area, porosity and ionic and electronic conductivity, offer enhanced specific power when used as electrode materials, being able to improve the energy density and specific capacitance.[94] Developing systems that are able to convert renewable energy to electrical power is an important step towards alleviating the current problems of huge energy consumption. Chemical fuel cells, biomass fuel cells and solar cells are able to directly perform this task through electrochemical processes, such as oxygen evolution, oxygen reduction and hydrogen production. All of these reactions are performed through catalytic processes, being the engineering of a proper catalysts required to enhance the catalytic efficiency. Graphene aerogels are able to positively contribute to such reactions either by acting as supports to distribute the catalyst or by themselves ensuring fast electron transfer on the conductive graphene layers and appropriate contact with the reactants due to their high surface area.[95] Finally, owing to the hierarchical porous structure, and the high surface area, graphene-based aerogels are able to adsorb pollutants, like toxic gasses from air, heavy metal ions or dyes from water or other contaminants.[96–98] Further potential applications rely on the excellent acoustic behavior of graphene oxide aerogel composites reinforced with polymers, obtained by their controllable pore size and orientation, capable of attenuate the incident sound waves.[99]

4. Metal-organic frameworks

This section aims to describe MOFs, the second family of porous structures prepared in this thesis. A general overview of these materials is first given, including the composition, some properties and common preparation methods to obtain MOFs. Then, the attention is turned to two particular sub-classes of MOFs: those containing mesopores and those that are lacking long range order (amorphous MOFs). Finally, some of the most important applications are presented, emphasizing those structures that belong to the previous two sub-classes.

4.1. General description

4.1.1. Structure

MOFs are hybrid inorganic-organic structures, composed of metal cations or clusters coordinated with polytopic (minimum ditopic) organic linkers. The extension of the composing units forms one- (1D), two- (2D) or three- (3D) dimensional structures, depending on the number and arrangement of the bonds between the metal centers and the linkers (Figure 14). Such arrangement is the consequence of the coordination geometry of the metal nodes and its ligands, and the steric characteristics of the linker.
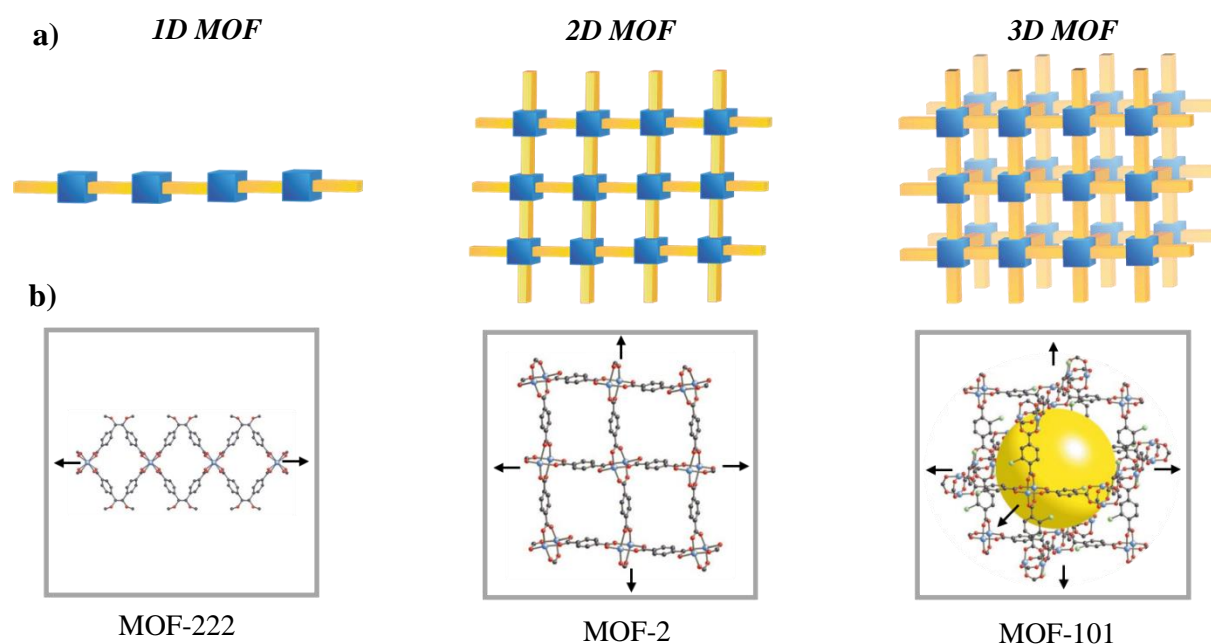
Figure 14. Structures of MOFs with different dimensionalities controlled by the linker geometry: (a) schematic representation of 1D, 2D and 3D structures, in which metal nodes are marked with blue squares, while yellow columns are assigned to the organic linkers, and (b) fragments of assembled described frameworks, corresponding 1D MOF-222, 2D MOF-2 and 3D MOF-101. Images of MOF structures are adapted.[100]

Regarding the void organization in the spatial dimensions, four types of porous structures can be distinguished: 0D cavities (refer to pores that are isolated from the others by the walls of the framework), 1D channels, 2D layers and 3D intersecting channels. The latter is formed by the interconnection of 1D channels directed in several directions (Figure 15).[101]
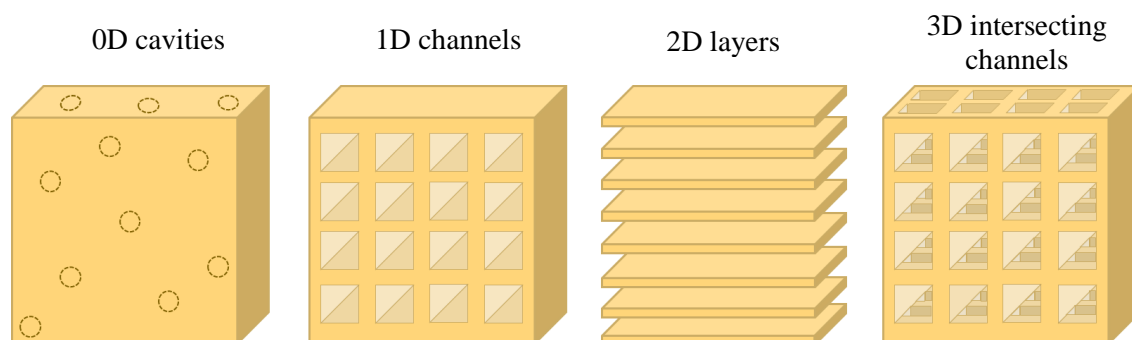
Figure 15. MOFs structures classified based on void organization.

The high variety of metal centers and organic linkers used as building blocks results in numerous possible MOF structures with the flexibility of constructing products with diverse physiochemical properties. In the last two decades more than 20000 different MOF structures have been studied and reported.[102] The following section deals with the choice of building units, giving some of the most common categories together with some examples.

Metal centers

Metal centers are key compartments of MOFs, as they are largely determining the topology and physicochemical properties of the end product. Most metals have been already applied as building units, although the most frequent choices are 3d transition metals and divalent or trivalent 3p ions.[103] In the first described MOF structures, single metal nodes were coordinated with ditopic or tritopic organic linkers. This is the case of one of the most studied MOF, the ZIF-8, where Zn tetrahedral nodes are coordinated with 2-methyl-imidazolate linkers (Fig. 16).
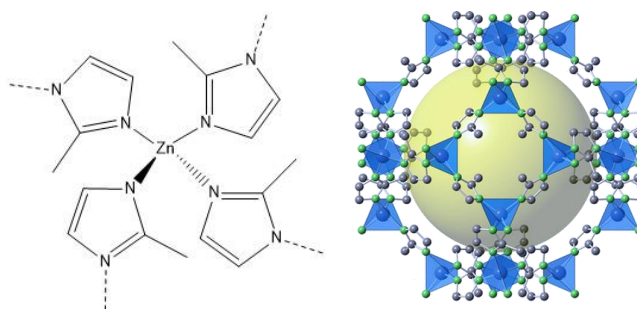
Figure 16. Coordination of Zn tetrahedral nodes with 2-methyl-imidazolate linkers forming the ZIF-8 framework. Images are adapted.[104]

Since then, the attention turned towards the substitution of single metals by polynuclear inorganic metal-based clusters, called secondary building units (SBU). SBUs are composed of metal ions (M) connected either *via* non-metal links, forming M-X-M bonds (X: N or O), or through common extension points, such as carboxylate units (M-O-C-O-M). This latter is actually the most typical case, offering a wide variety of clusters, with well-defined geometrical shape, for instance square or octahedron, guiding the end structure of the MOF.[105] SBUs are finite entities. One example is the octahedral SBU in MOF-5 composed of four Zn_4O tetrahedral complexes (Figure 17a). A well-known finite SBU is the copper/carboxylate paddle wheel cluster ($Cu_2(-COO)_4$) found in the HKUST-1 structure (Figure 17b). In the MIL-100(Fe) and MIL-101(Fe) MOFs, the metal-oxide nodes (Fe_3O), with trigonal prismatic coordination geometry, are giving the centers for a cage-like structure (Figure 17c).[106] Additionally, infinite metal cluster units in one dimension (referred as rods) can also be positioned among the polytopic linkers. A representative example of this structure is the MOF-71, where the SBU has the composition of $(Co_2O(-COO_4))_\infty$ (Figure 17d). In this case, the extension points are the carbon atoms forming a zig-zag shape and being able to coordinate ditopic linkers.[105]

a)

MOF-5
SBU

M₄O nodes with
octahedral coordination

b)

HKUST-1
SBU

Paddle-wheel nodes with
square coordination

c)

MIL-100
SBU

M₃O nodes with trigonal
prismatic coordination

d)

MOF-71
SBU

Rod-like structure
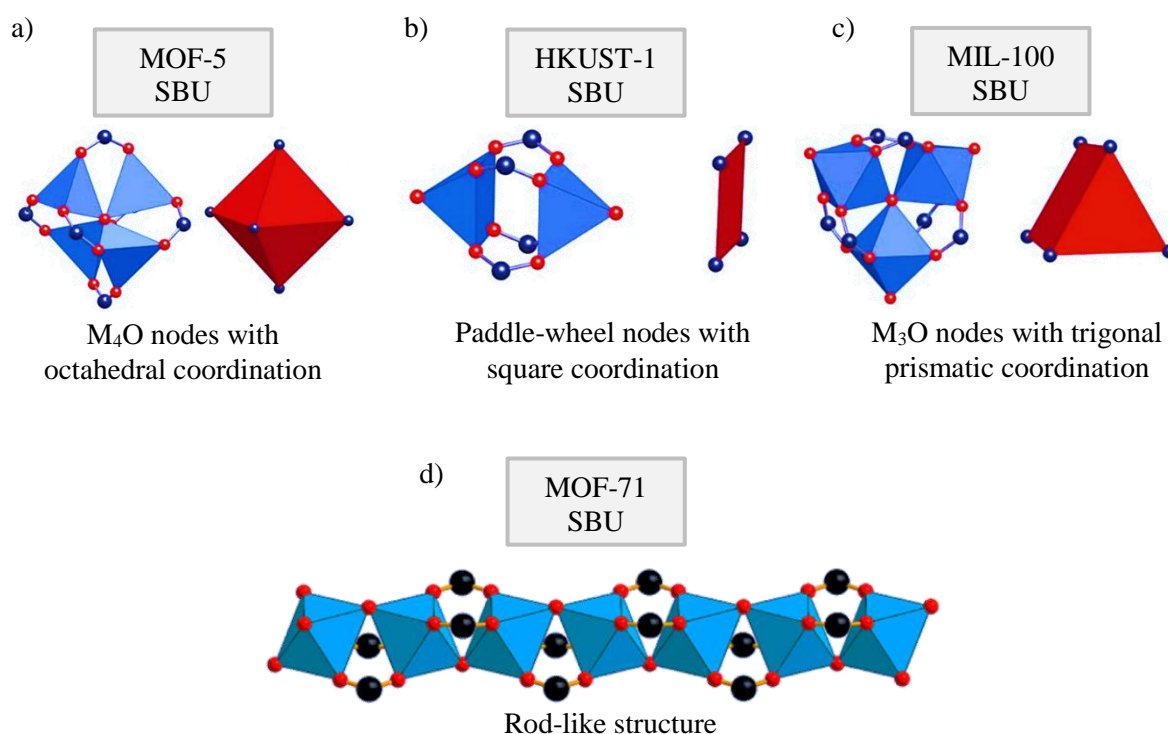
Figure 17. Examples of the inorganic SBUs from carboxylate MOFs and their coordination geometries: (a) MOF-5, (b) HKUST-1, (c) MIL-100(Fe), and (d) MOF-71. Metal-oxygen polyhedrons are blue, polygon/polyhedron defined by the carboxylate carbon atoms are red. Oxygen atoms are red, while carbon atoms are black. Images are adapted.[100,105]

The previous examples show the importance of the innovation given by the development of SBUs, in which the large number and variety of provided coordination points secure the position of the metal centers, and ensures a thermodynamically and mechanically stable environment, but still a flexible framework.[107] In addition, modifications, such as alteration of certain cations, changing their oxidation state or generation of defects within the SBUs, further increases the diversity of the produced MOFs.[108]

Organic linkers

Currently, databases with a large number of organic linkers are available to choose the most suitable for the desired structure, taking into account the length, geometry, functionalities, number of electron donors, *etc.* In principle, any organic molecule, having at least two donor atoms, which are capable of coordinating with metal centers, can be used as a linker. Typically, the donor atoms are oxygen or nitrogen, and most of the described MOFs involve homotopic organic units, where all the coordination ligands are of the same type. Most common linkers can be classified as carboxylate, nitrogen or azole, but apart from these, other organic anions, like sulfonates, phosphonates, or heterocyclic compounds, can also be linker molecules. Representative examples of these groups are listed in Figure 18.

A family of well-known MOFs is the one coordinated through carboxylate linkers. Clear examples are the ditopic 1,4-benzenedicarboxylate in the Zr-based UiO-66, and the tritopic 1,2,4-benzenedicarboxylate in the Cu-based HKUST-1. Among N-donor linkers, the series of di- and tripyridine molecules (*e.g.*, 4,4′-dipyridine; 2,4,6-tris(3-pyridyl)-1,3,5-triazine) is widely used to precipitate 1D and 2D MOFs.[109,110] 2-methylimidazolate, the building unit of ZIF-8, is a typical example of an azole linker. Beyond the most common categories, biologically related organic molecules have great potential in MOF chemistry. For instance, adenine nucleobase has been used as a rigid linker, with five potential binding sites, able to coordinate with metal nodes, offering augmented number of possibilities for coordination.[111] Using planar, relatively large, highly symmetric aromatic linkers is appealing for several reasons, such as their structural versatility, various options for functionalization and optoelectronic features. Widely used examples of this category, are the porphyrin macrocycles.[112]

a)

Precursors of carboxylate linkers

Precursors of azole linkers

Nitrogen linkers

1,4-benzene-dicarboxylate acid *(bdc)*

*1,3,5-benzene-tricarboxylate acid *(btc)*

2-methyl-imidazole

4,4'-dipyridine

2,4,6-tris(3-pyridyl)-1,3,5-triazine

b)

Biologically related linkers

Nucleobase linkers

Porphyrin-derived linkers

*5,10,15,20-Tetra(4-pyridyl)-21H,23H-porphine *(H₂TPyP)*

R=

R=

Adenine

4,4',4'',4'''-(porphine-5,10,15,20-tetrayl) tetrakis(benzoic acid) *(H₄TCPP(H₂))*

Figure 18. (a) Precursors of some commonly used organic linkers in MOF synthesis and (b) biologically related linkers. Those used in this work are marked with *.

There are plenty of possibilities to modify the macroscopic properties of the MOFs by tuning the characteristics of the linkers and metal nodes, as well as the number and type of coordination between them. The choice of the building units determines the strength of the metal-linker interaction, influencing the thermodynamic stability of the MOF. Carboxylate linkers tend to form strong interaction with high-valent metal ions (Zr(IV), Fe(III)), while soft N-donor ligands favor coordination to soft divalent metal ions (Zn(II), Cu(II)).[113] The coordination mode between the linkers and the metal clusters determines the dimensionality and the topology of the end product. For example, a V-shaped anionic ditopic linker most likely would grow in one

dimension with zig-zag chains, while linkers with several coordination sites favor structures with increased dimensionality.[114] The number of the coordination points in the linker influences the flexibility of the network. As a general rule, MOFs with few coordination points generate flexible bonds in the structure that can be bent easily, thus the structure is easily deformed; while highly coordinated topologies are rigid.[115]

4.1.2. Preparation methods

Apart from choosing the composing units, the appropriate synthesis protocol allows the fine-tuning of end MOF characteristics, such as porosity, particle size and morphology. The principal objective in MOF synthesis is to induce the assembly of the defined inorganic building blocks and the organic linkers into a 1 to 3D network. Nucleation and crystal growth can be controlled to achieve highly crystalline structures.[116] MOFs are frequently synthesized by solvothermal/hydrothermal methods, however other synthetic approaches such as mechanochemical, microwave assisted, electrochemical, spray drying, sonochemical, layering and $scCO_2$ synthesis have been used as preparation options (Table 1).

For the procedures performed in liquid phase, the protocol is the heating of a mixture of organic linkers and a metal salt/cluster in a solvent. In these cases, the control of the synthesis is difficult, since, even starting from the same mixture of precursors, often various products can be achieved by slightly modifying the reaction conditions, such as time, solvent, pH or temperature. All these experimental parameters also have strong influence on the yield, morphology, porosity, particle size, *etc*. Usually, applying mild temperatures is sufficient to form the coordination bonds, although this parameter influences the nucleation/crystal growth ratio, and thus the crystal size and morphology.[117] The pH of the reaction medium affects the number of coordination points available in anionic linkers due to the different deprotonation level. At high pH values, deprotonation is extended and the coordination number increases.[118] A strongly influencing parameter is the used solvent, which also impacts the linker deprotonation degree and rate. Different crystal structures are often achieved by modifying the solvent.[119] Among other effects, the solvent molecules can coordinate to the metal ions or fill void spaces within the network. In the latter, the removal of the solvent molecules is necessary to maximize the textural properties of the MOF. The activation is usually carried out using high temperature and vacuum, microwave irradiation or supercritical CO_2 treatment (Figure 19).[120]

Table 1. Summary of some of the most common preparation methods for MOFs, with the basic principles and characteristics related to the experimental conditions and product quality.

Preparation method	Short principles, source of energy	Characteristics
Solvothermal/ hydrothermal synthesis[121]	Metal precursor and organic linkers are heated in a high boiling point solvent (less frequently in water) in a closed autoclave. The source of energy for reaction is thermal.	- Most frequently used method - High crystallinity can be reached. - Reactions often take several hours/days.
Mechanochemical synthesis[122]	Metal salt and organic linkers are grinded in a mortar to induce the break of intramolecular bonds and chemical transformation.	- Environmentally friendly, as no solvent (or only a small amount) is used. - Fine particles are produced. - High yields -Low purity in many cases
Microwave assisted synthesis[123]	Metal precursors and organic linkers are heated in a high boiling point solvent. The reaction energy is provided in the form of microwaves.	- Fast crystallization - Narrow particle size distribution - Precise morphological control
Electrochemical synthesis[124]	Metal ions are supplied in the form of an anionic dissolution to the reaction medium that already contains the dissolved organic linker and a conducting salt. The MOF is formed on the surface of an electrode through an electrochemical reaction.	- Formation of homogenous MOF films - Mild experimental conditions, short reaction time
Sonochemical synthesis[125]	Metal precursors and organic linkers are dissolved in a solvent. Ultrasonic radiation is used to provide energy for nucleation.	- Homogenous, accelerated nucleation results in small particles. - Easy morphological control (with reaction time, reagent concentration, temperature) - Short reaction time
Layer by layer method[126]	Functionalized surfaces are sequentially immersed in solutions of either metal ions or organic linkers.	-MOF thin films with highly oriented growth can be prepared.
Layering[116]	Metal precursor and organic linkers are usually dissolved in two different, but miscible solvents, which are carefully added to a vial. Two different layers are obtained. Slow solvent diffusion induces the mixing of the reactants and the precipitation of the MOF.	- Large crystals can be obtained, as the crystal growth is favored over the nucleation. - Low yields - Performed at room or low temperature
Supercritical CO_2 assisted method[127,128]	Metal precursors and organic linkers are solubilized (or dispersed) in $scCO_2$ without or with the help or a so-solvent. The source of energy is thermal.	- Small particles precipitate - Environmentally friendly - Performed at low temperature
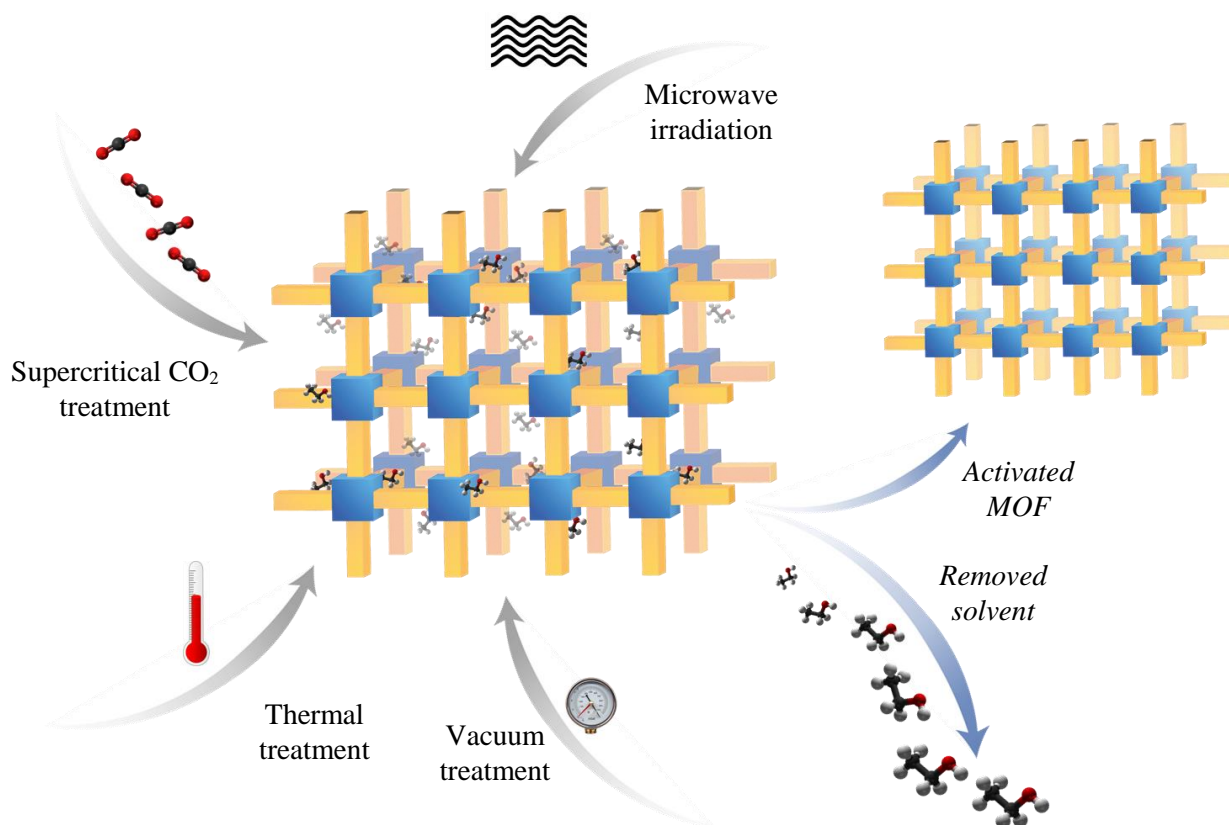
Figure 19. Typical methods for activating MOFs.

4.2. Mesoporous MOFs

4.2.1. Particular characteristics

Most MOFs have pores in the micropore range (<2 nm), hence, they display high micropore volume and large surface area values. Several advantages arise from these characteristics (*e.g.,* high adsorption capacity, structural stability). However, certain drawbacks are also entailed with such small pores.[33] Narrow pores are typically not able to accommodate relatively large entities (drugs, NPs, *etc.*), and the functionalization of the walls is also restricted. Fast diffusion and mass transport are hindered through the small pores, setting a limit to drug delivery, catalytic or gas separation applications. The design of mesoporous MOFs, with pores in the low range of mesosize, alleviate these limitations. Mesoporous structures with remarkable values of surface area, in the range of 2000-6000 m^2g^{-1}, have already been described.[129] Generally speaking, mesoporous MOFs tend to form more fragile frameworks than microporous MOFs, thus appropriate design is necessary to tolerate the instability arising from the large voids.[130] Based on the pore structure, channel-type and cage-type MOFs are distinguished in the family of mesoporous MOFs.[129] In the former, mesosize channels accessible at least from one, but often from three directions, are found. This is the case of the first mesoporous MOF, synthesized

by Yaghi *et al.*, the IRMOF-16 (Zn).[131] Cage-type MOFs have cavities of mesosize, which are often accessible through windows in the microsize range. Some of the most typical examples of this class are the members of the MIL family.[132]

4.2.2. Preparation methods

Beyond the general preparation methods to synthesize MOFs, there are specific strategies that can be considered to form MOFs with mesopores. Firstly, the choice of ligand and SBU is a crucial factor, because the network needs to be robust enough to support the large mesopores. Rigid linkers, such as aromatic molecules with limited flexibility are appropriate options, often containing carboxyl functional groups to provide sufficiently strong coordination. As for the SBUs, for instance robust polynuclear building units are suitable to form strong metal-oxygen bonds.[33] An apparent strategy to form MOFs with mesoporous cages is to incorporate large ligands in the framework using isoreticular chemistry to expanded MOF pores up to the mesosize, meanwhile to topology of the MOF is preserved (Figure 20).[133,134] Nevertheless, ligand extension has the drawback of interpenetration among different networks, which drastically reduce the textural properties.[130] Similarly to the organic linkers, the size of the metal nodes also influences the pore size and the rigidity of the framework.[135]

Another approach to increase the size of the cavities is to introduce mesopores into the microporous MOFs. This can be accomplished by stepwise ligand exchange, to progressively insert long ligands in the place of the short ones.[136] Forming a microporous MOFs with defective linkers can also result in large functionalized cages.[137] Kim *et al.* established a procedure, where MOFs with mesopores (3-20 nm) were formed by removing certain constituents from a microporous MOF by hydrolytic transformation.[138]

Hierarchical micro/mesoporous systems are also appealing for certain applications and their synthesis have been adapted following various approaches. Using surfactants as templates, ordered mesopores are generated within the microporous network.[139,140] Both hard and soft-templating methods have been used, followed of template removal. Disordered mesopores can be introduced within microporous MOF particles by gelation to obtain MOF gels, where the features arising from the MOF and aerogel structure are combined.[141] Several examples of MOF aerogels have already been presented, demonstrating elevated performance in multiple applications.[142–144] Nonetheless, the huge potential of these materials still remains unexploited due to the high number of structural variations, and pore diversity arising from the combination of ordered and disordered pores in different size ranges.

Organic linkers

4,4',4''-benzene-1,3,5-triyl-tribenzoate (**BTB**)	*4,4',4''-(benzene-1,3,5-triyl-tris (ethyne-2,1-diyl))tribenzoate* (**BTE**)	*4,4',4''-(benzene-1,3,5-triyl-tris (benzene-4,1-diyl))tribenzoate* (**BBC**)

MOFs

| *MOF-177* | *MOF-180* | *MOF-200* |
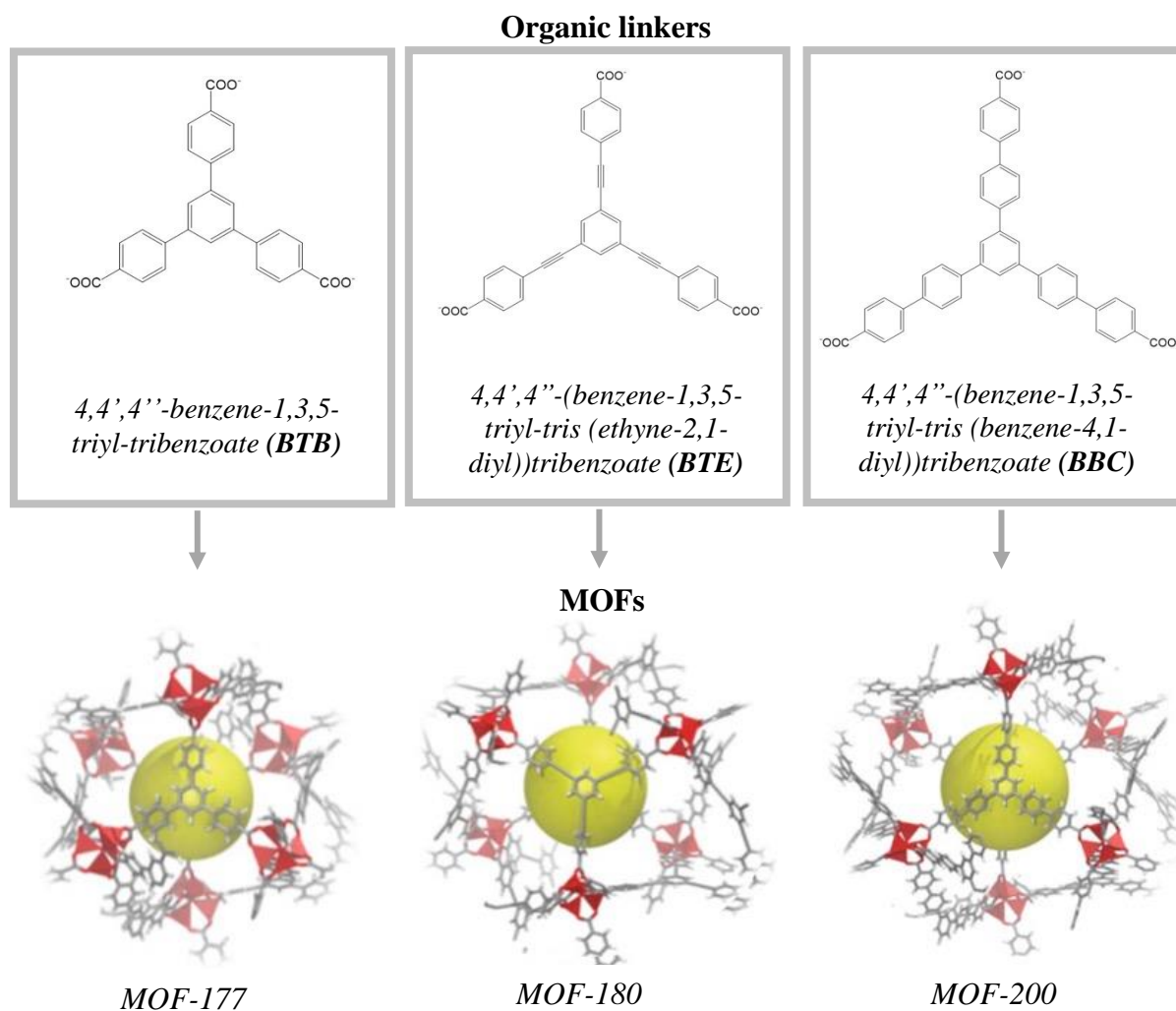
Figure 20. Isoreticularly expanded MOF structures by increasing the chain length of the organic linker. Images are adapted.[133,134]

4.3. Amorphous MOFs

4.3.1. Particular characteristics

The most investigated MOFs are highly porous materials with crystalline structure. One of the main drawbacks of this kind of materials is that its preparation is difficult to scale up economically, since synthesizing such highly ordered crystals require specific, often time-consuming procedures that yield low quantity of product.[145] This is one of the reasons why the amorphous counterparts of highly crystalline MOFs are gaining attention in the scientific literature. These MOFs can be synthesized following direct synthesis approaches. Currently, the number of reported amorphous MOFs is close to 100, although some commercial representatives have already appeared in the market, *e.g.,* Basolite F300, commercialized by BASF, equivalent to MIL-100(Fe).[34] The amorphous structures do not present long-range order,

but locally their building units are identical to those of the crystalline analogue.[146] Still, they exhibit diffuse X-ray scattering, thus broad bands in their X-ray diffraction patterns provide valuable information. The short-range order has been proved with local proves, such as X-ray absorption spectroscopy or solid-state magnetic resonance spectroscopy.[34] A powerful technique to ascertain local ordering is to generate pair distribution function from X-ray or neutron total scattering experiments, which provides insight about certain structural properties (*e.g.,* atom-atom distances).[147] Besides, more conventional techniques, such as Raman or infrared spectroscopy gives useful information about the chemical moieties present in amorphous MOFs.

4.3.2. Preparation methods

The amorphous compounds can be obtained either by amorphization of the counterpart crystalline MOF or by direct synthesis (Figure 21).[34] In direct synthesis, usually nucleation is favored vs. crystal growth by rapid mixing of the reagents. Instead of growing into crystals, the nuclei accumulate and form structures surrounding voids. One of the few example reported for direct synthesis is the amorphous phase of a zeolitic imidazolate framework Zn(ICA)-2.[148] Actually, the majority of reported examples of amorphous MOFs are based on the amorphization approach, which can be induced by various external forces, like pressure, heating, radiation, mechanical stress and electrical discharge. In other cases, chemical treatment causes the loss of the long-range order. More specifically, this category involves processes where the coordinated solvent is removed, and amorphization occurred by ligand competition or by loading with NPs.[34] In a less common scenario, amorphous MOFs are directly assembled from their precursors. Fe(BTC) aerogels, with solvent impurities in the framework, amorphous UiO-66 or FeMn-MOF-74 are some of the reported examples.[143,149,150]
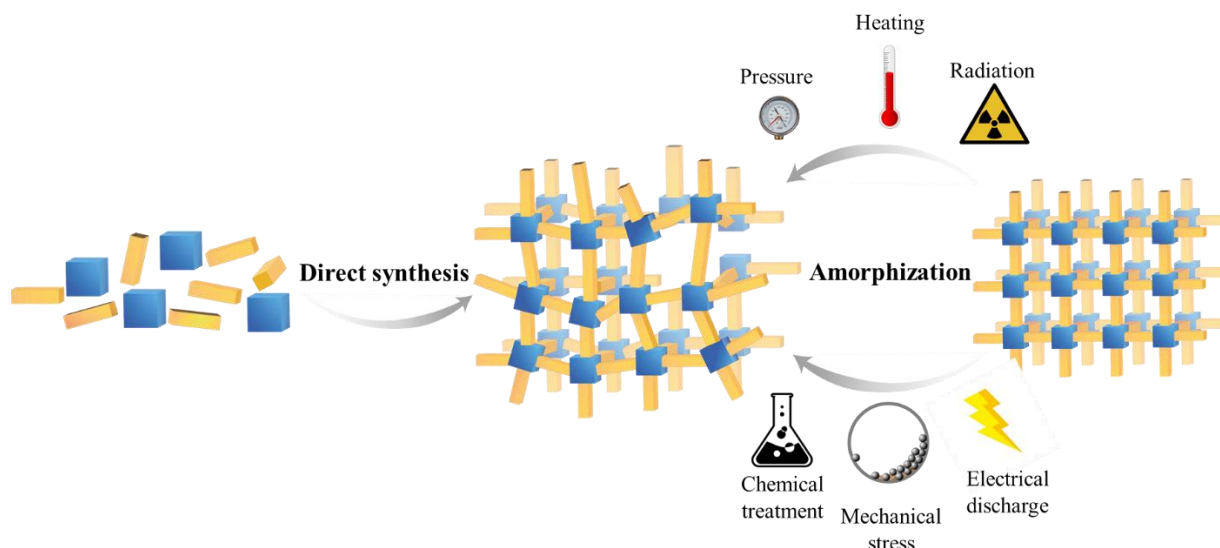
Figure 21. Methods to prepare amorphous MOFs.

4.4. Applications

Taking benefit principally of their exceptional surface properties and significant chemical/thermal stability, MOFs have found application in environmental, energy and biomedical fields, among many others. Some of the most widespread uses are covering gas separation, catalysis, drug delivery and pollutant removal. Apart from these, applications counting on unique characteristics of particular MOFs, such as optical, electrical or magnetic properties, are also emerging. In the huge family of MOFs, mesoporous frameworks are gaining prompt attention in uses where large pores are necessary for encapsulating external substances (*e.g.,* drug delivery, catalysis). The possibility of pore functionalization, incorporation of further micro- and mesopores, enhanced mass transfer in larger cavities and tunable geometry open up new ways for their utilization. At the same time, the particular characteristics of amorphous MOFs, such as surface defects are appealing in certain applications.
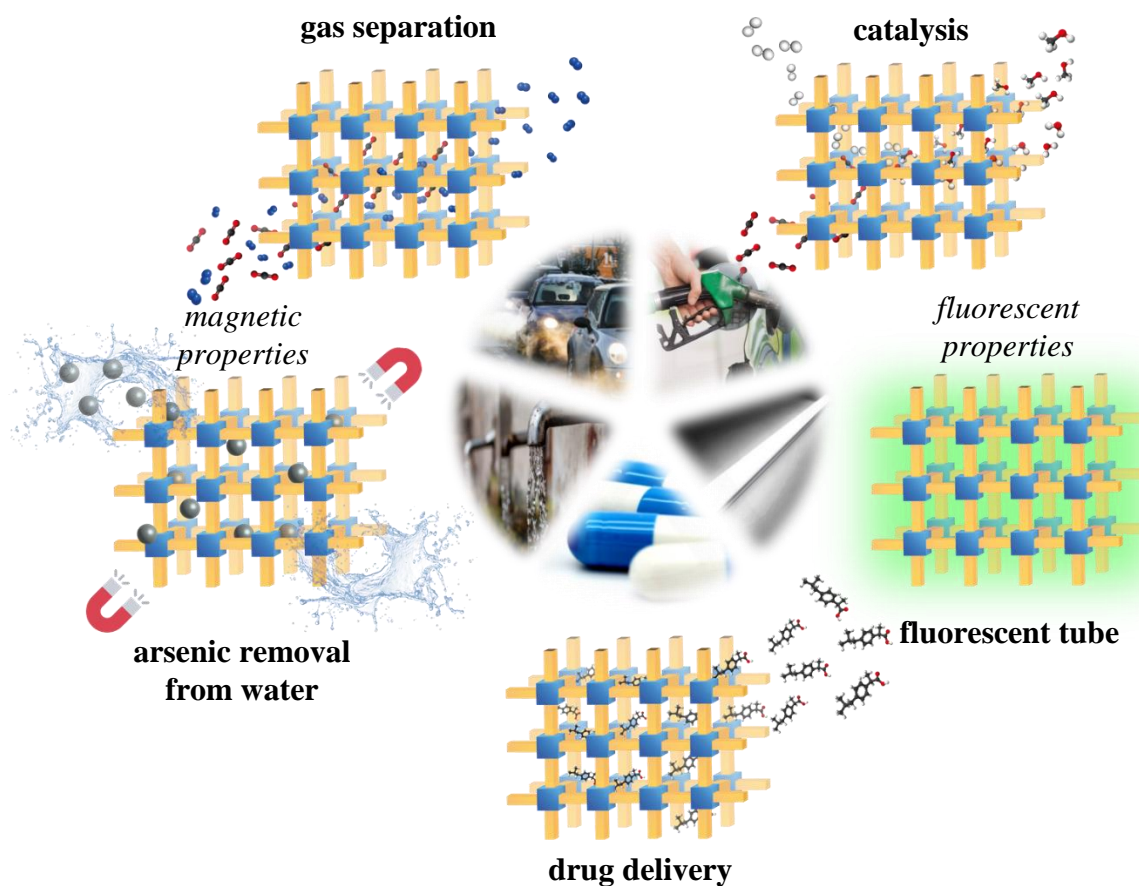
Figure 22. Schematic representation of some of the most common applications of MOFs.

Gas capture and separation

One of the most well-known properties of MOFs is their exceptional surface characteristics, with surface areas higher than 1000 m^2g^{-1}, although structures approaching to 7000 m^2g^{-1} have also been reported.[151] The microvoids generated inside the porous network of MOFs enable to trap significant amounts of small molecules, making them exceptional compounds in gas separation and capture. Actually, most of the research in MOFs is related to clean energy applications, focused on hydrogen (*e.g.,* NU-100) and methane (*e.g.,* HKUST-1) storage and carbon dioxide (*e.g.,* NU-1000) capture.[152–154] An important advantage of MOFs compared to other porous materials, such as zeolites or carbons, is the possibility of varying the structure of the material (*e.g.,* length of the organic linker, composition of the SBU, functionalization of pore walls), thus tuning the surface properties, and, along with that, the adsorbent capabilities.[155] Among them, using mesoporous MOFs with functional pores and tuned geometries, especially precise control of separation is possible.[156] The larger cavities, apart from small gas molecules are suitable to accommodate large molecules, such as fluorocarbons or chlorofluorocarbons.[157] Interesting possibility for reversibly store gasses is the pressure-

induced amorphization of the MOF structure, by applying low pressures to cause reversible transitions in the structure and alter the porous properties.[147]

Drug delivery

MOFs tunability makes these materials suitable for different biomedical applications. Particularly, in drug delivery, MOFs with pores of sufficient size (mesopores) are able to encapsulate active substances. Typically, the biocompatible MIL(Fe) family has been investigated for this purpose, because their relevant surface area (1000-5000 m^2g^{-1}) is accompanied with relatively large pores in the small mesopore range (2.5-3.0 nm).[158] The presence of functional groups on the pore walls of these MOFs allowed the interaction with loaded substances, resulting in high loading capacity and well-controlled drug liberation, avoiding initial burst release. The MIL(Fe) MOFs possess hydrophobic pores that can encapsulate hydrophobic active molecules with poor solubility in aqueous media. Pore walls can be modified to design hydrophilic surfaces, thus adsorbing preferentially hydrophilic drugs. The surface can also be modified to make it charged, thus drugs with opposite charges to the MOF walls can be carried efficiently.[159] To allow the systemic circulation and to improve the pharmacokinetic properties, the size of the MOF particles should be reduced to the nano range.[160] Amorphization of the framework can be an advantage also in drug delivery, as by partially collapsing the framework, the release time can be controlled.[161] An important factor regarding biomedical applications is the biocompatibility and biodegradability of the MOFs. By composing them from biocompatible precursors (bioMOFs), forming sufficiently small NPs (<200 nm), controlling the surface chemistry and the stability, several structures have been designed to meet these requirements.[162]

Catalysis

The use of MOFs in heterogeneous catalysis has developed a high potential in different applications, as the porous properties of MOFs can be combined with the possibility of immobilizing isolated well-defined active centers in the voids within the structure with a suitable environment for performing regio-, shape- and size-selective reactions.[163] In these applications, mesoporous MOFs often outperform the microporous ones regarding the efficient mass transport of large substances, such as reaction precursors and products. MOFs can play different roles in the catalytic reactions. On one hand, their compartments can be straightforwardly homogenously distributed active centers, where the catalytic reaction takes place. The surface of the pores stabilizes the transition state and orients the adsorbate

molecules.[164] The catalytic reaction can be activated on unsaturated metal centers, when coordination vacancies are available, or on the organic linkers, when certain functionalities are introduced to them.[165] Moreover, high density of structural defects (cleavaged chemical bonds, lattice distortion) present in amorphous MOFs could facilitate certain catalytic reactions.[166,167] In an indicative example, the catalytic activity of amorphous and crystalline iron trimesate was compared in several reactions. In catalytic reactions, where generally strong Lewis acid sites are required, the amorphous MOF showed better performance, even having less of these sites, due to its additional Brønsted acid sites (surface defects). Although in oxidation reaction the crystalline MOF, benefitting from its structural robustness during Fe(II)/Fe(III) transition, was the better choice.[167] Following another approach, mesoporous MOFs can provide a stable support for the active species to be deposited, such as NPs, enzymes, *etc*.[168] In some cases, MOFs have been used as precursors for the formation of catalytic NPs *via* a decomposition reaction.[169]

Other applications

Although the most extensive research has been carried out in the previously mentioned fields, promising results have been achieved in some other areas as well, where MOFs might be competitors to well-known, industrially tested materials. Among these, important electrochemical applications can be mentioned, highlighting the case of Co-based MOFs showing significant electrical storage capacity and good cycling stability.[170] Certain MOFs possess magnetic properties, depending on the nature of both metal nodes and organic linkers, and their particular level of organization. Among the transition metals, MOFs of the first row (Fe, Co, Mn) have a magnetic behavior by usually choosing oxo-, cyano-, and polycarboxylic linkers.[171] Short conjugated bonds formed among the metal clusters, or radicals present on the organic linker, tend to enhance the magnetic characteristics.[172] Advantage can be taken from such magnetic properties, for example in arsenate removal from water. After the adsorption facilitated by the MOFs' surface properties, the magnetic material can be easily recovered using an external magnetic field, instead of more time-consuming filtration and centrifugation methods.[173,174] Some MOFs are photoluminescent materials due to the excitation of aromatic units in the linkers, which can adsorb and emit UV-vis light. Both, the metal units and the linkers, can synergically contribute to the luminescence. For example, the electronic transition of trivalent lanthanide metal ions (Eu(II/III), Tb(III), *etc.*) is often accompanied by photoemission; while, among the organic linkers, functionalized molecules based on naphthalene, anthracene and pyrene, are mostly used as building blocks in luminescent

MOFs.[174] Such properties can be utilized in several sensing related applications, such as cathode ray tubes, fluorescent tubes, pH sensors or X-ray detectors.[175,176]

4.5. Structure of the MOFs used in this thesis

In this section the structures of the MOFs used in this thesis are summarized. More detailed descriptions are given in each corresponding chapters (Chapter III and Chapter IV).

4.5.1. Iron trimesate
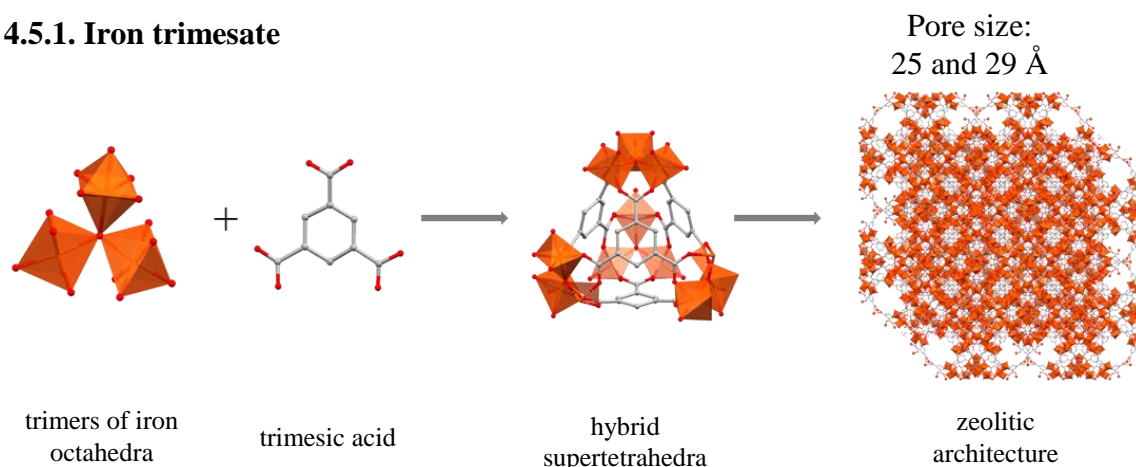
Figure 23. Precursors and structure of iron(III) trimesate MOF.

Crystalline iron(III) trimesate (MIL-100(Fe)) was synthesized and structurally elucidated in 2007.[132] This MOF is composed of SBUs of iron octahedra trimers with a shared vertex of an O atom. The trimers are connected through benzene-1,3,5-tricarboxylate moieties, leading to the formation of hybrid supertetrahedras. These further assembles into a MTN zeolitic framework. Two types of mesoporous cages are present in the structure, with 2.5 and 2.9 nm diameter, which are accessible through microporous window of *ca.* 0.6 and 0.9 nm. A Langmuir surface area of 2800 m^2g^{-1} was estimated from the N_2 adsorption/desorption isotherm, showing the characteristic of a microporous solid with two secondary uptakes at low relative pressures, corresponding to the mesoporous cages with micropore windows. The compound is thermally stable until 543 K.

MIL-100(Fe) can be hydrothermally synthesized. Firstly, the procedure involves the use of hydrofluoric acid, acting as a mineralizing agent, promoting the crystal growth.[177] Several other techniques have been developed to avoid the use of harsh conditions and toxic compounds, resulting in crystalline and amorphous iron trimesate phases with surface areas in the order of 1500-3000 m^2g^{-1} and 1000-1500 m^2g^{-1}, respectively (see in Chapter III).[178–180] In this work, both

crystalline and amorphous phases were synthesized and used for diverse applications in drug delivery (Chapter III) and catalysis (Chapter IV).

4.5.2. Porphyrin-based
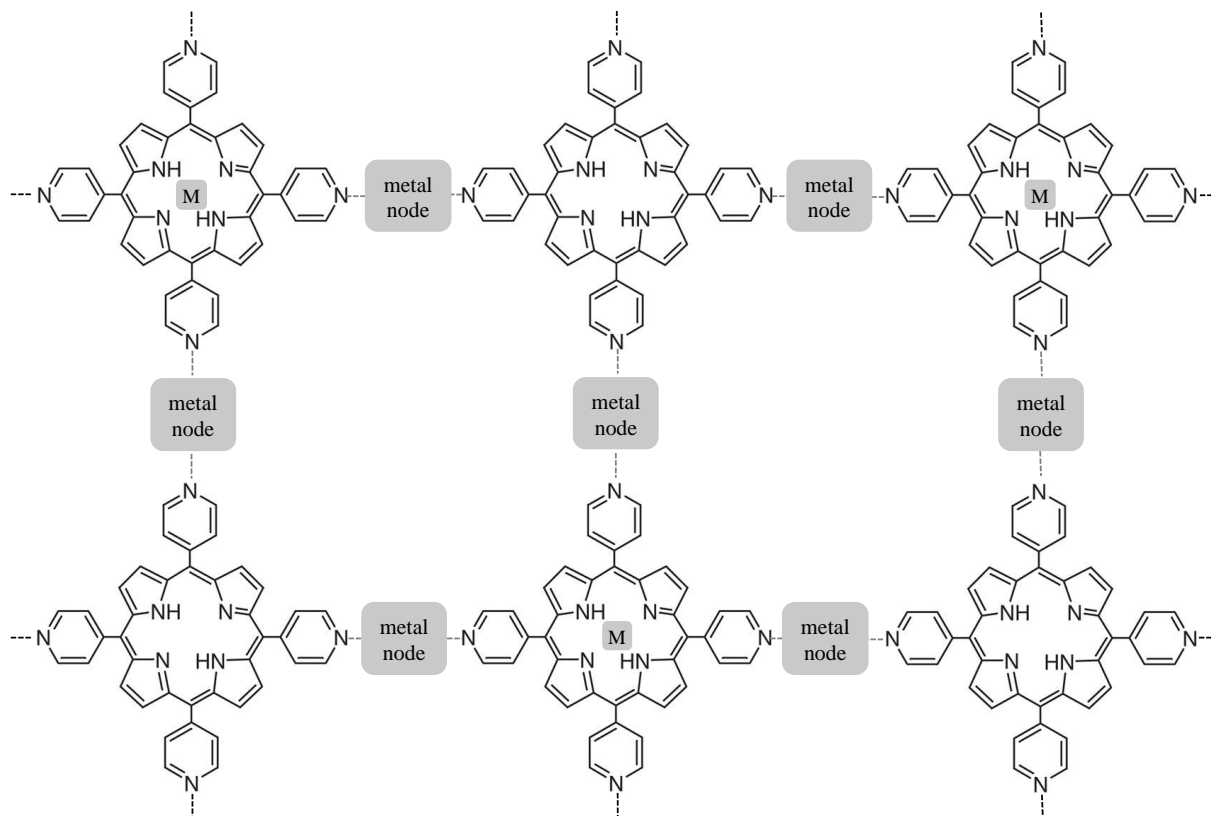
Figure 24. Scheme for a H_2TPyP – metal coordination.

Porphyrin macrocycles are interesting organic linker molecules for MOFs, providing a highly symmetric, planar and aromatic building units, with an extremely rich chemistry.[181] Both the four meso- and the eight β-positions of the porphyrin heterocycle can be substituted, but the most frequent cases are the meso-substituted carboxy- or pyridyl linkers. Metal coordination on the side substitutions, and also tetra-pyrrole based ligation, are possible inside the porphyrin ring, further increasing the diversity of the obtainable structures.[112] Their coordination with metals or secondary building units, with a suitable composition, size and geometry, lead to porous porphyrin MOF structures.[182] As for the metal nodes, the first stable porphyrin MOFs involved Na(I) or Zn(II) ions, coordinated with carboxyl-substituted linkers.[183] After these compounds, trinuclear Co-based clusters and ZnO_4 SBUs were linked with the same type of porphyrin, giving microporous MOFs.[184] Since then, a large variety of nodes, forming more complex clusters, has been reported.[185]

In this thesis, the 5,10,15,20-tetra(4-pyridyl)-21H,23H-porphine (H$_2$TPyP) molecule was used to synthesize a series of new MOFs. This molecule has the possibility of coordination to metals through the N-heteroatom of the pyridyl ring and inside the porphyrin cycle (Figure 24). Pyridyl-based ligands typically have affinity to form coordination bonds with soft metal cations (Cu(II), Zn(II), Ag(I)). Hence, in this work Zn(II), Cu(II), Co(II) and Ni(II) were chosen to build the MOF. The extraordinary physicochemical versatility, and unique electrochemical and photophysical properties of porphyrin-based MOFs can be exploited in various applications, including (photo)electrocatalysis, organic photovoltaics and biomedical applications, such as drug delivery or tumor therapy.[112] These aspects are further discussed in Chapter V.

5. Supercritical Fluids

Supercritical CO$_2$ technology is the basis of all the procedures carried out in this thesis for obtaining nanostructured materials. For this reason, defining and describing the most important properties of supercritical fluids, and specifically of scCO$_2$, is essential to understand the performed work. According to the classical definition, a pure substance is in supercritical conditions when its pressure and temperature are simultaneously equal or higher than those of its critical point. The critical point is an exact physical (pressure and temperature) parameter and defines the lowest conditions of pressure and temperature of the supercritical phase. Theoretically, every substance has a critical point. However, in practice, most of the materials chemically decompose before reaching the supercritical condition. For practical reasons, only fluids with critical values reasonably low have some applicability in these conditions (Table 2). In most developed processes, these fluids are used in the region close to the critical point, with the reduced pressure (p/p$_{crit}$) within 1-10, and the reduced temperature (T/T$_{crit}$) within 1-1.5.[186] Currently, mainly CO$_2$ and water have widely extended large scale relevance, although in certain cases, the potential of other supercritical fluids are exploited. For instance, supercritical argon, ethane, propane and dimethyl ether have been tested for extracting bioactive compounds, showing advantages in certain aspects (low P$_{crit}$, high yield), although the use of scCO$_2$ remains the widespread and economically more viable choice for this purpose.[187,188] Many other solvents (nitrogen, methanol) have been studied as alternatives, but they have not gained broad attention, likely due to the abundance, low price and relatively safe use of CO$_2$ and water.

Table 2. Critical parameters of some common substances used in supercritical conditions.

Substance	Critical pressure (MPa)	Critical temperature (K)
Carbon-dioxide	7.38	304
Water	22.1	647
Argon	4.87	151
Ethane	4.89	305
Propane	4.26	370
Nitrogen	3.39	126
Methanol	8.10	513
Dimethyl ether	5.38	400

5.1. General properties of the supercritical phase

Around the supercritical region, the fluids possess unique properties. Their behavior can be studied on the phase diagram showing the relationship between the pressure and temperature at each phase transition (Figure 25).[189,190] In the phase diagram, the continuous lines mark the coexistence of two phases. For each pure substance, above a certain pressure-temperature combination, the density of the gas and the liquid is equal, resulting in a single phase, called supercritical phase, in which the fluid fills all the available space. By decreasing the temperature or the pressure separately, the fluid transforms to liquid or gas, respectively. The supercritical fluid/gas transformation occurs without any detectable phase transition (Figure 25). In this case, the lack of phase boundaries entails that no surface tension is generated in the system, as it occurs in the liquid/gas transition. To develop mathematical models that properly describe the supercritical region, it is often divided in two parts by the Widom lines, separating the region where the liquid-like or gas-like properties dominates.[191]
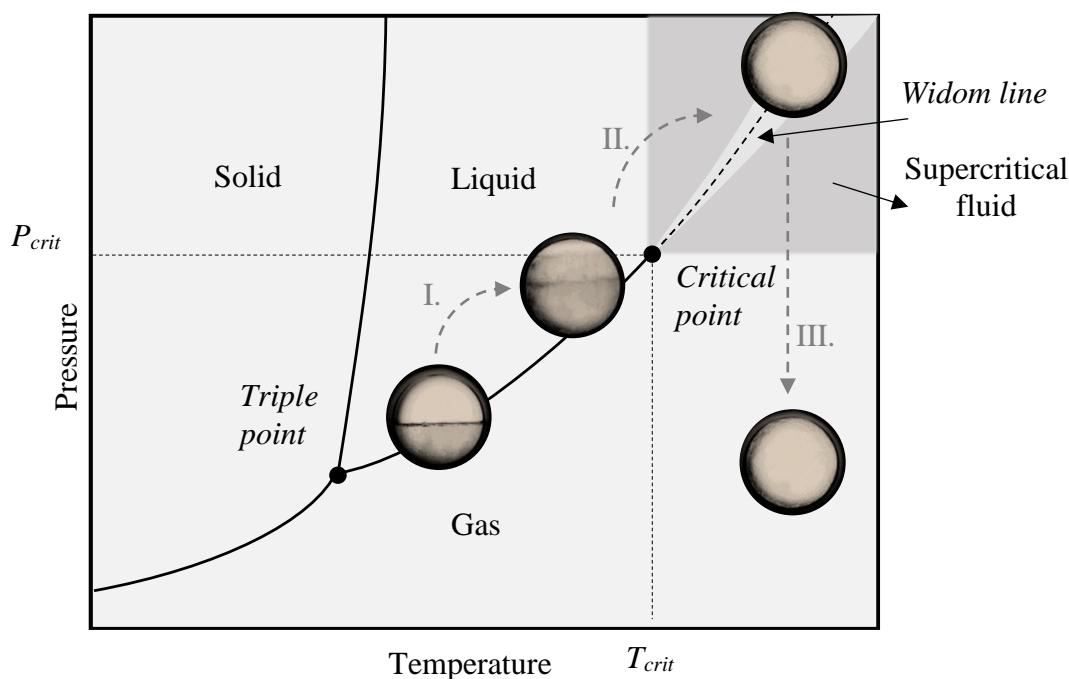
Figure 25. Pressure-temperature phase diagram of a fluid showing the phase equilibria lines (continuous lines). The supercritical region is above the critical point, separated by the Widom line. Adapted images represent the phase transitions of CO_2 observed through a sapphire window in a flow reactor.[192] The clear meniscus established between vapor-liquid phases starts to disappear by increasing the pressure and temperature (I), with a further increase of these parameters the phase boundary is not distinguishable anymore (II). By decreasing the pressure, the supercritical fluid–gas transition occurs without any detectable phase transition (III.).

The main characteristics of the supercritical conditions are generally described in comparison with the liquid and gas phases of the fluid (Figure 26). The density, viscosity and the diffusivity, which are all function of the pressure and temperature, are usually used to describe these fluids. Besides, other physical parameters (heat capacity, heat conductivity, speed of sound, *etc*.) can elucidate specific phenomena observed in supercritical media.[193] The density of a supercritical fluid can be continuously modified from the liquid-like to gas-like values by changing the pressure or the temperature. Close to the critical point, the increase of the pressure causes an extreme raise in density, while at high pressures this effect is not that pronounced. Along with this, several density-depending parameters are also altered in the supercritical region, such as the dielectric constant and viscosity. The modification of these physical parameters is the reason behind the liquid-like solubilizing ability that is typical of the supercritical region. In chemistry, the solvation of a solute in a solvent is described of being primarily dependent on its close

surrounding and the established interactions with the fluid. The high density of supercritical fluids can induce significant interactions of the solute-solvent type, together with those of solvent-solvent (Figure 26). These interactions cause microscopic local density fluctuations that can be extended to the macroscopic dimension. Again, this effect is observable close to the critical point, and is the origin of unexpected high solubility of some solutes in supercritical fluids.[186,194] At the same time, the viscosity values of supercritical fluids are approaching that of gasses, meaning that any flowing substance through supercritical media is facing less resistance in comparison to liquids. The diffusivity in supercritical media depends on the fluid pressure and temperature, and the characteristics of the diffusing component. Under constant pressure, the diffusivity tends to increase along with the temperature. Moreover, the pressure influences the diffusivity through the density and the viscosity. At a high density and viscosity, the diffusion is hindered. On the other hand, at a high pressure (or low temperature) the molar volume of the diffusing molecule decreases, which would facilitate the diffusion.[186] It is important to point out that all these properties are strongly related to each other, and slight changes in the pressure or/and temperature can affect them in numerous combinations.

	Solid	Liquid	Supercritical fluid	Gas
Density (kg m^{-3})		1000	100-1000	1
Viscosity (µPa s)		500-1000	50-100	10
Diffusivity (mm^{2}s^{-1})		0.001	0.01-0.1	1-10
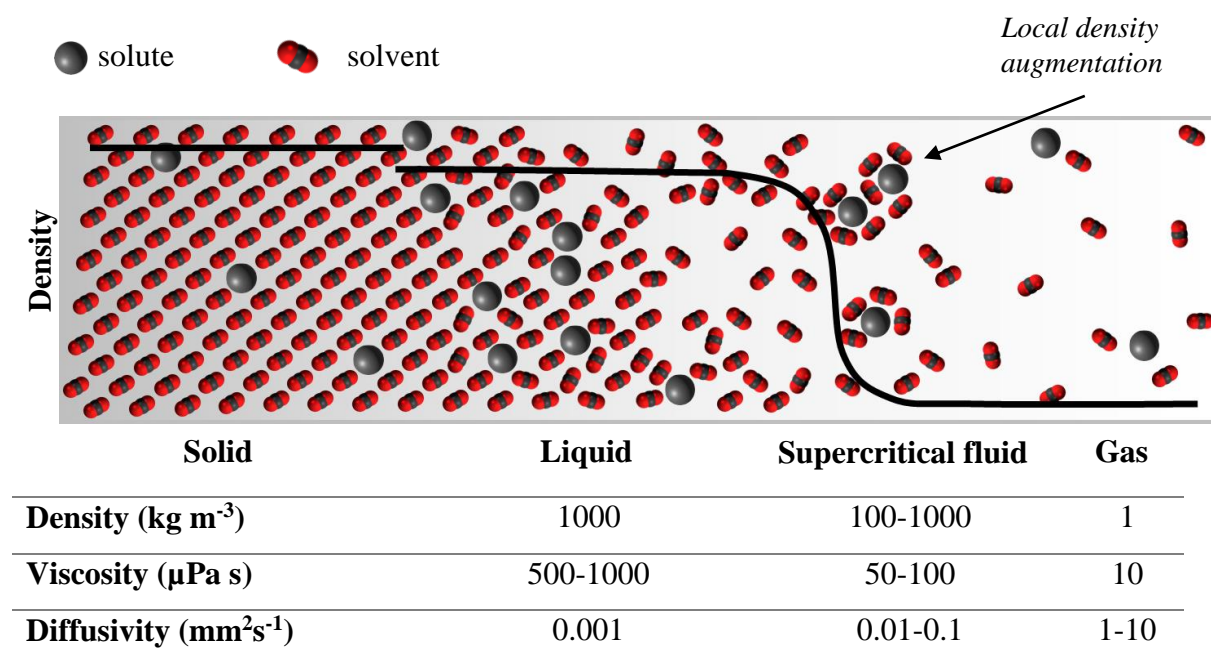
Figure 26. Schematic representation of the density of a fluid giving place to different regions and comparison of average values of liquids, supercritical fluids and gasses.[190,195]

5.2. Supercritical CO$_2$

5.2.1. Properties

Among supercritical fluids, undoubtedly CO$_2$ has gained the most attention because of its convenient applicability and environmental considerations. In this section some of the advantages related to the use of this fluid are discussed. The above mentioned properties for supercritical fluids in general can be applied to CO$_2$, playing key roles in its wide spread feasibility.

- The density of CO$_2$ is highly tunable with pressure and temperature, which has a strong contribution to the solubility. Hence, by slightly modifying these process parameters, the solvating power can be manipulated, facilitating the design of extraction, separation, deposition, particle formation, foaming processes.

- CO$_2$ is a non-polar, linear molecule, with a quadrupole moment. These characteristics of the molecule favor the solubilization of non-polar volatile compounds with a low molar mass (short hydrocarbons, small aromatics, esters). The presence in the solute of certain atoms or functional groups has been reported to enhance the solubility. Typically, high solubility has been observed for fluorinated and perfluorinated alkyl chains or even in organometallic complexes involving fluorine in the structure.[196] A clear example is the behavior of Cu(II) acetylacetonate fluorinated derivatives in scCO$_2$, for which a two-order enhancement solubility was observed with respect to the acetylacetonate Cu(II) precursor.[197] To understand this behavior the interactions between the CO$_2$ molecules and the solute have been investigated by Monte Carlo simulations.[198,199]

- Some processes are better performed with the addition of a small amount of cosolvent (1-5 v%). The main objective of adding cosolvent is to increase the solubility of polar molecules in scCO$_2$ by enhancing the attractive forces between solute and solvent and increase the local density of the solvent mixture. Typically, short chain alcohols (methanol, ethanol, isopropanol), or less polar dichloromethane or hexane are used for this purpose. Water, the most common, cheap and safe solvent, cannot be utilized due to its poor miscibility with scCO$_2$.

- ScCO$_2$ has mass transport properties similar to those of gasses. This property allows the fast penetration of this fluid into porous matrices, thus reducing processing time in some

applications, such as extraction and impregnation or functionalization. Additionally, this parameter has a great impact in reactions carried out in $scCO_2$.

5.2.2. Economic, environmental and safety considerations

CO_2 has a relatively low critical pressure and temperature, which can be easily reached with low energy consumption, and allows to process thermally labile substances. Besides, this fluid is considered inert, unlike, for instance, the supercritical water, where corrosion due to the oxidizing ability of the fluid at high temperature is a notable concern.[200] Regarding safety, the non-flammable character of the CO_2 is an important factor, contrasted to ethane, that has been tested as an alternative in extraction processes, but can form explosive mixture with air.[201] CO_2 is one of the most abundant components of air, and also the by-product of several industrial processes, being the reason behind its low cost in comparison to conventional solvents and chemicals. Industrial plants using $scCO_2$ are able to operate with economic efficiency because of the relative low operation conditions of pressure and temperature, and also because the post-processing steps are reduced and the generated volume of waste disposal after $scCO_2$ treatment is minimized. As the recycling of the CO_2 is already solved in several units, it can be regarded practically as zero waste technology in regard of solvent. These considerations facilitate the scale-up of $scCO_2$ based processes. The non-toxic character of CO_2 has a positive impact on security, both in research laboratories and industrial environment. $scCO_2$ technology allows the preparation of safe consumables for human use, by replacing organic solvents during production, and thus preventing toxic residues in products, such as food, pharmaceuticals or cosmetics. CO_2 is generally recognized as safe (GRAS) chemical by the United States Food and Drug Administration (FDA).[202]

5.2.3. Concerns related to risk and safety

Most concerns regarding $scCO_2$ processes are associated with cost and safety. Operating chemical units with $scCO_2$ requires high pressure, which entails security issues. The equipment must be mounted with series of safety devices to minimize risks. Comparing to conventional chemical processes, the high-pressure vessel and further machinery have major initial costs. For these reasons, supercritical technology is worth to use only on those cases where tangible advantage appears. Regarding feasibility, the low solubility in $scCO_2$ of numerous polar or ionic substances, even with the addition of a cosolvent, set the limits for processing a large number of materials.

5.2.4. Applications examined in this thesis

Supercritical fluid technology has been applied in numerous fields, from laboratory to industrial scales. Some of the most investigated areas are related to natural products, biomedical or pharmaceutical applications. Although the first report about the existence of the critical point was already released in 1875, wide-spread recognition for supercritical technology was only attained in the early 1980s.[203,204] First applications, almost invariably, were extraction of active components from botanical substrates. Later, in the 1990s, particle formation comes into sight. Still, the development of industrial scale processes was delayed due to the lack of awareness in large scale potential, and concerns about replacing mature technology with one in relatively initial stages, especially because of the use of high pressure and relevant initial investment.[190] Even so, today a large series of already existing or new products are manufactured or investigated using high performance $scCO_2$ assisted processes, such as natural food products, cosmetics, pharmaceuticals, catalysts, sensors, textile products, *etc*. The supercritical fluid usually has a distinct role in each process, which must be studied case by case. This section deals with the main uses of $scCO_2$ in this thesis, which are fundamentally focused in reactions (MOFs synthesis), impregnation (composites formation) and drying (aerogels preparation).

Supercritical CO₂ in MOF preparation

- *Drying and activation*

Eliminating residual solvent molecules and excess reagents trapped inside the pores is necessary to realize high porosity in MOFs.[205] Conventional methods, such as thermal activation or solvent exchange with a lower boiling point solvent and its subsequent evaporation were widely applied for this purpose.[19,206] Although with these methods surface properties, far from those that were expected by computational estimations were realized.[205] Such differences are often attributed to the collapse and the blockage of the pores occurring due to the awakening capillary forces during the solvent evaporation. In contrary, it was pointed out by Nelson *et al.*, and it is in align to our experience, that the relative strength of the bonds within most MOFs are sufficiently strong to be able to resist such forces, even in case of high boiling point solvents.[207] This is supported by the fact, that crystalline structure is maintained in thermally activated MOFs. Thermogravimetric analysis also suggests thermal stability for MOFs, much higher than the boiling point of common solvents in MOF preparation. Low N_2 adsorption values seem to be more the consequence of the collapse of the voids with mesosize between the particles, inhibiting the access of gas molecules to the microporous system.[207]

Alternatively, scCO$_2$ drying can be applied after exchanging the residual solvent to one that is miscible with CO$_2$ (*e.g.*, ethanol).[208] By avoiding the materialization of capillary forces, structures with surface properties much closer to the theoretical values can be obtained. For instance, in the order of 3 to 20-fold increase in surface area values was described after scCO$_2$ drying for MIL-53(Fe) and Cu$_3$(BTC)$_2$ MOFs, without any alteration in the crystalline structure.[209] Furthermore, there are other methods for activating MOFs, such as freeze-drying or chemical treatment, although in these cases indeed the crystal structure can be compromised.[205]

- *Synthesis in scCO$_2$*

The solubility of many of the components of MOFs, *e.g.,* polar organic linkers with high molecular weight and metal precursors, is low in scCO$_2$. As a consequence, this medium can be used as a pristine fluid only in particular cases to synthesized MOFs. Nevertheless, some specific class of compounds have the potential to still achieve this aim, thus eliminating the need of any additional organic solvent. The first example of the preparation of 1D coordination polymers using exclusively scCO$_2$ was reported in 2015 (Figure 27).[127] Specifically, copper(II) acetylacetonate complexes were coordinated with two linear linkers, namely bidentate 4,4′-bipyridine (bpy) and 4,4′-trimethylenedipyridine (tpy). In the following years, other representatives of the same organometallic family (Zn and Cu-hexafluoro acetylacetonate) and bipyridyl or triazine linkers were used to precipitate 1 and 2D MOF crystals without the use of any cosolvent added to scCO$_2$.[210,211] 3D MOFs microstructures could be also prepared using net scCO$_2$, highlighting the synthesis of ZIF-8.[212] Moreover, heterometallic coordination polymers of Zn(II) and Co(II) with 1,4-bis(4-pyridylmethyl)benzene were synthesized in scCO$_2$.[213] The crystals were composed of evenly mixed metals and acted as a field-induced single molecular magnet. These examples show that the precipitation of a large number of MOFs using pure scCO$_2$ as a solvent is indeed possible, when sufficient solubility of at least one of the precursors is achieved. In general, the procedure leads to nano sized crystals, since the low attained solubility results in early nucleation stages. A methodology for MOF synthesis in liquid and scCO$_2$, preferably without any additional cosolvent, has been patented by the ACSYNAM company, which is currently fabricating several well-known MOFs (ZIF-8, HKUST-1, MOF-5).[214]

Small amounts of a second solvent (2-5 v%) are often used to increase the solubility of the reagents in scCO$_2$. Under these conditions, the solvent and cosolvent are forming a single-phase solvent mixture, in which the formation of certain MOFs can be achieved.[215] In a different

approach, a high liquid solvent/CO_2 ratio (> 10%) is used. In this case the MOF precursors are dissolved in the liquid phase, and the formation of the end product occurs in a CO_2 expanded liquid mixture. The liquid phase expansion due to CO_2 dissolution drives the MOF nucleation and growth.[209] Dimethylformamide, dimethyl sulfoxide and alcohols have been used to prepare various MOFs in scCO$_2$.[209,216] Beside conventional solvents, ionic liquids have attracted much attention in MOF synthesis.[217,218] These liquids are comprised of cations and anions and can be adjusted to possess superior solubilizing ability. The main drawback of the ionic liquids is the high viscosity of these fluids that hinders the diffusion of the reagents. The addition of scCO$_2$ to ionic liquids has been reported to modify the ionic liquid properties, thus facilitating the synthesis of diverse MOFs.[140,219,220]
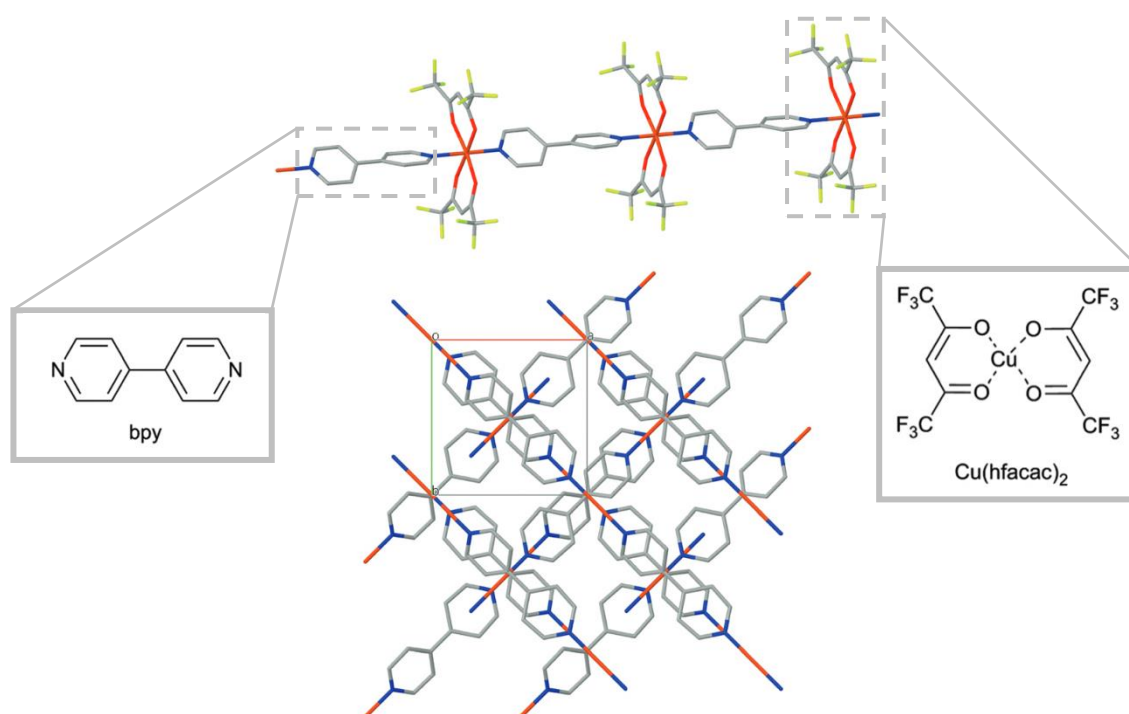
Figure 27. A single chain of the scCO$_2$ synthesized $(Cu(hacac)_2$-bpy)n MOF (top) and the propagation of the chain to 3 dimensions (bottom).[127]

scCO$_2$ assisted impregnation into porous structures

The immobilization of various substances, such as nanoparticles or small organic molecules, in porous supports provides unique characteristics to the end product that cannot be achieved by the individual components. Such composites have attained remarkable performance in applications related to drug release, catalysis, electron transfer, gas sorption, *etc*. Conventional procedures to synthesize these composites usually involves a liquid as a carrier (impregnation

from solution), requires volatile compounds (chemical vapor infiltration, mechanical grinding) or applies large mechanical stress (mechanical grinding) for introducing such substances into the pores.[221–223] All of these techniques exhibit certain advantages and drawbacks, but in general the control of the dimension and dispersion of the NPs is challenging.[224] For instance, homogenous impregnation in the bulk from liquid solutions is sometimes difficult to achieve when substrates with fine pores are treated. This is due not only to slow diffusion, but also to the competition between the solute and solvent molecules for the substrate adsorption sites.[190] Using scCO$_2$ has the advantage that the solute-solvent competition is eliminated, as the condensation of CO$_2$ is impossible under supercritical conditions, and any established interaction between the solvent molecules and the internal surface is weak. scCO$_2$ is also able to overcome the diffusivity and mass transfer limitations, the drawbacks that are characteristic of liquids. Hence, the scCO$_2$ solubilized substances can rapidly penetrate into micro/mesopores, being able to extendedly and uniformly decorate the internal structure.

- *Immobilization of metallic NPs in porous substrates*

Enhanced catalytic performance of metallic NPs can be reached in metal@porous support, such as by using porous MOFs as support. The advantage is, primarily, the prevented aggregation with the consequent loss of activity of the metallic NPs during the catalytic processes. The impregnation procedure of the metallic NPs inside of a porous substrate is usually performed by infusing the reagents. This is the method used when scCO$_2$ is the used solvent. The process involves three main stages illustrated in Figure 28.
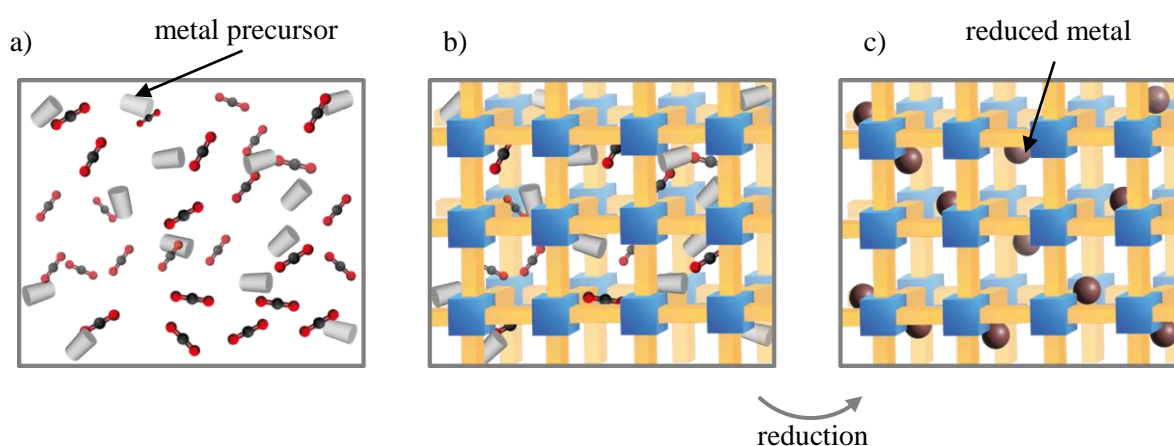
Figure 28. General supercritical CO$_2$ impregnation procedure of metallic NPs into a MOF: (a) dissolution of the metallic precursor in scCO$_2$, (b) diffusion of the precursor to the interior of the pores and adsorption on the pore walls of the support, (c) reduction of the precursor to obtain the desired metallic form.[224]

The first step (a) is often aided with a cosolvent and carried out at high pressure to improve the solubility of the metal salt. Moderate temperatures are used to avoid the early decomposition of the precursor. In case of using organometallic precursors (diketones, dithiocarbamates, macrocycles, organophosphates, *etc.*), the addition of cosolvents is sometimes not needed, since these compounds show enough solubility in pristine $scCO_2$. The second step (b) is the impregnation, when the already dissolved metal precursor penetrates into the pores and gets deposited on the internal surface. Finally, the transformation of the metal precursors to the active metallic NPs (c) is usually carried out by the injection of a reducing agent, such as H_2 or alcohol, or also by a heat treatment causing the decomposition of the precursor. An interesting and convenient approach is to carry out the reduction under the $scCO_2$ atmosphere. In this way, the organic by products coming from the precursor can be released upon depressurization.[225] Several examples are reported in the literature dealing with metallic NPs encapsulated into mesoporous substrates. Some Co-, Ni and Ru NPs derived from organometallic complexes have been encapsulated in mesoporous silica and activated carbon supports using exclusively $scCO_2$.[224] Similarly, uniformly dispersed Pt NPs, derived from an organometallic platinum complex, have been deposited onto porous alumina, silica and carbonaceous substrates without the use of a cosolvent.[226] The impregnation of MOFs, particularly into those that possess large micropores or small mesopores, is also described in the literature. For instance, the impregnation of H_2PtCl_6 into the pores of MIL-101(Cr) (pore size 2 nm) has been carried out using an ethanol/$scCO_2$ mixture, which was further reduced with H_2 flow to obtain monodispersed Pt NPs.[227] A Ru-salt has been impregnated into nanorods of a lanthanum-BTC MOF by using a methanol/$scCO_2$ mixture at high temperature. After reduction, the composite demonstrated high stability due to the strong intermolecular interaction established between the carboxylate groups of BTC and Ru.[228]

- *Drug impregnation in porous substrates*

It has been recognized long time ago that simple pills and injections are not suitable for the administration of some active compounds. The reasons are low bioavailability, fast drug absorption and thus short medical effect, high toxicity, and so on. A more effective therapy, with a designed and prolonged drug release profile, can be achieved by the use of controlled drug delivery systems, where the bioactive compound is released to a specific location and rate. The $scCO_2$-assisted impregnation process of active ingredients in porous substances has been used since the initial stages of the supercritical fluid technology development.[190] The impregnation procedure involves the following three main steps:

a) solubilization of the pharmaceutical in $scCO_2$, often with the aid of a cosolvent,

b) diffusion of the drug into the porous substrate, and

c) elimination of the solvent by depressurization.

The positive impact of using $scCO_2$ when processing pharmaceuticals is two-fold. First, the low temperature conditions needed in the process reduces the risk of any degradation of the bioactive compounds, which are often sensitive to thermal decomposition. Second, leaving no residual organic solvent diminishes the toxicity of the end product. Moreover, the intrinsic sterility of processes carried out in compressed CO_2 is of particular interest.[190] In comparison to impregnation from a liquid phase, the excess of usually expensive bioactive compound can be recovered straightforwardly in the dry form upon depressurization. Literature on the use of $scCO_2$ for drug impregnation covers mainly the use of aerogels, biopolymers, silica and zeolites as porous substrates.[229] MOF loading using this fluid as a carrier is much more scarce, although the high and regular porosity of most MOFs, together with their amphiphilic internal structure, makes them excellent candidates for drug delivery systems.[230,231] Examples are the impregnation in ibuprofen into MIL-53(Fe) and MIL-100(Fe) with the aid of hexane cosolvent.[232] Caffein and carvacrol could be impregnated into carboxylate-based MOFs without the aid of any cosolvent, attaining drug loadings >30 wt%.[233]

Polymer foaming with supercritical CO_2

Compressed CO_2 can be used as a blowing agent in polymers. This process has gained increasing popularity in the production of porous polymer structures for a wide variety of applications, involving thermal insulation, packaging materials, molecular separation, catalysis, dielectric application, drug delivery systems or synthetic scaffolds for regenerative purposes.[234–237] In the latter, together with the foaming, one-step impregnation of bioactive substances can simultaneously be carried out aided by $scCO_2$. In a general foaming process, as the $scCO_2$ dissolves in the matrix, the swelling of the polymer occurs and its glass/melting temperature decreases. Usually, in comparison to other foaming methods (*e.g.,* gas or liquid foaming), lower temperature is required in the supercritical approach, which is favorable for the impregnation of thermally labile biological substances. The penetration of the impregnated component is facilitated through the entangled polymer chains in the plasticized state, thus high loading can be reached.[238] During pressure release, the plasticizing effect is gradually eliminated, causing the vitrification of the polymer. At the same time, the supersaturation of the dissolved CO_2 in the matrix causes a thermodynamically instable state, that induces cell

nucleation and growth. The foaming procedure continues until the foam is rigid enough to resist further expansion.[239] The manufacturing method and the properties of the polymer determines the cellular morphology and biocompatibility of the foamed product. In this sense, the sustainability (low toxicity, low flammability, recyclability, *etc*.) of the scCO$_2$ provides important advantages in biomedical applications. Furthermore, the tunability of scCO$_2$ with processing conditions (pressure, temperature), being determinant for the interactions between the polymer and the fluid, allows the formation of foams with variable characteristics (pore size, interconnectivity, stiffness). At high, temperature the density of the CO$_2$ and its solubility into the polymer decreases, while the diffusivity is enhanced. On the contrary, with a pressure increase, the solubilization of CO$_2$ is favored, thus high supersaturation and enhanced nucleation are attained. The pore size is influenced by the depressurization rate, *e.g.,* slow venting results in pores of large diameter with increased the interconnectivity, while fast venting produces small, often isolated, pores. The supercritical foaming process has certain limitations. The use of pure scCO$_2$ is limited to amorphous polymers with relatively low glass temperature. The foaming of the polymer often needs to be promoted with plasticizing agents or organic solvents. A regular phenomenon, occurring due to the high diffusivity of the scCO$_2$, is that the outside layer of the foam is non-porous, and needs to be removed before application.[236,239]

scCO$_2$ in aerogel preparation

ScCO$_2$ is an efficient media to obtain light-weight porous aerogels, as has been described in 2.2.2. and 3.4 sections. The drying process is preceded by gelification in a liquid solvent, which is later interchanged with CO$_2$ in the pores of the wet gel. Finally, phase transition from the supercritical to the gas phase occurs, lacking the awakening of capillary forces, thus the porous structure is preserved in the dry product. Aerogels with various types of composition have been already prepared with scCO$_2$ drying, including silica, cellulose, carbon-based, polymer, *etc*. In the last decades, scCO$_2$ technology for aerogel preparation has been applied at industrial scale in textile and cosmetic sectors.[41,240,241]

References

1.   J.T. Culp, Flexible Solid Sorbents for CO_2 Capture and Separation, *Novel Materials for Carbon Dioxide Mitigation Technology* **2015**, 149-176.

2.   P.S. Liu, G.F. Chen, Porous Materials - Processing and Applications **2014**.

3.   M.Z. Ahmad, A. Fuoco, Porous liquids – Future for CO_2 capture and separation?, *Current Research in Green and Sustainable Chemistry* **2021**, *4*, 100070.

4.   B.D. Zdravkov, J.J. Čermák, M. Šefara, J. Janků, Pore classification in the characterization of porous materials: A perspective, *Central European Journal of Chemistry* **2007**, 5, 385-395.

5.   K. Kaneko, Determination of Pore Size and Pore Size Distribution: 1. Adsorbents and Catalysts, *Journal of Membrane Science* **1994**, *96*, 59-89.

6.   S. Mondal, P. Sibanda, Computational Study on Convective Flows in Presence of Chemical Reaction and Thermal Radiation in Porous/Non-Porous Cavities, *Global Journal of Pure and Applied Mathematics* **2016**, *12*, 3641-3671.

7.   M.I. Osotsi, W. Zhang, I. Zada, J. Gu, Q. Liu, D. Zhang, Butterfly wing architectures inspire sensor and energy applications, *Natl Sci Rev*. **2021**, *8*, nwaa107.

8.   X.S. Zhao, Novel porous materials for emerging applications, *J Mater Chem* **2006**, *16*, 623-625.

9.   G.S. Day, H.F. Drake, H.C. Zhou, M.R. Ryder, Evolution of porous materials from ancient remedies to modern frameworks, *Commun Chem*. **2021**, *4*, 114.

10.   C.P. Bryan, G.E. Smith, Ancient Egyptian Medicine: The Papyrus Ebers. **1974.**

11.   F. Cecen, Ö. Aktas, Water and Wastewater Treatment: Historical Perspective of Activated Carbon Adsorption and Its Integration with Biological Processes, *Activated Carbon for Water and Wastewater Treatment: Integration of Adsorption and Biological Treatment* **2011.**

12.   E.M. Diamond, K.T.H. Farrer, Watering the fleet and the introduction of distillation, *Mariners Mirror* **2005**, *91*, 548-553.

13.   C.W. Scheele, Chemical Observations and Experiments on Air and Fire, **1780**.

14.   A.F. Cronstedt, J.L. Schlenker, G.H. Kühl, Observations and Description, *Proceedings from the Ninth International Zeolite Conference* **1993**.

15.   M.H. Sainte-Claire-Deville, Chimie Minéralogique—Reproduction de La Lévyne, *Comptes Rendus de l'Académie des Sciences* **1862**, *54,* 324-327.

16.   R.M. Milton, Molecular Sieve Science and Technology, *Zeolite Science* **1989**, *398,* 1-10.

17.   C.T. Kresge, M.E. Leonowicz, W.J. Roth, J.C. Vartuli, J.S. Beckt, Ordered Mesoporous Molecular Sieves Synthesized by a Liquid-Crystal Template Mechanism, *Nature* **1992**, *359*, 710-712.

18.   S.S. Kistler, Coherent Expanded Aerogels and Jellies, *Nature* **1931,** *127,* 741.

19.   H. Li, M. Eddaoudi, M. O'Keeffe, O.M. Yaghi, Design and synthesis of an exceptionally stable and highly porous metal-organic framework, *Nature* **1999**, *402,* 276-279.

20.   S.Y. Ding, W. Wang, Covalent organic frameworks (COFs): From design to applications, *Chem Soc Rev*. **2013**, *42*, 548-568.

21.   J.S.M. Lee, A.I. Cooper, Advances in Conjugated Microporous Polymers, *Chem Rev*. **2020**, *120*, 2171-2214.

22.   W. Lu, D. Yuan, D. Zhao, C.I. Schilling, O. Plietzsch, T. Muller, S. Brase, J. Guenther, J. Blümel, R. Krishna, Z. Li, H. Zhou, Porous polymer networks: Synthesis, porosity, and applications in gas storage/separation, *Chemistry of Materials* **2010**, 22, 5964-5972.

23.   K.S.W. Sing, Reporting Physisorption Data for Gas/Solid Systems-with Special Reference to the Determination of Surface Area and Porosity (IUPAC), *Pure & Appl. Chem.* **1985**, *57*, 603-619.

24.   F. Xiao, X. Yin, Geometry models of porous media based on Voronoi tessellations and their porosity-permeability relations, *Computers and Mathematics with Applications* **2016**, *72*, 328-348.

25.   T.-D. Ngo, Introduction to Composite Materials, *Composite and Nanocomposite Materials – From Knowledge to Industrial Applications* **2020.**

26.   M. K. Egbo, A fundamental review on composite materials and some of their applications in biomedical engineering, *Journal of King Saud University - Engineering Sciences* **2021**, *33*, 557-568.

27.   P.M. Visakh, M.J. Martínez Morlanes, Nanomaterials and Nanocomposites: Zero- to Three-Dimensional Materials and Their Composites Nanomaterials and Nanocomposites: Zero- to Three-Dimensional Materials and Their Composites **2016**.

28.   N. Pal, A. Bhaumik, Soft templating strategies for the synthesis of mesoporous materials: Inorganic, organic-inorganic hybrid and purely organic solids, *Adv Colloid Interface Sci*. **2013**, *189-190*, 21-41,

29.   R. Ryoo, S.H. Joo, S. Jun, Synthesis of highly ordered carbon molecular sieves via template-mediated structural transformation, *Journal of Physical Chemistry B*. **1999**, 103, 7743-7746.

30.   Y. Shi, Y. Wan, D. Zhao, Ordered mesoporous non-oxide materials, *Chem Soc Rev*. **2011**, *40*, 3854-3878.

31.   W. Yue, W. Zhou, Crystalline mesoporous metal oxide, *Progress in Natural Science* **2008**, 18, 1329-1338.

32.   M. Hu, W. Yang, H. Tan, L. Jin, L. Zhang, P. Kerns, Y. Dang, S. Dissanayake, S. Schaefer, B. Liu, Y. Zhu, S.L. Suib, J. He, Template-free Synthesis of Mesoporous and Crystalline Transition Metal Oxide Nanoplates with Abundant Surface Defects, *Matter* **2020**, *2,* 1244-1259.

33.   W. Xuan, C. Zhu, Y. Liu, Y. Cui, Mesoporous metal–organic framework materials, *Chem Soc Rev*. **2012**, *41*, 1677-1695.

34.   J. Fonseca, T. Gong, L. Jiao, H.L. Jiang, Metal-organic frameworks (MOFs) beyond crystallinity: amorphous MOFs, MOF liquids and MOF glasses, *J Mater Chem A Mater*. **2021**, *9*, 10562-10611.

35.   J. Yang, X. Li, S. Han, Y. Zhang, P. Min, N. Koratkar, Z.-Z. Yu, Air-dried, high-density graphene hybrid aerogels for phase change composites with exceptional thermal conductivity and shape stability, *J Mater Chem A Mater*. **2016**, *4,* 18067-18074.

36.   C. Simón-Herrero, S. Caminero-Huertas, A. Romero, J.L. Valverde, L. Sánchez-Silva, Effects of freeze-drying conditions on aerogel properties, *J Mater Sci*. **2016**, *51*, 8977-8985.

37.   C.A. García-González, M.C. Camino-Rey, M. Alnaief, C. Zetzl, I. Smirnova, Supercritical drying of aerogels using CO_2: Effect of extraction time on the end material textural properties, *Journal of Supercritical Fluids*. **2012**, *66*, 297-306.

38.   Y. Cheng, S. Zhou, P. Hu, G. Zhao, Y. Li, X. Zhang, W. Han, Enhanced mechanical, thermal, and electric properties of graphene aerogels via supercritical ethanol drying and high-Temperature thermal reduction, *Sci Rep*. **2017**, *7*, 1439.

39.   J. Luo, H. Wang, Preparation and characterization of supercritical CO_2 nanocellulose aerogels, *Chem Eng Trans*. **2018**, *66,* 49-54.

40.   J.V. Alemán, A.V. Chadwick, J. He, M. Hess, K. Horie, R.G. Jones, P. Kratochvíl, I. Meisel, I, Mita, G. Moad, S. Penczek. R.F.T. Stepto, Definitions of terms relating to the structure and processing of sols, gels, networks, and inorganic-organic hybrid materials (IUPAC recommendations 2007), *Pure and Applied Chemistry* **2007**, 79, 1801-1829.

41.   J. Fricke, A. Emmerling, Aerogels-Recent Progress in Production Techniques and Novel Applications, *Journal of Sol-Gel Science and Technology* **1998,** *13,* 299-303.

42.   J.P. Vareda, A. Lamy-Mendes, L. Durães, A reconsideration on the definition of the term aerogel based on current drying trends, *Microporous and Mesoporous Materials* **2018,** *258*, 211-216.

43.   C.A. García-González, T. Budtova, L. Durães, C. Erkey, P. Del Gaudio, P. Gurikov, M. Koebel, F. Liebner, M. Neagu, I. Smirnova, An opinion paper on aerogels for biomedical and environmental applications, *Molecules* **2019**, *24*, 1815.

44.   S. Karamikamkar, H.E. Naguib, C.B. Park, Advances in precursor system for silica-based aerogel production toward improved mechanical properties, customized morphology, and multifunctionality: A review, *Adv Colloid Interface Sci*. **2020**, 276, 102101.

45.   L.E. Nita, A. Ghilan, A.G. Rusu, I. Neamtu, A.P. Chiriac, New trends in bio-based aerogels, *Pharmaceutics* **2020**, *12,* 449.

46.   J.L. Gurav, I.K. Jung, H.H. Park, E.S. Kang, D.Y. Nadargi, Silica aerogel: Synthesis and applications, *J Nanomater*. **2010**, *24*, 409310.

47.   I. Smirnova, W. Arlt, Synthesis of Silica Aerogels and Their Application as Drug Delivery System, *Supercritical Fluids as Solvents and Reaction Media* **2004**, 381-427.

48.   A. Soleimani Dorcheh, M.H. Abbasi, Silica aerogel; synthesis, properties and characterization, *J Mater Process Technol*. **2008,** *199,* 10-26.

49.   C.E. Carraher Jr., General topics: Silica Aerogels - Properties and Uses, *Polymer News* **2005**, *30,* 386-388.

50.   K.I. Jensen, J.M. Schultz, F.H. Kristiansen, Development of windows based on highly insulating aerogel glazings, *Journal of Non-Crystalline Solids* **2004**, *350*, 351-357.

51.   S.M. Jones, Aerogel: Space exploration applications, *Journal of Sol-Gel Science and Technology* **2006**, *40*, 351-357.

52.   C.T. Wang, C.L. Wu, I.C. Chen, Y.H. Huang, Humidity sensors based on silica nanoparticle aerogel thin films, *Sensors and Actuators, B: Chemical* **2005**, 107, 402-410.

53.   N. Leventis, C. Sotiriou-Leventis, G. Zhang, A.M.M. Rawashdeh, Nanoengineering Strong Silica Aerogels, *Nano Lett*. **2002**, *2*, 957-960.

54.   H. Maleki, L. Durães, A. Portugal, An overview on silica aerogels synthesis and different mechanical reinforcing strategies, *J Non Cryst Solids*. **2014**, *385,* 55-74.

55.   L. Zuo, Y. Zhang, L. Zhang, Y.E. Miao, W. Fan, T. Liu, Polymer/Carbon-Based Hybrid Aerogels: Preparation, Properties and Applications, *Materials* **2015**, *8*, 6806-6848.

56.   P. Paraskevopoulou, D. Chriti, G. Raptopoulos, G.C. Anyfantis, Synthetic polymer aerogels in particulate form, *Materials* **2019**, *12*, 1543.

57.   J.P. Lewicki, C.A. Fox, M.A. Worsley, On the synthesis and structure of resorcinol-formaldehyde polymeric networks - Precursors to 3D-carbon macroassemblies, *Polymer (Guildf)*. **2015**, *69*, 45-51.

58.   Y. Tao, M. Endo, K. Kaneko, A Review of Synthesis and Nanopore Structures of Organic Polymer Aerogels and Carbon Aerogels, *Recent Patents on Chemical Engineering* **2010**, *1*, 192-200.

59.   Y. Tao, Y. Hattori, A. Matumoto, H. Kanoh, K. Kaneko, Comparative study on pore structures of mesoporous ZSM-5 from resorcinol-formaldehyde aerogel and carbon aerogel templating, *Journal of Physical Chemistry B*. **2005**, *109*, 194-199.

60.   G. Amaral-Labat, A. Szczurek, V. Fierro, A. Pizzi, A. Celzard, Systematic studies of tannin-formaldehyde aerogels: Preparation and properties, *Sci Technol Adv Mater*. **2013**, *14*, 015001.

61.   M.A. Aegerter, N. Leventis, M.M. Koebel, Aerogels Handbook (Advances in Sol-Gel Derived Materials and Technologies) **2011**.

62.   S. Manandhar, P.B. Roder, J.L. Hanson, M. Lim, B.E. Smith, A. Mann, Rapid sol-gel synthesis of nanodiamond aerogel, *J Mater Res*. **2014**, *29,* 2905-2911.

63.   M.A. Worsley, T.F. Baumann, Carbon Aerogels, *Handbook of Sol-Gel Science and Technology* **2016**, 1-36.

64.   P.J. Pauzauskie, J.C. Crowhurst, M.A. Worsley, T.A. Laurence, A.L.D. Kilcoyne, Y. Wang, T.M. Willey, K.S. Visbeck, S.C. Fakra, W.J. Evans, J.M. Zaug, J.H. Satcher Jr., Synthesis and characterization of a nanocrystalline diamond aerogel, *Pnas* **2011**, *108*, 8550-8553.

65.   N. Rey-Paap, A. Arenillas, J.A. Menéndez, Carbon Gels and Their Applicartions: A Review of Patents, *Submicron Porous Materials* **2017**, 25-52.

66.   H. Sun, Z. Xu, C. Gao, Multifunctional, ultra-flyweight, synergistically assembled carbon aerogels, *Advanced Materials* **2013**, *25*, 2554-2560.

67.   T.F. Baumann, M.A. Worsley, T.Y.J. Han, J.H. Satcher, High surface area carbon aerogel monoliths with hierarchical porosity, *J Non Cryst Solids* **2008**, *354,* 3513-3515.

68. J.H. Lee, S.J. Park, Recent advances in preparations and applications of carbon aerogels: A review, *Carbon NY* **2020**, *163*, 1-18.

69. S.A. Al-Muhtaseb, J.A. Ritter, Preparation and Properties of Resorcinol-Formaldehyde Organic and Carbon Gels, *Advanced Materials* **2003**, *15*, 101-114.

70. D.K. Sam, E.K Sam, A. Durairaj, X. Lv, Z. Zhou, J. Liu, Synthesis of biomass-based carbon aerogels in energy and sustainability, *Carbohydr Res*. **2020**, *491*, 107986.

71. M. Enterría, J.L. Figueiredo, Nanostructured mesoporous carbons: Tuning texture and surface chemistry, *Carbon NY* **2016**, *108*, 79-102.

72. M.B. Bryning, D.E. Milkie, M.F. Islam, L.A. Hough, J.M. Kikkawa, A.G. Yodh, Carbon nanotube aerogels, *Advanced Materials* **2007**, *19*, 661-664.

73. Z. Xu, Fundamental properties of graphene, *Graphene: Fabrication, Characterizations, Properties and Applications* **2017**, 73-102.

74. S. Korkmaz, A. Kariper, Graphene and graphene oxide based aerogels: Synthesis, characteristics and supercapacitor applications, *J Energy Storage* **2020**, *27*, 101038.

75. B. Xu, S. Yue, Z. Sui, X. Zhang, S. Hou, G. Cao, Y. Yang, What is the choice for supercapacitors: Graphene or graphene oxide?, *Energy Environ Sci*. **2011**, *4*, 2826-2830.

76. G. Gorgolis, C. Galiotis, Graphene aerogels: A review, *2D Mater*. **2017**, *4,* 032001.

77. W.S. Hummers, R.E. Offeman, Preparation of Graphitic Oxide, *J. Am. Chem. Soc.* **1958,** *80*, 1339.

78. B. Paulchamy, G. Arthi, B.D. Lignesh, A Simple Approach to Stepwise Synthesis of Graphene Oxide Nanomaterial, *J Nanomed Nanotechnol*. **2015**, *6*, 1000253.

79. D.C. Marcano, D.V. Kosynkin, J.M. Berlin, A. Sinitskii, Z. Sun, A. Slesarev, L.B. Alemany, W. Lu, J.M. Tour, Improved synthesis of graphene oxide, *ACS Nano* **2010**, *4*, 4806-4814.

80. N.I. Zaaba, K.L. Foo, U. Hashim, S.J. Tan, W.W. Liu, C.H. Voon, Synthesis of Graphene Oxide using Modified Hummers Method: Solvent Influence, *Procedia Engineering* **2017,** *184*, 469-477.

81. Y. Xu, K. Sheng, C. Li, G. Shi, Self-assembled graphene hydrogel via a one-step hydrothermal process, *ACS Nano* **2010,** *4,* 4324-4330.

82. K. Vrettos, N. Karouta, P. Loginos, S. Donthula, D. Gournis, V. Georgakilas, The role of diamines in the formation of graphene aerogels, *Front Mater*. **2018**, *5*, 20.

83. G. Nassar, E. Daou, R. Najjar, M. Bassil, R. Habchi, A review on the current research on graphene-based aerogels and their applications, *Carbon Trends* **2021**, *4*, 100065.

84. L. Xu, G. Xiao, C. Chen, R. Li, Y. Mai, G. Sun, D. Yan, Superhydrophobic and superoleophilic graphene aerogel prepared by facile chemical reduction, *J Mater Chem A Mater*. **2015,** *3,* 7498-7504.

85. W. Chen, L. Yan, In situ self-assembly of mild chemical reduction graphene for three-dimensional architectures, *Nanoscale* **2011**, 3, 3132-3137.

86. Q. Fang, B. Chen, Self-assembly of graphene oxide aerogels by layered double hydroxides cross-linking and their application in water purification, *J Mater Chem A Mater*. **2014,** 2, 8941-8951.

87. G. Kamble, Graphene Oxide - Applications and Opportunities, **2018**.

88. N. Sahiner, Conductive polymer containing graphene aerogel composites as sensor for CO_2, *Polym. Compos.* **2019**, 40, 1208-1218.

89. C. Li, L. Qiu, B. Zhang, D. Li, C.Y. Liu, Robust Vacuum-/Air-Dried Graphene Aerogels and Fast Recoverable Shape-Memory Hybrid Foams, *Advanced Materials* **2016**, *28,* 1510-1516.

90. H. Li, Y. Tao, C. Zhang, D. Liu, W. Fan, X. Xu, Y. Li, C. You, Z.-Z. Pe, M. Ye, Z. Chen, Z. Dong, D.-W. Wang, F. Kang, J. Li, Q.-H. Yang, Dense Graphene Monolith for High Volumetric Energy Density Li–S Batteries, *Adv Energy Mater*. 2018, 8, 1703438.

91. M. Ding, C. Li, Recent Advances in Simple Preparation of 3D Graphene Aerogels Based on 2D Graphene Materials, *Front Chem*. **2022,** *10,* 815463.

92. A. Borrás, G. Gonçalves, G. Marbán, S. Sandoval, S. Pinto, P.A.A.P. Marques, J. Fraile, G. Tobias, A.M. López-Periago, C. Domingo, Preparation and Characterization of Graphene Oxide Aerogels: Exploring the Limits of Supercritical CO_2 Fabrication Methods, *Chemistry - A European Journal* **2018**, *24*, 15903-15911.

93. A.G. Pandolfo, A.F. Hollenkamp, Carbon properties and their role in supercapacitors, *J Power Sources* **2006**, 157, 11-27.

94. H.F. Ju, W.L. Song, L.Z. Fan, Rational design of graphene/porous carbon aerogels for high-performance flexible all-solid-state supercapacitors, *J Mater Chem A Mater*. **2014**, *2*, 10895-10903.

95. J. Mao, J. Iocozzia, J. Huang, K. Meng, Y. Lai, Z. Lin, Graphene aerogels for efficient energy storage and conversion, *Energy Environ Sci*. **2018,** *11,* 772-799.

96. H. Sun, Y. Lin, H. Takeshi, X. Wang, D. Wu, Y. Tian, Synthesis of 3D graphene-based materials and their applications for removing dyes and heavy metals, *Environ Sci Pollut Res Int*. **2021**, *28*, 52625-52650.

97. A. Borrás, B. Henriques, G. Gonçalves, J. Fraile, E. Pereira, A.M. López-Periago, C. Domingo, Graphene Oxide/Polyethylenimine Aerogels for the Removal of Hg(II) from Water, *Gels* **2022**, *8*, 452.

98. A. Rosado, A. Borrás, J. Fraile, J.A.R. Navarro, F. Suárez-García, K.C. Stylianou, A.M. López-Periago, J.G. Planas, C. Domingo, A. Yazdi, HKUST-1 Metal-Organic Framework Nanoparticle/Graphene Oxide Nanocomposite Aerogels for CO_2 and CH_4 Adsorption and Separation, *ACS Appl Nano Mater*. **2021,** *4*, 12712-12725.

99. J.H. Oh, J. Kim, H. Lee, Y. Kang, I.K. Oh, Directionally Antagonistic Graphene Oxide-Polyurethane Hybrid Aerogel as a Sound Absorber, *ACS Appl Mater Interfaces*. **2018,** *10*, 22650-22660.

100. O.M. Yaghi, N.W. Ockwig, H.K. Chae, M. Eddaoudi, J. Kim, Reticular Synthesis and the Design of New Materials, *Nature* **2003**, *423,* 705-714.

101. S. Kitagawa, R. Kitaura, S.I. Noro, Functional porous coordination polymers, *Angewandte Chemie - International Edition* **2004**, *43*, 2334-2375.

102. H. Furukawa, K.E. Cordova, M. O'Keeffe, O.M. Yaghi, The chemistry and applications of metal-organic frameworks, *Science (1979)* **2013**, *341,* 6149.

103. S. Kaushal, G. Kaur, J. Kaur, P.P. Singh, First transition series metal-organic frameworks: Synthesis, properties and applications, *Mater Adv*. **2021**, *2,* 7308-7335.

104. N. Hara, ZIF-8 Membrane*, Encyclopedia of Membranes* **2016,** 2064-2067.

105. A. Schoedel, M. Li, D. Li, M. O'Keeffe, O.M. Yaghi, Structures of Metal-Organic Frameworks with Rod Secondary Building Units, *Chem Rev*. **2016,** *116,* 12466-12535.

106. A.C. Sudik, A.P. Côté, O.M. Yaghi, Metal-organic frameworks based on trigonal prismatic building blocks and the new "acs" topology, *Inorg Chem*. **2005**, *44,* 2998-3000.

107. L. Sarkisov, R.L. Martin, M. Haranczyk, B. Smit, On the flexibility of metal-organic frameworks, *J Am Chem Soc*. **2014,** *136,* 2228-2231.

108. J. Ha, J.H. Lee, H.R. Moon, Alterations to secondary building units of metal-organic frameworks for the development of new functions, *Inorg Chem Front*. **2019,** *7,* 12-27.

109. N. Portolés-Gil, A.M. López-Periago, A. Borrás, J. Fraile, E. Solano, O. Vallcorba, J.G. Planas, J.A. Ayllón, C. Domingo, Tuning the Structure and Flexibility of Coordination Polymers via Solvent Control of Tritopic Triazine Conformation during Crystallization, *Cryst Growth Des*. **2020,** *20,* 3304-3315.

110. N. Portolés-Gil, S. Gowing, O. Vallcorba, C. Domingo, A.M. López-Periago, J.A. Ayllón, Supercritical CO_2 utilization for the crystallization of 2D metal-organic frameworks using tert-butylpyridine additive, *Journal of CO2 Utilization* **2018**, *24,* 444-453.

111. R.K. Gupta, M. Riaz, M. Ashafaq, Z.-Y. Gao, R.S. Varma, D.-C. Li, P. Cui, C.-H. Tung, D. Sun, Adenine-incorporated metal–organic frameworks, *Coord Chem Rev*. **2022,** 464, 214558.

112. S.S. Rajasree, X. Li, P. Deria, Physical properties of porphyrin-based crystalline metal–organic frameworks, *Commun Chem*. **2021**, *4,* 47.

113. S. Yuan, L. Feng, K. Wang, J. Pang, M. Bosch, C. Lollar, Y. Sun, J. Qin, X. Yang, P. Zhang, Q. Wang, L. Zou, Y. Zhang, L. Zhang, Y. Fang, J. Li, H.-C. Zhou, Stable Metal–Organic Frameworks: Design, Synthesis, and Applications, *Advanced Materials* **2018**, 30, 1704303.

114. R. Haldar, T.K. Maji, Metal-organic frameworks (MOFs) based on mixed linker systems: Structural diversities towards functional materials, *CrystEngComm*. **2013**, 15, 9276-9295.

115. P.Z. Moghadam, S.M.J. Rogge, A. Li, C.-M. Chow, J. Wieme, N. Moharrami, M. Aragones-Anglada, G. Conduit, D.A. Gomez-Gualdron, V. V. Speybroeck, D. Fairen-Jimenez, Structure-Mechanical Stability Relations of Metal-Organic Frameworks via Machine Learning, *Matter* **2019,** *1,* 219-234.

116. N. Stock, S. Biswas, Synthesis of metal-organic frameworks (MOFs): Routes to various MOF topologies, morphologies, and composites, *Chem Rev*. **2012**, 112, 933-969.

117. K.-L. Zhang, C.-T. Hou, J.-J. Song, Y. Deng, L. Li, S. Weng Ng, G.-W. Diao, Temperature and auxiliary ligand-controlled supramolecular assembly in a series of Zn(ii)-organic frameworks: Syntheses, structures and properties, *CrystEngComm*. **2012,** *14,* 590-600.

118. Q. Chu, G.X. Liu, T. Okamura, Y.Q. Huang, W.Y. Sun, N. Ueyama, Structure modulation of metal-organic frameworks via reaction pH: Self-assembly of a new carboxylate containing

ligand N-(3-carboxyphenyl)iminodiacetic acid with cadmium(II) and cobalt(II) salts, *Polyhedron* **2008**, *27,* 812-820.

119. R. Seetharaj, P. v. Vandana, P. Arya, S. Mathew, Dependence of solvents, pH, molar ratio and temperature in tuning metal organic framework architecture, *Arabian Journal of Chemistry* **2019**, 12, 295-315.

120. X. Zhang, Z. Chen, X. Liu, S.L. Hanna, X. Wang, R. Taheri-Ledari, A. Maleki, P. Li, O. K. Farha, A historical overview of the activation and porosity of metal-organic frameworks, *Chem Soc Rev*. **2020**, *49,* 7406-7427.

121. Y.R. Lee, J. Kim, W.S. Ahn, Synthesis of metal-organic frameworks: A mini review, *Korean Journal of Chemical Engineering* **2013**, *30,* 1667-1680.

122. D. Chen, J. Zhao, P. Zhang, S. Dai, Mechanochemical synthesis of metal–organic frameworks, *Polyhedron* **2019,** *162,* 59-64.

123. J. Klinowski, F.A. Almeida Paz, P. Silva, J. Rocha, Microwave-assisted synthesis of metal-organic frameworks, *Dalton Transactions* **2011**, *40,* 321-330.

124. M. V. Varsha, G. Nageswaran, Review—Direct Electrochemical Synthesis of Metal Organic Frameworks, *J Electrochem Soc*. **2020**, *167,* 155527.

125. C. Vaitsis, G. Sourkouni, C. Argirusis, Metal Organic Frameworks (MOFs) and ultrasound: A review, *Ultrason Sonochem.* **2019,** *52,* 106-119.

126. O. Shekhah, Layer-by-layer method for the synthesis and growth of surface mounted metal-organic frameworks (SURMOFS), *Materials* **2010**, *3,* 1302-1315.

127. A.M. López-Periago, O. Vallcorba, C. Frontera, C. Domingo, J.A. Ayllón, Exploring a novel preparation method of 1D metal organic frameworks based on supercritical CO2, *Dalton Transactions* **2015**, *44,* 7548-7553.

128. M.F. Dapaah, B. Liu, Recent Advances of Supercritical CO_2 in Green Synthesis and Activation of Metal–Organic Frameworks, *J Inorg Organomet Polym Mater*. **2020,** *30,* 581-595.

129. Q.R. Fang, T.A. Makal, M.D. Young, H.C. Zhou, Recent advances in the study of mesoporous metal-organic frameworks, *Comments on Inorganic Chemistry* **2010**, *31,* 165-195.

130. D. Zhao, D.J. Timmons, D. Yuan, H.C. Zhou, Tuning the topology and functionality of metal-organic frameworks by ligand design, *Acc Chem Res*. **2011,** *44,* 123-133.

131. M. Eddaoudi, J. Kim, N. Rosi, D. Vodak, J. Wachter, M. O'Keeffe, O.M. Yaghi, Systematic Design of Pore Sizeand Functionality in Isoreticular MOFs and Their Application In Methane Storage, *Science* **2002**, 295.

132. P. Horcajada, S. Surblé, C. Serre, D.-Y. Hong, Y.-K. Seo, J.-S- Chang, J.-M. Grenéche, I. Margiolaki, G. Férey, Synthesis and catalytic properties of MIL-100(Fe), an iron(III) carboxylate with large pores, *Chemical Communications* **2007,** *27,* 2820-2822.

133. I.R. Perera, C. V. Hettiarachchi, U. Ranatunga, Metal–Organic Frameworks in Dye-Sensitized Solar Cells, *Advances in Solar Energy Research* **2019,** 175-219.

134. H. Furukawa, N. Ko, Y. B. Go, N. Aratani, S. B. Choi, E. Choi, A. Ö. Yazaydin, R. Q. Snurr, M. O'Keeffe, J. Kim, O.M. Yaghi, Ultrahigh Porosity inMetal-Organic Frameworks, *Science (1979)*, **2010**, *329,* 421-424.

135. J. An, O.K. Farha, J.T. Hupp, E. Pohl, J.I. Yeh, N.L. Rosi, Metal-adeninate vertices for the construction of an exceptionally porous metal-organic framework, *Nat Commun*. **2012,** *3,* 604.

136. T. Li, M.T. Kozlowski, E.A. Doud, M.N. Blakely, N.L. Rosi, Stepwise ligand exchange for the preparation of a family of mesoporous MOFs, *J Am Chem Soc*. **2013,** *135,* 11688-11691.

137. J. Park, Z.U. Wang, L.B. Sun, Y.P. Chen, H.C. Zhou, Introduction of functionalized mesopores to metal-organic frameworks via metal-ligand-fragment coassembly, *J Am Chem Soc*. **2012,** *134,* 20110-20116.

138. Y. Kim, T. Yang, G. Yun, M.B. Ghasemian, J. Koo, E: Lee, S.J. Cho, K. Kim, Hydrolytic Transformation of Microporous Metal–Organic Frameworks to Hierarchical Micro- and Mesoporous MOFs, *Angewandte Chemie* **2015**, *127,* 13471-13476.

139. L.-G. Qiu, T. Xu, Z.Q. Li, W. Wang, Y. Wu, X. Jiang, X.-Y. Tian, L.-D. Zhang, Hierarchically micro- and mesoporous metal-organic frameworks with tunable porosity, *Angewandte Chemie - International Edition* **2008,** *47,* 9487-9491.

140. Y. Zhao, J. Zhang, B. Han, J. Song, J. Li, Q. Wang, Metal-Organic Framework Nanospheres with Well-Ordered Mesopores Synthesized in an Ionic Liquid/CO$_2$/Surfactant System, *Angewandte Chemie* **2011,** *123,* 662-665.

141. P. Kanti Chattopadhyay, N. Ranjan Singha, MOF and derived materials as aerogels: Structure, property, and performance relations, *Coord Chem Rev*. **2021**, *446*, 214125.

142. L. Li, S. Xiang, S. Cao, J. Zhnag, G. Ouyang, L. Chen, C.-Y. Su, A synthetic route to ultralight hierarchically micro/mesoporous Al(III)-carboxylate metal-organic aerogels, *Nat Commun*. **2013,** *4,* 1774.

143. M.R. Lohe, M. Rose, S. Kaskel, Metal-organic framework (MOF) aerogels with high micro- and microporosity, *Chemical Communications* **2009,** *40,* 6056-6058.

144. P. Cheng, M. Kim, H. Lim, J. Lin, N.L. Torad, X. Zhang, S.A. Hossain, A General Approach to Shaped MOF-Containing Aerogels toward Practical Water Treatment Application, *Adv Sustain Syst*. **2020**, *4,* 2000060.

145. M. Rubio-Martinez, C. Avci-Camur, A.W. Thornton, I. Imaz, D. Maspoch, M.R. Hill, New synthetic routes towards MOF production at scale, *Chem Soc Rev*. **2017**, *46*, 3453-3480.

146. A.F. Sapnik, I. Bechis, S.M. Collins, D.N. Johnstone, G. Divitini, A.J. Smith, P.A. Chater, M.A. Addicoat, T. Johnson, D.A. Keen, K.E. Jelfs, T.D. Bennett, Mixed hierarchical local structure in a disordered metal–organic framework, *Nat Commun*. **2021**, *12,* 2062.

147. T.D. Bennett, A.K. Cheetham, Amorphous metal-organic frameworks, *Acc Chem Res*. **2014**, *47*, 1555-1562.

148. Z. Xin, X. Chen, Q. Wang, Q. Chen, Q. Zhang, Nanopolyhedrons and mesoporous supra-structures of Zeolitic Imidazolate framework with high adsorption performance, *Microporous and Mesoporous Materials* **2013**, *169*, 218-221.

149. F. Yang, W. Li, B. Tang, Facile synthesis of amorphous UiO-66 (Zr-MOF) for supercapacitor application, *J Alloys Compd*. **2018,** *733,* 8-14.

150. T. Zhang, J. Wang, W. Zhang, C. Yang, L. Zhang, W. Zhu, J. Sun, G. Li, T. Li, J. Wang, Amorphous Fe/Mn bimetal-organic frameworks: Outer and inner structural designs for efficient arsenic(iii) removal, *J Mater Chem A Mater*. **2019**, *7,* 2845-2854.

151.   T.C.Wang, W. Bury, D.A. Gómez-Gualdrón, N.A. Vermeulen, J.E. Mondloch, P. Deria, K. Zhang, P.Z. Moghadam, A.A. Sarjeant, R.Q. Snurr, J.F. Stoddart, J.T. Hupp, O.K. Farha, Ultrahigh Surface Area Zirconium MOFs and Insights into the Applicability of the BET Theory, *J Am Chem Soc*. **2015,** *137*, 3585-3591.

152.   D. Li, L. Chen, G. Liu, Z. Yuan, B. Li, X. Zhang, J. Wei, Porous metal–organic frameworks for methane storage and capture: Status and challenges, *New Carbon Materials* **2021**, *36,* 468-496.

153.   A. Ahmed, S. Seth, J. Purewal, A.G. Wong-Foy, M. Veenstra, A.J. Matzger, D.J. Siegel, Exceptional hydrogen storage achieved by screening nearly half a million metal-organic frameworks, *Nat Commun*. **2019,** *10*, 1568.

154.   M. Ding, R.W. Flaig, H.L. Jiang, O.M. Yaghi, Carbon capture and conversion using metal-organic frameworks and MOF-based materials, *Chem Soc Rev*. **2019**, *48,* 2783-2828.

155.   S. Ma, H.C. Zhou, Gas storage in porous metal-organic frameworks for clean energy applications, *Chemical Communications* **2010**, *46*, 44-53.

156.   D. Liu, D. Zou, H. Zhu, J. Zhang, Mesoporous Metal–Organic Frameworks: Synthetic Strategies and Emerging Applications, *Small* **2018**, 14, 1801454.

157.   T.-H. Chen, I. Popov, W. Kaveevivitchai, Y.-C. Chuang, Y.-S. Chen, O. Daugulis, A.J. Jacobson, O.S. Miljanic, Thermally robust and porous noncovalent organic framework with high affinity for fluorocarbons and CFCs, *Nat Commun*. **2014,** *5,* 5131.

158.   C.R. Quijia, C. Lima, C. Silva, R.C. Alves, R. Frem, M. Chorilli, Application of MIL-100(Fe) in drug delivery and biomedicine, *J Drug Deliv Sci Technol*. **2021**, *61,* 102217.

159.   R.C. Huxford, J. Rocca, W. Lin, Metal-organic frameworks as potential drug carriers, *Curr Opin Chem Biol*. **2010**, *14,* 262-268.

160.   K. Raza, P. Kumar, N. Kumar, R. Malik, Pharmacokinetics and biodistribution of the nanoparticles, *Advances in Nanomedicine for the Delivery of Therapeutic Nucleic Acids* **2017**, 165-186.

161.   C. Orellana-Tavra, E.F. Baxter, T. Tian, T.D. Bennett, N.K.H. Slater, A.K. Cheetham, D. Fairen-Jimenez, Amorphous metal-organic frameworks for drug delivery, *Chemical Communications* **2015,** *51,* 13878-13881.

162.   N. Singh, S. Qutub, N.M. Khashab, Biocompatibility and biodegradability of metal organic frameworks for biomedical applications, *J Mater Chem B*. **2021,** *9,* 5925-5934.

163.   J. Guo, Y. Qin, Y. Zhu, X. Zhang, C. Long, M. Zhao, Z. Tang, Metal-organic frameworks as catalytic selectivity regulators for organic transformations, *Chem Soc Rev*. **2021,** *50,* 5366-5396.

164.   C. Pettinari, F. Marchetti, N. Mosca, G. Tosi, A. Drozdov, Application of metal − organic frameworks, *Polym Int*. **2017,** *66*, 731-744.

165.   C.-D. Wu, W. Lin, Heterogeneous asymmetric catalysis with homochiral metal-organic frameworks: Network-structure-dependent catalytic activity, *Angewandte Chemie - International Edition*. **2007**, *46,* 1075-1078.

166.   J. Wang, L. Liu, C. Chen, X. Dong, Q. Wang, L. Alfilfil, M.R. Alalouni, K. Yao, J. Huang, D. Zhang, Y. Han, Engineering effective structural defects of metal-organic frameworks to enhance their catalytic performances, *J Mater Chem A Mater*. **2020,** *8,* 4464-4472.

167. A. Dhakshinamoorthy, M. Alvaro, P. Horcajada, E. Gibson, M. Vishnuvarthan, A. Vimont, J.-M. Grenéche, C. Serre, M. Daturi, H. Garcia, Comparison of porous iron trimesates basolite F300 and MIL-100(Fe) as heterogeneous catalysts for lewis acid and oxidation reactions: Roles of structural defects and stability, *ACS Catal*. **2012**, *2,* 2060-2065.

168. M. Saito, T. Toyao, K. Ueda, T. Kamegawa, Y. Horiuchi, M. Matsuoka, Effect of pore sizes on catalytic activities of arenetricarbonyl metal complexes constructed within Zr-based MOFs, *Dalton Transactions* **2013**, *42,* 9444-9447.

169. L.A. Lozano, B.M.C. Faroldi, M.A. Ulla, J.M. Zamaro, Metal–Organic framework-based sustainable Nanocatalysts for CO Oxidation, *Nanomaterials* **2020,** *10,* 165.

170. R. Díaz, M.G. Orcajo, J.A. Botas, G. Calleja, J. Palma, Co8-MOF-5 as electrode for supercapacitors, *Mater Lett*. **2012,** *68,* 126-128.

171. M. Kurmoo, Magnetic metal–organic frameworks, *Chem Soc Rev*. **2009,** *38,* 1353-1379.

172. D. Maspoch, D. Ruiz-Molina, K. Wurst, N. Domingo, M. Cavallini, F. Biscarini, J. Tejada, C. Rpvira, J. Vecina, A nanoporous molecular magnet with reversible solvent-induced mechanical and magnetic properties, *Nat Mater*. **2003,** *2,* 190-195.

173. Y.J. Tu, C.F. You, C.K. Chang, S.L. Wang, XANES evidence of arsenate removal from water with magnetic ferrite, *J Environ Manage* **2013,** *120,* 114-119.

174. S. Soni, P.K. Bajpai, C. Arora, A review on metal-organic framework: synthesis, properties and application, *Characterization and Application of Nanomaterials* **2018,** *2,* 2.

175. J. Rocha, L.D. Carlos, F.A.A. Paz, D. Ananias, Luminescent multifunctional lanthanides-based metal–organic frameworks, *Chem Soc Rev*. **2011,** *40,* 926-940.

176. B.V. Harbuzaru, A. Corma, F. Rey, J.L. Jordá, D. Ananias, L.D. Carlos, J. Rocha, A miniaturized linear pH sensor based on a highly photoluminescent self-assembled Europium(III) metal-organic framework, *Angewandte Chemie - International Edition* **2009,** *48,* 6476-6479.

177. F. Zhang, J. Shi, Y. Jin, Y. Fu, Y. Zhong, W. Zhu, Facile synthesis of MIL-100(Fe) under HF-free conditions and its application in the acetalization of aldehydes with diols, *Chemical Engineering Journal* **2015**, *259,* 183-190.

178. Y.-K. Seo, J.W. Yoon, J.S. Lee, U.-H. Lee, Y.K. Hwang, C.-H. Jun, P. Horcajada, C. Serre, J.-S. Chang, Large scale fluorine-free synthesis of hierarchically porous iron(III) trimesate MIL-100(Fe) with a zeolite MTN topology, *Microporous and Mesoporous Materials* **2012,** *157,* 137-145.

179. G. Majano, O. Ingold, M. Yulikov, G. Jeschke, J. Pérez-Ramírez, Room-temperature synthesis of Fe-BTC from layered iron hydroxides: The influence of precursor organization, *CrystEngComm*. **2013,** *15,* 9885-9892.

180. A. García Márquez, A. Demessence, A.E. Platero-Prats, D. Heurtaux, P. Horcajada, C. Serre, J.-S. Chang, G. Férey, V.A. de la Peña-O'Shea, C. Boissiére, D. Grosso, C. Sanchez, Green microwave synthesis of MIL-100(Al, Cr, Fe) nanoparticles for thin-film elaboration, *Eur J Inorg Chem*. **2012,** *32,* 5165-5174.

181. Y.G Gorbunova, Y.Y. Enakieva, M.V. Volostnykh, A.A. Sinelshchikova, I.A. Abdulaeva, K.P. Birin, A.Y. Tsivadze, Porous porphyrin-based metal-organic frameworks: synthesis, structure, sorption properties and application prospects, *Russian Chemical Reviews* **2022,** *91,* 4.

182. X. Zhang, M.C. Wasson, M. Shayan, E.K. Berdichevsky, J. Ricardo-Noordberg, Z. Singh, E.K. Papazyan, A.J. Castro, P. Marino, Z. Ajoyan, Z. Chen, T. Islamoglu, A.J. Howarth, Y. Liu, M.B. Majewski, M.J. Katz, J.E. Mondloch, O.K. Farha, A historical perspective on porphyrin-based metal–organic frameworks and their applications, *Coord Chem Rev*. **2021,** *429*, 213605.

183. Y. Diskin-Posner, S. Dahal, I. Goldberg, New effective synthons for supramolecular self-assembly of meso- carboxyphenylporphyrins, *Chemical Communications* **2000**, *7,* 585-586.

184. M.E. Kosal, J.H. Chou, S.R. Wilson, K.S. Suslick, A functional zeolite analogue assembled from metalloporphyrins, *Nat Mater*. **2002,** *1,* 118-121.

185. P. Cai, Y. Huang, M. Smith, H.C. Zhou, Structural Design of Porphyrin-based MOFs, *Porphyrin-based Supramolecular Architectures: From Hierarchy to Functions* **2021**, 1-58.

186. E. Székely, Oldószer, Reagens Vagy Kicsapószer: A Szuperkritikus Szén-Dioxid Változatos Felhasználási Lehetőségei, *MTA Doktori Értekezés Tézisei,* **2019**.

187. C.G. Pereira, M.A.A. Meireles, Supercritical fluid extraction of bioactive compounds: Fundamentals, applications and economic perspectives, *Food Bioproc Tech*. **2010,** *3,* 340-372.

188. M. Knez Hrnčič, M. Škerget, Ž Knez, Non-conventional supercritical fluids as potential solvents in extraction processes, *Journal of Hygienic Engineering and Design* **2014**, *8,* 153-157.

189. A. A. Clifford, J.R. Williams, Introduction to Supercritical Fluids and Their Applications, *Supercritical Fluid Methods and Protocols* **2008,** 1-16.

190. C. Domingo, P. Subra-Paternault, Supercritical Fluid Nanotechnology: Advances and Applications in Composites and Hybrid Nanomaterials, **2015**.

191. S. Artemenko, P. Krijgsman, V. Mazur, The Widom line for supercritical fluids, *J Mol Liq*. **2017,** *238,* 122-128.

192. L. P. Cunico, C. Turner, Supercritical Fluids and Gas-Expanded Liquids, *The Application of Green Solvents in Separation Processes* **2017,** 155-214.

193. Y. Arai, T. Sako, Y. Takebayashi, Supercritical Fluids: Molecular Interactions, Physical Properties, and New Applications, **2002.**

194. S.C. Tucker, Solvent Density Inhomogeneities in Supercritical Fluids, *Chem Rev*. **1999,** *99*, 391-418.

195. Y.W. Lee, Design of Particles Using Supercritical Fluids, *Korean Chemical Engineering Research* **2003**, *41,* 679.

196. W.H. Teoh, R. Mammucari, N.R. Foster, Solubility of organometallic complexes in supercritical carbon dioxide: A review, *J Organomet Chem*. **2013,** *724,* 102-116.

197. R.B. Gupta, J.J. Shim, Solubility in Supercritical Carbon Dioxide, **2006.**

198. M. Tafazzoli, A. Khanlarkhani, Investigation of the enhanced solubility of fluorinated methanes in CO_2 by Monte Carlo simulation: Absolute free energy of solvation and structural properties of solution, *Journal of Supercritical Fluids* **2007**, *40,* 40-49.

199. B. Baradie, M.S. Shoichet, Z. Shen, M.A. McHugh, L. Hong, Y. Wang, J.K. Johnson, E.J. Beckman, R.M. Enick, Synthesis and solubility of linear poly(tetrafluoroethylene-co-vinyl

acetate) in dense CO_2: Experimental and molecular modeling results, *Macromolecules* **2004**, *37*, 7799-7807.

200. P. Kritzer, Corrosion in high-temperature and supercritical water and aqueous solutions: A review, *Journal of Supercritical Fluids* **2004**, *29*, 1-29.

201. S. Raeissi, S. Diaz, S. Espinosa, C.J. Peters, E.A. Brignole, Ethane as an alternative solvent for supercritical extraction of orange peel oils, *Journal of Supercritical Fluids* **2008**, *45*, 306-313.

202. U.S. Food and Drug Administration, Code of Federal Regulations - Food and Drugs, Food and Drug Administration, Food for Human Consumption. *21CFR1841240*.

203. T. Andrews, XVII. The Bakerian Lecture - On the Gaseous State of Matter, *The Royal Society Publishing* **1876**.

204. C.L. Phelps, N.G. Smart, C.M. Wai, Past, Present, and Possible Future Applications of Supercritical Fluid Extraction Technology, *Journal of Chemical Education* **1996**, *73*, 1163-1168.

205. J.E. Mondloch, O. Karagiaridi, O.K. Farha, J.T. Hupp, Activation of metal-organic framework materials, *CrystEngComm.* **2013**, *15*, 9258-9264.

206. G. Férey, C. Mellot-Draznieks, C. Serre, F. Millange, J. Dutour, S. Surblé, I. Margiolaki, A chromium terephthalate-based solid with unusually large pore volumes and surface area, *Science* **2005**, *309*, 2040-2042.

207. A.P. Nelson, O.K. Farha, K.L. Mulfort, J.T. Hupp, Supercritical processing as a route to high internal surface areas and permanent microporosity in metal-organic framework materials, *J Am Chem Soc.* **2009**, *131*, 458-460.

208. O.K. Farha, J.T. Hupp, Rational design, synthesis, purification, and activation of metal-organic framework materials, *Acc Chem Res.* **2010**, *43*, 1166-1175.

209. K. Matsuyama, Supercritical fluid processing for metal–organic frameworks, porous coordination polymers, and covalent organic frameworks, *Journal of Supercritical Fluids* **2018**, *134*, 197-203.

210. A.M. López-Periago, N. Portolés-Gil, P. López-Domínguez, J. Fraile, J, Saurina, N. Aliaga-Alcade, G. Tobias, J.A. Ayllón, C. Domingo, Metal-Organic Frameworks Precipitated by Reactive Crystallization in Supercritical CO_2, *Cryst Growth Des.* **2017**, *17*, 2864-2872.

211. N. Portolés-Gil, R. Parra-Aliana, Á. Álvarez-Larena, C. Domingo, J.A. Ayllón, A.M. López-Periago, Bottom-up approach for the preparation of hybrid nanosheets based on coordination polymers made of metal-diethyloxaloacetate complexes linked by 4,4′-bipyridine, *CrystEngComm.* **2017**, *19*, 4972-4982.

212. P. López-Domínguez, A.M. López-Periago, F.J. Fernández-Porras, J. Fraile, G. Tobias, C. Domingo, Supercritical CO_2 for the synthesis of nanometric ZIF-8 and loading with hyperbranched aminopolymers. Applications in CO_2 capture, *Journal of CO_2 Utilization* **2017**, *18*, 147-155.

213. N. Portolés-Gil, S. Gómez-Coca, O. Vallcorba, G. Marbán, N. Aliaga-Alcalde, A.M. López Periago, J.A. Ayllón, C. Domingo, Single molecule magnets of cobalt and zinc homo- and heterometallic coordination polymers prepared by a one-step synthetic procedure, *RSC Adv.* **2020**, *10*, 45090-45104.

214.   T. Fricic, C.-J. Li, S. Girard, C. Mottillo, C. W. Nickels, Method for the preparation of metal-organic compounds, **2016,** WO2016134459A1.

215.   N. Portolés-Gil, A. Lanza, N. Aliaga-Alcalde, J.A. Ayllón, M. Gemmi, E. Mugnaioli, A.M. López-Periago, C. Domingo, Crystalline Curcumin bioMOF Obtained by Precipitation in Supercritical CO_2 and Structural Determination by Electron Diffraction Tomography, *ACS Sustain Chem Eng*. **2018,** *6,* 12309-12319.

216.   H.V. Doan, Y. Fang, B. Yao, Z. Dong, T.J. White, A. Sartbaeva, U. Hintermair, V.P. Ting, Controlled Formation of Hierarchical Metal-Organic Frameworks Using CO_2-Expanded Solvent Systems, *ACS Sustain Chem Eng*. **2017,** *5,* 7887-7893.

217.   E.R. Parnham, R.E. Morris, Ionothermal synthesis of zeolites, metal-organic frameworks, and inorganic-organic hybrids, *Acc Chem Res*. **2007,** *40*, 1005-1013.

218.   B. Zhang, J. Zhang, B. Han, Assembling Metal-Organic Frameworks in Ionic Liquids and Supercritical CO_2, *Chemistry – An Asian Journal* **2016,** *11*, 2610-2619.

219.   S. Keskin, D. Kayrak-Talay, U. Akman, Ö. Hortaçsu, A review of ionic liquids towards supercritical fluid applications, *Journal of Supercritical Fluids*. **2007**, *43,* 150-180.

220.   A. López-Periago, P. López-Domínguez, J. Pérez Barrio, G. Tobias, C. Domingo, Binary supercritical CO_2 solvent mixtures for the synthesis of 3D metal-organic frameworks, *Microporous and Mesoporous Materials* **2016**, *234,* 155-161.

221.   D. Esken, X. Zhang, O.I. Lebedev, F. Schröder, R.A. Fischer, Pd@MOF-5: Limitations of gas-phase infiltration and solution impregnation of $[Zn_4O(bdc)_3]$ (MOF-5) with metal-organic palladium precursors for loading with Pd nanoparticles, *J Mater Chem*. **2009**, *19*, 1314-1319.

222.   J. Yang, Y.W. Yang, Metal–Organic Frameworks for Biomedical Applications, *Small* **2020**, *16*, 1906846.

223.   M. Meilikhov, K. Yusenko, D. Esken, S. Turner S, G. van Tendeloo, R.A. Fischer, Metals@MOFs - Loading MOFs with metal nanoparticles for hybrid functions, *Eur J Inorg Chem*. **2010**, 3701-3714.

224.   S. G. Aspromonte, F. A. Piovano, E. Alonso, A. V. Boix, Synthesis of Supported Mesoporous Catalysts Using Supercritical CO_2, *Advances in Microporous and Mesoporous Materials* **2020**.

225.   C. Erkey, Preparation of metallic supported nanoparticles and films using supercritical fluid deposition, *Journal of Supercritical Fluids* **2009**, *47*, 517-522.

226.   Y. Zhang, D. Kang, C. Saquing, M. Aindow, C. Erkey, Supported platinum nanoparticles by supercritical deposition, *Ind Eng Chem Res*. **2005,** *44*, 4161-4164.

227.   K. Matsuyama, M. Motomura, T. Kato, T. Okuyama, H. Muto, Catalytically active Pt nanoparticles immobilized inside the pores of metal organic framework using supercritical CO_2 solutions, *Microporous and Mesoporous Materials* **2016**, *225,* 26-32.

228.   Y. Zhao, J. Zhang, J. Song, J. Li, J. Liu, T. Wu, P. Zhang, B. Han, Ru nanoparticles immobilized on metal–organic framework nanorods by supercritical CO_2-methanol solution: Highly efficient catalyst, *Green Chemistry* **2011**, *13*, 2078-2082.

229.   A.M. López-Periago, C. Domingo, Features of supercritical CO_2 in the delicate world of the nanopores, *Journal of Supercritical Fluids* **2018,** *134,* 204-213.

230. P. Horcajada, R. Gref, T. Baati, P.K. Allan, G. Maurin, P. Couvreur, G. Férey, R.E. Morris, C. Serre, Metal-organic frameworks in biomedicine, *Chem Rev*. **2012,** *112,* 1232-1268.

231. A.C. McKinlay, R.E. Morris, P. Horcajada, G. Férey, R. Gref, P. Couvreur, C. Serre, BioMOFs: Metal-organic frameworks for biological and medical applications, *Angewandte Chemie - International Edition* **2010**, *49,* 6260-6266.

232. K. Matsuyama, N. Hayashi, M. Yokomizo, T. Kato, K. Ohara, T. Okuyama, Supercritical carbon dioxide-assisted drug loading and release from biocompatible porous metal-organic frameworks, *J Mater Chem B*. **2014**, *2*, 7551-7558.

233. R. Monteagudo-Olivan, M.J. Cocero, J. Coronas, S. Rodríguez-Rojo, Supercritical CO_2 encapsulation of bioactive molecules in carboxylate based MOFs, *Journal of CO_2 Utilization* **2019**, *30*, 38-47.

234. C. Forest, P. Chaumont, P. Cassagnau, B. Swoboda, P. Sonntag, Polymer nano-foams for insulating applications prepared from CO_2 foaming, *Prog Polym Sci*. **2015**, *41*, 122-145.

235. T. Zhang, Y. Jang, E. Lee, S. Shin, H.J. Kang, Supercritical CO_2 Foaming of Poly(3-hydroxybutyrate-co-4-hydroxybutyrate), *Polymers (Basel)* **2022**, *14,* 2018.

236. A.M. López-Periago, A. Vega, P. Subra, A. Argemí, J. Saurina, C.A. García-González, C. Domingo, Supercritical CO_2 processing of polymers for the production of materials with applications in tissue engineering and drug delivery, *J Mater Sci*. **2008**, *43*, 1939-1947.

237. C.A. García-González, A. Concheiro, C. Alvarez-Lorenzo, Processing of Materials for Regenerative Medicine Using Supercritical Fluid Technology, *Bioconjug Chem*. **2015**, *26*, 1159-1171.

238. K. Tutek, A. Masek, A. Kosmalska, S. Cichosz, Application of fluids in supercritical conditions in the polymer industry, *Polymers (Basel)*, **2021**, *13*, 1-17.

239. V. Santos-Rosales, A. Iglesias-Mejuto, C.A. García-González, Solvent-free approaches for the processing of scaffolds in regenerative medicine, *Polymers (Basel)*, **2020**, *12*, 533.

240. M. Perrut, Supercritical fluid applications: Industrial developments and economic issues, *Industrial and Engineering Chemistry Research* **2000**, *39*, 4531-4535.

241. Natex Prozesstechnologie, Special applications, https://www.natex.at/industries/special-applications

Objectives

This section summarizes the general objectives of the thesis.

The focus of this thesis was built around two classes of porous compounds, all prepared using $scCO_2$ assisted procedures: (i) graphene-oxide aerogels, and (ii) metal organic frameworks (MOFs), particularly iron trimesates and porphyrin-based MOFs. These materials in their pristine form already possess promising properties given by the surface characteristics, porosity, robustness, chemical tunability, *etc.*, but to exploit their full potential, they often need to be functionalized or be involved in composites. By combining them with further substances (porous or non-porous), beside retaining most of their positive features, new characteristics arise. An efficient tool to fabricate such nanoporous functional composites is the use of $scCO_2$. The role of this medium can be diverse throughout the preparation, *e.g.*, solvent, antisolvent, drying agent, *etc*. It is worth to mention that, in many circumstances, the only way for obtaining the target material is by using this fluid. The methodology for synthesizing graphene oxide aerogels in $scCO_2$ was developed and patented in 2018 in the group where this thesis was carried out and, ever since, several examples of functionalizing the aerogel matrix were successfully accomplished. Besides, the *in situ* preparation of MOFs in $scCO_2$ media is a process first developed in the same group in 2015, with a large number of newly discovered MOF and coordination polymer phases. Even though, the potential of these classes of compounds is not yet totally attained, regarding the preparation method, processing and possible applications. Thus, developing new systems based on these porous materials, functionalizing them with different substances and involving them in new complex composite formulations, can open further possibilities towards enhanced, functional porous solids for new applications. With the objective of progressing in the develop of functional porous composites, the mentioned precedents give the basic principles for the preparation of the materials synthesized in this work.

Five particular technical and scientific objectives were settled for the development of this thesis that are listed in the followings.

1. To *in situ* synthetize mesoporous materials by using green technology based on $scCO_2$. The focus is on graphene oxide aerogels and MOFs. Both products are optimized to be used in diverse applications either as pristine compounds or composites.

2. To design processing methods based on $scCO_2$ green technology to synthesize functional mesoporous composites. Graphene oxide aerogels and MOFs are used as supports, which are further functionalized with either organic molecules (pharmaceutically active drug ingredients) or nanoparticles (catalytically active NPs) specifically selected for target applications.

3. To analyze the physicochemical properties of the newly synthesized pristine compounds and composites, as well as the intermediates obtained throughout the preparation processes. Protocols on the use of solid state characterization techniques are thus stablished.

4. To assess the performance in catalytic applications of catalytic NPs@graphene oxide aerogel and catalytic metal-clusters@Fe(BTC) MOF system. The target processes are the hydrogenation of CO_2 to methanol (typical NPs are based on copper and zinc oxide) and the photocatalytic H_2 formation from methanol/water (typical NPs are based on platinum and titanium dioxide).

5. To test different biological applications for the synthesized pristine and functionalized composite MOFs, with the target on azelaic acid@Fe(BTC) for transdermal drug delivery, and metalloporphyrin zinc MOFs for photodynamic cancer therapy.

Equipment and methodology

In this section, the high-pressure equipment used for the preparation of the materials obtained in this thesis (GO aerogels, carboxylic (Fe) MOFs and porphyrin MOFs, and composites derived from these structures) is described. The general procedure to operate the system and the applied techniques to characterize the new substances are detailed.

1. High pressure equipment

Most of the preparation methodologies presented in this thesis are based on the use of $scCO_2$. For reaching this condition, the critical values of this fluid need to be exceeded. The critical values for CO_2 are in an easily accessible range of both temperature and pressure (304 K and 7.38 MPa, respectively), but, in practice, processes are carried out in a higher pressure range (20 MPa) to tune the physical properties, such as the density or diffusivity of the medium. Meanwhile, regularly mild temperature is applied (318-353 K). Besides, the chemical nature of the reagents and cosolvents added to the high pressure equipment was chosen to avoid corrosive interactions. Accordingly, high pressure reactors and accessories were selected from the market and adapted for the conditions required in the designed processes. Figure 1. gives an overview of the system, displaying the main parts together with the most important operational and safety elements.
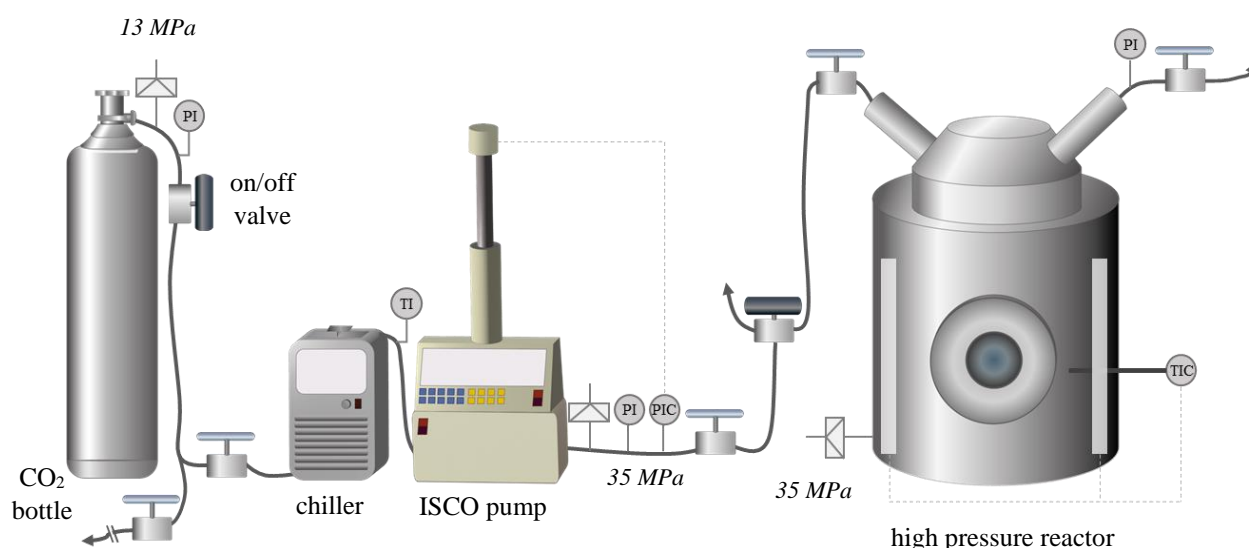
Figure 1. Scheme of the high pressure equipment.

Reactor vessel and accessories

The reactor vessel is the main compartment of the system, where the reagents are placed and contacted with the supercritical fluid for the reaction to take place. Cylindrical reactors of 100 and 200 mL volume are used. The 100 mL reactor was manufactured by TharDesign, with opposite sapphire windows, while the 200 mL reactor was home-made, following the same scheme but without the sapphire windows. Thus, the 200 mL reactor can operate at harsh conditions with high volume of solvent. The windows in the 100 mL reactor are used to

visualize any phase transformation and the current state of the reaction. Experiments were performed in batch mode. The choice of the building material is crucial, since it must withstand the applied high pressure/temperature and, sometimes, corrosive conditions. The reactors used in this work were constructed with stainless steel 316SS, which satisfy safety criteria. The rate settled in the safety devices as the maximum allowable working pressure and temperature is *ca.* 35 MPa at 393 K, which is high enough to allow operation, but much lower than the maximum pressure supported by the reactor. Optionally, stirring can be applied in the vessels by means of the addition of a magnetic bar to the vial and placing a magnetic stirrer below the reactor. This system is routinely used, often several times in a week, thus easy manipulation is important. Hence, the *in* and *out* tubes of the vessels are connected with hand-tight screw caps and quick fit closures for the CO_2 inlet and outlet, allowing fast and safe operation. Polymeric O-ring sealings are used in the connecting parts to diminish the possibility of leakage of the reactor. Accessories, such as thermocouples for temperature control, analogic manometers and digital electronic sensors for pressure measurement, and safety devices, are added to the vessel compartment. The operating units are connected with 1/4" or 1/8" 316SS stainless steel tubing.

a) b) c)
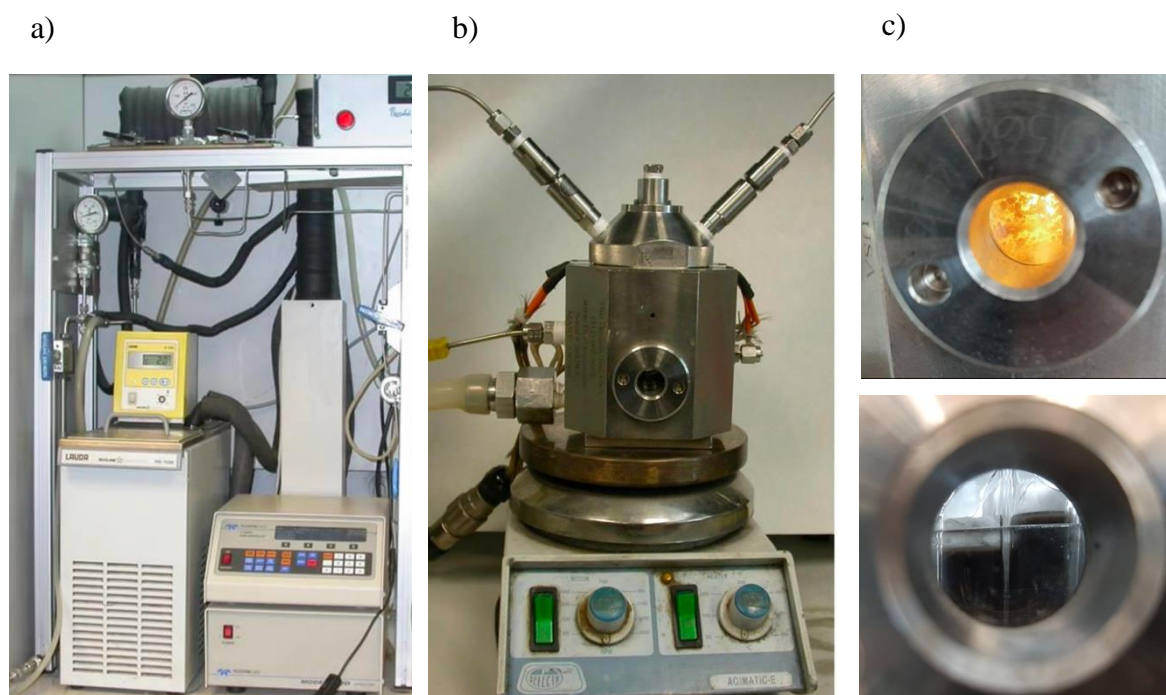
Figure 2. Photos of the compartments of the high-pressure equipment: (a) chiller and pump, (b) 100 mL reactor, (c) MOF and aerogel samples visible through the sapphire window during preparation.

High-pressure valves

The reactor system is equipped with two types of valves, needle valves for flow control and ball-types for on/off service. Valves are responsible for regulating the gas flow (in and out) with CO_2 and releasing the media after the reaction. Precise flow regulation is extremely important, especially in the outlet, because slow isothermal pressure release is required for obtaining appropriate products. Uncontrolled pressure drop can induce local freezing in the outlet tubes and valves, resulting in plugging. Moreover, extremely fast pressure release can originate mechanical forces that damage the samples, particularly the fragile aerogels. Needle valves are mounted before and after the high-pressure pump to separate the chamber from the CO_2 bottle and the reactor. (Figure 1) Ball valves are used in our system to isolate different sections of the system, such as two reactor segments or the CO_2 bottle from the atmosphere to avoid leakage in case of cylinder closure failure.

High pressure pump and cooling system

A Teleydine ISCO D260 syringe pump is used to increase the pressure of the CO_2 to the operating condition. In order to avoid cavitation, the fluid needs to be kept in liquid phase inside the pump, which is accomplished by cooling the inlet CO_2 to a temperature below 273 K with a Lauda Ecoline RE 106 Chiller. The pump is rated to 50 MPa. While using the pump, particular attention needs to be turned to the proper isolation of the pressurized section, to protect the surrounding compartments, and the CO_2 cylinder from exceeding their nominal pressure.

Safety accessories

The system is equipped with various pressure relief devices that opens to atmosphere in an unexpected event leading to pressure increase above the settle limit value. This value is much lower than the pressure rating of the units. For the designed equipment, rupture discs were preferred in comparison to relief valves, as their failure is less probable in case of any solid or sticky contamination. Rupture disks open completely and instantaneously in case of overpressure, while relief valves open only partially to evacuate the section to a pressure below a certain settle value. Rupture discs are mounted on the CO_2 cylinder rated at 13 MPa. The pump and reactor have rupture disks opening at 35 MPa. The rupture disks are equipped with a silicon tube to safely guide the expanding fluid to the fume hood in case of opening. The complete high pressure system, apart from the CO_2 cylinder, is built inside a fume hood with a safety glass to minimize risks that might affect the operator.

2. Methods

2.1. Preparation methods

Often, multiple-step preparation procedures are required to build up the functional porous composites synthesized in this work. The selection of the chosen methodology is based on the desired properties for the final material. In this thesis, preference was given to design simple and sustainable processes, when possible. The main preparation steps are summarized in Figure 3, while the detailed procedure for each different end product is described in each corresponding chapter.

The processes of synthesis involve conventional chemistry for the preparation of some of the constituents of the composites (*e.g.,* precipitation methods for bimetallic or MOF NPs). Then, the high pressure $scCO_2$ technology is used for diverse purposes:

- gel formation and drying, while maintaining the porous structure in case of GO-based aerogels (Chapter I and II)
- facilitating the elimination of organic solvent in case of Fe(BTC) MOF (Chapter III)
- drug or metal-based salt impregnation to the pores of Fe(BTC) MOF (Chapter III and IV)
- polyvinyl alcohol-based pellet formation with $scCO_2$ foaming (Chapter III)
- reaction solvent in porphyrin-based MOF preparation (Chapter V).

Eventually, some materials require post-synthetic treatment to obtain the desired products, such as thermal reduction.
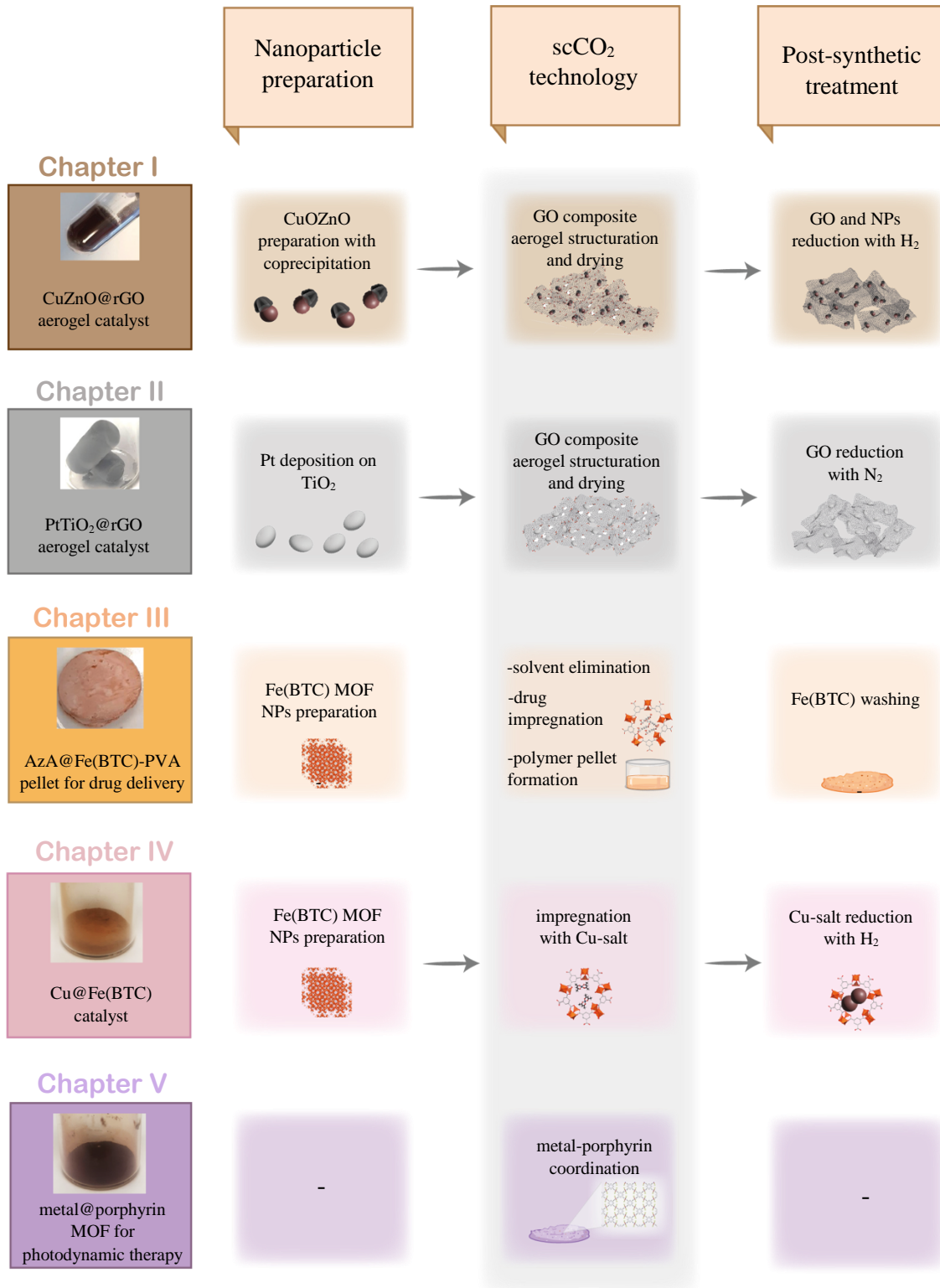
Figure 3. Main preparation steps applied in this thesis for synthesizing nanostructured porous materials.

Operation of the reactor

The procedure for operating the high pressure reactor is similar in all cases, even different products are pursued. A general description of the process is given following, matched with the codes on Fig. 1, while specific descriptions for each material are presented in the relating chapters. The scCO$_2$ procedure starts with setting the cooling system of the pump to *ca.* 271 K. Then, a vial filled with precursors, either as a solid powder or dispersed/dissolved in a small amount of organic solvent (*e.g.,* 1-2 mL) is placed in the high pressure vessel. After sealing the reactor at room temperature, the pump and the vessel are filled with liquid CO$_2$ up to the pressure of the bottle, *ca.* 6 MPa. The inlet and outlet valves of the pump are closed, and the pressure of the confined CO$_2$ in the pump cylinder is increased up to 20 MPa. By carefully opening the outlet valve of the pump and the inlet valve of the reactor, the compressed CO$_2$ is slowly added to the reactor. The operating temperature is set to the target value, in general in the 318-353 K range, and the pressure is adjusted to the final value of 20 MPa. These conditions are maintained until the reaction is completed (24 – 96 h). After isolating the vessel, the remaining CO$_2$ is released from the pump and the tubes located before the reactor. To recover the end product, the outlet valve of the reactor is slowly opened and the fluid is released to the atmosphere, while controlling the gas flow by bubbling in water. Finally, the temperature is decreased to room temperature and the sample is collected from the reactor vessel.

2.2. Characterization techniques

In this section, the main characterization techniques applied in this thesis are described, including their principles, the instrumentation and the information deduced from data analysis. Increased attention is devoted to those key techniques that were used more frequently and provided the most important information to understand the properties of the materials synthesized in this work.

2.2.1. X-ray diffraction (XRD)

X-ray diffraction is a non-destructive, non-contact characterization technique, ideal for the identification of crystallographic structures, chemical composition and some physical properties of crystalline solid materials.[1] The X-ray wavelengths (0.01 – 10 nm) are in the range of the spacings of the atomic-scale lattice planes, thus can interfere with the crystalline planes and provide relevant information about the structure of the crystals. The X-rays are generated in a cathode ray tube by accelerating electrons using a high voltage difference and bombarding them into a target material, most commonly copper. The striking of the target anode causes the

emission of X-rays, which is a superposition of continuous and discrete (K_α, K_β) radiation, latter being characteristic for the anode. Monochromatic X-rays are selected with filters, concentrated and directed towards the sample. Routinely, K_α radiation of copper is used, possessing a wavelength of 1.5418 Å. When the X-ray beam collide the sample, it is scattered by the atoms. At particular angles of the incident light, the scattered beams are in phase, satisfying the Bragg's law, thus they interfere constructively resulting in intensity maximums. The diffracted X-rays are detected and processed and can be converted to interplanar spacings, characteristics of the unit cell of the particular materials.[2] The recorded reflection intensities are used to resolve the structure or deduce further information about mono- or polycrystalline samples.

Single crystal and powder X-ray diffraction

Two main methods can be distinguished when researching the crystal structure of solid materials, namely single crystal X-ray diffraction (SCXRD) and powder X-ray diffraction (PXRD). SCXRD is very powerful to accurately elucidate cell dimensions and details regarding atomic arrangements for structures composed of relatively few atoms (< 100) in the asymmetric unit; however, it requires the preparation of single crystals, large and stable enough for a reliable analysis.[3] As this is often not possible, PXRD is used to study powdered materials. The analyzed powder is composed of randomly oriented crystallites and the diffraction intensities are given by the contribution of those. In PXRD, the intensity of the scattered light is represented customarily in the function of the diffraction angles, giving so-called diffraction patterns. In this work, single-crystal X-ray diffraction experiments were performed in the XALOC beamline at the ALBA synchrotron (Spain) to solve the crystal structure of a MOF. Moreover, PXRD patterns were recorded using a Siemens D5000 diffractometer, working with the Cu K_α incident radiation. The measured range was within the $2\theta = 2\text{-}80°$ interval. Data was acquired in steps of either 0.01 or 0.02° step, depending on the required resolution. Although structure determination is not possible as accurately as in case of the analysis of single crystals, diverse information about the bulk of the polycrystalline material -including physical and chemical properties- can be deduced.

a) Crystal phase identification: most frequently, crystalline phases are identified by comparison with recorded diffraction patterns collected in data bases (JCPDS cards) or from patterns simulated directly from SCXRD crystallographic data using different softwares (*e.g.,* Mercury). Each pure crystalline solid substance possesses a diffraction pattern, that acts like a fingerprint and can be independently detected in a mixture of substances. Some analytical and

graphical methods have been described for peak identification.[1] Contrarily, amorphous compounds are lacking the long-range order, thus no diffraction peaks are discernable in the X-ray spectra, and different techniques are required for their structural characterization.[4]

b) Crystallite size calculation: the diffraction pattern can be used to estimate the crystallite size from peak broadening, which occurs when the domain size decreases from bulk to nanoscale. More specifically, three factors contribute to the broadening of the peaks: (i) the used instrumental, (ii) the crystallite size and (iii) the local lattice strain that arises from crystal imperfections.[5] The instrumental broadening can be minimized by measuring a standard (*e.g.,* lanthanum hexaboride) under the same conditions, while the strain broadening can be distinguished from the target size broadening, as the angle dependence is much larger.[2] The size broadening of a peak is, then, calculated from the full width at the half maximum of the peak and corrected with the instrumental value (β_{corr})) at a specific angle (θ). The domain size of the crystallites (D) is estimated using the Scherrer equation.[6]

$$D = \frac{K \cdot \lambda}{\beta_{corr} \cdot \cos(\theta)}$$

where K is the Scherrer constant dependent on the morphology of the crystalline domain and λ is the applied X-ray wavelength. It is worth to note that the visual particle size not necessarily matches the domain size calculated from X-ray diffraction, as the particles in the powder usually consist multiple crystallites.[4]

c) Detection of crystal defects, alloy formation and pore filling: XRD analysis is suitable for detecting crystal defects in the structure, the presence of impurities or the formation of an alloy.[2] Defects on a crystalline structure can be originated by the expulsion of atoms from their lattice sites, thus increasing the interlayer lattice spacing causing the shift or the broadening of the peaks or a loss of intensity.[7] Frequently, such changes in the crystal structure are analyzed using more advanced instruments, such as *in situ* high temperature XRD or *ex situ* parallel beam XRD, capable of recording high-resolution spectra, although they often requires the preparation of single crystals.[8] In porous materials, the filling of the pores with solvents or solutes can be directly followed by the gradual decrease of the intensity of specific peaks in the XRD pattern. The reason is the loss in periodicity experienced by the filled pores.[9,10]

2.2.2. Fourier-transform infrared spectroscopy (FTIR)

Infrared spectroscopy is a well-established technique for the structural analysis of molecules by detecting their chemical bonds and functional groups. The wavelength of the electromagnetic

radiation in the infrared region is in the same range as the vibrational frequency of the chemical bonds, thus it can be absorbed by the molecules by promoting transitions between the vibrational levels of their lowest electronic energy state. Before directing the IR light to the sample, it is transformed to an interferogram by splitting the beam and, then, reflecting and recombining them with a different path. The interferogram passes through the sample and the transmitted signal is converted to a spectrum by Fourier transformation. Data is commonly plotted as the absorption or transmission values *versus* the wavenumber. Two widely used sampling methods are applied, the transmission and the attenuated total reflectance (ATR) methods. In transmission mode, the radiation is passing through the solid sample dispersed in KBr, giving information about the bulk. High resolution can be reached. On the contrary, in the ATR mode the light penetrates only around 0.5-2 µm in the sample, thus, the information is provided only from the surface. The advantage of ATR relies on the fact that it does not require sample preparation, since the material to analyze can be directly placed on the ATR prism that transmits the IR light. This method only gives reliable results at wavenumbers higher than 600 cm^{-1}, because below this value the most commonly applied prisms (ZnSe and Ge) absorb the IR radiation. In this work a Jasco 4700 Spectrophotometer was used using both sampling methods. The presence or absence of functional groups in different samples was qualitatively studied using this technique. IR frequencies corresponding to specific covalent bonds were compared to data published in literature. Moreover, from the measured relative peak areas, assumptions were made about the occurrence of molecular fragments. This technique allowed to follow the molecular changes upon sample reduction. The purity of the samples was investigated based on the presence and prevalence of unwanted moieties. Finally, the desired incorporation of guest molecules is also detected with this technique.

2.2.3. N_2 adsorption/desorption measurements

N_2 adsorption/desorption at low temperature is a standard technique aimed to study the textural properties of porous solid materials, such as surface area, pore volume, pore size distribution, *etc*. Automatic physisorption equipment (Micromeritics), with static manometric determination, was used for this purpose. In this equipment, before sample measurement, the free volume in the analysis tube surrounding the adsorbent is calibrated using helium. Then, a known amount of N_2 at 77 K is added to the calibrated tube which contains the adsorbent. The adsorption takes place until an equilibrium is reached and, as a consequence, the pressure in the tube decreases. The difference between the pressure at the equilibrium and the one given initially is used to determine the amount of adsorbed gas. The adsorbed gas volume is measured

at several pressure values from low vacuum ($p/p^0 = 10^{-4}$) to atmospheric pressure and their representation provides the adsorption isotherm.

The general mechanism of N_2 sorption in heterogeneous surfaces, involving different pore sizes, is schematized in Figure 4.[11] Due to the high adsorption potential in micrometric pores, the filling of these is achieved in the first place at very low relative pressures. Next, slowly increasing the pressure, a monolayer of the adsorbate is formed on the wall of the pores with mesopore diameter. Once this first covering layer is established, further layers start to accumulate inside the pores. After a certain relative pressure, capillary condensation begins. This phenomenon occurs because the gas condenses to a liquid-like phase in the small confined space at pressures lower than the saturation pressure in the bulk. By further increasing the pressure, multilayer formation in macropores is also possible at relative pressures close to 1. During the desorption process by decreasing the relative pressure, the liquid adsorbate evaporates and gets released slowly from the surface.
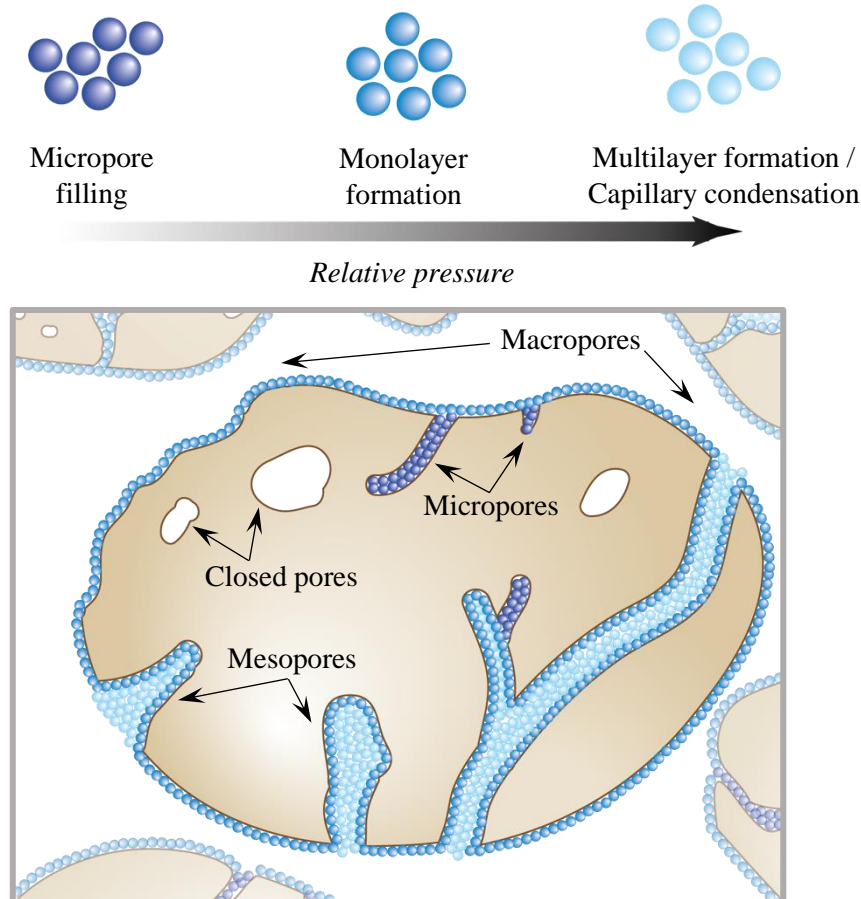

Figure 4. Schematic representation of the process of nitrogen adsorption on porous surfaces.

The sorption process is described by representing the adsorbed amount of N_2 vs. the relative pressure, providing the adsorption isotherm. The shape of the isotherm describes the nature of the adsorption process, arising from the textural properties of the adsorbent, thus the surface characteristics of the porous materials can be assessed. IUPAC classifies six types of isotherms, which are characteristic of microporous (type I), mesoporous (type IV and V) and non-porous or macroporous (type II, III, VI) materials (Figure 5).[12] Among these types, the materials synthesized in this thesis are predominantly mesoporous, hence they show the behavior of type IV isotherms. However, for the studied mesoporous MOFs, the pore size is extremely close to the micropores, only slightly larger than 2 nm. As a consequence, these materials are better described with type I isotherm, in which the curve is concave to the x-axis, the initial steep increase in the adsorption branch, is due to the strong adsorptive-adsorbent interaction in the narrow mesopores. The type IV isotherm displays hysteresis loops related to capillary condensation, in which the adsorption and desorption branches follow different paths.[13,14] The shape of the hysteresis loop depends on the texture of the sample, giving the basis for the IUPAC classification of loop shapes in H1 – H5 groups (Fig. 6).[13]

- H1: adsorbents containing uniform mesopores with a cylindrical shape.
- H2: complex mesopore structures, for example with ink-bottle shape pores, where during the desorption process a pore-blocking mechanism occurs, due to the small diameter of the neck of the pores in comparison to the pore body.

  a) pore-blocking in pore-necks with narrow size distribution

  b) pore-blocking, in pore-necks with wider size distribution

- H3: non-rigid aggregates of plate-like particles or presence of macropores. No limitation occurs in the adsorption at high pressure.
- H4: similar to H3, but with the additional presence of micropores.
- H5: containing both open and partially blocked mesopores.
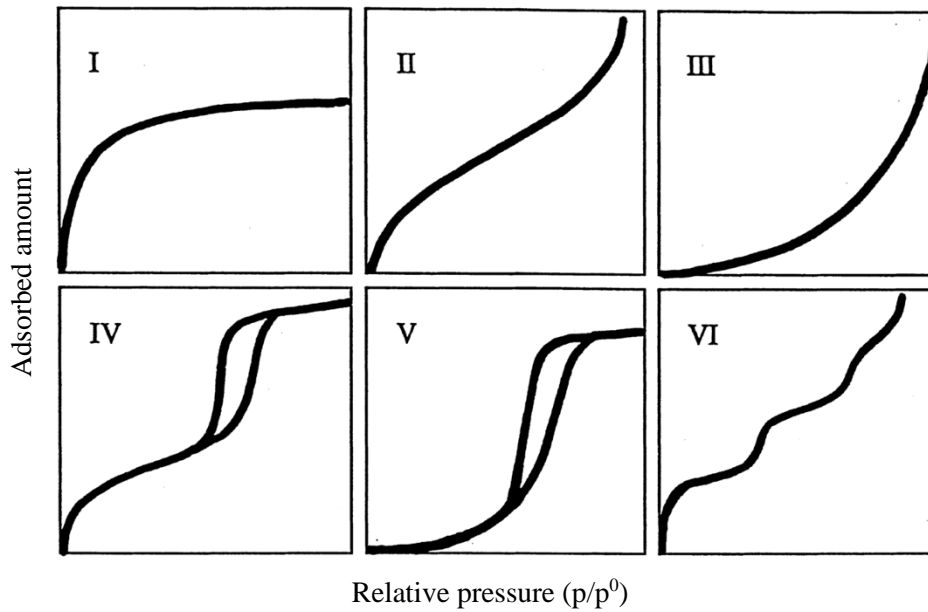
Figure 5. Type I-VI adsorption isotherms based on IUPAC classification, corresponding to microporous adsorbents (I), macroporous/non-porous adsorbent with strong adsorbate-adsorbent interaction (II), macroporous/non-porous adsorbent with weak adsorbate-adsorbent interaction (III), monolayer adsorption and capillary condensation in mesoporous solids (IV), multilayer adsorption and capillary condensation in some mesoporous systems with weak adsorbate-adsorbent interaction (V) and layer-by-layer adsorption on macroporous/non-porous solids (VI). Images are adapted.[12,13]
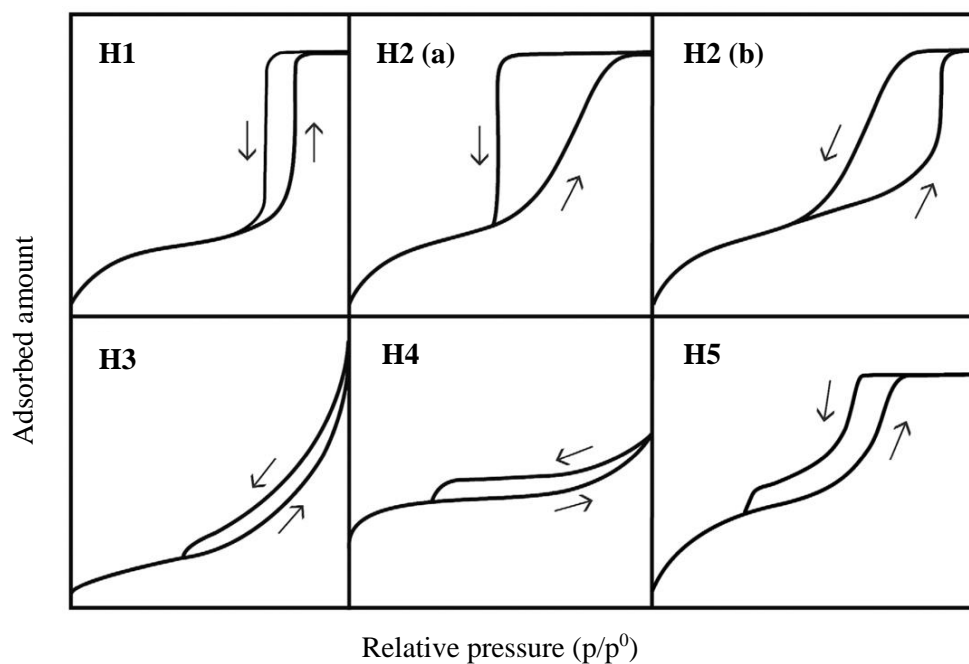
Figure 6. Empirical classification of hysteresis loops given by IUPAC classification. Images are adapted.[13]

From the adsorption isotherms, various textural properties can be determined using mathematical models, which are briefly discussed in the next paragraphs.

Specific surface area: for mesoporous materials, this parameter is calculated using the BET theory, named after Brunauer, Emmett and Teller, who developed the following equation.

$$\theta = \frac{C \cdot p}{\left(1 - \left(\frac{p}{p^0}\right)\right)(p^0 + p(c-1))}$$

In this equation, θ represents the surface coverage (amount of adsorbate / monolayer equivalent), $\frac{p}{p^0}$ is the relative pressure, while C is the BET constant, related to the energy of monolayer adsorption.

Even the method is also widely applied to microporous materials, the BET equation was designed for mesoporous structures with Type IV isotherms. In the presence of micropores, special attention needs to be taken to obtained data.[13] The model determines the effective area available for adsorption from the specific amount of adsorbed N_2. The most accurate fit is achieved above 0.3 p/p^0 relative pressure.[15] To calculate the specific surface area two steps need to be performed. First, the monolayer capacity is derived, representing the amount of adsorbate that is sufficient to completely cover the surface with one monolayer of molecules. Then, by adopting the cross-sectional area of the N_2 molecule, the monolayer capacity is transformed to the surface area.

***Pore volume:*** mesopore volume is often calculated from the adsorbed amount of gas corresponding to the plateau of the Type IV isotherms (*ca.* $p/p^0 = 0.95$). Using the condensate density (assuming that liquid N_2 is filling the pores), the mesopore volume can be estimated. Applying this approach, it is assumed that at the upper relative pressure range ($p/p^0 > 0.95$) the isotherm is horizontal, meaning that no significant amount of macropores is present. The micropore volume must be estimated following different methods, such as t-plot , α_s or Dubinin-Radushkevich equation.[13,16]

Pore size distribution: Regarding the pore size distribution analysis, the model proposed by Barret, Joyner and Halenda (BJH) is the most commonly used to assess mesopores.[17] This method is based on the Kelvin equation. As mentioned above, in confined meso spaces capillary condensation occurs, meaning that the gas-liquid transition takes place at lower pressure than the saturation pressure in bulk. This shift in the condensation depends on the radius of the

confined space (pore size). Such that, from the adsorption isotherm at each point, where this phenomenon occurs, information can be obtained about the volume of the gas adsorbed in different radius. This radius (Kelvin radius) is smaller than that of the actual pore, because when the capillary condensation begins already a monolayer is covering the surface of the pore. For calculating the actual pore radius, the Kelvin radius needs to be corrected with the thickness of the already adsorbed film.[13] The IUPAC classification regarding pore size is based on these frontiers in the adsorption behavior. Pores in the mesopore range (2-50 nm) is filled at such relative pressures (*ca.* 0.39-0.95) when the capillary condensation occurs and the Kelvin equation can be applied to this interval.[18] For the evaluation of micropore size, often semi-empirical methods are used, such as the Horváth and Kawazoe model.[19]

In this work the textural properties of the synthesized materials were assessed by N_2 adsorption/desorption at 77 K using an ASAP 2020 Micromeritics Inc.. The samples were outgassed prior to the analysis for 24 h under vacuum and elevated temperature, typically at 353-423 K to remove all the physisorbed substances. The same equipment was used to analyze the sorption of CO_2 at 273 K, interesting to evaluate the sorption capacity of a catalyst crucial for the catalytic application. Apart from the characteristics of the bare materials, any changes in the textural properties occurring during the modification of the samples, such as impregnation, deposition with NPs or thermal reduction, could be followed using this technique.

2.2.4. Electron microscopy

Electron microscopy is a visual tool for analyzing the morphological and structural features of samples in nano- and microscale. Two common types of electron microscopy can be distinguished, the scanning (SEM) and the transmission (TEM), both being suitable for obtaining high-resolution images by bombarding the surface of the samples with a focused electron beam under vacuum. In case of SEM, the beam is scanning the surface of the sample in a raster over a region and the images are created from the detection of the elastically scattered electrons (BSE) originated from the deeper part of the sample (in the order of 10^3 nm), or secondary electrons (SE) coming from the top 1-10 nm of the surface. In TEM a broader beam of electron is transmitted through a thin layer of the sample and the signal is detected on the opposite side of the specimen, generating images about the internal structure and allowing even higher magnification in comparison to SEM.[20]Arising from the origin of the signal, SEM provides lower resolution images than TEM, but carries compositional information, while SEM

is also suitable to study the topography of the material. The two techniques require different sample preparation.

- For SEM, the samples were placed either on a carbon tape or on top of a silicon wafer, and regularly covered with a few nanometer thickness Pd/Au layer to ensure a conductive surface, thus inhibiting electrostatic charging that may result in low quality images. The Pd/Au metal cover was made using a K550 Sputter Coater. SEM images were taken using a Quanta Fei 200 microscope at high vacuum and an electron beam of 10-20 kV.

- For TEM, a very thin layer of the sample is necessary, as the major part of the electron beam needs to be transmitted to obtain informative images. To prepare the samples, some drops of a diluted dispersion of the solid sample are placed on a copper grid, used as a support, and let to dry in open air. TEM images were taken with JEOL 1210 instrument of nanoparticles in <100 nm range.

2.2.5. Energy dispersive X-ray spectroscopy (EDS)

Vacancies are created in the inner shell of an atom by bombarding a solid with an electron beam, which are filled by electrons from the outer-shell. This relaxation process is accompanied with X-ray radiation, which is characteristic for each element, as there is a direct correlation between the frequency of the emitted X-ray and the atomic number. Together with the image created by the transmitted or scattered electron beam, the pattern can be related with the spatial location of the elements. In EDS, the complete elemental spectrum for every pixel of the image is collected, and each detected element is associated with a color for visualization, such that electron micrographs with the locations of the elements can be displayed. The EDS system can be set on TEM or SEM, but due to the better resolution of TEM it gives compositional information in a smaller scale than SEM. Although this technique is suitable to identify the relative proportion of most of the elements in the sample, those that has a low atomic number (< 10), or are present in a low concentration, are not emitting enough characteristic X-ray. In this work, a Quanta Fei 200 microscope mounted with an EDS detector was used to identify the relative percentage of metals in several appointed spots of bimetallic nanoparticles, as well as impregnated MOFs. The distribution of metallic particles in some sections was studied with XHRSEM FEI Magellan 400L STEM microscope by creating compositional maps of assigned sample areas.

2.2.6. X-ray photoelectron spectroscopy (XPS)

XPS is a technique capable of analyzing the elemental composition of the outer surface (1-10 nm) of solid samples. Moreover, it provides information about the chemical state of the elements composing the surface. The solid samples are exposed to high-energy X-ray radiation, that expulse core electrons from the surface atoms. By measuring the kinetic energy of these electrons, the binding energies can be calculated, which are sensitive to the chemical environment of the atom and characteristic of the element and its state. Data are usually interpreted as the intensity corresponding to the binding energy. From the peak areas the relative concentration of the elements can be estimated. To analyze different states of the same element, the peaks need to be deconvoluted by a specific software, as there are only slight differences between the binding energies.[21] Beside the photoelectrons, Auger electrons are also emitted from the surface atoms, which carries further information about the electronic state of the compounds. After the expulsion of the core photoelectron, another electron from the outer shell can fill the created vacancy, and the energy release can result in the emission of an Auger electron. From the kinetic energy of the expelled photoelectron and Auger transitions, the Auger parameter can be calculated. Additionally, displaying the most intense photoelectron binding energies *vs.* the Auger kinetic energies, the Wagner plot is established, which is a visual tool for chemical state identification. The position of different chemical species on the plot gives an indication about their chemical state, environment, interaction with other species, *etc.* In the NIST XPS database, energies of photoelectron and Auger-electron spectral lines are collected for most of the elements and can be used as the identification reference for surface species.[22]

In this thesis, XPS analysis was carried out in a Specs Spectrometer to determine the percentage and oxidation state of metals and their interactions in bare and graphene oxide supported bimetallic nanoparticles, as well as for analyzing metal-MOF composites.

2.2.7. Inductively coupled plasma mass spectrometry (ICP-MS)

ICP-MS is used for the quantification of the elemental constituents in solids up to trace levels. During measurements, the samples are fully decomposed to their elements, ionized and the ions are sorted by their mass-charge ratio before being detected by an ion detector. An Agilent 7700x ICP-MS was used in this work to determine atomic contents of supported bimetallic nanoparticles, as well as of bare MOFs and those impregnated with metal. Prior to the analysis, the samples were digested at high temperature in hydrochloric, nitric and hydrofluoric acids (3:1:0.5 v/v).

2.2.8. Dynamic light scattering (DLS)

The hydrodynamic size of small (nano)particles can be measured based on their Brownian motion when they are dispersed in a solution. In DLS analysis, a dispersion of nanoparticles is pointed with laser light that gets scattered in all directions. The intensity of the scattered light is detected as a function of time and linked with the size of the particles. Smaller particles move with higher speed in the dispersion than larger particles, thus exhibiting faster fluctuations. Hence, by using the parameters influencing the motion and the scattering (viscosity, temperature, and refractive index of the dispersant) the particle size distribution in the dispersion can be estimated. With this technique, the hydrodynamic diameter is determined assuming spherical particles. In comparison to TEM or SEM, which are direct techniques measuring particle size, DLS is an indirect technique. This measurement is used for particles in the submicron range, since homogenous stable dispersions are required. The sedimentation of large particles must be avoided, because they are disturbing the random Brownian motion. Besides, from the width of the size distribution the polydispersity index can be envisaged.[23] In this thesis, two different equipment were used, a Zetasizer Nano ZS Malvern Instrument and a DLS Coulter LS230. Data on the hydrodynamic size of the MOF particles and graphene oxide aerogel fragments after ultrasound treatment in water were obtained.

2.2.9. UV-vis spectrophotometry

Phenomena of absorption, fluorescence, phosphorescence *etc.* occurs when a solid or liquid sample is irradiated with UV or visible light. Light absorption on liquid/solid samples and reflectance on solids are analyzed to identify and quantify molecules, and to study their optical properties. The incident photons of UV and visible light are absorbed by some molecules in the samples. The absorption gives the energy to induce electronic transitions from a low to a high energy level. The energy of these transitions is characteristic of the material. Thus, plotting the wavelength vs. the degree of absorption, qualitative and quantitative determination of the molecules can be performed by previously collecting data on a calibration curve. In case of diffuse reflectance spectroscopy, the UV-vis beam is directed to a solid powder or a surface, and the reflected diffuse light is produced in all directions of the hemisphere of the incident light. The detected spectra are composed of the combination of several optical phenomena, such as multiple reflectance, scattering and refraction, and they are informative about the properties of the sample.[24] In this thesis, UV-vis spectrometry was used to analyze the optical properties of porphyrin-based MOFs by their absorption in water dispersion using Varian Cari 5000

equipment, while diffuse reflectance UV-vis spectra were recorded for a photoactive solid, namely graphene oxide based aerogels with Jasco V-560 equipment.

2.2.10. Photoluminescence spectroscopy (PL)

PL spectroscopy is a non-destructive technique, widely used to study the optical characteristics of photoactive materials. The electronic properties of a sample are analyzed based on the emitted light produced by the relaxation of a photoexcited electron from a higher to a lower electronic state. Often, PL intensity is used to study the recombination processes of the photoexcited electron-hole pairs of semiconductor materials used as photocatalysts. High PL intensity indicated high recombination rate of the charge carriers, which generally results in low photocatalytic efficiency. In this thesis, Jasco FP-8300 was applied to study the PL spectra of photoactive graphene oxide based materials.

2.2.11. Raman spectroscopy

Raman spectroscopy studies the scattered light induced by the interaction of chemical bonds with a high intensity laser beam. A minor part of this scattered light is found at a different wavelength than the incident radiation, and this shift (Raman shift) is in the focus of the technique, carrying structural information about the sample. The Raman spectrum is the fingerprint of a molecule, thus suitable for rapid identification of materials, phases, investigating crystallinity or detecting contaminants. This technique is widely used for studying indirectly the rate of disorder in carbon nanostructure. In this work, this technique was used to estimate the reduction of GO aerogels during thermal treatment, using a WITec alpha 300 R confocal Raman microscope (WITec, Germany).

2.2.12. Elemental analysis (EA)

In elemental analysis the ratio of particular elements, typically carbon, hydrogen and nitrogen, is quantified. The elements are analyzed in the gaseous state attained by sample combustion. In this thesis, a Flash EA2000 Thermo Fisher Scientific analyzer was applied to explore the composition of porphyrin-based MOFs.

2.2.13. Thermogravimetric analysis (TGA)

The thermal stability of materials is routinely analyzed by thermogravimetric analysis. The weight change occurring during constant heating, usually in N_2, air or Ar atmosphere is precisely monitored. The relative amount of components in a composite can also be evaluated

with this technique, if the constituents possess very different thermal stability. In this thesis, the thermal properties of porphyrin-based MOFs were evaluated under N_2 using a Perkin Elmer 7 equipment.

Table 1. List of characterization techniques applied in this thesis, and the location of the place where the analysis was performed.

Characterization technique	Abbreviation	Location
Powder X-ray diffraction	PXRD	ICMAB-CSIC
Single-crystal X-ray diffraction	SCXRD	ALBA synchrotron
Fourier-transform infrared spectroscopy	FTIR	ICMAB-CSIC
N_2 adsorption/desorption measurements	-	ICMAB-CSIC
Scanning electron microscopy	SEM	ICMAB-CSIC
Transmission electron microscopy	TEM	ICMAB-CSIC
Scanning transmission electron microscopy with energy-dispersive X-ray spectroscopy	STEM-EDS	ICN2
X-ray photoelectron spectroscopy	XPS	INCAR-CSIC
Inductively coupled plasma mass spectrometry	ICP-MS	INCAR-CSIC
Dynamic light scattering	DLS	ICMAB-CSIC
UV-vis spectroscopy (absorption)	UV-vis	ICMAB-CSIC
UV-vis diffuse reflectance spectroscopy	UV-vis DRS	Univ. do Porto
Photoluminescence spectroscopy	PL	Univ. do Porto
Raman spectroscopy	-	Univ. do Porto
Elemental analysis	EA	IQAC-CSIC
Thermogravimetric analysis	TGA	ICMAB-CSIC

References

1. R. Sharma, D.P. Bisen, U. Shukla, B.G. Sharma, X-ray diffraction: a powerful method of characterizing nanomaterials, *Recent Research in Science and Technology* **2012**, *4*, 77-79.

2. A.A. Bunaciu, E.G. Udriştioiu, H.Y. Aboul-Enein, X-Ray Diffraction: Instrumentation and Applications, *Crit. Rev. Anal. Chem.* **2015**, *45*, 289-299.

3. Q.Q. Pan, P. Guo, J. Duan, Q. Cheng, H. Li, Comparative crystal structure determination of griseofulvin: Powder X-ray diffraction versus single-crystal X-ray diffraction, *Chinese Science Bulletin* **2012**, *57*, 3867-3871.

4. C. F. Holder, R. E. Schaak, Tutorial on Powder X-ray Diffraction for Characterizing Nanoscale Materials, *ACS Nano* **2019**, *13*, 7359-7365.

5. P. Muhammed Shafi, A. Chandra Bose, Impact of crystalline defects and size on X-ray line broadening: A phenomenological approach for tetragonal SnO_2 nanocrystals, *AIP Adv.* **2015**, *5,* 057137.

6. P. Scherrer, Bestimmung der Grösse und der Inneren Struktur von Kolloidteilchen Mittels Röntgenstrahlen, *J. Nachrichten von der Gesellschaft der Wissenschaften, Göttingen Math Phys Kl.* **1918**, *2*, 98-100.

7. R. Phillips, K. Jolley, Y. Zhou, R. Smith, Influence of temperature and point defects on the X-ray diffraction pattern of graphite, *Carbon Trends* **2021**, *5*, 100124.

8. M. Oezaslan, F. Hasché, P. Strasser, In situ observation of bimetallic alloy nanoparticle formation and growth using high-temperature XRD, *Chemistry of Materials* **2011**, *23*, 2159-2165.

9. J. Liu, D.M. Strachan, P.K. Thallapally, Enhanced noble gas adsorption in Ag@MOF-74Ni, *Chemical Communications* **2014**, 50, 466-468.

10. C. Weinberger, M. Hartmann, S. Ren, T. Sandberg, J.H. Smått, M. Tiemann, Selective pore filling of mesoporous CMK-5 carbon studied by XRD: Comparison between theoretical simulations and experimental results, *Microporous and Mesoporous Materials* **2018**, *266*, 24-31.

11. T. Zelenka, Adsorption and desorption of nitrogen at 77 K on micro- and meso- porous materials: Study of transport kinetics, *Microporous and Mesoporous Materials* **2016**, *227,* 202-209.

12. M.D. Donohue, G.L. Aranovich, Classification of Gibbs Adsorption Isotherms, *Advances in Colloid and Interface Science* **1998**, *76-77*, 137-152.

13. M. Thommes, K. Kaneko, A. Neimark, J.O. Olivier, F. Rodriguez-Reinoso, J. Rouquerol, K.S.W. Sing, Physisorption of gases, with special reference to the evaluation of surface area and pore size distribution (IUPAC Technical Report), *Pure and Applied Chemistry* **2015**, *87*, 1051-1069.

14. M. Thommes, K.A. Cychosz, Physical adsorption characterization of nanoporous materials: Progress and challenges, *Adsorption* **2014**, *20,* 233-250.

15. K. Sing, The Use of Nitrogen Adsorption for the Characterisation of Porous Materials, *Colloids and Surfaces A: Physicochemical and Engineering Aspects* **2001**, *187-188*, 3-9.

16. S. Lowell, J.E. Shields, M.A. Thomas, M. Thommes, Characterization of Porous Solids and Powders: Surface Area, Pore Size and Density, Particle Technology Series **2004**.

17. E.P. Barrett, L.G. Joyner, P.P Halenda, The Determination of Pore Volume and Area Distributions in Porous Substances, *Computations from Nitrogen Isotherms*, J. Am. Chem. Soc. **1951,** *73,* 373-380.

18. B.D. Zdravkov, J.J. Čermák, M. Šefara, J. Janků, Pore classification in the characterization of porous materials: A perspective, *Central European Journal of Chemistry* **2007**, *5*, 385-395.

19. G. Horváth, K. Kawazoe, Method for the calculation of effective pore size distribution in molecular sieve carbon, *Journal of Chemical Engineering of Japan* **1983**, 16, 470-475.

20. R. Wang, C. Wang, H. Zhang, J. Tao, X. Bai, Progress in Nanoscale Characterization and Manipulation, *Springer Tracts in Modern Physics* **2018**.

21. S. Zou, T. Liu, Fundamentals of X-Ray Photoelectron Spectroscopy (XPS) **2020.**

22. G. Moretti, Auger Parameter and Wagner Plot in the Characterization of Chemical States by X-Ray Photoelectron Spectroscopy: A Review, *Journal of Electron Spectroscopy and Related Phenomena* **1998**, 95, 95-144.

23. S. Karmakar, Particle Size Distribution and Zeta Potential Based on Dynamic Light Scattering: Techniques to Characterise Stability and Surface Distribution of Charged Colloids, Recent Trends in Materials Physics and Chemistry **2019.**

24. J.P. Blitz, Diffuse Reflectance Spectroscopy, Modern Techniques in Applied Molecular Spectroscopy **1998**.

Summary of the results

In this section a short summary of the results obtained in this thesis is provided. The report is distributed in two parts based on the type of the studied material. First, composites based on graphene oxide aerogels are discussed, then the attention is turned towards MOF-based samples. Detailed discussion is given in the corresponding chapters.

1. Introduction

In this thesis, composites based on two classes of porous solids (MOFs and GO aerogels) were synthesized. All of them are characterized for possessing pores, primarily in the mesoscale range. For all of the preparation procedures, supercritical CO_2 was used, playing a diverse role in the synthesis (aerogel structuration and drying, solvent for impregnation, reaction solvent *etc.*). The porous materials were further functionalized and/or involved in a composite to reach specific properties, suitable for chosen applications.

2. GO aerogel-based composites

First, aerogels based on graphene oxide, with disordered pore arrangement were prepared. The basis of this work was settled in 2018 in our group, when, for the first time, robust pristine GO aerogels were successfully prepared using $scCO_2$ technology.[1] Due to the mild applied conditions and the lack of reducing agents in the process, the oxygen functionalities of the GO sheets were preserved. This approach contrasts with most reported procedures that generally result in reduced graphene-based aerogels. Such rich surface chemistry of GO offers the possibility for anchoring substances (*e.g.,* NPs, polymers) to the GO flakes, thus assembling functional GO aerogels. After successfully synthesizing composites of GO involving MOF NPs[2,3] and Fe_3O_4 NPs,[4] our attention turned towards dispersing catalytic active metal NPs within the GO aerogel matrix (Figure 1).

metal NP deposited
on GO flakes

metal@GO aerogel

gelation and drying in
$scCO_2$
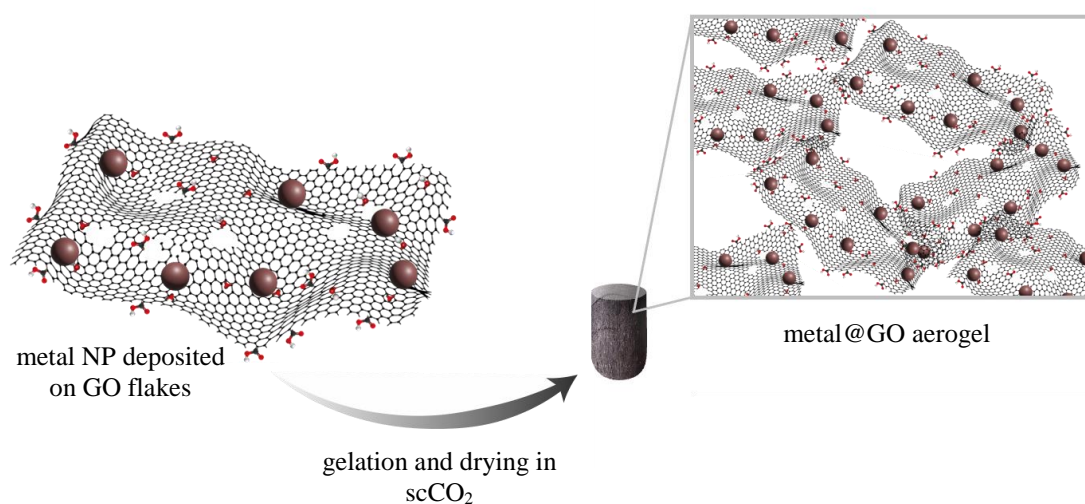
Figure 1. Illustration of metal NPs, as potential catalytic centers, dispersed on graphene oxide flakes and the formed composite aerogel. The oxygen-based functionalities of the GO are preserved through the aerogel formation.

This idea seemed to be achievable and carries an important potential, first because the nanometric size of the metallic particles generally used in catalytic systems fits well with our system, where the average size of the GO flakes is of few microns. In catalytic applications, the homogenous dispersion of the NPs on the support is of extreme importance to avoid the loss of activity due to aggregation. Such distribution is assured by the interactions between the functionalities on the GO flakes and the metallic NPs. This factor, together with the meso/macroporosity provided by the GO aerogel support that plays a key role in the reactant and product diffusion, resulted in new, promising catalytic systems showing high performance.

2.1. CuZnO@rGO composites for CO_2 hydrogenation to methanol

First, bimetallic NPs of CuO/ZnO were synthesized to be further deposited on the GO flakes, thus to build 3D composite aerogels. The synthesis involved the co-precipitation of CuOZnO NPs, the structuration of the CuOZnO@GO aerogels using $scCO_2$, and further H_2 treatment to obtain the final CuZnO@rGO catalyst. Homogenously distributed nanoparticles deposited on the GO flakes, composing the meso/macroporous aerogel, were displayed (Figure 2).
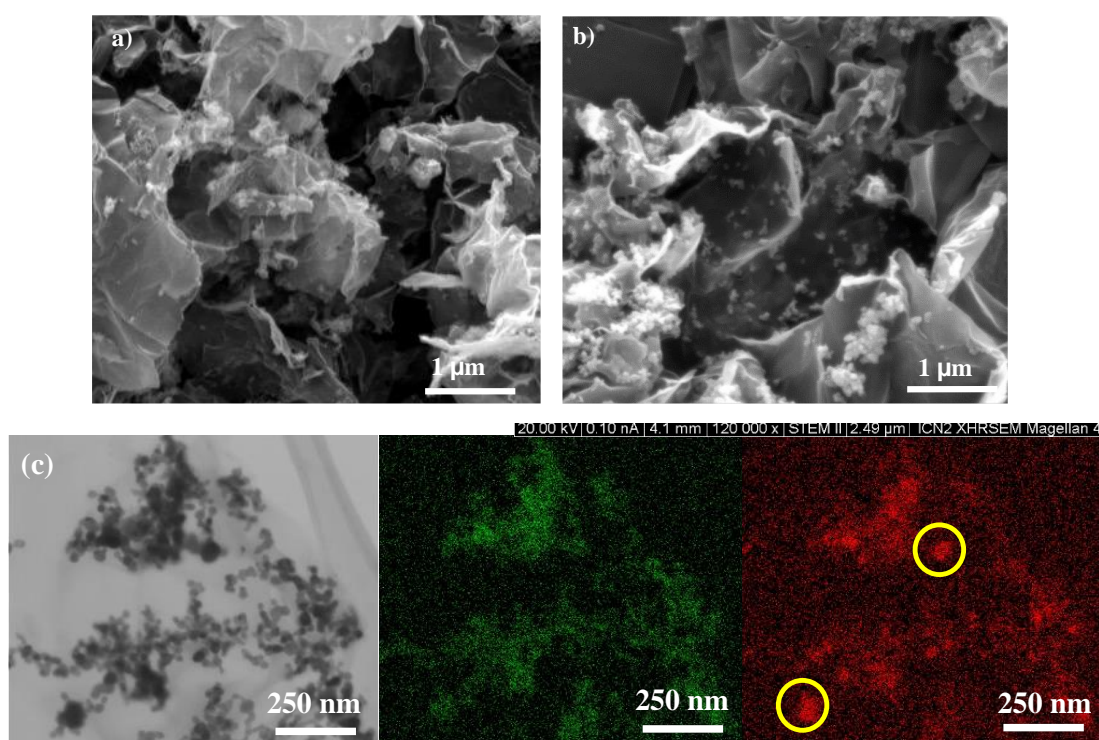


Figure 2. (a) and (b) SEM images of the CuZnO@rGO aerogel, (c) EDS elemental mapping of Zn and Cu (green and red, respectively), acquired from the STEM image (left) of sample CuZnO@rGO (yellow circles indicate few areas of sintered Cu NPs).

The aerogel was used as a catalyst for the gas phase CO_2 hydrogenation reaction used in the production of methanol. This study was carried out in collaboration with the GICOM research group in the Department of Chemical Biological and Environmental Engineering in the Universitat Autònoma de Barcelona. The effect of both the catalyst design (architecture and composition) and the reaction conditions (ratio of active centers to gas molecules, flow rate and distribution) were investigated with regards to the MeOH yield, conversion and the MeOH selectivity *vs.* CO. For this, three different systems were tested: the bare NPs, the composite aerogels directly synthesized in a tubular reactor, and the smashed aerogel (Figure 3a). The results showed outstanding methanol selectivity, near 100 % up to temperatures as high as 260 ℃ at 10 bar using the smashed aerogels (Figure 3b). This result shows even more prospect, when it is compared to the performance of the bare NPs, for which this value was only 7% under similar experimental conditions, accompanied with diminished methanol yield, as well. (20 $mg_{MeOH}g_{Cu}^{-1}h^{-1}$ *vs* < 5 $mg_{MeOH}g_{Cu}^{-1}h^{-1}$ at 260 ℃ and 5 mLmin^{-1} flow).
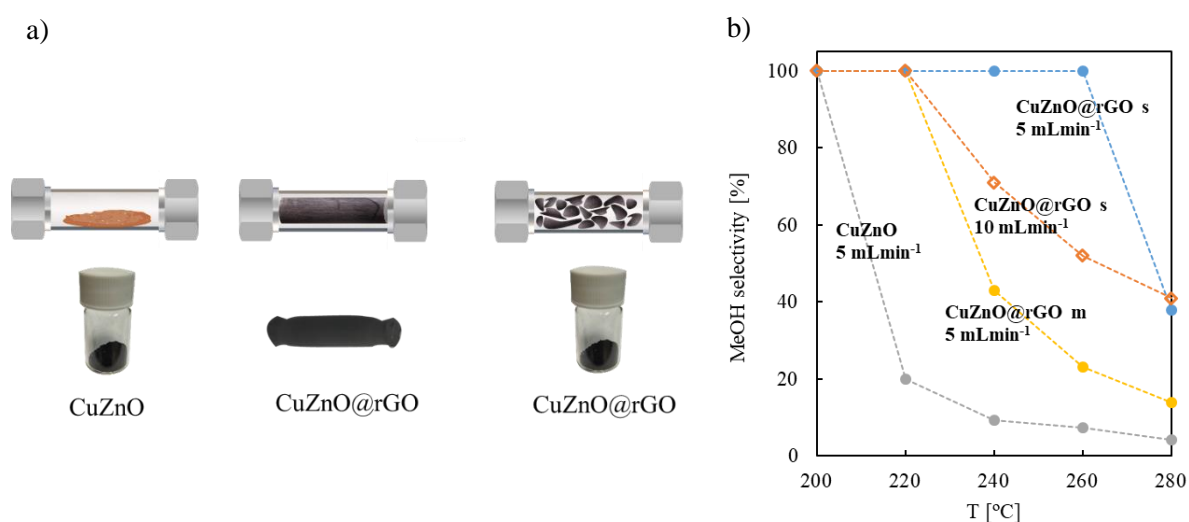
Figure 3. (a) Three different tested systems and (b) the obtained results regarding the selectivity of the samples.

These results were explained on the basis of the role of the rGO in the composite aerogel in acting as CO_2 reservoir, its hydrophobic character for water repulsion, and its ability to hinder the negative effects of NPs sintering and alloy formation between the two metals.

2.2. Pt/TiO₂@rGO composites for photocatalytic H₂ production from methanol

Excited by our previous results, we explored the use of these materials in other fuel production processes. Along these lines, performing catalysis in liquid phase using the aerogel composites

seemed more challenging, because of possible issues to maintain some of the aerogel properties in liquid phase, and the different permeation behavior of the reactant and products in liquid solvent inside the porous catalyst. This time, the chosen model reaction was the photocatalytic H_2 production reaction from methanol/water, which required to disperse expensive Pt/TiO_2 NPs within the GO aerogel.

Pt/TiO_2 NPs were prepared by drop-casting, followed by calcination and reduction steps. The bimetallic NPs were deposited on GO flakes and a 3D aerogel was thus formed. In this case, mild reduction under N_2 atmosphere was applied with the aim of reducing some of the oxygenated functionalities of the GO support. A porous morphology with homogenously dispersed NPs on the rGO flakes was depicted for the $Pt/TiO_2@rGO$ catalyst (Figure 4).
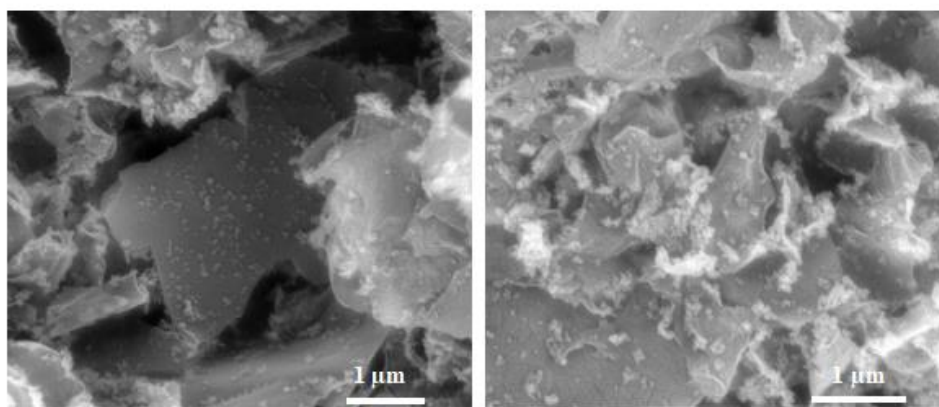

Figure 4. SEM images of $Pt/TiO_2@rGO$ aerogel composite.

The measurement of the photocatalytic H_2 production from aqueous methanol was carried out in collaboration with the Laboratory of Separation and Reaction Engineering – Laboratory of Catalysis and Materials in the Universidade do Porto (Portugal). Within the framework of a three months research stay, I performed the catalytic experiments under the direction of prof. Joaquim Faria and prof. Cláudia G. Silva. A systematic study with the focus on maximizing the H_2 production was carried out, optimizing all the reaction conditions (water/methanol ratio, catalyst concentration), the catalyst composition ($Pt/TiO_2/rGO$ ratio) and architecture (size of the aerogel pieces). As for the reaction conditions, the highest H_2 yield was obtained using a 0.5 $g_{NP}L^{-1}$ catalyst concentration in a 0.5 v/v methanol/water reaction solution. These parameters were settled for the following experiments. An important factor, resulting in two-fold enhancement in the H_2 production was the mild reduction of the GO support (Figure 5a). This effect was assigned to the generation of new electronic pathways upon the partial restoration of the graphene network, and the favored adsorption of the methanol in the reduced structure. Taking into account the dark color of the GO, smashing the one-piece monolith to

small pieces caused a 10-fold increase in the H_2 production, due to the improved light exposure of the active sites and increased reagent and product diffusion (Figure 5b).
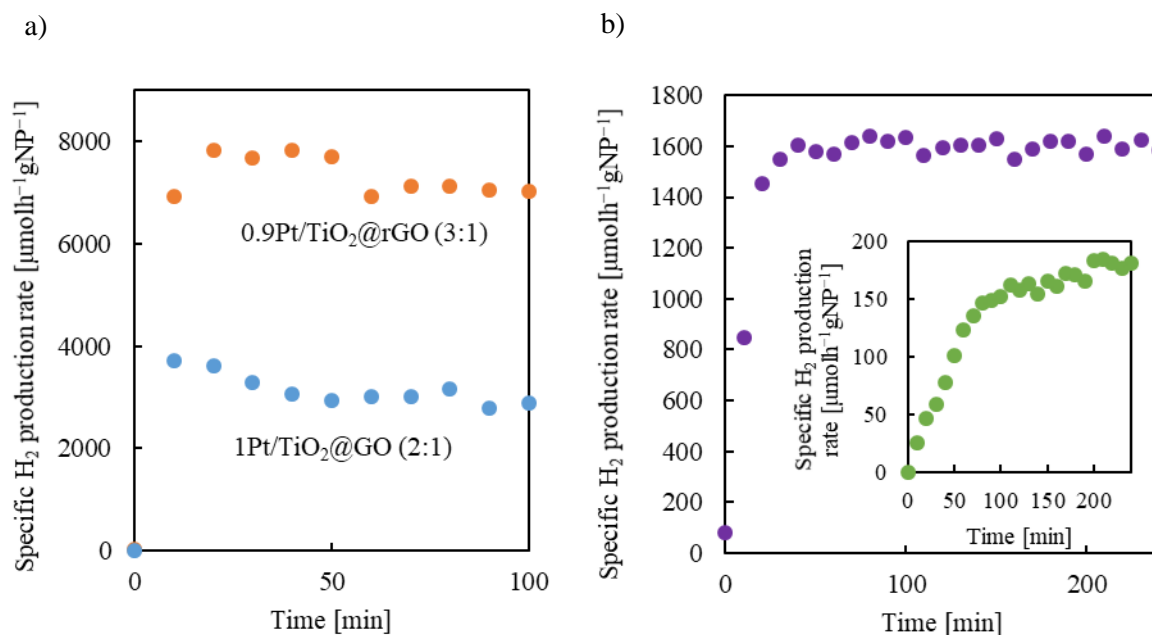
Figure 5. The effect of (a) the GO reduction to rGO, and (b) the smashing of the one-piece monolith on the H_2 production rate.

The catalyst composition also had an important effect on the performance. Thus, a 9:1 wt NP:GO composite, with a Pt content in the order of 0.9–0.5 wt% related to the total NP weight, was the most favorable. In the optimized system, H_2 production rate was remarkably higher (18800 μmolH$_2$ h^{-1} g$_{NP}^{-1}$) than the values found in the literature for similar Pt/TiO$_2$/rGO catalysts and reaction media (2000–10000 μmolH$_2$ h^{-1} g$_{NP}^{-1}$).

3. MOF-based composites

Following the interest in the field of porous composites, this thesis also focused on the preparation of MOFs under scCO$_2$ conditions. The MOF samples, possessed pores in the low region of the mesoscale (2-3 nm), and were actually lacking long-range order (semiamorphous MOFs). These materials were either used in the as-synthesized form, or drugs or metal-based compounds were encapsulated in the pores. Formulations appropriate for biomedical or catalytic application were obtained.

3.1. Azelaic acid@Fe(BTC) for cutaneous drug delivery

The targeted MOF for drug delivery was the semiamorphous mesoporous iron trimesate Fe(BTC), the counterpart of the crystalline MIL-100(Fe) MOF. A green preparation procedure

involving $scCO_2$ as a drying agent to obtain empty-pore Fe(BTC) powder at the nanoscale (10-20 nm) was developed. Then, the impregnation of a topical antibiotic drug, azelaic acid, into the porous structure was carried out, using $scCO_2$ as the impregnation vector (sc_AzA@Fe(BTC)). The drug-loading was compared with the traditional encapsulation methodology from aqueous solution (w_AzA@Fe(BTC)). Using the supercritical medium, significantly higher drug uptake values were attained than in the conventional method, likely owing to the lack of adsorption competition between the solvent and the solute molecules for the substrate sorption sites (Table 1).

Table 1. AzA loading (wt%) measured with different techniques, *e.g.*, TGA and HPLC.

	AzA loading (%)
sc_AzA@Fe(BTC)	17±3
w_AzA@Fe(BTC)	7.9±0.9

As this composite was considered to be employed as an effective structure for a drug delivery system, an appropriate formulation needed to be designed. For this purpose, a biocompatible polymer, polyvinyl-alcohol (PVA) was chosen as a support, which is also suitable to disperse the drug-loaded MOF. Macroporous patches, involving the PVA-matrix and the dispersed loaded MOF were formed using the $scCO_2$ medium for polymer plasticization and foaming (Figure 6).
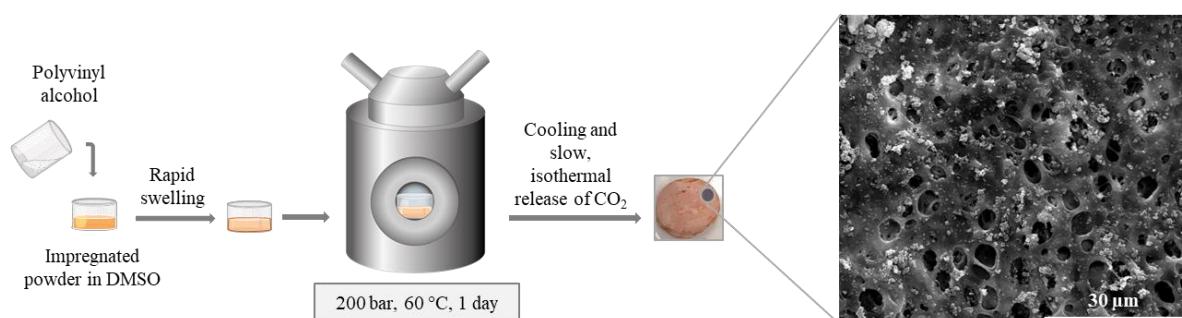
Figure 6. Preparation of macroporous patches involving the PVA-matrix and the dispersed loaded MOF.

Finally, the drug delivery and permeation profiles of the patches were investigated using *in vitro* and *ex vivo* tests by using porcine skin. This study was performed in collaboration with the IMDEA Energy Inst. in Madrid. The total amount of AzA diffused or retained through the skin is within the range of those typical in current commercial formulations.

3.2. Reduced copper clusters@Fe(BTC) composites for CO_2 hydrogenation to methanol and methane

Taking into account the successful drug impregnation into the porous Fe(BTC), showing high drug loading, the encapsulation of an organometallic compound with relatively small size and appropriate solubility in scCO$_2$ was intended in the same MOF. The aim of this study was to build a novel composite, where the metal centers are uniformly dispersed in the mesopores of the Fe(BTC) MOF (Fig. 7). The reduced metal phase serves as small and dispersed catalytic centers, as their growth and aggregation are hindered by the walls of the MOF cages.
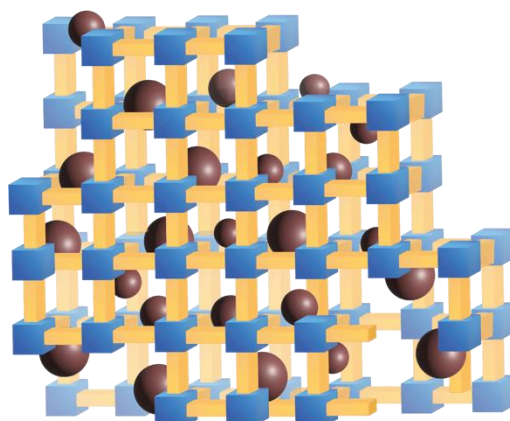
Figure 7. Reduced copper clusters (brown spheres) homogenously distributed in the mesoporous framework.

For this purpose, scCO$_2$ soluble copper acetylacetonate was chosen as the metal source, thus the impregnation was achievable without the use of any cosolvent. To reach a catalytically active material, with copper centers in a low oxidation state (+1 and 0), the composite was subjected to reduction in H$_2$ atmosphere. The catalytic activity of the reduced composite was tested again in CO$_2$ hydrogenation reaction. Methanol yield, conversion and selectivity were contrasted to the results obtained for the pristine (Fe(BTC)) MOF and previous studies performed using the typical CuZnO catalyst. Based on the obtained results in this study, the impregnated Fe(BTC) with clusters of reduced copper can produce significant amounts of methanol without the incorporation of ZnO species. Further optimization of the catalytically active composite is currently under investigation.

3.3. Synthesis of porphyrin MOFs

Based on the previous research in our group on the synthesis of MOFs in scCO$_2$ media,[5,6] part of this thesis addressed the preparation of a series of porous metalloporphyrin frameworks using scCO$_2$ as a reaction solvent. 5,10,15,20-tetra(4-pyridyl)porphyrin (H$_2$TPyP) linker and four

metal complexes M(hfac)$_2$ M= Cu, Zn, Co, Ni (hfac: 1,1,1,5,5,5-hexafluoroacetylacetonate) were used as precursors to form the porous MOFs, generically named as [M-TPyP]$_n$. All prepared materials were obtained as MOFs formed through the metal coordination to the exocyclic pyridine moieties in the porphyrin.
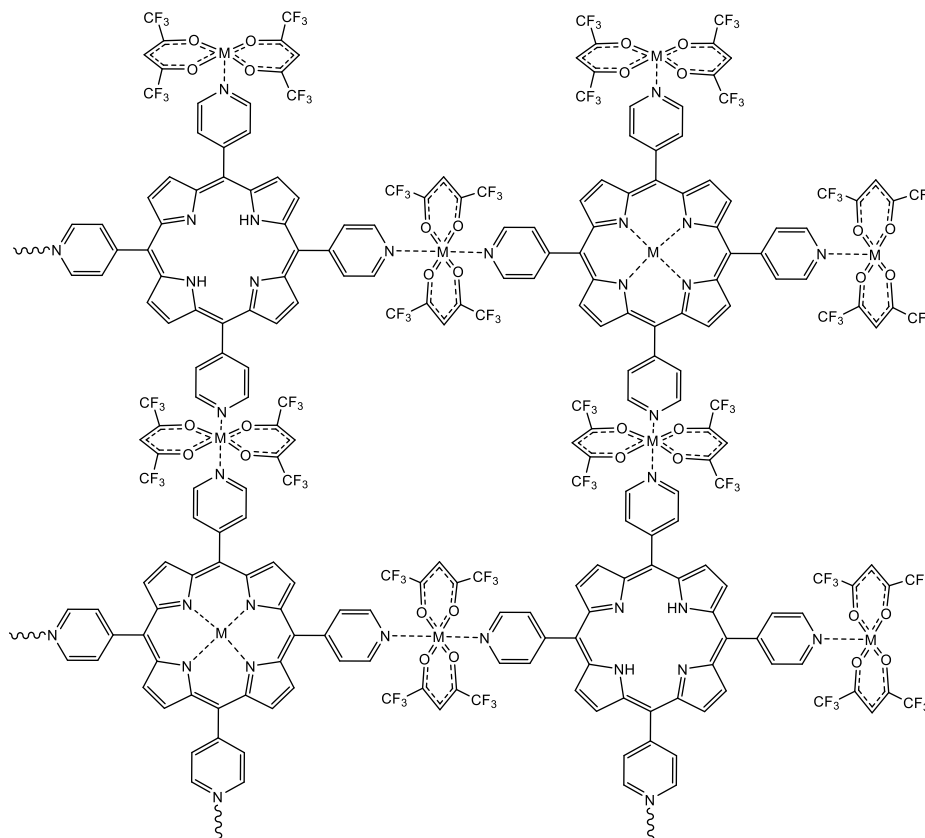
Figure 8. Scheme of coordination of [M-TPyP]$_n$ MOF.

For Cu, Zn and Co, incomplete metal coordination of the inner pyrrole ring throughout the structure was observed (Fig. 8). These defects lead to a certain level of disorder and limited crystallinity. In addition, crystalline [{Co(hfac)$_2$}2H$_2$TPyP]$_n$ was obtained from layering, which allowed structure elucidation from single crystal X-ray diffraction. From all the obtained MOFs, the [Zn-TPyP]$_n$ was selected to be tested as a photosensitizer in photodynamic therapy (PDT) in SKBR-3 tumoral cell line. Activating this compound with UV-light leads to the formation of reactive oxygen species. These highly reactive species induce cell death *via* oxidative processes, giving the basis for a potential cancer therapy. The PDT measurements were carried out in collaboration with the Department of Cellular Biology, Physiology and Immunology in the Universitat Autónoma de Barcelona. According to the results, outstanding performance was achieved, since after 15 min of irradiation at 630 nm, almost 70% of tumor cells died after 72 h (Fig. 9).
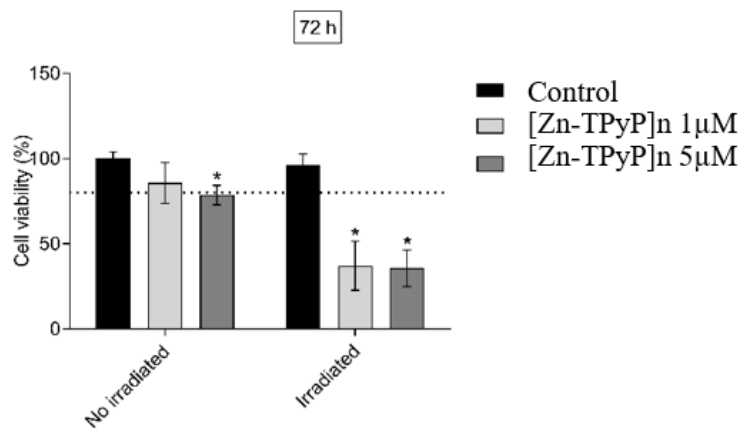
Figure 9. Photodynamic treatment effects after 15 min irradiation. Cell viability was determined by Alamar Blue for SKBR-3 cells incubated without (control) or with 1 µM or 5 µM of product for 4 h followed by cell wash. Cell viability was determined after incubation (24 h) either in dark conditions (not irradiated) or after 15 min irradiation at λ_{ex}620-630 nm (irradiated) and at 72 h. Three independent experiments were performed for each set of conditions. Asterisks indicate statistically significant differences in the cell viability between control and product at each time-point and condition.

References

1. A. Borrás, G. Gonçalves, G. Marbán, S. Sandoval, S. Pinto, P.A.A.P. Marques, J. Fraile, G. Tobias, A.M. López-Periago, C. Domingo, Preparation and characterization of graphene oxide aerogels: Exploring the limits of supercritical CO_2 fabrication methods, *Chemistry - A European Journal* **2018**, *24*, 15903-15911.

2. A. Rosado, A. Borrás, J. Fraile, J.A.R. Navarro, F. Suárez-García, K.C. Stylianou, A.M. López-Periago, J.G. Planas, C. Domingo, A. Yazdi, HKUST-1 metal-organic framework nanoparticle/graphene oxide nanocomposite aerogels for CO_2 and CH_4 adsorption and separation, *ACS Appl Nano Mater*. **2021,** *4*, 12712-12725.

3. A. Borrás, A. Rosado, J. Fraile, A.M. López-Periago, J. Giner Planas, A. Yazdi, C. Domingo, Meso/microporous MOF@graphene oxide composite aerogels prepared by generic supercritical CO_2 technology, *Microporous Mesoporous Mater.* **2022**, *335*, 111825.

4. A. Borrás, J. Fraile, A. Rosado, G. Marbán, G. Tobias, A.M. López-Periago, C. Domingo, Green and solvent-free supercritical CO_2-assisted production of superparamagnetic graphene oxide aerogels: Application as a superior contrast agent in MRI, *ACS Sustain. Chem. Eng.* **2020**, *8*, 4877–4888.

5. A.M. López-Periago, N. Portoles-Gil, P. López-Domínguez, J. Fraile, J, Saurina, N. Aliaga-Alcade, G. Tobias, J.A. Ayllón, C. Domingo, Metal-organic frameworks precipitated by reactive crystallization in supercritical CO_2, *Cryst Growth Des*. **2017,** *17,* 2864-2872.

6. N. Portolés-Gil, A. Lanza, N. Aliaga-Alcalde, J.A. Ayllón, M. Gemmi, E. Mugnaioli, A.M. López-Periago, C. Domingo, Crystalline curcumin bioMOF obtained by precipitation in supercritical CO_2 and structural determination by electron diffraction tomography, *ACS Sustain Chem Eng*. **2018,** *6,* 12309-12319.

Role of Graphene Oxide Aerogel Support on the CuZnO Catalytic Activity: Enhancing Methanol Selectivity in the Hydrogenation Reaction of CO$_2$
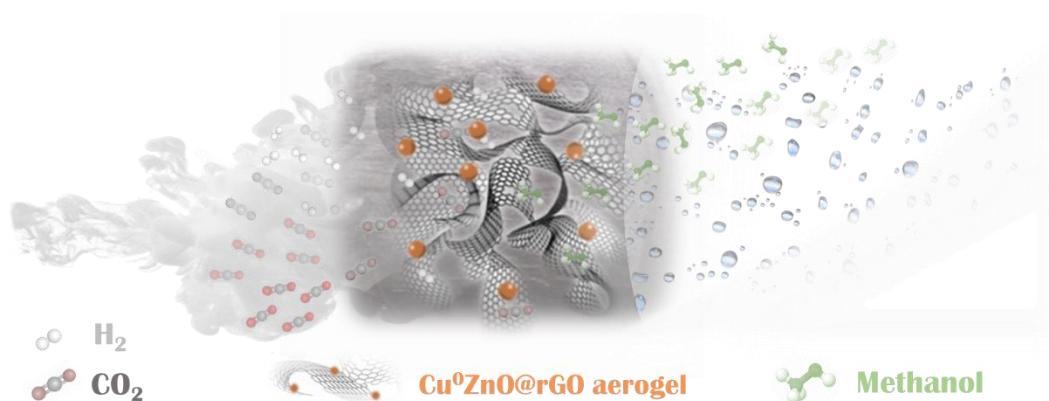
A novel graphene oxide aerogel supported CuZnO catalyst was synthesized for the selective CO$_2$ hydrogenation to methanol. The graphene oxide support played crucial role in the immobilization of the active nanoparticles, as well as in hindering the formation of diluted Cu-Zn surface alloy, which resulted in superior activity and methanol selectivity in comparison to unsupported CuZnO catalyst.

Abstract

A novel CuZnO multicomponent catalyst, involving reduced graphene oxide (rGO) as a support, was synthesized to be applied in the catalytic hydrogenation of CO_2 to methanol. The CuZnO@rGO composite was prepared as a 3D aerogel by a two-step process involving supercritical CO_2 for macrostructuration and H_2 treatment for reduction. Electron microscopy was applied to visualize the meso/macroporous morphology formed by the supercritical drying. The elemental mapping depicted a homogenous distribution of CuZnO nanoparticles deposited on the rGO flakes. It was demonstrated that methanol production increases for the CuZnO@rGO composite in comparison to unsupported similar CuZnO nanoparticles. This behavior was ascribed to a different interaction established between the Cu^0 and ZnO nanoparticles used as synthetized or deposited on rGO. It is shown that the highly reduced rGO component stimulates H_2O desorption produced during the hydrogenation reaction, thus it serves as a support hindering the sintering of Cu^0 nanoparticles. The formation of a diluted surface alloy of Zn into Cu^0 was determined for the unsupported CuZnO NPs, while for the CuZnO@rGO aerogel composite, the absence of any additional phase, *e.g.*, a surface alloy or reduced ZnO, was confirmed. The composite aerogels show excellent MeOH selectivity at high temperature (up to 260 ºC) and low pressure (10 bar).

1. Introduction

The world is already experiencing important indications of the imponderable climatic negative consequences caused by the rising of human CO_2 emissions and its elevated concentration in the atmosphere.[1] For this reason, both CO_2 capture and its further transformation into valuable products are currently research hot topics.[2,3] In this framework, the conversion of CO_2 to value-added chemicals, *e.g.*, light hydrocarbons and short chain alcohols, has been demonstrated to be efficiently achieved using heterogeneous catalysis. Among the obtained products, the synthesis of methanol (MeOH) has attracted remarkable interest, since it is a compound with an increased demand, not only for a wide range of daily goods, but also as a biodegradable fuel.[4–7] The overall industrial process of MeOH production from CO_2 involves an initial activation step, performed with $ZnAl_2O_4$, followed by water removal and MeOH synthesis over $CuZnO/ZrO_2/Ga_2O_3$.[8] The main disadvantage of this process is economical, since it requires two different catalysts and reactors. Current research is thus focused on the development of an efficient catalyst for one-step CO_2 conversion. $CuZnO/Al_2O_3$, the flagship catalyst for the synthesis of MeOH from CO and H_2,[2] is being considered for CO_2 transformation. However, in the reaction of CO_2 with H_2, the production of CO as the main component instead of MeOH cannot be prevented when using this catalyst.[9–11] To shift the equilibrium in the hydrogenation reaction from CO to MeOH, the process must be carried out at high pressure (*ca.* 50–100 bar) and low temperature.[12] Notwithstanding the above, industrial methanol synthesis from CO_2 over $CuZnO/Al_2O_3$ needs to be operate at high temperature (*ca.* 250–300 ºC) to activate the inert CO_2 molecule, which is detrimental for the exothermic production of MeOH *vs.* the endothermic formation of CO.[3,13] Moreover, catalyst nanoparticles (NPs) are prone to sintering at high temperature, again reducing MeOH yield.[14,15] Even using harsh conditions of pressure and temperature, the $CuZnO/Al_2O_3$ catalysts exhibit important disadvantages, such as short life-time, low activity for CO_2 conversion and more importantly low selectivity to MeOH.

Most efforts reported for the CuZnO system are targeted to design the best catalyst in regard of CO_2 conversion, but neglecting the consequences of low MeOH selectivity. Nevertheless, the increase in the selectivity of CO_2 conversion to MeOH *vs.* CO might be considered as very important in industrial processes, just to avoid the formation of undesired by-products, that are difficult to separate. Based on that, of paramount importance of the research performed in this work was the development of a composite catalyst, based on the low cost CuZnO, with improved selectivity for MeOH, preserved even at high temperature, which would allow an efficient CO_2 activation, and that works at low pressure to make the process economically

attractive with low installation and operation costs. In the scientific literature, the general trend to increase MeOH selectivity have consisted in adding to CuZnO different nanoparticulate promoters, such as Al_2O_3, MgO, ZrO_2, Ga_2O_3, Y_2O_3,[16,17] and/or supports chosen from non-metallic matrices, such as metal-organic frameworks, zeolites, porous silica, layered double hydroxides, porous polymers or carbonaceous materials, including activated carbon and graphene derivatives.[18–25] The objective of using these additives is always to achieve a large Cu^0 surface area, high Cu^0 dispersion and improved interaction with ZnO. In this work, a particular mode of reduced graphene oxide (rGO) is investigated as support for these purposes. Graphene-based supports possess many properties that provide further benefits in heterogeneous catalysis, such as enhanced electron mobility, thus assisting the reaction through charge-transfer processes, high mechanical strength, giving mechanical sustenance for the anchored NPs, and also thermal stability.[26]

The use of 3D graphene-based structures as supports for the catalytic NPs has been described recently, highlighting the advantages of using 2D materials[27] with high surface area for efficient NP dispersion.[26,28] In this work, these structures were built by using a supercritical CO_2 (scCO_2) route, starting with the formation of graphene oxide (GO) aerogels decorated with CuO and ZnO NPs.[29] This unique method applies mild temperature conditions during gelling and drying, thus preserving the fascinating surface chemistry of GO, with a large amount of carboxylic, epoxy and hydroxyl functional groups. The oxygenated groups on GO enable the easy functionalization of the flakes with catalyst NPs.[30] The further reduction of GO to reduced GO (rGO) ensures superior electron mobility.[27,31] The catalytic activity of the synthetized materials was tested in a low pressure CO_2 hydrogenation reaction described to produce methanol. Extensive solid state characterization of the catalyst, before and after catalysis, was performed. The catalytic performance and the selectivity of the 3D nanostructured material was compared to that of CuZnO unsupported NPs. The importance of the role of rGO support in the catalytic process was established in terms of its influence on the characteristics of the Cu^0-ZnO interaction of deposited NPs, deduced from X-ray photoelectron spectroscopy data. The synthetized composite aerogels show excellent MeOH selectivity at high temperature (up to 260 °C) and low pressure (10 bar). Other positive effects for MeOH production triggered by rGO addition were improved CO_2 adsorption and enhanced H_2O desorption during reaction.

2. Materials and methods

2.1. Materials

For the preparation of the catalytic NPs, $Cu(NO_3)_2\cdot3H_2O$ and $Zn(NO_3)_2\cdot6H_2O$, purchased from Sigma-Aldrich, and Na_2CO_3, provided by Carlo Erba, were used. For the aerogel preparation, a GO water dispersion, with a concentration of 4 $mgmL^{-1}$, was supplied by Graphenea Inc. (Spain). The water was further interchanged with ethanol (Carlo Erba).[29] Compressed CO_2 (99.95 wt%) was utilized for the composite aerogel synthesis. For the reduction of the catalyst, a flow of pure H_2 was employed, while a mixture of CO_2/H_2 with a molar ratio 1:3 was applied during the catalytic conversion experiments. All these gases were delivered by Carburos Metálicos S.A.

2.2. Synthetic methods

The end composite CuZnO@rGO was obtained following a step-wise synthetic protocol, involving conventional chemistry to prepare the precursor CuOZnO NPs, $scCO_2$ technology to settle the GO aerogel composite, and finally, reduction with H_2.

Preparation of CuOZnO NPs

CuOZnO NPs, with a molar ratio of either 2:1 or 1:1, were used as the starting material to obtain the catalytic units. They were prepared based on a conventional co-precipitation method reported elsewhere.[32] In short, either 2.4 or 1.2 g of $Cu(NO_3)_2.3H_2O$ and 1.5 g of $Zn(NO_3)_2.6H_2O$ were dissolved in 10 mL of distillated water. The solutions were heated at 70 ℃ and, then, 6 mL of 1 M Na_2CO_3 was added dropwise to the mixtures under stirring, until a pH of 7 was reached and maintained. The mixture was further stirred for 2 h at 70 ℃, and, after cooling down, a white precipitate was collected by centrifugation, which was washed with distilled water thrice. The obtained solid was dried in an air oven overnight at 110 ℃. Next, it was calcined at 350 ℃ in a tubular oven under a flow of air during 4 h.

Preparation of CuOZnO@GO composite aerogels

A $scCO_2$ process, schematized in Fig. 1, was used for the preparation of the composite aerogels by using an *ex situ* approach.[33] A weighted amount of the prepared CuOZnO NPs was dispersed in a GO-ethanol dispersion (3.5 $mgmL^{-1}$) to obtain a 3:1 NP:GO weight ratio. Composite aerogels were prepared inside of a stainless steel column for straightforwardly use as a fixed-bed column in the equipment for methanol production. In each experiment, part of the dispersion was added to small assay tubes to obtain a similar product for structural

characterization. The column and the tubes were filled with 2.2 and 1 mL of each ethanol dispersion, introduced into the high pressure reactor and treated with scCO$_2$ at 45 ºC and 200 bar for 48 h. This is a scCO$_2$ protocol previously established to obtain robust aerogels of GO.[29] Then, the reactor was isothermally depressurized at a flow rate of *ca.* 0.5 mLmin^{-1} and cooled down to room temperature, thus avoiding the liquid-to-gas transition of the fluid and preserving the 3D open structure of the aerogel. Grey, cylindrical monoliths were taken out from the assay tubes, while the column with the aerogel inside was further used as a fixed-bed reactor in the catalytic reaction. An aerogel of *ca.* 30 mg of the CuOZnO@GO composite was built *in situ* in a column of 0.7 x 5 cm (id x length).

Reduction of CuOZnO NPs and CuOZnO@GO aerogels

Previous to the catalytic experiments, samples were reduced with a flow of pure H$_2$ (20 mLmin^{-1}) at 350 ºC for 2 h in a stepwise progressive heating process, involving a temperature ramp of 5 ºCmin^{-1}, but keeping the sample for 30 min at 100, 200 and 300 ºC. The stepwise process is especially important for two reasons, first to minimize NPs sintering, and second to preserve the structure of the GO monoliths intact by avoiding their explosive breakage during reduction, due to the release of large amounts of H$_2$O and CO$_2$. The reduction step was straightforwardly carried out in the catalytic reaction set-up.

2.3. Structural Characterization

Pristine NPs and aerogel monoliths were characterized in the as-synthesized form (CuOZnO NPs and CuOZnO@GO aerogel), and also in the reduced spent catalyst, *i.e.*, after reduction and catalytic cycle (CuZnO NPs and CuZnO@rGO aerogels). The structural characterization was performed by powder X-ray diffraction (XRD) in a Siemens D5000, using Cu Kα incident radiation with a step scan of 0.01º in the 2θ 5-55º range. Scherrer equation was applied to XRD data to estimate the crystallite size of Cu^0 and ZnO. The molecular arrangement was investigated by means of Fourier transform infrared (FTIR) spectroscopy (Jasco 4700 Spectrophotometer), after dispersing the samples in KBr. The textural properties were determined by N$_2$ adsorption/desorption experiments at -196 ºC using an ASAP 2020 Micromeritics Inc. Previous to the analysis, samples were degassed at 80 ºC for 20 h. The surface area (S$_a$) was calculated with the Brunauer-Emmet-Teller (BET) equation. The same equipment was used to measure the adsorption isotherms of CO$_2$ at 0 ºC. The morphology of the NPs and the composite monoliths was investigated by using scanning (SEM, Quanta FEI 200) and scanning/transmission (STEM, XHRSEM FEI Magellan 400L) electron microscopes.

The latter was also used to perform the elemental mapping of selected samples by using energy dispersive spectroscopy (EDS) (X-Max Ultim Extreme EDX Oxford Inst.), with a resolution of *ca.* 1 nm. STEM images were used to estimate the size of the NPs in the reduced samples. Histograms of particle size distribution were obtained by measuring the size of *ca.* 150 NPs in the images. The Cu and Zn atomic contents in the reduced composites were determined by inductively coupled plasma mass spectrometry (ICP-MS, Agilent 7700x) after high temperature solid digestion in hydrochloric, nitric and hydrofluoric acids (3:1:0.5 v/v). *Ex situ* X-ray photoelectron spectroscopy (XPS) was carried out in a Specs Spectrometer to determine the percentage and oxidation state of copper and zinc in the reduced samples. For the analysis monochromatic Al-Kα radiation emitted from a double anode at 14 kV and 175 W was used. The binding energies of the resulting spectra were corrected employing the binding energy of adventitious carbon (284.6 eV) in the C1s. The backgrounds were corrected using Shirley baselines. All the analyzed regions (XPS Cu2p, Zn2p and Auger ZnLMM and CuLMM) were deconvolved by means of mixed Gaussian-Lorentzian functions (90:10). The quantitative analyses were based on atomic sensitivity factors stored in the CasaXPS database (v2.3.12Dev6). XPS, ICP and N_2 adsorption/desorption data was used to estimate the Cu^0 exposed surface area in the different samples.

2.4. Catalytic activity

The activity of the synthesized catalysts with respect to the hydrogenation of CO_2 to obtain methanol and CO was evaluated by using a fixed-bed tubular flow reactor system (Process Integral Development Engineered & Tech.). For the catalytic measurements, the aerogels were used either as-synthetized, *i.e.*, as a monolith filling the column, or were first extracted from the column, then smashed in small pieces (several microns) and finally added again to the column distributed over glass wool. For the CuZnO NPs, *ca.* 30 mg of powder was added to the same column that was plugged at both ends with glass wool. Two different gas flow rates of 5 and 10 mLmin^{-1}, which corresponded to gas hourly space velocities (GHSV) of 10 and 20 $L_{CO2}g_{cat}^{-1}h^{-1}$, respectively, were investigated. Measurement values were taken at 10 bar and different temperatures, in the range 200-280 ℃, when steady-state was reached. The percentage of MeOH in the gaseous product was analyzed by an online gas chromatograph (Shimadzu GC-2010) with a flame ionization detector (FID). CO and CO_2 in the produced gas mixture were measured by using an Agilent Tech. 7890B GC system, with a thermal conductivity detector (TCD) and He as a carrier gas. The CO_2 conversion was calculated from the percentage of introduced CO_2 and the formed CO and methanol, assuming that under the used

experimental conditions all the converted CO_2 was transformed to these two products. The methanol space-time yield (STY) was determined as the produced weight of MeOH with respect to the time and active catalyst (Cu^0) weight. The selectivity towards MeOH was calculated from the ratio of the amounts of produced MeOH and CO.

3. Results and discussion

3.1. scCO$_2$ synthesis method

Converting graphene sheets to graphene aerogels with a 3D structure has been demonstrated to be one of the best methods to prevent restacking of the flakes, thus attaining a high degree of exfoliation that facilitates functionalization and surface reactions. rGO aerogels are often prepared from the greatly dispersible GO precursor by a high temperature hydrothermal reduction method.[34–37] Quite the opposite, a low temperature scCO$_2$ approach was followed in this work for the preparation of CuOZnO@GO precursor aerogel, which after reduction with H_2 transforms to CuZnO@rGO aerogel (Fig. 1).
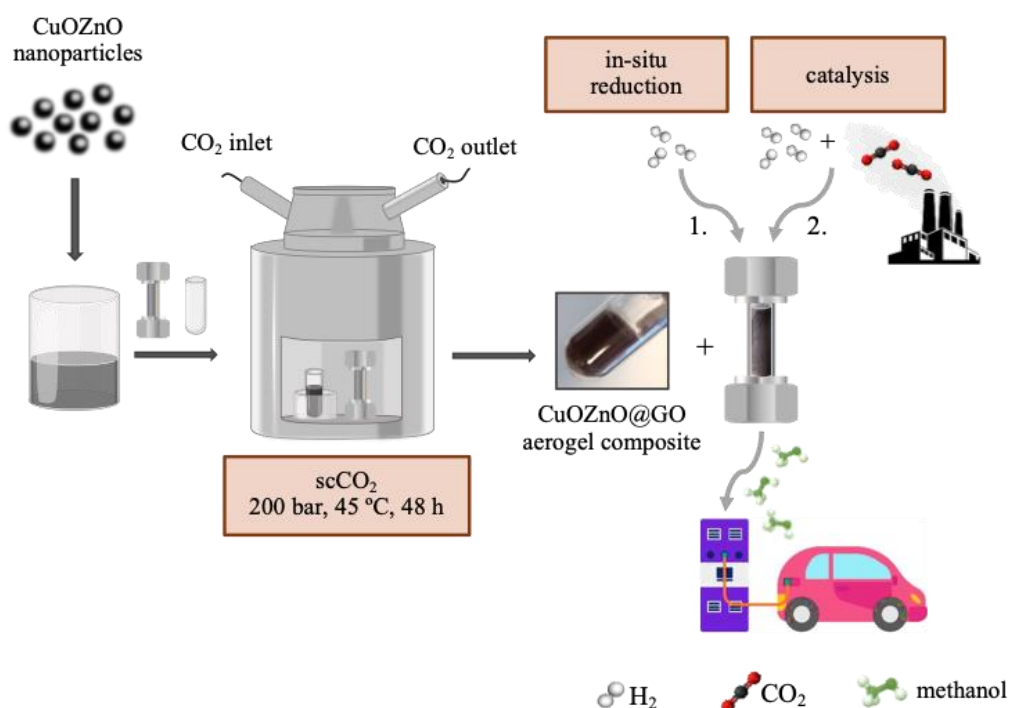

Figure 1. Schematic representation of the synthetic protocol followed to obtain the precursor CuOZnO@GO composite using supercritical CO_2, then the CuZnO@rGO aerogel upon in-situ reduction with H_2, and finally the catalytic CO_2 hydrogenation to methanol.

The scCO$_2$ solvent is used for the gelling and drying of GO/CuO/ZnO ethanol dispersions, thus avoiding the collapse of the interconnected meso/macroporous structure of the gel phase.[29] During supercritical treatment, the deposition of the NPs onto the GO sheets surface is driven by electrostatic interactions with the oxygenated functional groups of the support, mainly –OH and C-O-C. Finally, the elimination of the ethanol/scCO$_2$ solvent is carried out without crossing the liquid phase of the mixture, thus overcoming the materialization of capillary forces and the collapse of the 3D structure.

3.2. Catalyst composition and morphology

CuZnO@rGO composite aerogel catalysts, involving Cu^0 as the active phase, ZnO as the promoter and rGO as the support, were studied in this work. One of the most important functions of ZnO promoter has been described as limiting aggregation and sintering of Cu^0 NPs during reduction and thermocatalysis.[2] For this reason, ZnO should be incorporated to the system in a significant percentage. As the optimized composition, the molar ratio of the oxides in the precursor CuOZnO NPs was fixed in this work at 1:1. In fact, preliminary experiments performed with a weight ratio of 2:1 indicated a high degree of sintering for the NPs in the end product (CuZnO@rGO), evidenced by a low surface area value, measured by N$_2$ adsorption/desorption analysis of only 53 m^{2}g^{-1}, while for the 1:1 sample the surface area was almost double, of 94 m^{2}g^{-1} (see Fig. 2a for the recorded isotherms).The value measured for the net 1:1 NPs was 39 m^{2}g^{-1}. Hence, experiments in this work were performed with the 1:1 wt. CuO:ZnO NPs system that, after reduction, has a calculated Cu^0:ZnO weight ratio of 0.8:1. This ratio approximately matches the values measured by ICP (0.9:1 wt.). To prepare the composite CuZnO@rGO, the weight ratio of the NP:GO was fixed at 3:1, which after reduction results in a ratio of *ca.* 4:1 wt. for CuZnO:rGO. The ICP weight composition for this sample was 0.9:1:0.5 wt. (Cu^0:ZnO:rGO). Measured CO$_2$ adsorption isotherms of the reduced samples (Fig. 2b), indicated that, at atmospheric pressure, the volume of gas adsorbed was two-fold in the CuZnO@rGO sample (*ca.* 10 cm^{3}g^{-1}) compared to the bare NPs (*ca.* 5 cm^{3}g^{-1}).
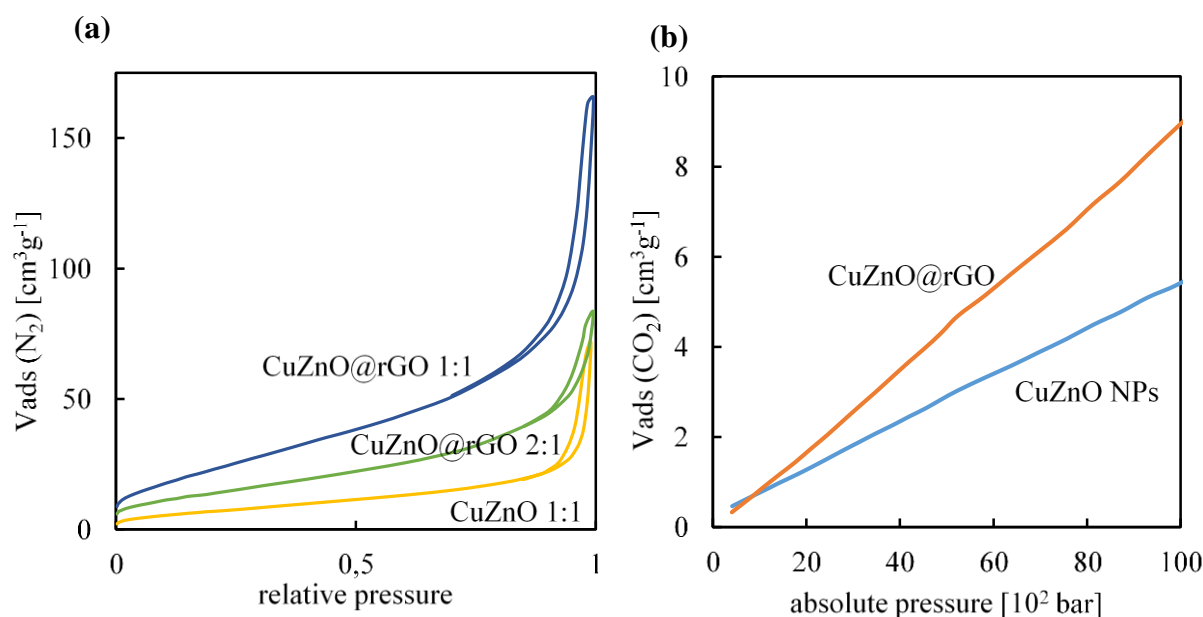
Figure 2. Isotherms obtained for the reduced samples: (a) N_2 adsorption/desorption for samples with 1:1 and 2:1 Cu^0:ZnO ratios, and (b) CO_2 adsorption isotherms of bare and deposited 1:1 NPs.

The morphology of the reduced aerogels was characterized by electronic microscopy. SEM images taken of the CuZnO@rGO monolith displayed the typical 3D porous interconnected meso/macroporous structure of supercritically prepared graphene aerogels, decorated with deposited NPs (Fig. 3).[29] For the reduced CuZnO system, ZnO faceted NPs can be observed intercalated between rounded Cu^0 NPs in the STEM images (Fig. 4a). For CuZnO@rGO aerogel, the morphology consisted of catalyst NPs distributed on the surface of rGO (Fig. 4b). The selected 4:1 composition for CuZnO:rGO in the aerogel allows building a catalyst with a loading of Cu^0 NPs high enough to have a considerable number of active sites, but at the same time, displaying a relatively low degree of aggregation. EDS analysis, performed on a section of the CuZnO@rGO aerogel, confirmed the homogeneous distribution of the Cu and Zn components in the sample, as well as a low degree of sintering of Cu^0 NPs occurring during reduction and/or catalysis (Fig. 4c). Indeed, only few spots with high density of copper can be observed by performing the EDS mapping of this sample. Histograms of particle size distribution obtained from STEM pictures of reduced samples (insets in Fig. 4a,b) gave similar average particle size (29±5 nm diameter) for the pristine and rGO deposited NPs (Table 1). Actually, with this technique it was not possible to distinguish between Cu^0 and ZnO NPs.
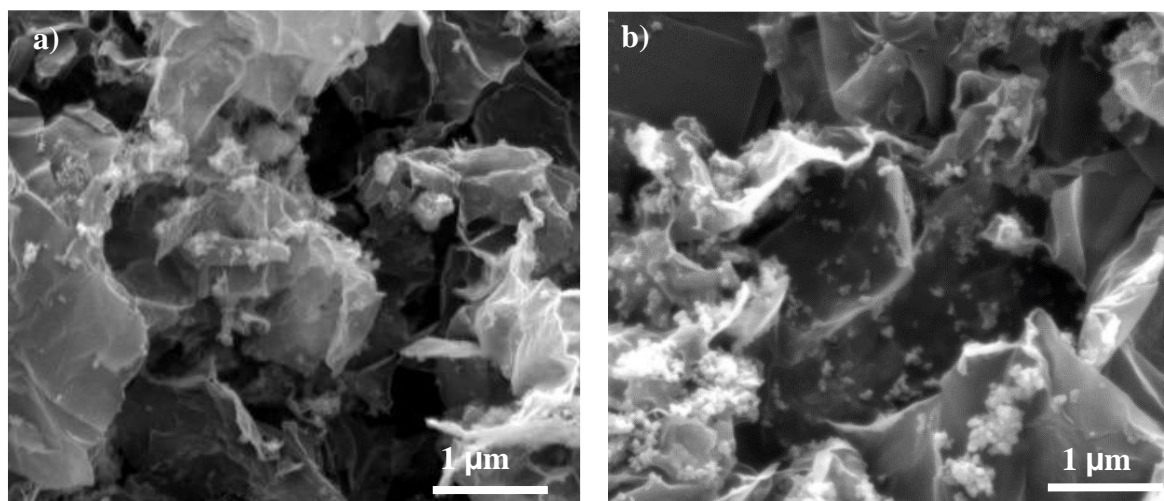
Figure 3. SEM images of the CuZnO@rGO aerogel at two magnifications: (a) portion taken from one-piece monolith (b) piece of smashed aerogel.
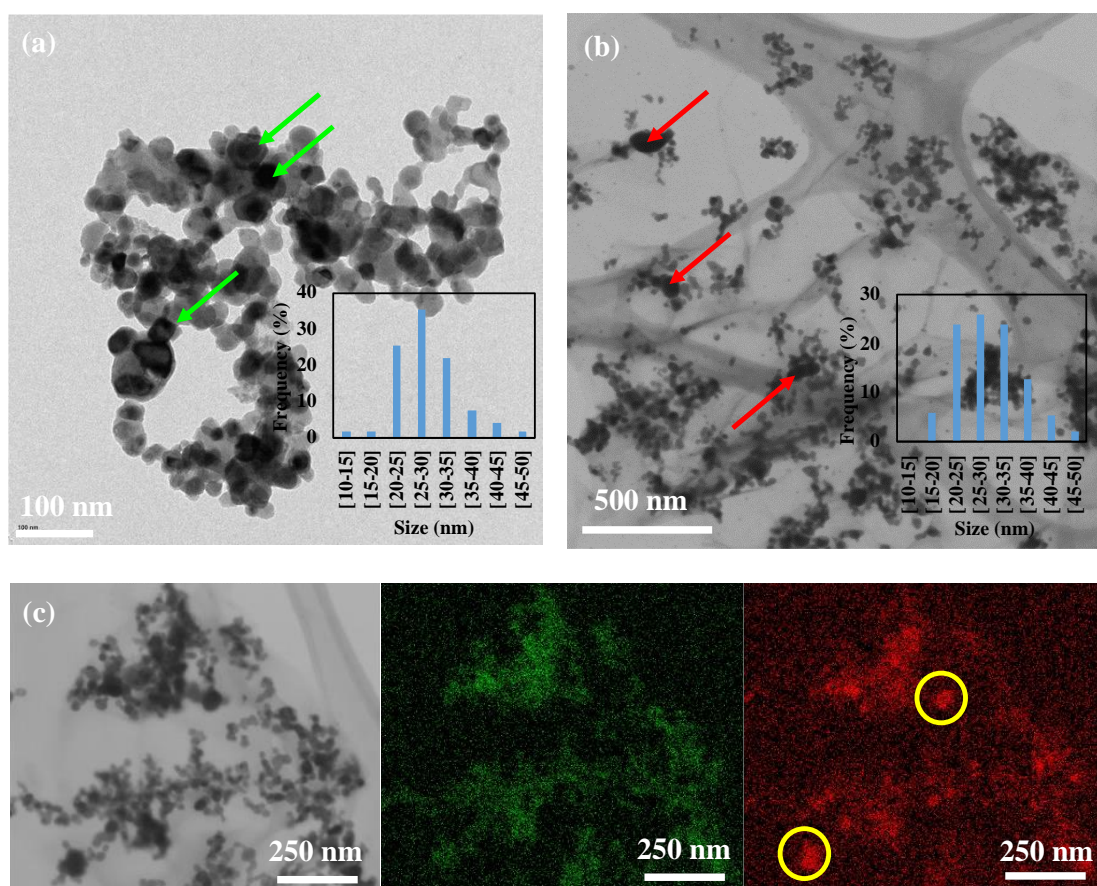
Figure 4. STEM micrographs of: (a) CuZnO NPs (green arrows indicate some ZnO cubic/hexagonal NPs, which are placed in between Cu^0 rounded and larger NPs), (b) CuZnO@rGO aerogel (red arrows indicate few large Cu^0 particles), and (c) EDS elemental mapping of Zn (green in the center) and Cu (red in the right), acquired from the STEM image (left) of sample CuZnO@rGO (yellow circles indicate few areas of sintered Cu NPs).

Table 1. Estimated particle size using TEM and XRD for characterization.

	d_{TEM} (nm)	d_{XRD} (nm)	
	Cu^0 and ZnO NPs	Cu^0 (111)	ZnO (101)
CuZnO	29 ± 6	20	23
CuZnO@rGO	29 ± 7	20	23

3.3. Catalyst structure

Phase changes occurring during reduction were analyzed by FTIR (Fig. 5a) and powder XRD (Fig. 5b). Actually, FTIR was applied to demonstrate the reduction of GO to rGO, while XRD technique was mainly used to extract information on the reduction of the metal oxide phase. FTIR spectra (Fig. 5a) showed that for the as-synthesized and reduced aerogel samples a wide absorption band appears in the range of 450-600 cm^{-1}, indicating the presence of metallic oxide NPs.[38,39] The spectrum of CuOZnO@GO is characterized by a large number of signals assigned to the oxygenated groups in GO, such as stretching's of O-H at *ca.* 3500 and 1620 cm^{-1}, C=O at 1710 cm^{-1}, C-O-C at 1380 cm^{-1}, C-OH at 1220 cm^{-1} and C-O at 1060 cm^{-1}. For the CuZnO@rGO sample, the bands corresponding to the oxygenated functionalities of GO disappeared from the spectrum. Only those corresponding to OH at 1220 and > 3000 cm^{-1} are still apparent, and assigned to sorbed water on the catalyst surface and on the used KBr. The methylene signals between 2925-2850 cm^{-1} are present in rGO, and the bands of C=C stretches at 1550 cm^{-1} increased in intensity, thus indicating a total reduction of GO to rGO. This was an expected result, since the chemical conditions used for reduction were extremely harsh in regard of the oxygenated groups of GO, *e.g.*, 350 ºC under H$_2$ atmosphere, followed of treatment at 280 ºC under a flow of high pressure H$_2$ (5-10 bar).

The broad XRD peaks of GO and rGO phases in the CuOZnO@GO and CuZnO@rGO aerogels, expected at 2θ *ca.* 11 and 25º, respectively,[40] can be sense in the recorded patterns (Fig. 5c). Note that the peak at 2θ *ca.* 11° representative of GO in CuOZnO@GO disappear in CuZnO@rGO, indicating the total reduction of the GO phase under H$_2$ atmosphere. The XRD patterns of the pristine CuOZnO NPs and CuOZnO@GO composite displayed both the most intense peaks of the oxides. Hence, the crystal structure of the metal oxides was preserved throughout the scCO$_2$ process, and the somehow expected ZnCO$_3$ phase, represented by a peak at $2\theta=32.5$º, was not formed. During the treatment with H$_2$, the CuO phase was reduced to copper metal with the development of sharp peaks corresponding to Cu^0 crystals. For all the studied samples, the Cu^0 signals were consistently shifted to lower angles compared to simulated lines, which indicates a distortion of the Cu^0 crystalline network.
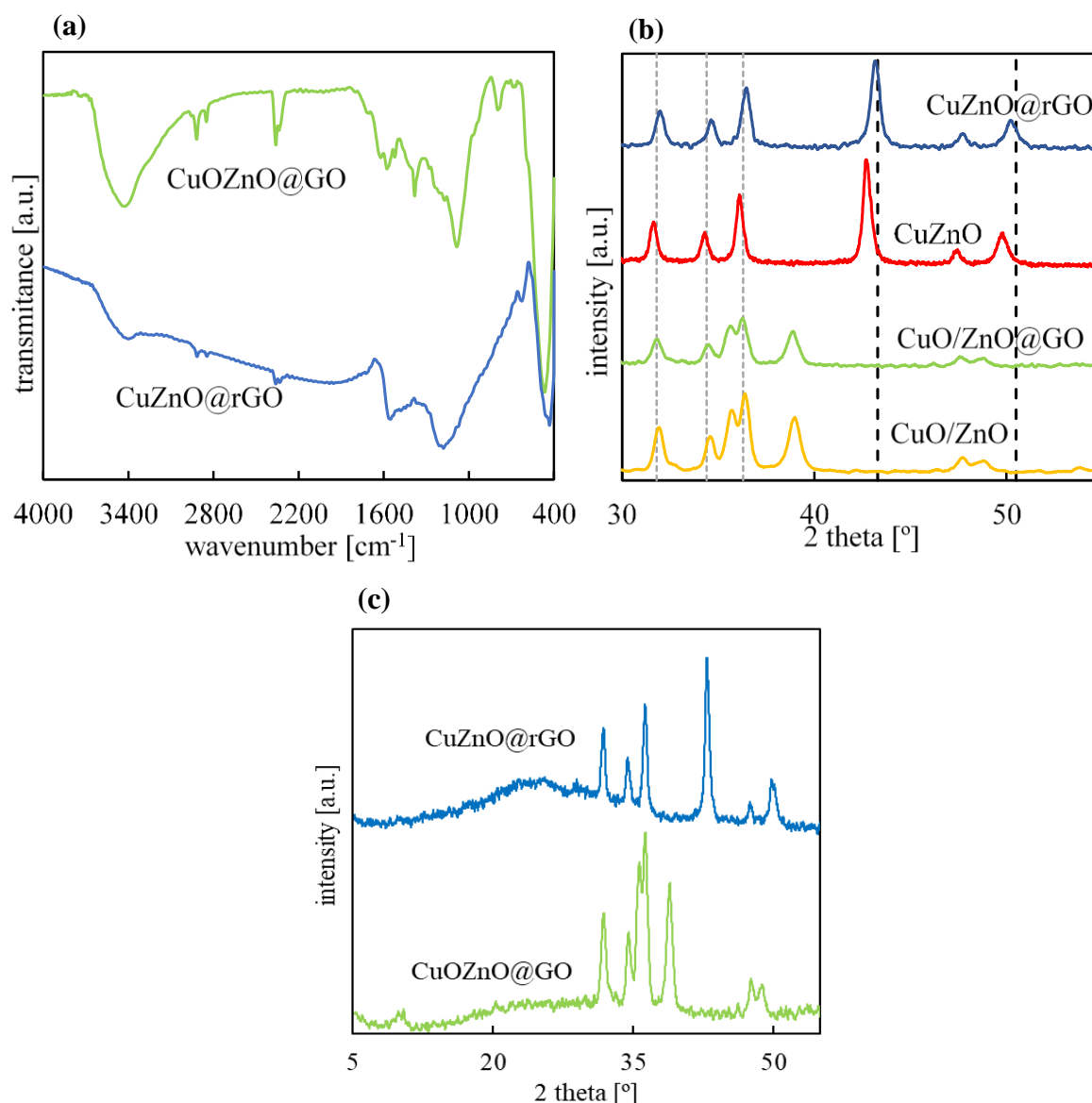
Figure 5. Structural characterization: (a) FTIR spectra (peaks between 2360 and 2330 cm^{-1} are an artefact of the measurement related to CO_2 presence and must be ignored), (b) XRD patterns in which grey dotted lines mark simulated ZnO dotted lines (2θ=31.8, 34.4 and 36.3º) and black dotted lines mark Cu^0 most intense peaks (2θ=43.3º and 50.5º), both as defined by single-crystal data. Peaks at 2θ=35.1 and 38.2º in CuOZnO and CuOZnO@GO are for CuO and (c) XRD patterns of CuOZnO@GO and CuZnO@rGO in 2θ 5-55º range.

This shift was significant for the pristine CuZnO NPs (*ca.* 1º in 2θ), while it was attenuated to only 0.3º in the composite. Whether the shift was originated by bulk defect equilibria, *e.g.*, microstructural strains and defects in Cu^0 appearing upon reduction due to an intimate contact between the metal and ZnO[41] or by alloy formation,[42–45] cannot be deduced from XRD data,

since both effects lead to an increase in the Cu^0 lattice parameters.[46,47] On the contrary, XRD data was suitable to estimate the average crystallite size of Cu^0 and ZnO.[48] The Scherrer equation was applied to the most intense peaks in each pattern, corresponding to Cu^0 (111) and ZnO (101). The crystallite sizes were calculated from the full width at half maximum. Instrument peak broadening was corrected by using lanthanum hexaboride. In both studied samples, XRD averaged crystal size values were 20 and 23 nm for Cu^0 and ZnO (Table 1), respectively, which is in the range of TEM measurements. XRD diameters of particle size are used in this work for further calculations.

The reduced catalysts (Cu^0ZnO NPs and Cu^0ZnO@rGO aerogel) were further investigated by XPS to complement the non-conclusive XRD analysis in regard of the established Cu-ZnO interactions. The complete description of XPS data (Table 2) and deconvolved curves are given in the followings (Fig. 6).

Table 2. XPS results for the different samples.

	Sample →	Cu⁰ZnO NPs	Cu⁰ZnO@rGO
Cu/Zn mass ratio	XPS	0.61	0.52
	ICP	1.10	1.12
B.E. shift (eV)		0.95	0.17
Cu2p3/2 peaks (B.E., eV)	#1	930.5	932.7
	#2	932.3	934.6
	#3 (sat)	-	940.8
	#4 (sat)	941.7	944.0
Cu2p3/2 peaks (fraction)	#1	0.41	0.35
	#2	0.19	0.21
	#3 (sat)	-	0.04
	#4 (sat)	0.07	0.06
Zn2p3/2 peaks (B.E., eV)	#1	1019.8	1021.9
	#2	1021.1	1022.4
Zn2p3/2 peaks (fraction)	#1	0.61	0.47
	#2	0.08	0.22
	#2	-	-
	#3 (sat)	-	-
K.E. CuLMM (eV)		915.5	916.2
K.E. ZnLMM (eV)		986.7	988.4
α' Cu		1846.0	1849.0
α' Zn		2006.5	2010.3

The XPS found values of the Cu/Zn atomic ratio (0.6 and 0.5 in the net NPs and aerogel, respectively) were significantly lower (*ca.* twice) than those evaluated by ICP (*ca.* 1.1 for NPs and aerogel), meaning that the ZnO NPs should be preferentially dispersed on the surface of

the copper particles. Essentially, the ICP ratio is taken as the most representative value of the bulk material, while the XPS ratio gives an idea of the surface composition, which, indeed, would be markedly important in the catalytic process. Binding energy positions, Auger parameters and chemical state (Wagner) plots for Cu2p and Zn2p (Fig. 6 and Fig. 7) are here used to understand the trends found for the synthesized CuZnO NPs and CuZnO@rGO aerogel. For the Cu2p3/2 region, both samples displayed the main peak at the lowest binding energy in this region (930.5 and 932.7 eV, respectively) that is assigned to Cu^0/Cu^+, and a small peak at slightly higher binding energy (932.3 and 934.6 eV, respectively) that suggests the presence of a very small fraction of Cu^{2+}.[49] The little significant area of the shake-up satellite peak at 941.7 eV (#4), not present on cuprous or metallic copper, further indicates the presence of a small amount of Cu^{2+}.[50,51] Both Cu^0 and Cu^+ species are believed to contribute to the activity of Cu-based catalysts.
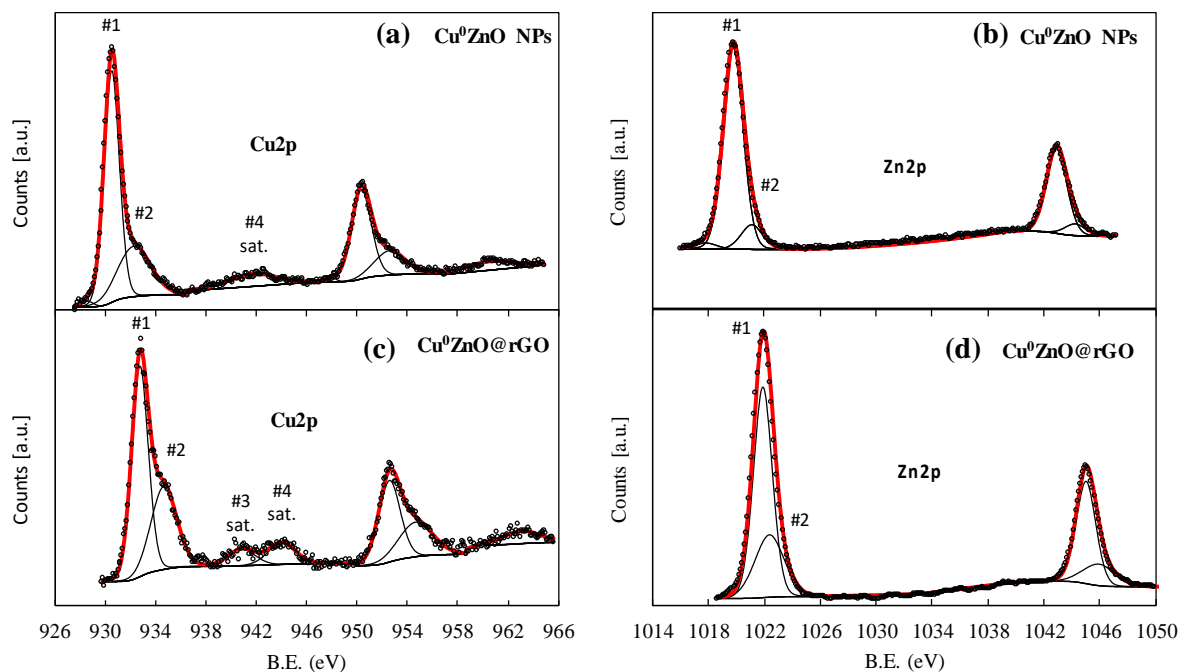
Figure 6. Cu2p and Zn2p regions for the different samples: (a,b) Cu^0ZnO NPs, and (c,d) Cu^0ZnO@rGO aerogel.

The Zn2p3/2 of CuZnO NPs and CuZnO@rGO aerogel were characterized by a main peak at binding energies of 1019.8 and 1021.9 eV, respectively, separated in both cases 23.1 eV from the main peak in the Zn2p1/2 region. This gap is typical of the Zn^{2+} state,[52] and, more specifically, corresponds to the tetrahedral form of ZnO. However, the low value of the binding energy found for ZnO in CuZnO NPs (*ca.* 2 eV below the value of crystalline ZnO) indicates amorphization of the surface of the oxide (Fig. 7a),[53,54] likely due to successful substitution of

Zn^{2+} by copper ions and the formation of a Cu-Zn alloy at the interphase.[55] Furthermore, the combination of low values of binding energy in Cu2p3/2 and Zn2p3/2 has been ascribed to Cu ions with the capacity to substitute successfully Zn^{2+} ions in the ZnO lattice.[55]

An extremely low value of the Auger parameter was found for zinc in CuZnO NPs (2006.5 eV, Fig. 7a). This observation was confirmed by the Cu position of this sample on the copper Wagner's plot, situated in the range of low binding energy (Fig. 7b). Finally, the low value of the Auger parameter for copper (1846 eV), is commonly ascribed to highly dispersed Cu^0.
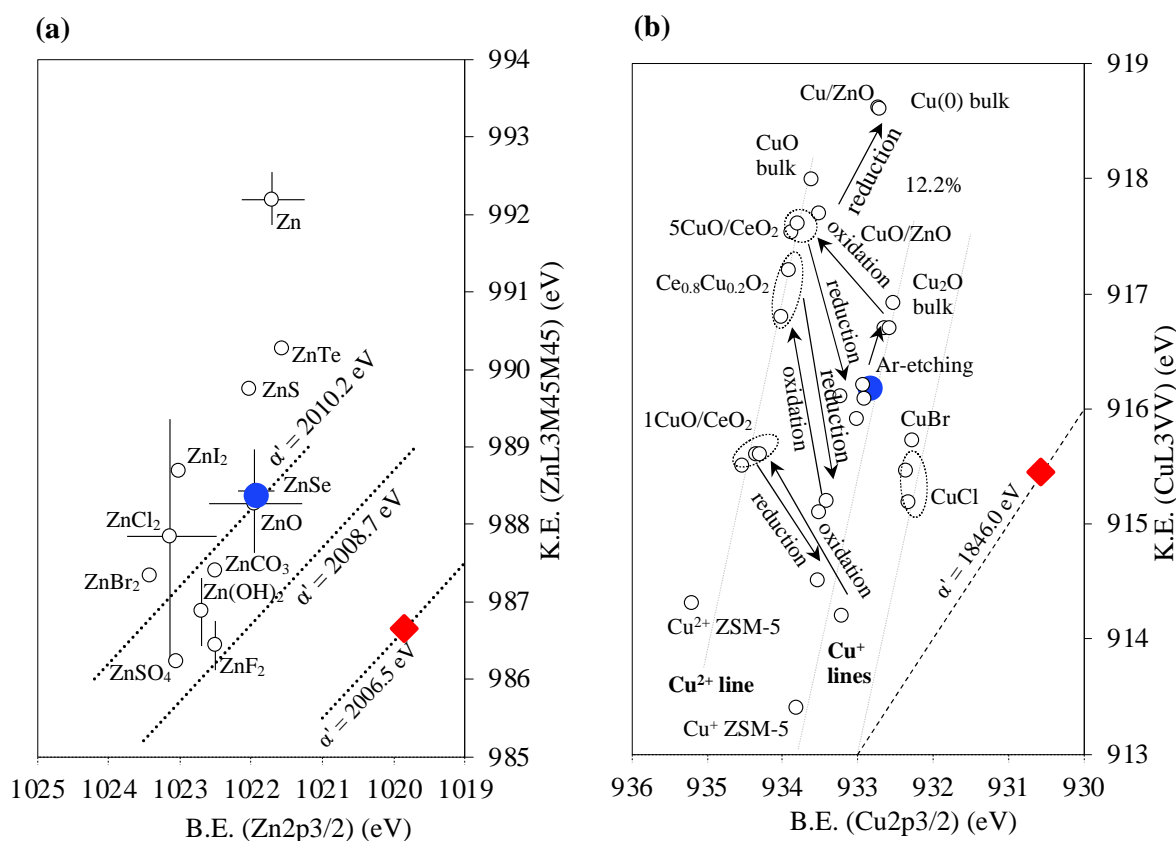
Figure 7. Wagner's plots of the two studied samples for: (a) zinc, and (b) copper. Empty circles correspond to data points for zinc[56], and copper[57–59]. Red ◆ indicates sample Cu^0ZnO NPs, while blue ● represents Cu^0ZnO@rGO aerogel.

For the Cu^0ZnO@rGO sample analyzed in the Cu2p region (Fig. 6c), the main peak at 932.7 eV (#1) is assigned to Cu^+.[50] The shake-up satellite peaks at 940.8 (#3) and 944.0 eV (#4) confirm the presence of some amount of Cu^{2+}, already suspected by the existence of the peak at 934.6 eV (#3).[50,51,60] It cannot be disregarded the possibility that the peak at 934.6 eV and the shake-up satellite at 944.0 eV may correspond to highly dispersed Cu^{2+} linked to Zn hydroxyls.[61,62]

The Zn2p3/2 region for the CuZnO@rGO (Fig. 6d) is characterized by a peak (#1) placed at a binding energy of 1021.9 eV, separated 23.1 eV from the main peak in the Zn2p1/2 region. These values are strong evidence for Zn^{2+} state, and more specifically correspond to the tetrahedral form of ZnO.[53,54]

On the contrary to the CuZnO NPs, for the CuZnO@rGO aerogel, no amorphization of the ZnO phase was observed. Moreover, the position of the binding energy for Cu in this sample was placed in the upper zone of the copper Wagner's diagram, thus evidencing a mainly reduced state of copper (Fig. 7b).[63] The position of zinc was close to crystalline ZnO in the diagram (Fig. 7a).[56] Hence, XPS measurements clearly indicate that the formation of a Cu-Zn bimetallic alloy was only clearly evidenced for the net CuZnO NPs, and not for the deposited NPs on rGO.

Cu^0 surface area calculations

XPS data was also used to estimate the exposed surface area of Cu^0 in the CuZnO system. Cu^0 surface area was calculated using the total surface area of the CuZnO NPs, measured by N_2 adsorption /desorption and the Cu/Zn molar fraction on the surface of the NPs obtained by XPS measurements. A value of $1.46 \cdot 10^{19}$ Cu atomm^{-2} surface density was used for copper,[64] corresponding to one monolayer of the metal. To calculate the surface density of Zn, one layer of the unit cell was considered as the monolayer, which consists in total two Zn and two O atoms.[65] The volume of one unit cell is 47.6 Å, and the lattice constant can be approximated as the cubic root of the unit cell volume, giving d = 3.62 Å.[66] The projected area of this unit cell –approached with a cube- is 13.1 Å^2, thus the surface density of the Zn is estimated as two Zn atoms in each 13.1 Å^2, resulting in $1.52 \cdot 10^{19}$ Zn atomm^{-2}.

The fractional surface coverage by ZnO and Cu can be estimated from the Cu/Zn surface molar fraction measured by XPS as follows:

$$A\%_{Cu} = \frac{\dfrac{X_{Cu} \cdot N_{Av}}{\rho_{Cu,surf}}}{\dfrac{X_{Cu} \cdot N_{Av}}{\rho_{Cu,surf}} + \dfrac{X_{Zn} \cdot N_{Av}}{\rho_{Zn,surf}}} \cdot 100 = \frac{\dfrac{0.61 \cdot 6 \cdot 10^{23}}{1.54 \cdot 10^{19} \dfrac{\text{Cu atom}}{\text{m}^2}}}{\dfrac{0.61 \cdot 6 \cdot 10^{23}}{1.54 \cdot 10^{19} \dfrac{\text{Cu atom}}{\text{m}^2}} + \dfrac{1 \cdot 6 \cdot 10^{23}}{1.52 \cdot 10^{19} \dfrac{\text{Zn atom}}{\text{m}^2}}} \cdot 100$$

$$= 37.7\%$$

where $X_{Cu} / X_{Zn} = 0.61$ is the Cu/Zn surface molar fraction, measured by XPS (Table 2), N_{Av} is the Avogadro constant, while $\rho_{Cu,surf}$ and $\rho_{Zn,surf}$ are the surface density of the metal atoms

in a monolayer. Consequently, 37.7 % of the surface monolayer is covered by a Cu atoms, while 62.3 % is covered by ZnO.

From the total surface area measured by N_2 adsorption/desorption (S_{BET}), the fractional coverage can be transformed to surface area corresponding to Cu^0 and ZnO.

$$S_{Cu}\left(\frac{m^2}{g_{NP}}\right) = \frac{A\%_{Cu}}{100} \cdot S_{BET} = 0.377 \cdot 39\frac{m^2}{g_{NP}} = 15\frac{m^2}{g_{NP}}$$

$$S_{ZnO}\left(\frac{m^2}{g_{NP}}\right) = \frac{A\%_{ZnO}}{100} \cdot S_{BET} = 0.623 \cdot 39\frac{m^2}{g_{NP}} = 24\frac{m^2}{g_{NP}}$$

The contribution of the NPs to the surface area in the CuZnO@rGO composite was approximated by the ICP measured weight fraction of the NPs and the surface value obtained for the net NPs. For both, bare NPs and aerogel, the estimated exposed surface area values for Cu^0 and ZnO were *ca.* 15 and 25 m^2g^{-1}, respectively. The increase in the surface area indicates that the ZnO is preferentially dispersed onto the copper NPs, reducing the exposed surface of Cu^0.

3.4. Catalytic activity screening

The catalytic activity of the synthesized samples was investigated in the reaction of CO_2 hydrogenation to methanol. A multifaceted bibliographic revision indicates that significant differences, and even contradictory results, for the catalytic activity can be observed among the diverse CuZnO catalysts described in the literature.[22–24,67–77] Schematically, representative CO_2 conversion and MeOH selectivity values that have been obtained with CuZnO systems are represented in Fig. 8, showing an extremely broadened data distribution. The widespread of the results is the consequence not only of building different catalysts, in regard of composition, used promoter/support and particle size, but also of analyzing them under different experimental parameters, such as temperature, pressure, flow rate and flow distribution, added mass of catalyst, reactor set-up, and so on. In any case, experimental conditions scattering makes difficult to contrast literature results with newly designed products. In this work, the most reliable approach to analyze the effect of the addition of promoters and/or supports has been considered to perform the comparison of the catalytic behavior of the composite system with that of a similar product lacking of the support and measured in the same equipment under similar experimental conditions. Only in this way, effects such as CuZnO composition and particle size, as well as set-up parameters, can be eliminated from the analysis. Temperature and pressure, as well as gas flow composition (H_2:CO_2 ratio) and rate, have been described as

the most relevant operational parameters in the studied fixed-bed hydrogenation reaction of CO_2. As it is shown in Fig. 8, temperatures and pressures in the ranges of 220-270 ℃ and 10-40 bar, respectively, have been chosen in the literature to evaluate most studied CuZnO catalysts, often by fixing the H_2:CO_2 ratio to 3:1. The catalytic tests in this work were performed at standard temperatures (200-280 ℃) and stoichiometric H_2:CO_2 ratio (3:1), but in the lowest pressure range (10 bar).
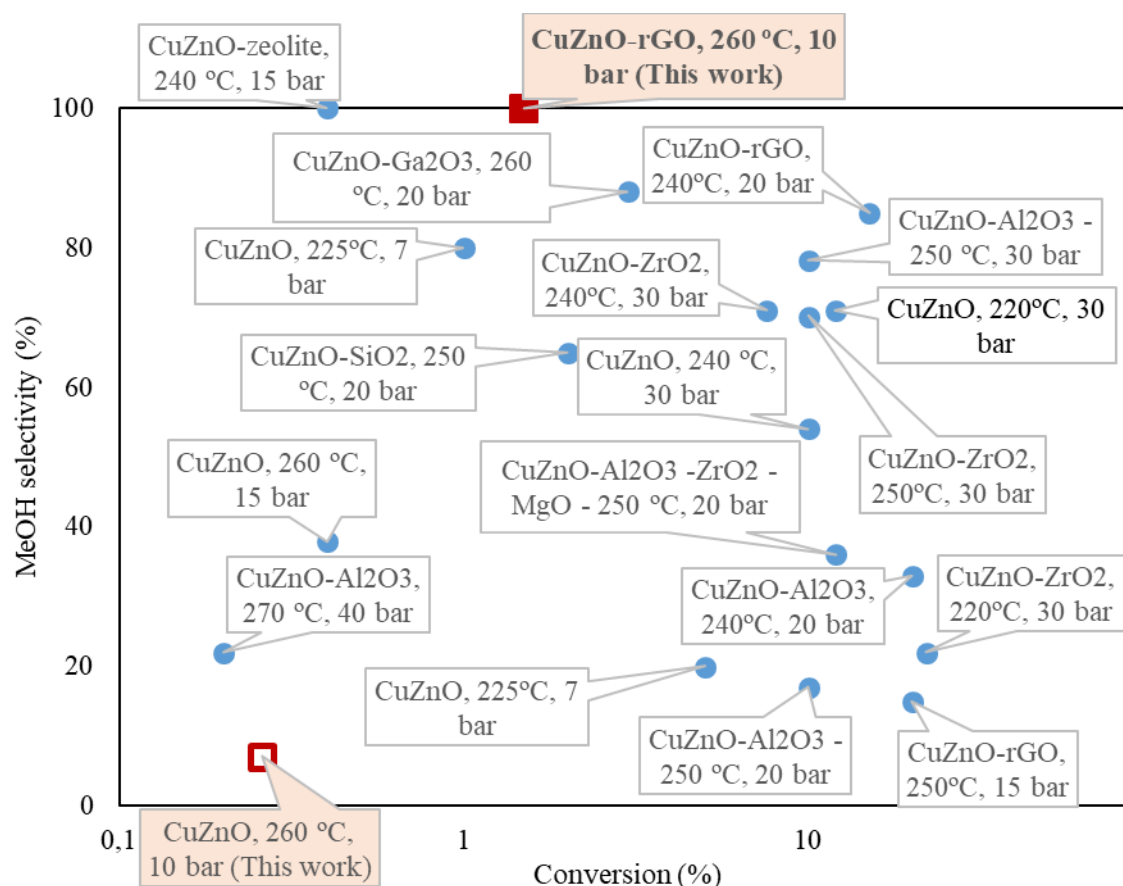
Figure 8. Literature data and those obtained in this work of CO_2 conversion and MeOH selectivity in the CO_2 hydrogenation reaction to methanol using the CuZnO system, either as bare NPs or supported on different matrixes.[22–24,67–77]

Effect of temperature

Rising the temperature from 200 to 280 ℃ resulted in a constant increase of the STY of MeOH for all the tested catalysts. This effect is exemplified in Fig. 9, in which STY data is represented both *vs.* the weight of Cu^0 and CuZnO in the composite. This interpretation mode aims to cover cases in which the ZnO is acting as a mere promoter to avoid Cu^0 NPs aggregation and those involving ZnO as a cocatalyst.[78,79] Nonetheless, a large degree of increase in the STY values at

the studied temperatures was observed for the CuZnO@rGO monoliths in either representation when compared to net CuZnO NPs (Fig. 9a).

(a)   **(b)**
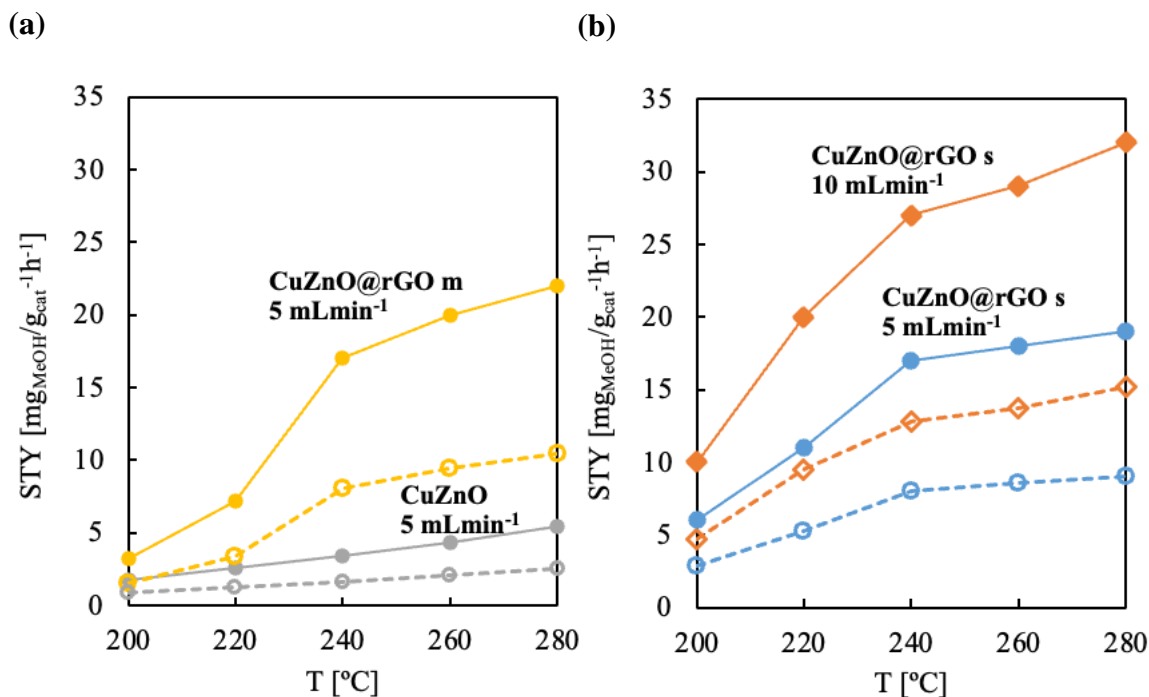
Figure 9. Representative STY catalytic data represented either *vs.* Cu^0 (full symbols and straight lines) or CuZnO weight (empty symbols and dotted lines) in the catalyst, obtained at GHSV of 10 $L_{CO2}g_{cat}^{-1}h^{-1}$ (5 mLmin^{-1}, round symbols) and 20 $L_{CO2}g_{cat}^{-1}h^{-1}$ (10 mLmin^{-1}, diamond) for samples: (a) CuZnO (grey) and CuZnO@rGO monolith (yellow), and (b) smashed CuZnO@rGO at GHSV of 10 $L_{CO2}g_{cat}^{-1}h^{-1}$ (blue) and 20 $L_{CO2}g_{cat}^{-1}h^{-1}$ (orange).

Remarkably, the methanol selectivity was maintained at 100 % up to high temperature values (≥ 220 ℃) for the composite aerogels, while it constantly decreased with temperature for pristine NPs (Fig. 10). Hence, at any of the studied temperatures, the addition of rGO to the system increases the CO_2 conversion to methanol when compared to pristine CuZnO NPs treated under similar reaction pressure (10 bar) and flow rate (5 mLmin^{-1}). For instance, at 220 ℃ a value of selectivity of only 20 % was measured for the net NPs, while it increased to near 100 % in the CuZnO@rGO catalyst. Increasing the reaction temperature to 240 ℃ provoked a reduction in the MeOH selectivity for both systems; however, the methanol selectivity of the CuZnO@rGO catalyst was still of 80 %, while that of the bare NPs was reduced to only 10 %. The result is a significant increase of the methanol production rate, *ca.* fourfold, by using rGO at temperatures of 220 ℃ and higher. Although, usually, increasing the conversion values is anticipated to be accompanied with reduced methanol selectivity, in the studied CuZnO@rGO system the selectivity was increased concomitantly with the conversion of CO_2 to methanol.

This behavior is attractive to facilitate the thermal activation of CO_2 molecules, which at low temperature are highly stable.
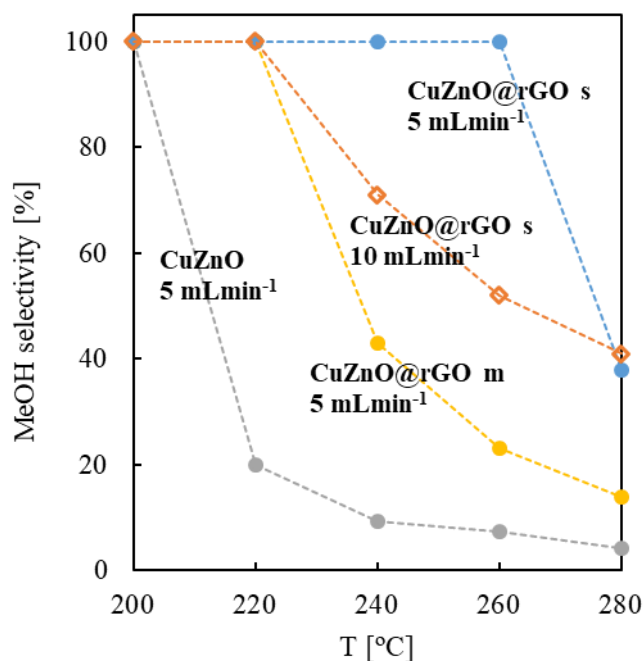
Figure 10. Methanol selectivity for the studied samples at different temperatures and GHSVs. CuZnO represents bare NPs, while CuZnO@rGO m and CuZnO@rGO s are the one-piece and smashed aerogels, respectively.

Effect of pressure

As mentioned in the introduction, one of the main objectives of this work was to design a catalyst able to effectively work under reduced H_2 pressure for safety and economic reasons.[76,80,81] Thus, even being a detrimental factor for total CO_2 conversion, the use of low pressure, *e.g.*, 10 bar, was here considered important, since milder reaction conditions are being anticipated for future CO_2-to-methanol processes. Even though many existing publications studied the catalytic properties of similar CuZnO catalysts, it is very rare to find documents with studies operating at pressures lower than 20-30 bar.[71] Note that at high pressures, conversion values could be increased because of broadening in the thermodynamic constraints.

Effect of GHSV

A second pertinent catalytic factor, often neglected, but substantially influencing the CO_2 conversion, is the amount of solid catalyst added to the reactor contrasted to the used flow of the inlet H_2:CO_2 gas. Most bench-scale catalytic tests depicted in the literature are carried out

with fixed-bed columns of 1 cm diameter and 10-20 cm length, to which catalyst powder was added in a weight range of 0.25-5 g, and operated at a GHSVs of 2-50 $L_{CO2}g_{cat}^{-1}h^{-1}$.[22–24,67–77] majority of these tests meet the characteristic of active site excess, *i.e*., the catalyst loading is enough, most likely in excess, to give an extremely high probability for the gas molecules to collide and be activated by the solid NPs, which lead to elevated conversion values. On the contrary, as it can be inferred from the analysis of diverse scientific reports, presented in Fig. 8, most of the experiments carried out with a low amount of catalyst, *e.g.*, 0.5 g or less, and at a high GHSV displayed low CO_2 conversion values, potentially limited by the amount of added catalyst. This is certainly the case for the essayed systems in this work, in which the amount of solid catalyst added to the column was of only 0.03 g, including the inactive support. This low value of the added mass of catalyst was chosen on the basis of the possibility given by the supercritical synthesis of straightforwardly preparing the CuZnO@rGO aerogel inside of a fixed-bed column. Note, that aerogels are low density materials. Particularly the rGO aerogels in this work, even with the added CuZnO NPs, have a density of only 10 $mgcm^{-3}$.

The absolute value of flow rate can be also an important factor to be considered in porous matrices, in which the diffusion of CO_2 into the pores (and of product out of the pores) can be an important kinetic constrain. In general, low flow rates are favorable for increasing the internal diffusion and, thus, the conversion values in highly porous catalysts.[82] Nevertheless, this factor is less significant for non-porous supports, which make difficult to straightforwardly compare catalytic results. Two operation mode regarding the GHSV were studied in this work, namely 20 $L_{CO2}g_{cat}^{-1}h^{-1}$ (10 $mLmin^{-1}$) and 10 $L_{CO2}g_{cat}^{-1}h^{-1}$ (5 $mLmin^{-1}$). The effect of decreasing the flow rate, while keeping constant the number of active centers loaded to the column, was twofold. On one side, the residence time of the CO_2 and H_2 molecules inside the column was raised, which increases the probability for the gas molecules to find an active site for collision due to enhanced time for diffusion inside the porous matrix. On the other side, the amount of gas travelling throughout the column diminishes, thus reducing the number of CO_2 molecules that can be transformed by unit time. The experimentally observed behavior for the CuZnO@rGO system was some decrease in the MeOH production rate when decreasing the flow rate (Fig. 9b). However, under the conditions of low flow, keeping all the other parameters constant, a remarkable MeOH selectivity of near 100 % was attained up to temperatures as high as 260 ℃. Contrarily, the increase in the GHSV was leading to higher conversion values, which is often concomitant to a decrease in the selectivity of the process. It has been demonstrated that high CO_2 conversion values can lead to partial deactivation of the catalyst due to the increase of the surface coverage with reaction products or intermediates. Particularly,

the formation of water, produced in an equimolar amount with respect to MeOH, has been described as a cause of the decrease in selectivity at high conversion values, since water is responsible for the partial oxidation of Cu^0 metallic sites, inhibiting the formation of MeOH.[69,78]

Effect of sample preparation

The previous analysis of the effect of some experimental parameter (pressure, flow rate, catalyst loading) in the catalytic conversion of CO_2 to methanol indicates that the limit for methanol production in the CuZnO@rGO aerogel was not the design of the material, but the used set-up. Hence, it would be possible to further improve and rationalize the methanol production rate by modified aspects ahead of the material composition or design. Prime example is the way in which the catalyst is added to the fixed-bed column. The use of monoliths straightforwardly grown into the catalytic columns, although interesting from an operational point of view, not only substantially limits the amount of applicable catalyst, but also prompts the establishment of preferred flow pathways for H_2 and CO_2 (Fig. 11). The latter is an important factor in heterogeneous porous systems that causes the gas molecules to bypass large portions of active catalyst. Actually, due to shrinkage, ubiquitous during aerogels drying, the generation of void at the interphase between the CuZnO@rGO monolith and the column is unavoidable. Through this void space a large part of the gas can flow without restrictions and without colliding with catalyst NPs, resulting in a lower number of activated CO_2 molecules (Fig. 11a). To minimize this effect, the CuZnO@rGO aerogel monolith growth in the column with *ca.* 0.030 g weight was extracted, smashed in small pieces and added again to the column, but distributed over glass wool. The smashing of the aerogel was gentle, since the objective was to break the aerogel in small pieces of few hundreds of microns, but without losing the macro/mesoporous character, which is still evident in the SEM pictures of the smashed portions (Fig. 3b). In point of fact, the main objective of building mesopores in the rGO 3D aerogels was, on one hand, to have a system with high specific surface area (*ca.* 100 m^2g^{-1}) available for metal active centers deposition on both sides of the flakes, and, on the other hand, to increase the internal mass transfer of the reactants and products by creating large mesopores in the aerogel *vs.* small mesopores and micropores in aggregated NPs, the latter being one of the most important kinetic bottle-neck to be solved in the heterogeneous catalysis mechanism.[27] Ahead of improving flow distribution, by breaking the monolith in small pieces it is expected to facilitate reactants access to the catalytic active sites at the interior and, simultaneously, the diffusion of products to the exterior, in both cases by reducing internal diffusion length (Fig. 11b). The experimental observation obtained by smashing the CuZnO@rGO aerogel in small

pieces was a significant increase in the methanol production rate, for instance from 7.2 to 20 $mg_{MeOH}g_{Cu}^{-1}h^{-1}$ at 220 ºC, and from 20 to 30 $mg_{MeOH}g_{Cu}^{-1}h^{-1}$ at 260 ºC (Fig. 9). Outstandingly, the smashed aerogel maintains the selectivity to MeOH at 100 % up to a temperature as high as 260 ºC (Fig. 10). A second important effect of smashing the aerogel is that it allows to significantly increase the amount of catalyst added to the fixed-bed column, and, hence, the total conversion of CO_2 by decreasing the GHSV without modifying the absolute flow rate.
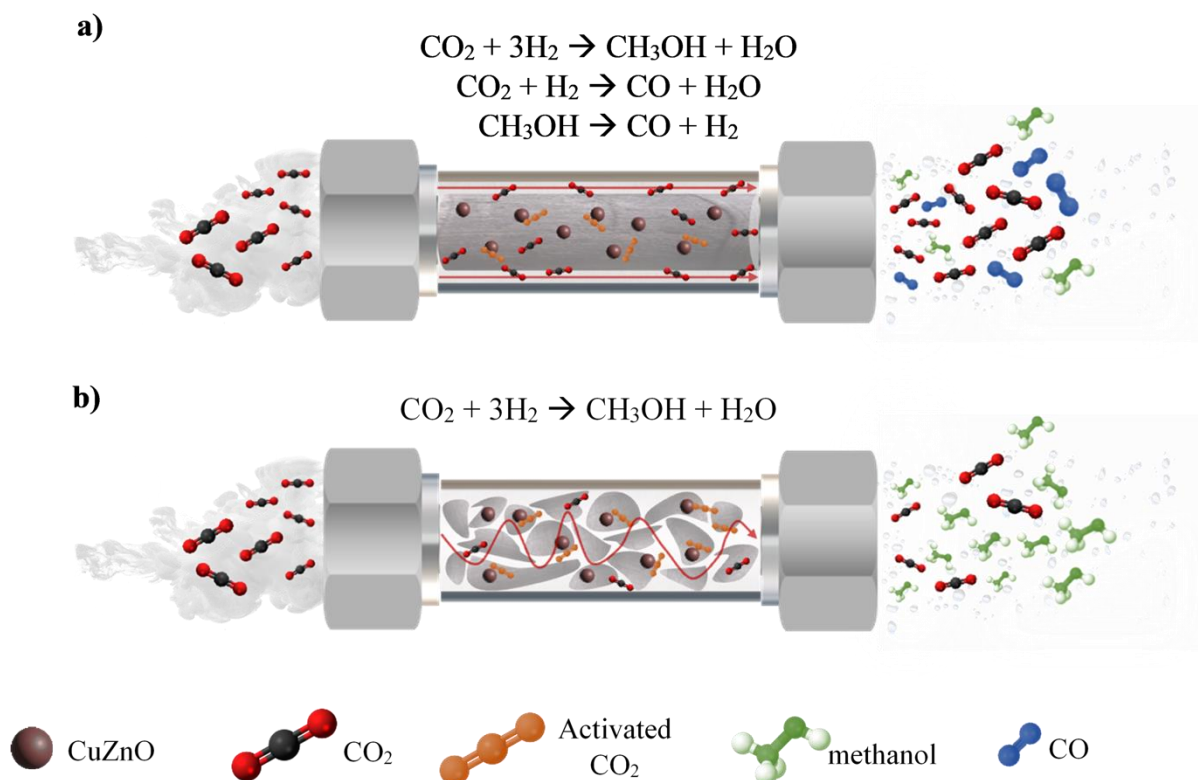
Figure 11. Schematic representation of the effect of CuZnO@rGO sample preparation on the conversion of CO_2 to methanol at high temperature and pressure (H_2 is omitted for clarity), indicating resulting products, for: (a) one-piece monolith and (b) smashed aerogel.

3.5. Mechanistic considerations

For most studied CuZnO@support catalysts, efforts have been mainly focused in finding systems with enhanced CO_2 conversion, but often neglecting the usually concomitant consequences of low MeOH selectivity. For instance, Cu^0ZnO NPs have been previously deposited on rGO or nitrogen-doped rGO supports reporting conversion values at 15-20 bar higher than those measured in this work (at 10 bar), but with methanol selectivity values either not studied or being in the order of only 15-30 % at 250 ºC.[24,26,28] The highest reported methanol selectivity value for a similar system involving rGO and CuZnO NPs was 30 % (at 240 ºC), but the addition of the expensive ZrO_2 promoter was needed, together with an applied reaction

pressure to 20 bar.[22] The work performed here with the designed CuZnO@rGO aerogel gives clear evidences of the main effect of using rGO aerogel as a support of the CuZnO NPs, being an outstanding increase in MeOH selectivity to near 100 % maintained, in the most favorable conditions, in the temperature range of 200-260 ºC. For the exothermic reaction of CO_2 conversion, MeOH selectivity becomes an extremely important issue because CO is the main secondary product. MeOH, together with water, is obtained by the exothermic straightforward reaction of CO_2 and H_2. In contrast, CO is obtained in two endothermic reactions, involving, the first, the reverse water-gas shift reaction of CO_2 and H_2 to give CO and water and, the second, the decomposition of methanol into CO and H_2. Hence, the use of high temperature should be a disadvantage to increase the selectivity of MeOH *vs.* CO. Even so, for the thermally efficient methanol production the use of relatively high temperature is needed, in order to reduce the kinetically-limited activation of the critically inert CO_2 molecule with a threshold of near 240 ºC.[83,84,85] From an operational point of view, a MeOH selectivity close to 100% is also advantageous, since product condensation (water and ethanol) could be easily utilized as a method for CO_2 separation/recycling, thus circumventing drawbacks of unconverted feed gas.[86] On the contrary, in systems with low MeOH selectivity, exhausted CO_2 is mixed with large amounts of difficult to separate CO. In this work, it is remarked that the secondary reactions related to CO formation are not occurring at high temperatures, in some cases up to temperatures as high as 260 ºC, by using the designed CuZnO@rGO aerogel composite. Several reasons are outlined to explain this behavior:

(i) The formation of water in the catalytic hydrogenation reaction of CO_2 during MeOH/CO production is known to be responsible for the partial oxidation of Cu^0 metallic sites in the CuZnO NPs, hindering the formation of MeOH and directing the reaction to CO.[69] In the systems studied in this work, the hydrophobicity of rGO support in the basal plane is expected to inhibit the adsorption of water and to protect Cu^0 from oxidation and sintering at high temperatures. This effect circumvents catalyst deactivation during MeOH production due to extensive surface coverage with water. A more conventional option to speed water desorption from the adsorbent surface is to increase reagents flow rate, *e.g.*, from 5 to 10 mLmin^{-1} in this work, which in our case implied an increase in the total methanol yield (Fig. 9b), but concomitant with a decrease in the methanol selectivity (Fig. 10). Hence, the option of using hydrophobic substrates seems more appropriate to increase methanol production rate by gaining methanol selectivity.

(ii) The widely accepted dual site mechanism for stepwise hydrogenation of CO_2, which involves the dissociative adsorption of H_2 on metallic copper surface and the adsorption of CO_2 on and near the surface of ZnO and ZnO-Cu^0 interface,[87] indicates preferential MeOH *vs.* CO production at high concentration of adsorbed CO_2. As demonstrated with the isotherms of CO_2 adsorption measurements on pristine and deposited NPs on rGO (Fig. 2b), the presence of rGO highly enhances CO_2 adsorption. Hence, rGO can act as a CO_2 reservoir, thus favoring MeOH formation.

(iii) The morph structural arrangement of the NP aggregates would play one of the most important roles in the catalyst selectivity towards methanol.[69,84] Evidently, the organization of Cu^0 and ZnO structure and established interfacial contacts were influenced in the studied catalysts by the presence of rGO. The planar surface of rGO, together with the possibility of the NPs to be deposited on both sides of the flakes, is expected to facilitate NPs dispersion, to increase exposed Cu^0 surface area and to decrease NPs sintering during reduction and catalytic tests. In the dual site mechanism, the nature and location of the Cu-ZnO active sites have been the subject of a vast number of researches, although low consensus has been attained.[45–47,69–72] Actually, debate is still continuing distinguishing several active sites categories, such as Cu species (Cu^0 and Cu^+), Cu-ZnO interface with ZnO oxygen vacancies, defective Cu surface, Cu-ZnO alloy, and so on. The historical description of the Cu-ZnO interface was dominated by the Cu-Zn alloy active site approach.[42–44] This appears to be the structure obtained for the pristine CuZnO NPs synthetized in this work after reduction, for which XPS data indicated the formation of a diluted alloy of Zn in Cu. This mechanism has been described by the "active site creation model", in which ZnO provides Zn atoms to the Cu surface upon reduction leading to the formation of the alloy.[42–45] On the contrary, the formation of the alloy was not detected during the XPS study for the CuZnO@rGO aerogel. Nevertheless, even not detecting the formation of the alloy by XPS, the MeOH production rate was highly enhanced with respect to bare similar NPs. Actually, recent studies have indicated that the formation of a Cu-Zn alloy at the interphase is not required to achieve high methanol yields and selectivity values.[25] Quite the opposite, the formation of the alloy can significantly decrease the conversion rate, due to the limited ability of the alloy to activate H_2.[47] Hence, the system constituted by Cu^0 and ZnO NPs deposited onto the surface of rGO would be better described by the "bulk defect equilibria model", with abundant Cu^0 microstructural strains leading to edge/defect sites with coordinately unsaturated reactive atoms, necessary for

facilitating hydrogen spillover, and creation of ZnO-Cu^0 interfacial active sites.[15,41,69,84,88–90] The catalytic behavior of the CuZnO@rGO sample is in line with recent studies that advocated for an enhancement of the intrinsic activity of copper due to strain imposed at the ZnO interphase causing misfit at the contact surface,[76] but without significant alloy formation. This experimental observation is rationalized on the basis of the oxygenated character of the precursor GO substrate (Fig. 12).
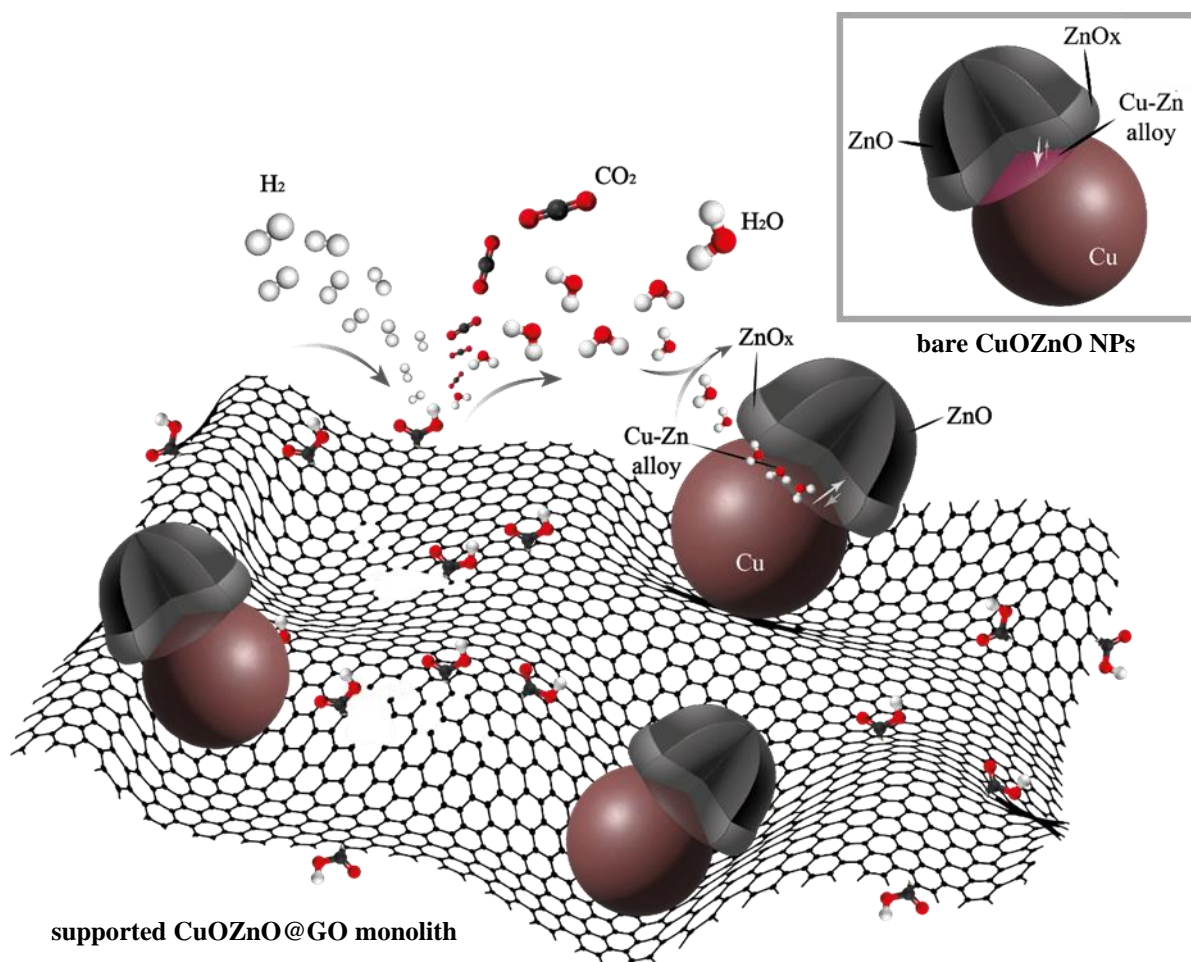
Figure 12. Illustration of the ongoing process occurring during the reduction step to form rGO from GO and CuZnO from CuOZnO (under H_2 atmosphere), previous to the catalytic procedure (under H_2 and CO_2 atmosphere). For the bare CuOZnO NPs (grey frame), the Cu-Zn alloy formation occurs at the interface, while for the CuOZnO@rGO aerogel the alloy formation is mainly inhibited during reduction by the water expelled from the oxygen functionalities on GO surface.

The oxygenated functionalities of GO, during the reduction of CuOZnO@GO to CuZnO@rGO at high temperature, would expel important amount of water. The water molecules, generated near the oxides can be used by the system to re-oxidize back to ZnO the traces of reduced zinc,

thus inhibiting the permanent formation of the alloy.[47] On the contrary, during the reduction of bare CuOZnO NPs, lacking of the oxygenated support, the development of reduced Zn at the Cu-ZnO interphase leading to Cu-Zn alloy formation is favored (Fig. 12, inset). Both, water and Cu-Zn alloy, are produced in continuous ongoing processes during the reduction step; therefore, they can be mutually balanced, since the formation of the alloy is considered a reversible phenomenon when it occurs only at the interphase.

4. Conclusions

CuZnO NPs supported on rGO aerogels are designed as efficient 3D catalysts, tested here in the CO_2 hydrogenation reaction in terms of methanol yield and selectivity. The composite aerogel CuZnO@rGO was synthesized by using a green method applying supercritical CO_2 for the nanostructuration and the fabrication of 3D devices with macro and mesoporosity, followed of H_2 reduction. The development of a highly selective catalyst is performed taking into account that the leading pathway to MeOH in CO_2 hydrogenation is determined by both the reaction conditions (ratio of active centers to gas molecules, flow rate and distribution), and the design (composition and architecture) of the applied catalyst. Under the most favorable conditions, MeOH selectivity values of near 100 % were preserved for the aerogel composite CuZnO@rGO up to temperatures as high as 260 ℃ at a pressure as low as 10 bar, while the MeOH selectivity of bare CuZnO NPs was of only 7 % under similar experimental conditions. Ahead of the highly hydrophobic character of rGO for water repulsion and its behavior as a reservoir for CO_2 adsorption, reasons related to the morpho-arrangement of the Cu^0 and ZnO NPs on the rGO surface explain the different catalytic behavior of the aerogel and the bare NPs. Results are rationalized on the basis, that the presence of the oxygenated GO support in the CuOZnO@GO precursor alleviated, with respect to net NPs, those negative effects of sintering and alloy formation during the necessary high temperature reduction step. This phenomenon highlights the benefits of the low temperature scCO$_2$ synthetic method that allows the formation of highly oxygenated precursors. The designed CuZnO@rGO catalysts are not yet optimized, but already show interesting MeOH activity and outstanding MeOH selectivity for low-pressure/high temperature catalytic processes. Lowering H_2 pressure has the advantage of safer operation. Importantly, the designed catalysts are superior to the existing products with respect to their ability to reduce the presence of CO to a minimum in favor of methanol production at high temperature, which can make the process economically viable.

References

1.   R. Lindsey, Climate Change: Atmospheric Carbon Dioxide. NOAA Climate.gov. Published **2020**.

2.   U.J. Etim, Y. Song, Z. Zhong, Improving the Cu/ZnO-Based Catalysts for Carbon Dioxide Hydrogenation to Methanol, and the Use of Methanol As a Renewable Energy Storage Media, *Front Earth Sci*. **2020**, *8*, 1-26.

3.   S. Saeidi, N.A.S Amin, M.R. Rahimpour, Hydrogenation of CO_2 to value-added products - A review and potential future developments, *J CO2 Util*. **2014**, *5*, 66-81.

4.   M.D. Porosoff, B. Yan, J.G. Chen, Catalytic reduction of CO_2 by H_2 for synthesis of CO, methanol and hydrocarbons: Challenges and opportunities, *Energy Environ. Sci*. **2016**, *9*, 62-73.

5.   Y. Sun, Z. Lin, S.H. Peng, V. Sage, Z. Sun, A Critical Perspective on CO_2 Conversions into Chemicals and Fuels, *J. Nanosci. Nanotechnol*. **2019**, *19*, 3097-3109.

6.   S. A. Mazari, N. Hossain, W.J. Basirun, N. M. Mubarak, R. Abro, N. Sabzoi, An overview of catalytic conversion of CO_2 into fuels and chemicals using metal organic frameworks, *Process Saf. Environ. Prot*. **2021**, *149*, 67-92.

7.   J. Sehested, Industrial and scientific directions of methanol catalyst development, *J. Catal*. **2019**, *371*, 368-375.

8.   J. Zhong, X. Yang, Z. Wu, B. Liang, Y. Huang, T. Zhang, State of the art and perspectives in heterogeneous catalysis of CO_2 hydrogenation to methanol, *Chem Soc Rev*. **2020**, *49*, 1385-1413.

9.   E. Samei, M. Taghizadeh, M. Bahmani, Enhancement of stability and activity of $Cu/ZnO/Al_2O_3$ catalysts by colloidal silica and metal oxides additives for methanol synthesis from a CO_2-rich feed, *Fuel Process Technol*. **2012**, *96*, 128-133.

10.   H. Ruland, H. Song, D. Laudenschleger, S. Stürmer, S. Schmidt, J. He, K. Kähler, M. Muhler, R. Schlögl, CO_2 Hydrogenation with $Cu/ZnO/Al_2O_3$: A Benchmark Study, *ChemCatChem*. **2020**, *12*, 3216-3222.

11. B. Liang, J. Ma, X. Su, C. Yang, H. Duan, H. Zhou, S. Deng, L. Li, Y. Huang, Investigation on Deactivation of Cu/ZnO/Al$_2$O$_3$ Catalyst for CO$_2$ Hydrogenation to Methanol, *Ind. Eng. Chem. Res*. **2019**, *58*, 9030-9037.

12. C.H. Bartholomew R.J. Farrauto, Fundamentals of industrial catalytic processes **2011**, 2nd ed., John Wiley and Sons Inc.

13. X. M. Liu, G.Q. Lu, Z. F. Yan, J. Beltramini, Recent Advances in Catalysts for Methanol Synthesis via Hydrogenation of CO and CO$_2$, *Ind. Eng. Chem. Res*. **2003**, *42*, 6518-6530.

14. C. J. Wu, S. L. Cheng, Y. J. Sheng, H. K. Tsao, Reduction-assisted sintering of micron-sized copper powders at low temperature by ethanol vapor, *RSC Adv*. **2015**, *5*, 53275-53279.

15. S. Natesakhawat, J. W. Lekse, J. P. Baltrus, P. R. Ohodnicki, B. H. Howard, X. Deng, C. Matranga, Active sites and structure-activity relationships of copper-based catalysts for carbon dioxide hydrogenation to methanol, *ACS Catal*. **2012**, *2*, 1667-1676.

16. D. Großmann, A. Dreier, C. Lehmann, W. Grünert, Methanol synthesis over Cu-ZnO aggregates supported on carbon nanotubes, *Appl. Cata.l A. Gen*. **2015**, *504*, 351-360.

17. E. T. Liakakou, E. Heracleous, K. S. Triantafyllidis, A. A. Lemonidou, K-promoted NiMo catalysts supported on activated carbon for the hydrogenation reaction of CO to higher alcohols: Effect of support and active metal, *Appl. Catal. B Environ*. **2015**, *165*, 296-305.

18. G. Wang, L. Chen, Y. Sun, J. Wu, M. Fu, D. Ye, Carbon dioxide hydrogenation to methanol over Cu/ZrO$_2$/CNTs: Effect of carbon surface chemistry, *RSC Adv*. **2015**, *5*, 45320-45330.

19. X. Dong, H. B. Zhang, G. D. Lin,Y. Z. Yuan, K. R. Tsai, Highly active CNT-promoted Cu–ZnO–Al$_2$O$_3$ catalyst for methanol synthesis from H$_2$/CO/CO$_2$, *Catal. Letters*. **2003**, *85*, 237-246.

20. X. L. Liang, J. R. Xie, Z. M. Liu, A Novel Pd-decorated Carbon Nanotubes-promoted Pd-ZnO Catalyst for CO$_2$ Hydrogenation to Methanol, *Catal Letters*. **2015**, *145*, 1138-1147.

21. X. L. Liang, X. Dong, G. D. Lin, H. B. Zhang, Carbon nanotube-supported Pd-ZnO catalyst for hydrogenation of CO$_2$ to methanol, *Appl. Catal. B Environ*. **2009**, *88*, 315-322.

22. T. Witoon, T. Numpilai, T. Phongamwong, W. Donphai, C. Boonyuen, C. Warakulwit, M. Chareonpanich, J. Limtrakul, Enhanced activity, selectivity and stability of a CuO-ZnO-ZrO$_2$ catalyst by adding graphene oxide for CO$_2$ hydrogenation to methanol, *Chem. Eng. J*. **2018**, *334*, 1781-1791.

23. Y. J. Fan, S. F. Wu, A graphene-supported copper-based catalyst for the hydrogenation of carbon dioxide to form methanol, *J. CO2 Util*. **2016**, *16*, 150-156.

24. V. Deerattrakul, P. Dittanet, M. Sawangphruk, P. Kongkachuichay, CO$_2$ hydrogenation to methanol using Cu-Zn catalyst supported on reduced graphene oxide nanosheets, *J. CO2 Util*. **2016**, *16*, 104-113.

25. M. Zabilskiy, V. L. Sushkevich, M. A. Newton, J. A. Van Bokhoven, Copper-Zinc Alloy-Free Synthesis of Methanol from Carbon Dioxide over Cu/ZnO/Faujasite, *ACS Catal*. **2020**, *10*, 14240-14244.

26. V. Deerattrakul, P. Puengampholsrisook, W. Limphirat, P. Kongkachuichay, Characterization of supported Cu-Zn/graphene aerogel catalyst for direct CO$_2$ hydrogenation to methanol: Effect of hydrothermal temperature on graphene aerogel synthesis, *Catal. Today*, **2018**, *314*, 154-163.

27. F. Xiaobin, Graphene: a promising two-dimensional support for heterogeneous catalysts, *Front. Mater*. **2015**, *1*, 39.

28. V. Deerattrakul, N. Yigit, G. Rupprechter, P. Kongkachuichay, The roles of nitrogen species on graphene aerogel supported Cu-Zn as efficient catalysts for CO_2 hydrogenation to methanol. *Appl. Catal. A Gen*. **2019**, *580*, 46-52.

29. A. Borrás, G. Gonçalves, G. Marbán, S. Sandoval, S. Pinto, P.A.A.P. Marques, Preparation and Characterization of Graphene Oxide Aerogels: Exploring the Limits of Supercritical CO_2 Fabrication Methods, *Chem - A Eur J*. **2018**, *24*, 15903-15911.

30. A. Borrás, J. Fraile, A. Rosado, G. Marbán, G. Tobias, A.M. López-Periago, C. Domingo, Green and Solvent-Free Supercritical CO 2 -Assisted Production of Superparamagnetic Graphene Oxide Aerogels: Application as a Superior Contrast Agent in MRI, *ACS Sustain Chem Eng*. **2020**, *8*, 4877-4888.

31. P. Luo, Y. Lin, Further thermal reduction of reduced graphene oxide aerogel with excellent rate performance for supercapacitors, *Appl. Sci*. **2019**, *9*, 2188.

32. C. Li, X. Yuan, K. Fujimoto, Development of highly stable catalyst for methanol synthesis from carbon dioxide, *Appl. Catal. A Gen*. **2014**, *469*, 306-311.

33. A. Borrás, A. Rosado, J. Fraile, A. M. López-Periago, J. G. Planas, Y. Amirali, C. Domingo, Meso/microprorous MOF@graphene oxide composite aerogels prepared by generic supercritical CO2 technology, *Microporous Mesoporous Mater*. **2022**, *335,* 111825.

34. G. Nassar, E. Daou, R. Najjar, M. Bassil, R. Habchi, A review on the current research on graphene-based aerogels and their applications, *Carbon Trends*. **2021**, *4*, 100065.

35. N. Kostoglou, V. Tzitzios, A.G. Kontos, K. Giannakopoulos, C. Tampaxis, A. Papavasiliou, G. Charalambopoulou, T. Steriotis, Y. Li, K. Liao, K. Polychronopoulou, C. Mitterer, C. Rebholz, Synthesis of nanoporous graphene oxide adsorbents by freeze-drying or microwave radiation: Characterization and hydrogen storage properties, *Int. J. Hydrogen Energy*. **2015**, *40*, 6844-6852.

36. A. K. Geim, K. S. Novoselov, The rise of graphene progress, *Nat. Mater*. **2007**, *6*, 183-191.

37. A. R. Kumarasinghe, L. Samaranayake, F. Bondino, E. Magnano, N. Kottegoda, E. Carlino, U. N. Ratnayake, A. A. P. de Alwis, V. Karunnaratne, G. A. J. Amaratunga, Self-assembled multilayer graphene oxide membrane and carbon nanotubes synthesized using a rare form of natural graphite, *J. Phys. Chem. C*. **2013**, *117*, 9507-9519.

38. C. Sarkar, S. K. Dolui, Synthesis of copper oxide/reduced graphene oxide nanocomposite and its enhanced catalytic activity towards reduction of 4-nitrophenol, *RSC Adv*. **2015**, *5*, 60763-60769.

39. S. Sagadevan, Z. Z. Chowdhury, M. R. B. Johan, F. A. Aziz, E. M. Salleh, A. Hawa, R. F. Rafique, A one-step facile route synthesis of copper oxide/reduced graphene oxide nanocomposite for supercapacitor applications, *J. Exp. Nanosci*. **2018**, *13*, 284-295.

40. H. Saleem, M. Haneef, H. Y. Abbasi, Synthesis route of reduced graphene oxide via thermal reduction of chemically exfoliated graphene oxide, *Mater. Chem. Phys*. **2018**, *204*, 1-7.

41. K.Klier, Methanol Synthesis, *Adv Catal*. **1982**, *31*, 243-313.

42. S. Kattel, P. J. Ramírez, J. G. Chen, J. A. Rodriguez, P. Liu, Response to Comment on "Active sites for CO_2 hydrogenation to methanol on Cu/ZnO catalysts.", *Science* **2017**, *357*, 4-6.

43. S. Kuld, M. Thorhauge, H. Falsig, C. F. Elkjaer, S. Helveg, I.B. Chorkedorff, J. Sehested, Quantifying the promotion of Cu catalysts by ZnO for methanol synthesis, *Science* **2016**, *352*, 969-974.

44. T. Fujitani, J. Nakamura, The chemical modification seen in the Cu/ZnO methanol synthesis catalysts, *Appl. Catal. A Gen*. **2000**, *191*, 111-129.

45. T. Fujitani, J. Nakamura, The effect of ZnO in methanol synthesis catalysts on Cu dispersion and the specific activity, *Catal. Letters*. **1998**, *56*, 119-124.

46. F. Zhang, X. Xu, Z. Qiu, B. Feng, Y. Liu, A. Xing, M. Fan, Improved methanol synthesis performance of Cu/ZnO/Al$_2$O$_3$ catalyst by controlling its precursor structure, *Green Energy Environ*. **2022**, *7*, 772-781.

47. E. Frei, A. Gaur, H. Lichtenberg, L. Zwiener, M. Scherzer, F. Girgsdies, T. Lunkenbein, R. Schlögl, Cu−Zn Alloy Formation as Unfavored State for Efficient Methanol Catalysts, *ChemCatChem* **2020**, *12*, 4029-4033.

48. M. Rabiei, A. Palevicius, A. Monshi, S. Nasiri, A. Vilkauskas, G. Janusas, Comparing methods for calculating nano crystal size of natural hydroxyapatite using X-ray diffraction, *Nanomaterials* **2020**, *10*, 1-21.

49. H. Duan, Y. Li, X. Lv, D. Chen, M. Long, L. Wen, CuO-ZnO anchored on APS modified activated carbon as an enhanced catalyst for methanol synthesis-The role of ZnO. *J. Mater. Res*. **2018**, *33*, 1625-1631.

50. H. Zhao, M. Lin, K. Fang, J. Zhou, Y. Sun, Preparation and evaluation of Cu-Mn/Ca-Zr catalyst for methyl formate synthesis from syngas, *Appl. Catal. A Gen*. **2016**, *514,* 276-283.

51. A. Wöllner, F. Lange, H. Schmelz, H. Knözinger, Characterization of mixed copper-manganese oxides supported on titania catalysts for selective oxidation of ammonia, *Appl. Catal. A Gen*. **1993**, *94*, 181-203.

52. R. Ma, F. Yang, S. Li, X. Zhang, S. Cheng, Z. Liu, Fabrication of Cu$_2$ZnSn(S,Se)$_4$ (CZTSSe) absorber films based on solid-phase synthesis and blade coating processes, *Appl. Surf. Sci*. **2016**, *368*. 8-15.

53. T. T. Vu, T. Valdés-Solís, G. Marbán, Novel high surface area stainless steel wire mesh supported Ni0.7Zn0.3O solid solution prepared by room temperature sacrificial template accelerated hydrolysis. Application in the production of hydrogen from methanol, *Appl. Catal. B Environ*. **2014**, *160–161*, 57-66.

54. M. Ahmad, E. Ahmed, Z. L. Hong, W. Ahmed, A. Elhissi, N. R. Khalid, Photocatalytic, sonocatalytic and sonophotocatalytic degradation of Rhodamine B using ZnO/CNTs composites photocatalysts, *Ultrason. Sonochem*. **2014**, *21*, 761-773.

55. S. Karamat, R. S. Rawat, T. L. Tan, P. Lee, S. V. Springham, A. Rehman, R.Chen, H.D. Sun, Exciting dilute magnetic semiconductor: Copper-doped ZnO, *J. Supercond. Nov. Magn*. **2013**, *26*, 187-195.

56. M. A. Gomez-Alvarez, C. Morales, J. Méndez, A. del Campo, F. J. Urbanos, A. Díaz, L. Reséndiz, J. I. Flege, D. Granados, L. Soriano, A Comparative Study of the ZnO Growth on Graphene and Graphene Oxide: The Role of the Initial Oxidation State of Carbon, *C.* **2020**, *6*, 41.

57. D. Gamarra, A. Hornés, Z. Koppány, Z. Schay, G. Munuera, J. Soria, A. Martínez-Arias, Catalytic processes during preferential oxidation of CO in H_2-rich streams over catalysts based on copper-ceria, *J. Power Sources*. **2007**, *169,* 110-116.

58. J. Agrell, M. Boutonnet, I. Meli n-Cabrera, J. L. G. Fierro, Production of hydrogen from methanol over binary Cu/ZnO catalysts Part I. Catalyst preparation and characterisation, *Appl. Catal. A Gen*. **2003**, *253*, 201-211.

59. M. C. Biesinger, Advanced analysis of copper X-ray photoelectron spectra, *Surf. Interface Anal*. **2017**, *49*, 1325-1334.

60. D. A. Bulushev, A. L. Chuvilin, V. I. Sobolev, S. G. Stolyarova, Y. V. Shubin, I. P Asanov, A. V. Ishchenki, G. Magnani, M. Riccó, A. V. Okoturb, L.G. Bulusheva, Copper on carbon materials: Stabilization by nitrogen doping, *J. Mater. Chem. A*. **2017**, *5*, 10574-10583.

61. S. Lai, D. Men, W. Zhan, Y. Guo, Y. Guo, Z. Zhang, G. Lu, The promotional role of Ce in Cu/ZSM-5 and in situ surface reaction for selective catalytic reduction of NO_x with NH_3, *RSC Adv*. **2015**, *5*, 90235-90244.

62. K. S. Lin, C. Y. Pan, S. Chowdhury, M. T. Tu, W. T. Hong, C. T. Yeh, Hydrogen generation using a CuO/ZnO-ZrO_2 nanocatalyst for autothermal reforming of methanol in a microchannel reactor, *Molecules* **2011**, *16,* 348-366.

63. G. Marbán, I. López, T. Valdés-Solís, Preferential oxidation of CO by CuO_x/CeO_2 nanocatalysts prepared by SACOP. Mechanisms of deactivation under the reactant stream, *Appl. Catal. A Gen*. **2009**, *361*, 160-169.

64. J. W. Evans, M. S. Wainwright, A. J. Bridgewater, D. J. Young, On the determination of copper surface area by reaction with nitrous oxide, *Appl. Catal*. **1983**, *7*, 75-83.

65. E. A. Araújo, F. X. Nobre, G. D. S. Sousa, L. S. Cavalcante, M. R. de Morais Chaves Santos, F. L. Souza, J. M. E. de Matos, Synthesis, growth mechanism, optical properties and catalytic activity of ZnO microcrystals obtained via hydrothermal processing, *RSC Adv*. **2017**, *7,* 24263-24281.

66. A. Öchsner, A. Shokuhfar, New Frontiers of Nanoparticles and Nanocomposite Materials - Novel Principles and Techniques. **2013**.

67. H. Ren, C. H. Xu, H. Y. Zhao, Y. X. Wang, J. Liu, J. Y. Liu, Methanol synthesis from CO_2 hydrogenation over Cu/γ-Al_2O_3 catalysts modified by ZnO, ZrO_2 and MgO, *J. Ind. Eng. Chem*. **2015**, *28*, 261-267.

68. X. Guo, D. Mao, G. Lu, S. Wang, G. Wu, Glycine-nitrate combustion synthesis of CuO-ZnO-ZrO_2 catalysts for methanol synthesis from CO_2 hydrogenation, *J. Catal*. **2010**, *271*, 178-185.

69. G.Bonura, M. Cordaro, C. Cannilla, F. Arena, F. Frusteri, The changing nature of the active site of Cu-Zn-Zr catalysts for the CO_2 hydrogenation reaction to methanol, *Appl. Catal. B Environ*. **2014**, *152-153*, 152-161.

70. H. Jeong, C. H. Cho, T. H. Kim, Effect of Zr and pH in the preparation of Cu/ZnO catalysts for the methanol synthesis by CO_2 hydrogenation, *React. Kinet. Mech. Catal*. **2012**, *106*, 435-443.

71. A. Carrasco, J. Moral-Vico, A. A. Markeb, Conversion of Carbon Dioxide into Methanol Using Cu – Zn Nanostructured Materials as Catalysts, *Nanomaterials* **2022,** *12*, 999.

72.   J. Toyir, P. R. De la Piscina, J. L. G. Fierro, N. Homs, Catalytic performance for CO_2 conversion to methanol of gallium-promoted copper-based catalysts: Influence of metallic precursors, *Appl. Catal. B Environ*. **2001**, *34*, 255-266.

73.   J. Toyir, P. R. De La Piscina, J. L. G. Fierro, N. Homs, Highly effective conversion of CO_2 to methanol over supported and promoted copper-based catalysts: Influence of support and promoter, *Appl. Catal. B Environ*. **2001**, *29*, 207-215.

74.   S. Gesmanee, W. Koo-Amornpattana, Catalytic hydrogenation of CO_2 for methanol production in fixed-bed reactor using Cu-Zn supported on gamma-Al_2O_3, *Energy Procedia*. **2017**, *138*, 739-744.

75.   H. Lei, R. Nie, G. Wu, Z. Hou, Hydrogenation of CO_2 to CH_3OH over Cu/ZnO catalysts with different ZnO morphology, *Fuel*. **2015**, *154,* 161-166.

76.   A. Karelovic, P. Ruiz, The role of copper particle size in low pressure methanol synthesis via CO_2 hydrogenation over Cu/ZnO catalysts. *Catal Sci Technol*, *Catal. Sci. Technol*. **2015**, *5*, 869-881.

77.   Q. Sun, Y. L. Zhang, H.Y. Chen, J. F. Deng, D. Wu, S. Y. Chen, A Novel Process for the Preparation of Cu/ZnO and Cu/ZnO/Al_2O_3 Ultrafine Catalyst: Structure, Surface Properties, and Activity for Methanol Synthesis from CO_2+H_2, *J. Catal*. **1997**, *167,* 92-105.

78.   F. Arena, G. Italiano, K. Barbera, S. Bordiga, G. Bonura, L. Spadaro, F. Frusteri, Solid-state interactions, adsorption sites and functionality of Cu-ZnO/ZrO_2 catalysts in the CO_2 hydrogenation to CH_3OH, *Appl .Catal. A Gen*. **2008**, *350*, 16-23.

79.   T. Lunkenbein, J. Schumann, M. Behrens, R. Schlögl, M.G. Willinger, Formation of a ZnO Overlayer in Industrial Cu/ZnO/Al_2O_3 Catalysts Induced by Strong Metal-Support Interactions, *Angew. Chemie - Int Ed*. **2015**, *54*, 4544-4548.

80.   M. M. J. Li, S. C. E. Tsang, Bimetallic catalysts for green methanol production via CO_2 and renewable hydrogen: A mini-review and prospects, *Catal. Sci. Technol*. **2018**, *8*, 3450-3464.

81.   F. Studt, I. Sharafutdinov, F. Abild-Pedersen, C. F. Elkjaer, J. S. Hummelshoj, S. Dahl, I. Chorkendorff, J. K. Norskov, Discovery of a Ni-Ga catalyst for carbon dioxide reduction to methanol, *Nat. Chem*. **2014**, *6,* 320-324.

82.   C. K. Ho, S. Webb, Gas Transport in Porous Media, **2006**.

83.   R. Mutschler, E. Moioli, W. Luo, N. Gallandat, A. Züttel, CO_2 hydrogenation reaction over pristine Fe, Co, Ni, Cu and Al_2O_3 supported Ru: Comparison and determination of the activation energies, *J. Catal*. **2018,** *366*, 139-149.

84.   S. Kattel, P. Liu, J. G. Chen, Tuning Selectivity of CO_2 Hydrogenation Reactions at the Metal/Oxide Interface, *J. Am. Chem. Soc*. **2017**, *139,* 9739-9754.

85.   S. G. Jadhav, P. D. Vaidya, B. M. Bhanage, J. B. Joshi, Catalytic carbon dioxide hydrogenation to methanol: A review of recent studies, *Chem. Eng. Res. Des*. **2014**, *92*, 2557-2567.

86.   A. Goeppert, M. Czaun, J. P. Jones, G. K. Surya Prakash, G. A. Olah, Recycling of carbon dioxide to methanol and derived products-closing the loop, *Chem. Soc .Rev*. **2014**, *43*, 7995-8048.

87.   F. Dalena, A. Senatore, M. Basile, S. Knani, A. Basile, A. Iulianelli, Advances in methanol production and utilization, with particular emphasis toward hydrogen generation via membrane reactor technology, *Membranes*. **2018**, *8*, 98.

88.   M. Behrens, F. Studt, I. Kasatkin, S. Kühl, M. Hävecker, F. Abild-Pedersen, S. Zander, F. Girgsdies, P. Kurr, B. Kniep, M. Tovar, R. W. Fischer, J. K. Norskov, R. Schlögl, The active site of methanol synthesis over Cu/ZnO/Al$_2$O$_3$ industrial catalysts, *Science (80-)* **2012,** *336,* 893-897.

89.   M. M. Günter, T. Ressler, B. Bems, C. Büscher, T. Genger, O. Hinrichsen, M. Muhler, R. Schlögl, Implication of the microstructure of binary Cu/ZnO catalysts for their catalytic activity in methanol synthesis, *Catal. Letters*. **2001**, *71*, 37-44.

90.   H. Ahouari, A. Soualah, A. Le Valant, L. Pinard, P. Magnoux, Y. Pouilloux, Methanol synthesis from CO$_2$ hydrogenation over copper based catalysts, *React. Kinet. Mech. Catal*. **2013**, *110,* 131-145.

Photocatalytic hydrogen production using porous 3D graphene-based aerogels supporting Pt/TiO₂ nanoparticles
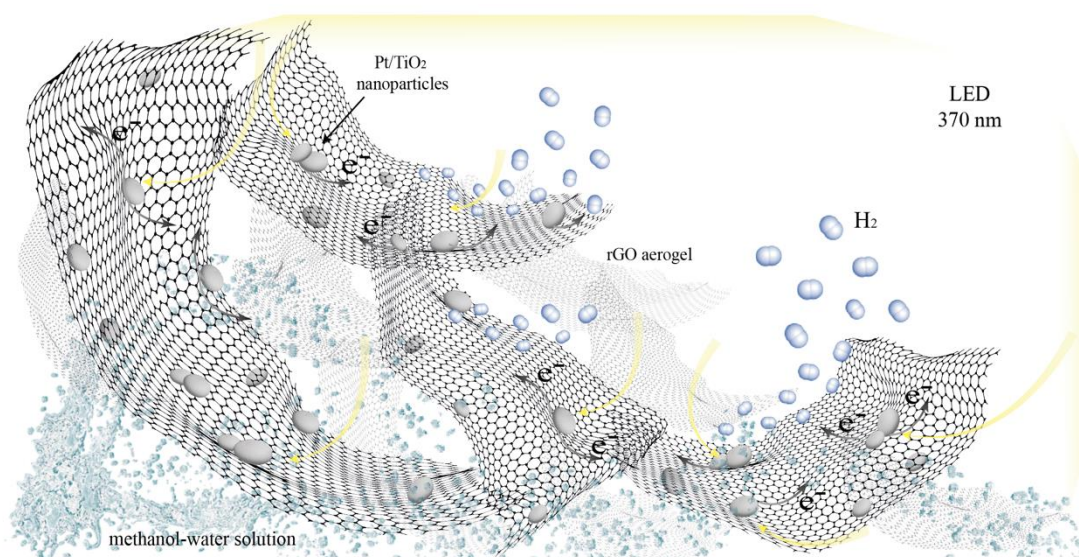
Graphene oxide aerogel supported Pt/TiO₂ catalyst was synthesized in this work for photocatalytic hydrogen production from aqueous methanol solution. A comprehensive evaluation of the synthesized photocatalyst was carried out with a focus on the target application.

Abstract

Composites involving reduced graphene oxide (rGO) aerogels supporting Pt/TiO_2 nanoparticles were fabricated using a one-pot supercritical CO_2 gelling and drying method, followed by mild reduction under a N_2 atmosphere. Electron microscopy images and N_2 adsorption/desorption isotherms indicate the formation of 3D monolithic aerogels with a meso/macroporous morphology. A comprehensive evaluation of the synthesized photocatalyst was carried out with a focus on the target application: the photocatalytic production of H_2 from methanol in aqueous media. The reaction conditions (water/methanol ratio, catalyst concentration), together with the aerogel composition ($Pt/TiO_2/rGO$ ratio) and architecture (size of the aerogel pieces), were the factors that varied in optimizing the process. These experimental parameters influenced the diffusion of the reactants/products inside the aerogel, the permeability of the porous structure, and the light-harvesting properties, all determined in this study towards maximizing H_2 production. Using methanol as the sacrificial agent, the measured H_2 production rate for the optimized system ($18800 \ \mu mol H_2 \, h^{-1} \, g_{NPs}^{-1}$) was remarkably higher than the values found in the literature for similar $Pt/TiO_2/rGO$ catalysts and reaction media ($2000–10000 \ \mu mol H_2 \, h^{-1} \, g_{NPs}^{-1}$).

1. Introduction

Hydrogen (H_2) is one of the most promising carbon-neutral alternatives as a renewable energy source, mainly due to its high calorific value and attainable purity.[1] Large-scale H_2 production *via* photocatalytic water splitting is a simple and cheap method, although the low reached conversion values (*ca.* 1%) cause the procedure to still be in-efficient and economically unviable.[2] Consequently, the study of new catalytic systems that enhance the conversion is important to improve the efficiency and sustainability of the process.[3] Heterogeneous photocatalysis, working *via* water splitting or by the photoreforming of organic waste, is an attractive solution for H_2 production, since the utilization of solar energy moderates urgent environmental and energy issues.[4]

In the photocatalytic H_2 production process, a light beam with sufficient energy irradiates a semiconductor material. The thus attained excited electrons (e^-) and holes (h^+) migrate onto the surface of the catalyst and act as reducing and oxidizing agents, respectively. Hence, the reduction and oxidation potentials of the reactant (*e.g.*, water, alcohol, glycerol) must be within the band gap of the photocatalyst.[5] Semiconductors, such as titanium dioxide (TiO_2), cadmium sulfide (CdS), and carbon nitride (C_3N_4), fulfill this condition and are often used as photocatalytic systems.[6-8] TiO_2 is traditionally one of the most utilized semiconductors owing to its highly negative conduction band potential, and thus strong reduction ability. This oxide is chemically stable, cheap, and abundant. However, its use also experienced some drawbacks. First, due to its wide band gap, UV light is necessary for activation, and this light is present in a percentage lower than 5% in sunlight.[9] Second, TiO_2 experienced an extremely rapid recombination rate of the photogenerated h^+ and e^-, in the order of $10^{-12} - 10^{-11}$ s, while a value in the interval of $10^{-9} - 10^{-7}$ s is required for capturing the generated species in a successful redox reaction.[7] To improve the photocatalytic efficiency, the semiconductor must be combined with agents that can scavenge the photogenerated e^-, *e.g.*, Pt.[1,10] It is worth mentioning that Pt has been recently included in the list of "critical raw materials -with economic importance, but high supply risk" by the European Commission.[11] The target objective must be to decrease our dependence on these critical raw materials by minimizing their percentage of use in the designed product.[12]

A newly designed and feasible strategy to moderate the detrimental effects of the large band gap and high e^-/h^+ recombination rate of TiO_2 is to incorporate graphene into the catalyst.[13] Undoubtedly, 2D graphene sheets are becoming a top choice as catalyst compartment/supports due to their unique physicochemical properties, related to their large surface area, high thermal

and electrical conductivity, and ability to tailor the band gap energy level of the semiconductor.[14-16] Furthermore, due to its high work function, e^- from the conduction band of the semiconductor can be accepted and transferred by the graphene.[17] In parallel, the 2D sheets ensure an appropriate surface for extensively anchoring the semiconductor in the form of nanoparticles (NPs), which can be deposited on both sides of exfoliated graphene flakes, displaying the end composite with a high concentration of active sites for the catalytic reaction.[18,19] The main drawback of using this support is the large tendency of 2D graphene flakes to aggregate, which results in the poor accessibility of the reagents and the light to the catalytically active NPs trapped between the flakes, e^- transport hindering, and the poor diffusion of the gaseous product.[7,20,21] The penetration depth of the UV light in TiO_2 is limited to *ca.* 100 nm; thus, the formation of large aggregates of NPs would result in an increased amount of semiconductors not affected by the radiation.[22] Several works can be found in the literature using composites of $(Pt)TiO_2$ NPs and reduced graphene oxide (rGO).[22-28] These systems are composed of either multiple stacked layers of rGO covered with NPs agglomerates[26,27] or photoactive NPs covered with an rGO layer.[28] In other works, the aggregation of the Pt/TiO_2 NPs has been directed to build 3D porous composites with rGO added as an additive.[29,30]

In this study, a different approach is presented to build a 3D structure, in which an rGO aerogel matrix provides support for the photoactive NPs: $Pt/TiO_2@rGO$. The precursor is a 3D aerogel structure of graphene oxide (GO): $Pt/TiO_2@GO$. GO is a highly oxygenated precursor, with mainly hydroxyl, epoxy, and carboxylic functionalities, easily exfoliated in polar liquids, and capable of establishing strong metal–support interactions to ensure NPs dispersion and to avoid NPs leaching during catalytic reaction.[31-33] As with other common aerogels,[34,35] those of GO have a low-density network with a meso/macroporous structure. The $Pt/TiO_2@GO$ intermediate composite was synthesized in the form of a monolith using a previously described one-pot supercritical CO_2 (scCO_2) methodology.[36] After aerogel synthesis, the number of oxygenated groups on the support can be modulated by thermal treatment to prepare the desired $Pt/TiO_2@rGO$ end product.[37] The macroscopic size and variable shape of the synthesized 3D aerogel macrostructures bring advantages of operability and recoverability. The obtained aerogel composites were structural and texturally characterized. Moreover, the new catalytic system was evaluated for its photocatalytic H_2 production in aqueous methanol solutions. The process was adjusted for effective H_2 production regarding the reaction conditions (catalyst concentration, composition of reaction mixture), catalyst composition ($Pt:TiO_2:rGO$ ratios), and architecture (one-piece monolith or smashed aerogel). Optimizing the $Pt/TiO_2@rGO$ composite

leads to H_2 production rates in an aqueous methanol solution of *ca.* 2–10 times higher than the values reported for similar systems in the literature.[25,29]

2. Materials and methods

2.1. Materials

For the preparation of the Pt/TiO_2 NPs, chloroplatinic acid hexahydrate ($H_2PtCl_6.6H_2O$) and TiO_2 NPs (AEROXIDE P25, *ca.* 20 nm), provided by Alfa Aesar and Evonik, respectively, were used. For the aerogel preparation, a GO water dispersion of 4 mgmL^{-1}, supplied by Graphenea Inc. (Spain), was employed. Ethanol and methanol were purchased from Carlo Erba. Liquid CO_2 (99.95 wt%), N_2 and H_2 gasses were delivered by Carburos Metálicos S.A.

2.2. Synthetic methods

2.2.1. Preparation of NPs of xPt/TiO₂ composite

NPs of Pt/TiO_2 with different Pt contents were prepared following a reported incipient impregnation deposition and followed by reduction methodology.[38] Briefly, a weighted amount of $H_2PtCl_6.6H_2O$, *e.g.*, 2.7, 13, or 26 mg, was dissolved in 2.5 mL of ultrapure water and used to obtain Pt/TiO_2 composites with 0.1, 0.5, and 1.0 wt% Pt contents, respectively. Each Pt solution was added dropwise to 1 g of TiO_2 NPs at a rate of 8.33 μL min^{-1}, achieved by using a peristaltic pump, while the resulting slurry was continuously sonicated. After that, the deposited suspension was kept under sonication for 2 h. The dense dispersion was dried at 100 °C overnight in an air oven. The recovered powder was treated at 200 °C in a tubular oven, increasing the temperature with a heating ramp of 10 °C min^{-1}, first under N_2 for 1 h and then reduced under a H_2 flow of 50 mL min^{-1} for 3 h. A grey powder was obtained and named as xPt/TiO_2, where x indicates the added Pt weight content in percentage.

2.2.2. Preparation of xPt/TiO₂@rGO composite aerogels

For the composite aerogels, a suspension of GO in ethanol with an adjusted con-centration of 3.5 mg mL^{-1} was first prepared from water dispersion following a reported protocol.[36] Weighted amounts of bare TiO_2 and composed xPt/TiO_2 NPs were dispersed by sonication in aliquots of 1 mL of the GO-ethanol suspension to obtain weight ratios of 2:1 and 6:1 for NPs:GO. The suspensions were added to assay tubes of *ca.* 1 cm diameter and 2 mL volume and placed in a 200 mL high-pressure reactor (TharProcess). The aerogels were prepared by drying the suspensions with scCO$_2$ in the batch mode, keeping the autoclave at 200 bar and 45

°C for 48 h (Figure 1).[36] Finally, the CO_2 was slowly released from the reactor under isothermal conditions. The $xPt/TiO_2@GO$ samples were recovered as one-piece cylindrical monoliths. The reduction of the recovered 3D GO aerogels to rGO was carried out in a tubular oven at 300 °C under N_2 flow. To reach the target temperature, a heating ramp of 5 °C min^{-1} was used, upholding the temperature for 20 min after reaching 100 and 200 °C, and then maintaining it for 2 h at 300 °C. The reduced $xPt/TiO_2@rGO$ aerogels were also recovered as one-piece monoliths and used either as-synthesized or smashed into small pieces.
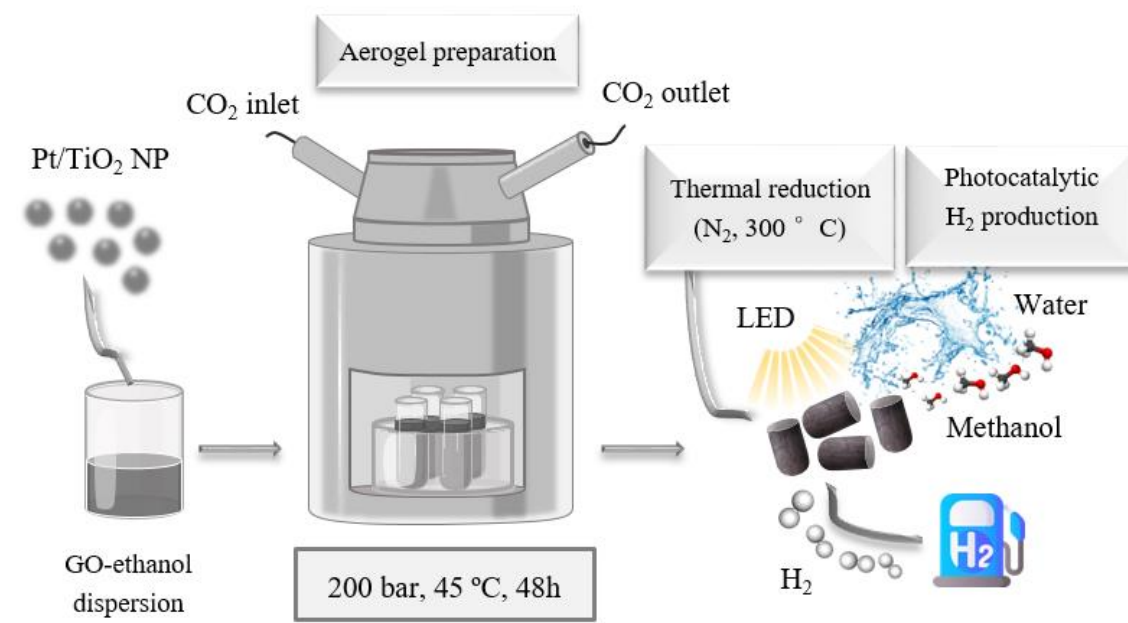

Figure 1. Scheme of the scCO2-assisted synthesis for $Pt/TiO_2@rGO$ aerogels.

2.3. Characterization

The platinum content in the $xPt/TiO_2@rGO$ aerogels was quantified by inductively coupled plasma mass spectrometry (ICP-MS, Agilent 7700x) after digesting the samples in hydrochloric, nitric, and hydrofluoric acids (3:1:0.5 v/v). The structural characterization of the prepared NPs and the reduced composite aerogels was performed by powder X-ray diffraction (PXRD) in a Siemens D5000, using the Cu Kα incident radiation with a step scan of 0.02° in the 2θ 5–40° range. The size of the NPs was estimated using PXRD data and the Scherrer equation. Surface functional groups were studied by Fourier transform infrared (FTIR) spectroscopy (Jasco 4700 Spectrophotometer), after the dispersion of the samples in potassium bromide (KBr). Raman spectra were recorded to ascertain the reduction in GO by using an excitation wavelength of 532 nm. The morphology of the composite aerogels and the size of

the NPs, as well as their degree of dispersion on the rGO platelets, were investigated by scanning (SEM, Quanta FEI 200) and transmission (TEM, JEOL 1210) electron microscopies. The BET (Brunauer, Emmet, Teller) surface area (S_a), the BJH (Barrett, Joyner, and Halenda), and cumulative adsorption pore volume (V_p) were determined by collecting N_2 adsorption/desorption isotherms at 77 K (ASAP 2020, Micromeritics Inc., US), after degassing the samples at 393 K for 20 h. For the smashed aerogels, dynamic light scattering (DLS Coulter LS230) was used to study the hydro-dynamic size of the aerogel broken pieces dispersed in methanol/water (0.5 v/v). The wettability of the reduced and non-reduced composites was investigated by water contact angle measurement (Biolin Sci. Attension Theta Lite) after preparing a compressed pellet with the monoliths. The optical properties of the aerogels were investigated by UV-vis diffuse reflectance (Jasco V-560) and photoluminescence (Jasco FP-8300) spectroscopies using the smashed solid samples. For the UV experiments, barium sulfate ($BaSO_4$) powder was used as blank.

2.4. Photocatalytic H_2 production

The photocatalytic activity of the synthesized composite aerogels for H_2 production was tested by immersing the reduced monoliths, either as recovered in one piece or ultrasonically smashed, in an aqueous methanol solution. For the one-piece samples, a specifically designed basket composed of polylactic acid (PLA) polymer was fabricated with 3D printing to hold four monoliths and prevent them from floating during the reaction. The basket was settled inside a cylindrical glass reactor of 20 mL that was filled with 14 mL of a methanol/water mixture (Figure 2).
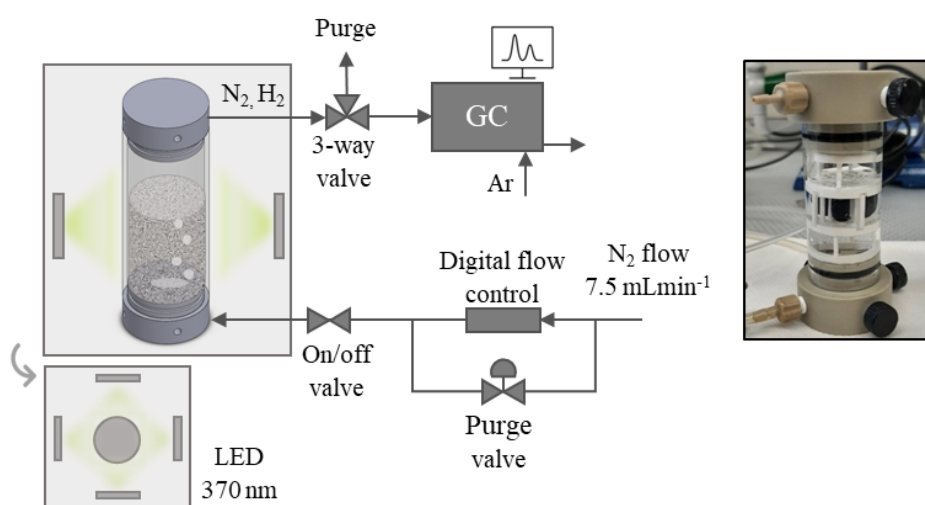

Figure 2. Scheme of the catalyst reactor setup and picture of the vessel involving the hand-made support holding the one-piece aerogel monolith.

For the tests with the smashed aerogels, four monoliths were added to the methanol/water solution, gentile sonicated for 5 min in an ultrasonic bath, and poured into the 20 mL reactor vessel without the basket but under mechanical stirring (100 rpm). The methanol percentage in the methanol/water mixture was varied from 0.01 to 1 v/v. Different aerogel catalyst concentrations, from 0.04–2.67 $g_{aerogel}$ L^{-1} (equivalent to 0.03 to 2 $g_{NPs}L^{-1}$) were also tested. Before starting the catalytic reaction, the system was purged with N_2, and a stream of this inert gas was continued at a rate of 7.5 mL min^{-1} during the entire experiment. The reaction mixture was irradiated with a four visible-LED system placed at a 4 cm distance from the cylindrical reactor wall. The emission spectrum is shown in Figure 3. The average nominal irradiance of each LED was 45.0 mW cm^{-2}, determined by using a UV–vis spectroradiometer (OceanOptics USB2000+). The H_2 production rate was analyzed online every 10 min in the headspace of the reactor by using a gas chromatograph (Inficon 3000 MicroGC). The results are expressed referring to either the rate of H_2 production [$\mu molH_2$ h^{-1}] or the rate per mass of the NPs [$\mu molH_2$ h^{-1} g_{NPs}^{-1}]. Steady-state H_2 production data recorded after 60 min were calculated for all the analyses performed with the smashed monoliths.
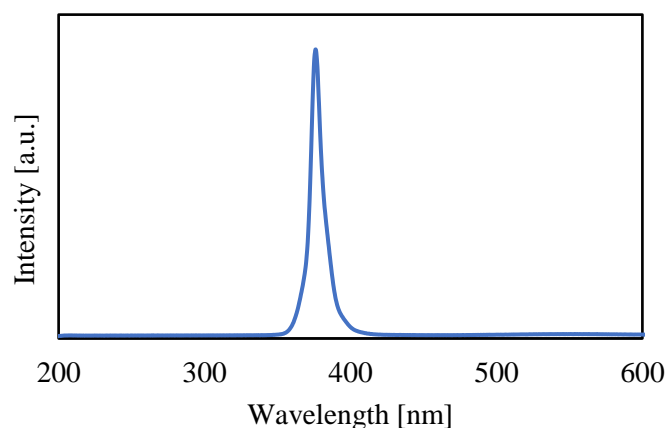
Figure 3. Emission spectrum of the used light source.

3. Results and discussion

3.1. Aerogel synthesis

The xPt/TiO$_2$@rGO composite aerogels were synthesized through the intermediate xPt/TiO$_2$@GO aerogel (Figure 1), involving a non-reduced GO matrix containing a high amount of oxygenated functional groups, mainly hydroxyl, epoxy, and carboxylic, which are located on the basal plane and at the edges of the 2D platelets. The oxygenated functionalities facilitate the dispersion and exfoliation of GO in aqueous and polar solutions *via* simple

sonication. Moreover, preserving the oxygenated functional groups in GO during scCO$_2$ aerogel synthesis was essential to ensure the presence of many anchoring points on the substrate for the NPs, which guarantees the establishment of strong interactions with a net or composed hydrophilic TiO$_2$ involving hydroxyl groups on the surface.[32,39,40] Three different compositions for the NPs in the intermediate were tested, namely, 1Pt/TiO$_2$@GO, 0.5Pt/TiO$_2$@GO, and 0.1Pt/TiO$_2$@GO, corresponding to an initially mixed amount of Pt with the TiO$_2$ NPs of 1, 0.5 and 0.1 wt%, respectively. To activate the aerogel for the catalytic process, the xPt/TiO$_2$@GO intermediate samples were exposed to a temperature of 300 °C in a N$_2$ atmosphere. This treatment eliminates most of the oxygenated groups in GO. The reduction step is crucial to further achieve an efficient photocatalytic reaction, since important graphene-like characteristics, such as high e$^-$ mobility, are partially restored by removing some of the oxygenated groups. Hence, the rGO matrix can act as an efficient sink, where the photogenerated e$^-$ are stored and transferred.[13,41] During reduction, *ca.* 30 wt% is eliminated from the sample, corresponding mostly to oxygenated functionalities. Taking this into account, the estimated ratios of the NPs:rGO phase in the xPt/TiO$_2$@rGO samples were calculated as 3:1 and 9:1, corresponding to the intermediates with NPs:GO ratios of 2:1 and 6:1, respectively. The Pt content in the reduced composites was measured by ICP-MS, giving values close to the expected quantity, 0.9, 0.5, and 0.1 wt%, percentages calculated concerning TiO$_2$ weight. Thus, practically, no noble metal loss occurs during the preparation procedure. The obtained samples were named as 0.9Pt/TiO$_2$@rGO, 0.5Pt/TiO$_2$@rGO, and 0.1Pt/TiO$_2$@rGO.

3.2. Aerogel structure

The composite components, as well as the intermediate xPt/TiO$_2$@GO and reduced xPt/TiO$_2$@rGO aerogels, were structurally analyzed by PXRD. Figure 4a shows the main signals in the patterns obtained in the 2θ interval of 20 to 40°, with the lines corresponding to anatase (2θ = 25.4, 37.0, 37.9, and 38.7°) and rutile (2θ = 27.4 and 36.2°), which were identical in the bare TiO$_2$ P25 and composed Pt/TiO$_2$ patterns. The signal of GO is described to appear at low angles, *ca.* 11°.[42]
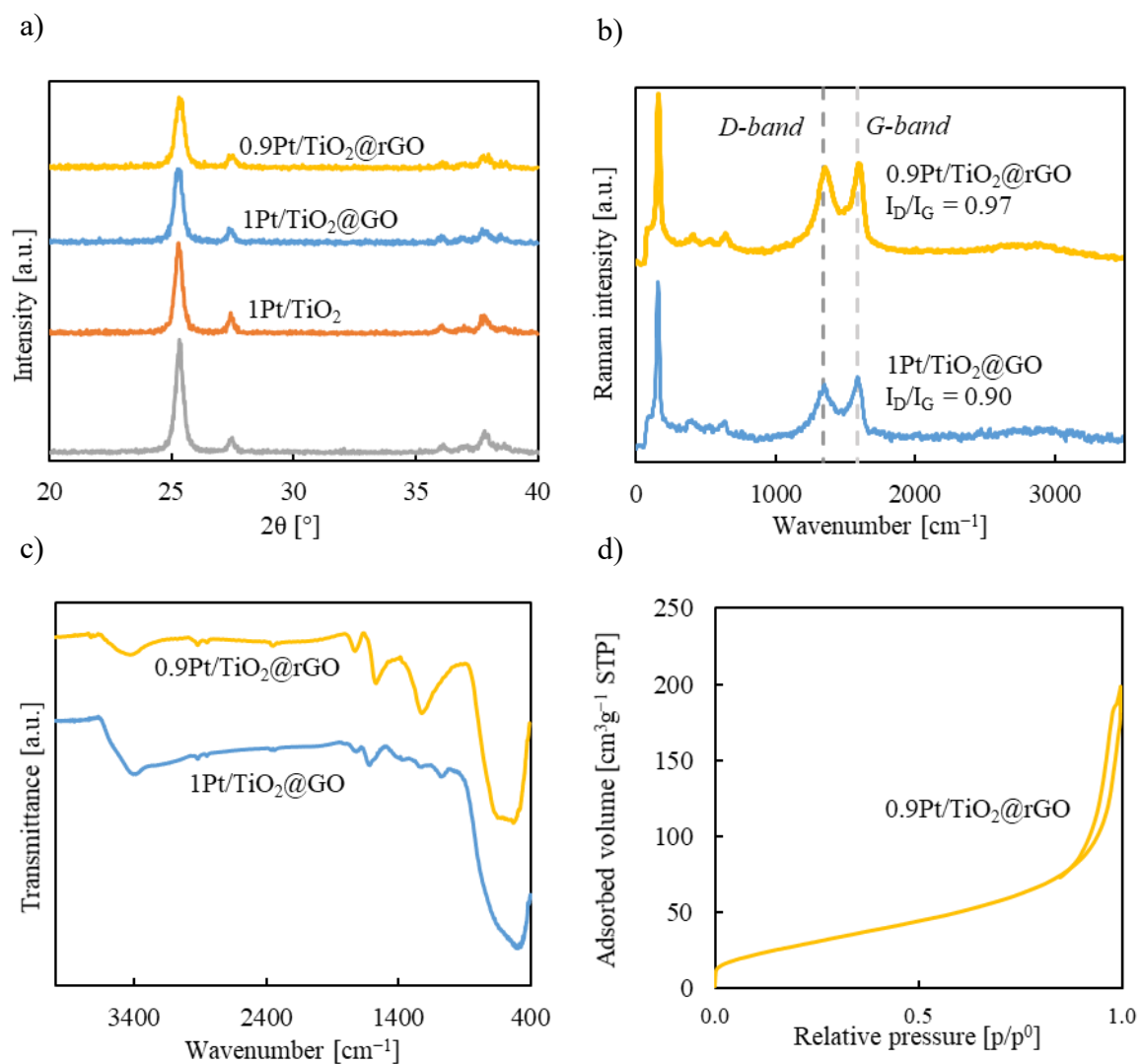
Figure 4. Structural characterization of bare NPs and as-synthesized or reduced aerogel composite for the $1Pt/TiO_2@GO$ (2:1) and $0.9Pt/TiO_2@rGO$ (3:1) samples: (a) PXRD patterns, (b) Raman spectra, in which D and G bands are indicated with dashed lines, (c) FTIR spectra, and (d) N_2 adsorption/desorption analysis of the reduced aerogel.

This signal could be observed for the intermediate non-reduced sample as a minor peak at this 2θ (Figure 5), while it disappears from the pattern of the reduced composite. The broadening of the diffraction lines was used to estimate NPs diameter by using the Scherrer equation. For bare TiO_2 and binary xPt/TiO_2 NPs, a size of *ca.* 21–22 nm was estimated, similar to that observed with TEM microscopy (Figure 6a,b). The NPs size in the reduced composites was similar, *ca.* 19–20 nm. The estimated particle size was, in all cases, in the range of the mean value given for the commercial TiO_2 P25 (*ca.* 20 nm). Consequently, no significant alteration of the crystalline structure or in the particle size of the TiO_2 took place throughout the deposition of Pt on its surface or the during aerogel formation and reduction.
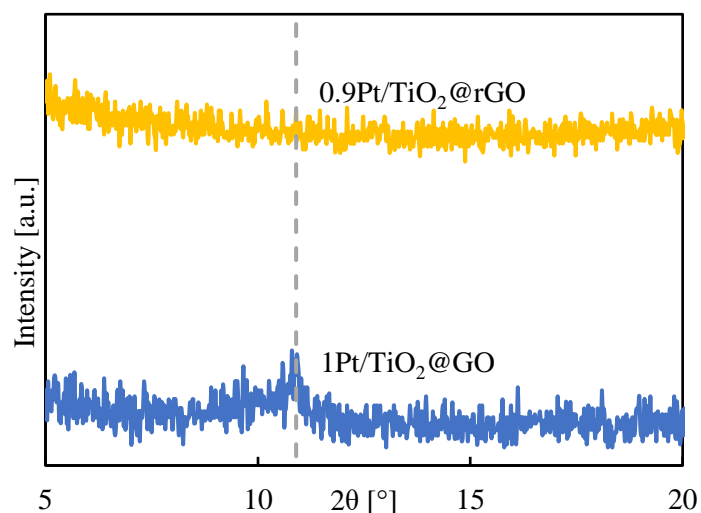
Figure 5. XRD spectra of the non-reduced 1Pt/TiO$_2$@GO and reduced 0.9Pt/TiO$_2$@rGO (3:1) composites. The small peak representative of GO is marked with a grey dashed line.
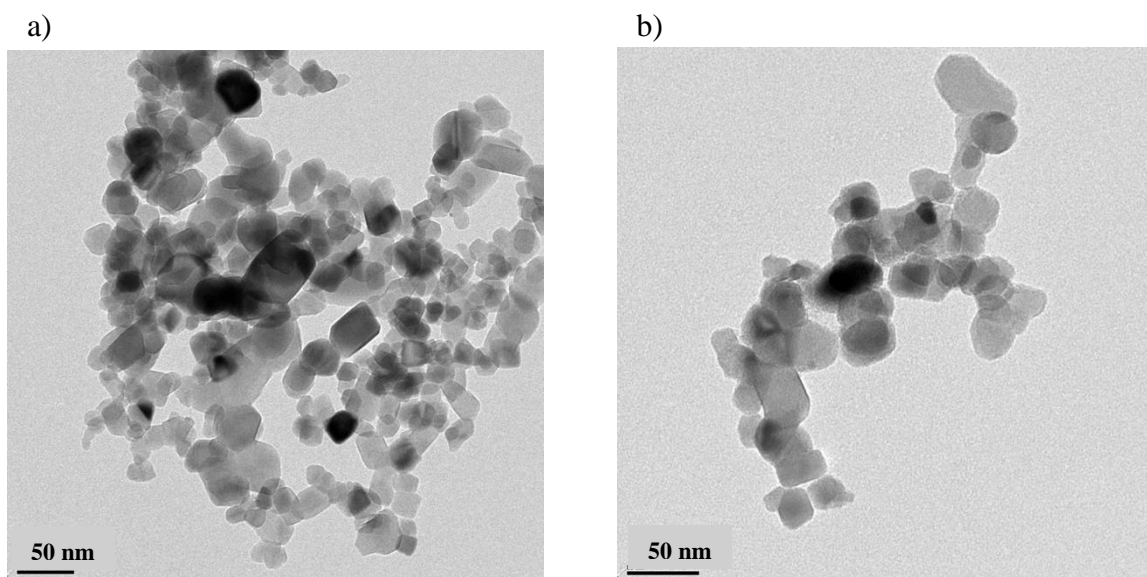
Figure 6. TEM images of: (a) bare TiO$_2$, and (b) 0.9Pt/TiO$_2$ NPs obtained by subjecting 1Pt/TiO$_2$ NPs to the reduction treatment.

Raman spectroscopy was used to investigate the structural changes occurring in the GO functional groups during the reduction process of the aerogel. The as-synthesized and reduced aerogels recorded spectra were characterized by the presence of the typical G and D bands at 1590 and 1345 cm^{-1}, respectively (Figure 4b). The G band is generated by the in-plane vibrations of sp^2-bonded carbon atoms (C–C stretching), while the D-band represents the out-

of-plane sp^3 vibrations corresponding to the defects in the graphitic structure. The ratios of the intensities of the D and G bands (I_D/I_G) were 0.90 and 0.97 for the GO and rGO composite aerogels, respectively. This result indicates that both synthesized and reduced samples have an elevated degree of sp^3 defects in the graphitic structure. For the xPt/TiO$_2$@GO samples, the defects represent the highly oxygenated character of GO. For the xPt/TiO$_2$@rGO composites, defects not only originated from the residual oxygenated groups but there are also structural defects (holes, vacancies, dislocations, *etc*.) caused by the thermal treatment applied for sample reduction. It has been described that reduction under relatively mild conditions, such as the ones used in this work, triggers the formation of these defects in rGO.[43] A considerable number of new sp^2 graphitic domains are formed, but of small size.[44] Moreover, a broadened band observed in the 2700–3000 cm^{-1} region of the Raman spectra, the usual position of the 2D peak in graphene, is indicative of randomly oriented multilayer graphene composing the aerogels.[45] Finally, the presence of the NPs in the composite was noticed by the detection of the TiO$_2$ bands at 151, 394, 515 and 630 cm^{-1}. The oxygenated character of GO in the intermediate composite and reduced aerogel was further analyzed by FTIR spectroscopy. The spectra of the intermediate samples (Figure 4c) show the GO functional groups by displaying the vibrational modes of C=O at 1719 cm^{-1}, C-OH at 1221 cm^{-1}, C-O at 1060 cm^{-1}, C-O-C at 1370 cm^{-1}, and OH at 1618 and 3400 cm^{-1}, the latter indicating also adsorbed water. The reduced sample displayed an intense C=C band at 1550 cm^{-1}, indicating the partial restoration of the graphitic structure. However, the bands of most of the oxygen groups in GO were somehow preserved in the rGO samples, only the peaks corresponding to epoxy vanished totally, while the peak at 3400 cm^{-1} corresponding to the hydroxyl groups diminished. The presence of the NPs in the composites is shown by the intense and broad stretching band appearing at 500–800 cm^{-1}. Raman and FTIR characterization indicate that, under the used experimental conditions for the reduction, 300 °C and a N$_2$ atmosphere, the GO phase was partially reduced, but a significant amount of oxygenated functionalities was conserved in the structure of rGO.

3.3. Textural properties and morphology

The textural properties of the synthesized aerogels were analyzed by N$_2$ adsorption/desorption at low temperatures. Figure 4d shows the isotherm recorded for the sample 0.9Pt/TiO$_2$@rGO (3:1), representative of all the studied systems, while the isotherms of the precursors are displayed in Figure 7a. The isotherm of the 0.9Pt/TiO$_2$@rGO is described as type IV at low and medium relative pressure and type II at high relative pressure, which is characteristic of nanoporous structures with both meso- and macropores and a negligible contribution of

microporosity. A similar shape was found for the non-reduced GO precursor, while the 0.9Pt/TiO$_2$ NPs constitute a meso-porous system originated by particle aggregation. The S_a value for the 0.9Pt/TiO$_2$@rGO sample was in the order of 110 m^{2}g^{-1}. This value is inferior to that found in the non-reduced GO sample (*ca.* 150 m^{2}g^{-1}) but is superior to pristine NPs (*ca.* 50 m^{2}g^{-1}).
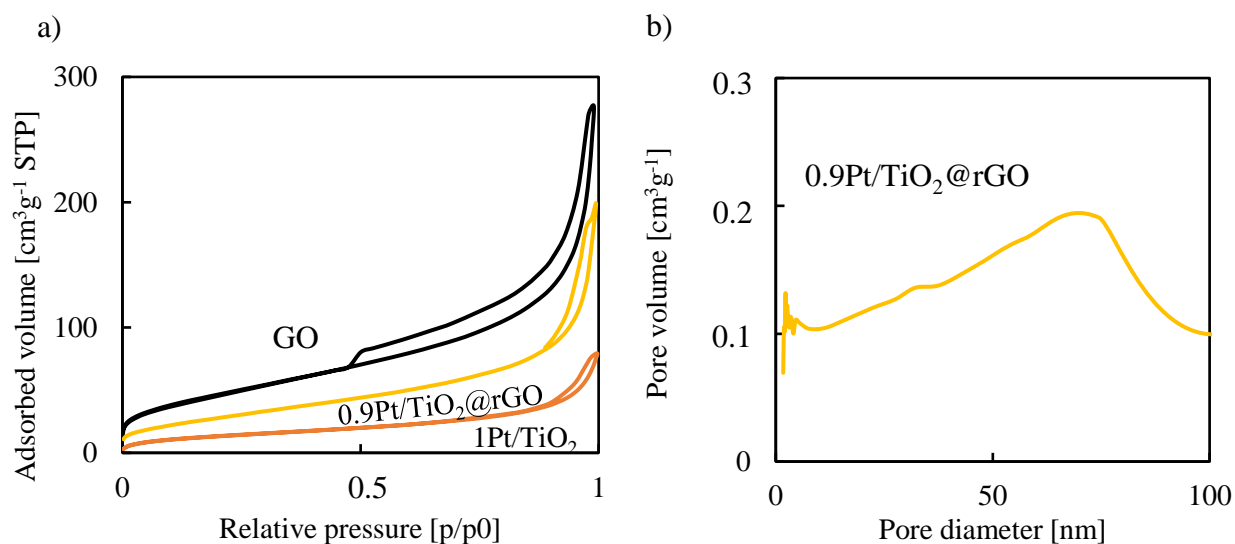

Figure 7. (a) N$_2$ adsorption/desorption isotherms for the 0.9Pt/TiO$_2$@rGO sample compared to the precursors GO and 1Pt/TiO$_2$ NPs and (b) BJH volumetric pore size distribution calculated from the adsorption branch of the isotherm.

Drying gels with scCO$_2$ is known to produce relatively denser aerogels than drying at the critical point of the alcohol due to moderate shrinkage occurring upon gelation and drying. In this work, a diameter of *ca.* 0.8 cm was measured for the cylindrical aerogel intermediates xPt/TiO$_2$@GO, indicating that they suffered some contraction in the axial direction since they were synthesized in a vial of 1 cm diameter. Further, some extra tightening occurs during reduction, leading to monoliths of *ca.* 0.7 cm diameter for the end products xPt/TiO$_2$@rGO. Aerogels with mesoporosity homogeneously distributed along all the mesopore range were obtained (Figure 7b), with a BJH V_p of 0.30 cm^{3}g^{-1} and an average mesopore size of 10 nm.

All the different xPt/TiO$_2$@GO synthesized intermediate aerogels have similar morphology; they are highly porous with a sponge-like macrostructure, as shown in the SEM image of Figure 8a. The SEM images of the reduced monoliths displayed, similarly to the intermediates, a 3D structure with interconnected meso- and macropores (Figure 8b).
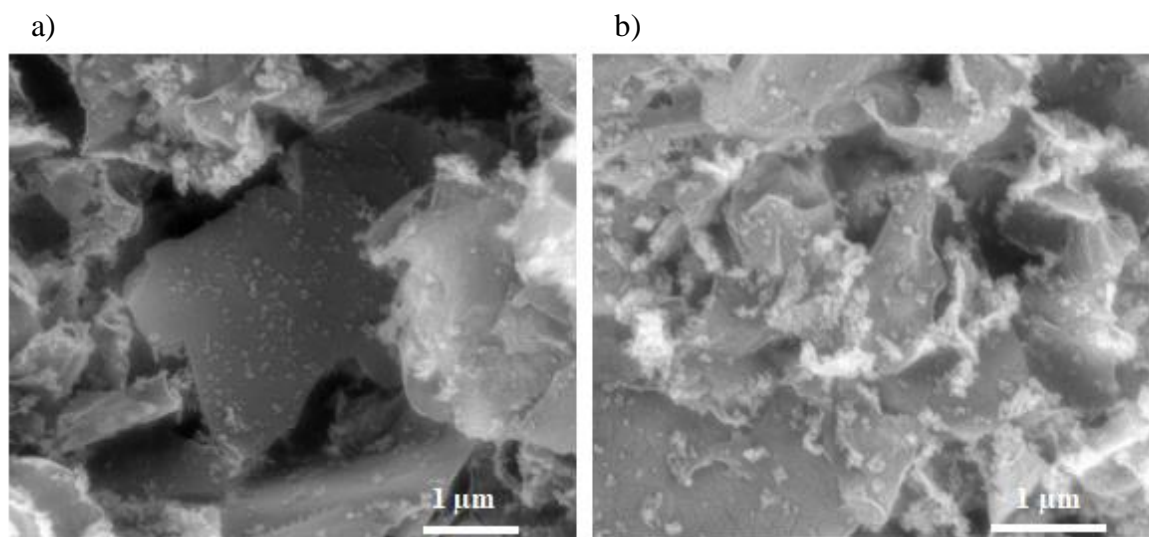
Figure 8. SEM images of samples: (a) 1Pt/TiO$_2$@GO (2:1), and (b) 0.9Pt/TiO$_2$@rGO (3:1), representative of the morphology of as-synthesized and reduced aerogels.

In most of the as-synthesized and reduced samples, the NPs can be discerned as a highly dispersed phase deposited on the surface of the GO or rGO plates (Figure 9a). However, the formation of large aggregates was also detected for the samples with the highest NPs:rGO (9:1) ratio (Figure 9b).
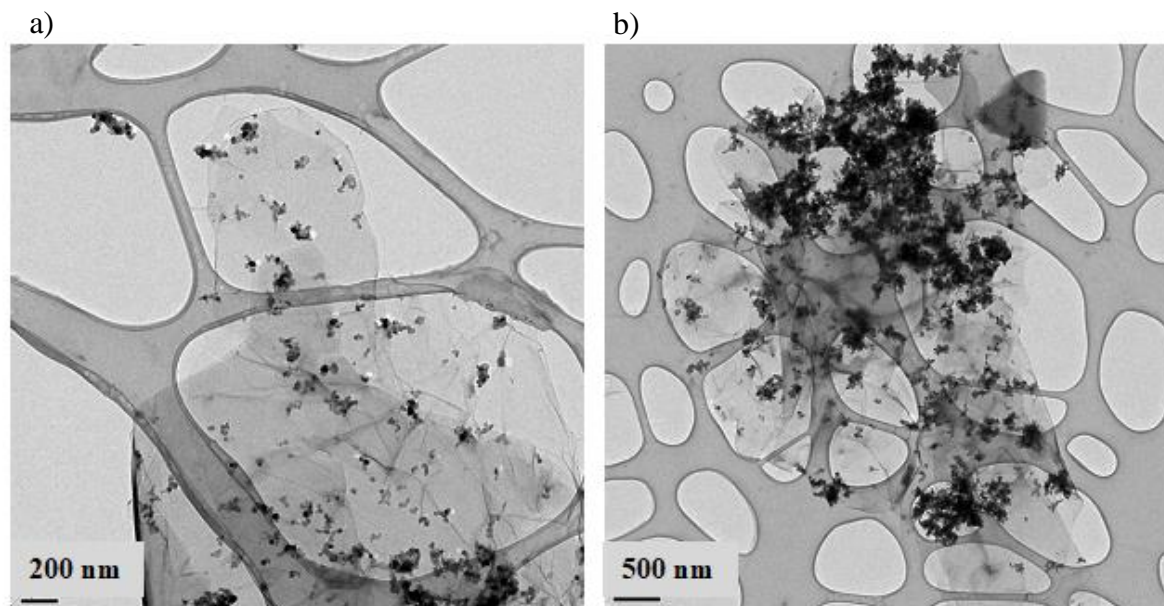
Figure 9. TEM images of the 0.9Pt/TiO2@rGO samples with NPs:rGO ratios: (a) 3:1 and (b) 9:1.

3.4. Aerogels optical properties

The optical properties of the reduced composites, as well as those of bare TiO_2 and rGO, were analyzed by UV-vis diffuse reflectance spectroscopy to investigate the samples' photoresponse (Figure 10a). TiO_2 was active in the UV zone and exhibited an abrupt absorption edge around 400 nm, while rGO displayed a continuous absorption in the visible range. For the reduced composites, a broad background absorption in the visible range was observed as a consequence of rGO black characteristics, more notable in the sample with the lowest percentage of NPs, *e.g.*, $xPt/TiO_2@rGO$ (3:1). The contribution of the NPs to the absorption in the UV zone can be clearly appreciated in the composites' spectra, although with a red shift in the adsorption edge that was slight, to 450 nm, for the (9:1) composite and pronounced, to 750 nm, when the amount of rGO was increased in the (3:1) sample. This shift indicates an increased photoresponse in the visible range of the composite aerogels with respect to net TiO_2 NPs. To study the indirect optical band gap of the photocatalyst, a Tauc plot was determined, calculated from the UV-vis absorption spectrum (Figure 10b).[46,47] For the bare TiO_2, a band gap energy of 3.1 eV was estimated from the x-axis intercept of the extrapolated line fitted to the linear region of the plot. The effect of the Pt content was analyzed for the $xPt/TiO_2@rGO$ (3:1) composites with an x range of 0.9–0.1 wt%. The three measured bandgap values (at Pt contents of 0.9, 0.5, and 0.1 wt%) were of *ca.* 1.5 eV, thus demonstrating the low influence of this parameter. Contrarily, enhancing the ratio of NPs:rGO in the $0.9Pt/TiO_2@rGO$ sample from 3:1 to 9:1 results in an increase in the bandgap from 1.5 to 2.8 eV, with a concomitant increase in the transition energy of the photoexcited electrons. This phenomenon is assigned to the generation of impurity energy levels above the valance band in the NPs upon their incorporation onto the rGO surface. Thus, for the excitation of the charge carriers, less energy is required.[48] It is worth mentioning that the shift in the absorption edge and the decrease in the band gap energy are both more notable in the studied compounds than in similar published systems, reporting shift values of only 0.1–0.4 eV.[17,26] This important result is explained by the formation of a large number of Ti–O–C bonds in the $xPt/TiO_2@rGO$ samples, established between the surface of the TiO_2 and the rGO flakes,[49] and occurring during the reduction and elimination of water from the pre-settle hydrogen bond interactions Ti–OH...OH–GO in the $xPt/TiO_2@GO$ intermediates. Although the low band gap energy in the (3:1) aerogel suggests a high photoresponse, this feature does not necessarily mark out the best photocatalyst system, since other factors should be taken into account. Importantly, using a high amount of rGO can evoke some activity loss, as the dark flakes can shield some active NPs, such that not all catalytic units are exposed to the light. Hence, to design the right catalyst, a compromise must be attained between the percentage of

components (NPs:rGO) in the composite; on the one hand, to increase the band gap through the decrease in the number of NPs and, on the other hand, to reduce darkness *via* a decrease in the proportion of rGO.
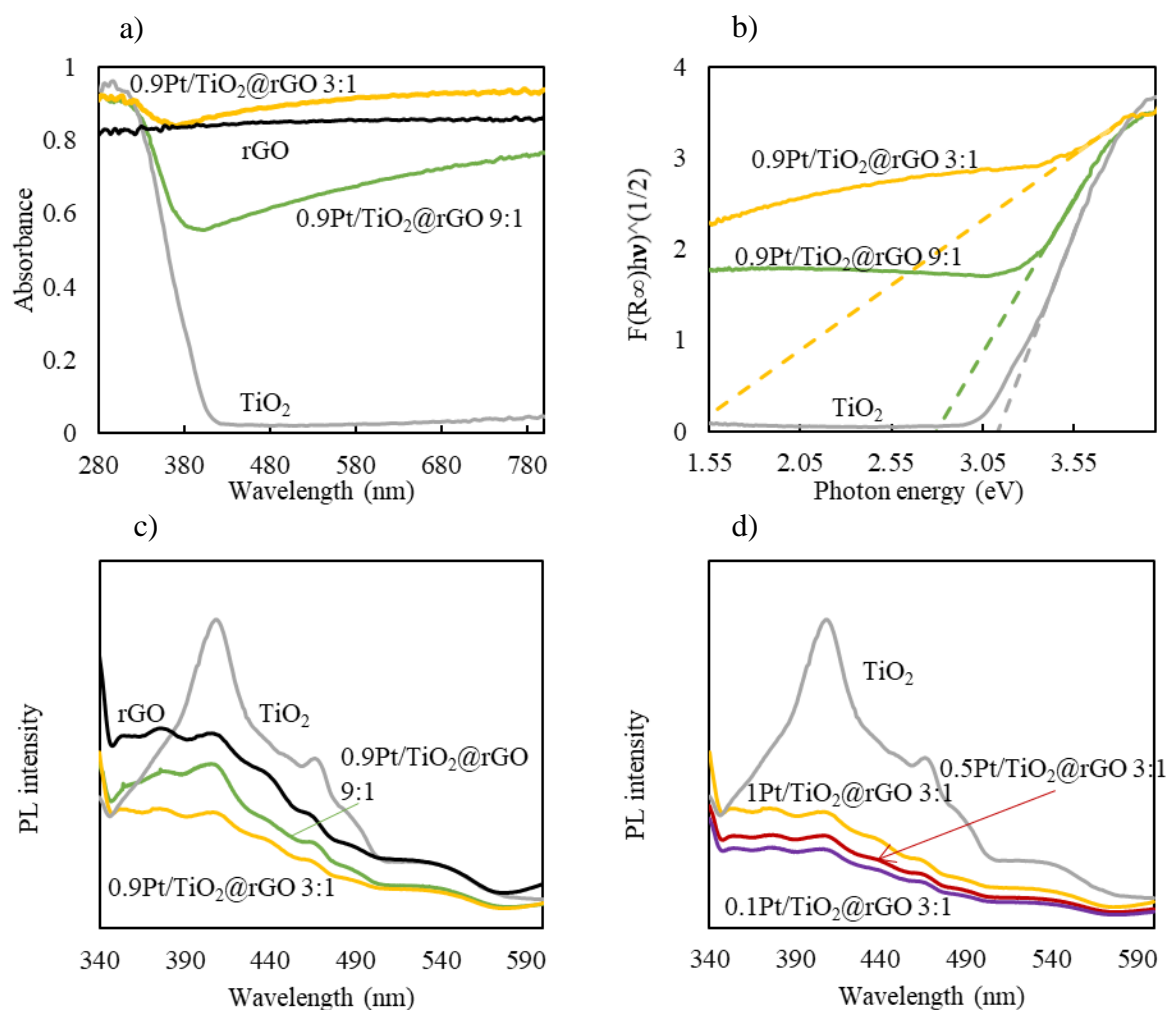
Figure 10. Optical characterization of bare NPs and reduced aerogel composites: (a) UV-vis diffuse reflectance spectra, (b) band gap energy determined from the Tauc plot (the linear part of the plot is extrapolated to the x-axis), (c) photoluminescence spectra at an excitation wavelength of 320 nm, and (d) samples of $xPt/TiO_2@rGO$ (3:1) with different Pt ratios.

Photoluminescence experiments were carried out to study the recombination rate of the photogenerated e^-/h^+ pairs in the aerogel catalyst. One of the main drawbacks described for the use of TiO_2 semiconductors in photocatalytic processes is the fast recombination of the photogenerated species.[7] This behavior is clearly evidenced in the photoluminescence spectrum with an intense emission after the photoexcitation of the bare NPs under UV light at 320 nm (Figure 10c). A wide luminescence band is observed for TiO_2, with a maximum at 410 nm

(close to the band gap energy of TiO$_2$), which is followed by a less intense signal at 468 nm. The spectra of the reduced xPt/TiO$_2$@rGO (3:1) and (9:1) composites did not have the same pattern as that of net TiO$_2$, being indeed similar to that of rGO. Thus, the photoluminescence intensity was diminished in the composites with respect to bare NPs, which is a usual behavior originated by the e$^-$ acceptor and transport features given by the rGO support, resulting in suppressed charge recombination and less intense light emission. However, the composites with the lowest percentage of rGO showed the weakest photoluminescence intensity values, indicating that there is an optimal rGO content regarding the recombination rate. For the composite with the largest number of NPs, quantitatively more photoelectrons can be generated, thus resulting in a high number of potential recombinations and increased photoluminescence intensity. The deposited Pt on the TiO$_2$ surface has been described to act as an electron sink, by trapping the electrons and further transferring them to the rGO support.[25] Comparing the applied Pt ratios, *e.g.*, 0.1, 0.5, and 0.9 wt%, the lower the Pt loading, the weaker the photoluminescence response (Figure 10d). This result suggests that Pt can also act as a recombination center.[50]

3.5. Photocatalytic hydrogen production

Studies of photocatalytic H$_2$ production were performed to evaluate the new catalytic system. For that, the applied conditions were first extensively examined and optimized. The most favorable conditions for the use of the new catalyst in a particular catalytic process would depend on both the character of the material (composition and structure) and the setup used. In this study, the analysis is focused on the optimization of the synthesized xPt/TiO$_2$@rGO composite aerogel in regard to its photocatalytic activity in irradiated aqueous methanol solutions. The applied setup for the photocatalytic reaction is schematized in Figure 2. The studied parameters were catalyst reduction degree (from any to mild reduction), catalyst architecture (one-piece monolith or smashed aerogel), methanol concentration in the aqueous solution (from 0.01 to 1 v%), the added amount of catalyst to the reactor (from 0.03 to 2 g$_{NPs}$ L^{-1}), Pt percentage in the catalyst (from 0 to 1 wt% in the Pt/TiO$_2$ NPs), and NPs ratio with respect to rGO (3:1 and 9:1). In a typical experiment performed with the sample 0.9Pt/TiO$_2$@rGO (3:1), the aerogel was recovered after the photocatalytic reaction and analyzed in regard to composition. The sample maintained the ratio 3:1 for NPs:rGO, thus indicating the lack of NPs leaching, which opens the door for the recyclability of the material.

3.5.1. Aerogel reduction degree

The straight use of GO monolithic aerogels with highly hydrophilic character in polar solvents causes the destruction of the macroscopic structure, provoked by strong electrostatic interactions with the solvent once it is immersed into the liquid. To avoid this drawback, the reduction in the GO phase to rGO was the applied solution in this work. The reduction step must be precisely controlled, since excessive reduction leads to highly hydrophobic aerogels that can suffer from low wettability when soaked in polar liquids, such as the water/methanol reaction medium used in this work. Hence, reaching an appropriate reduction degree of the GO composite aerogel is crucial to design an efficient catalyst in which the aqueous solution must easily travel inside the 3D structure.[7] In this work, a soft thermal treatment was applied for the reduction of the intermediate aerogel NPs@GO to NPs@rGO, *e.g.*, 300 °C under a N_2 atmosphere. A reduced aerogel with amphiphilic properties, involving graphitic hydrophobic regions and remaining hydrophilic oxygenated groups (hydroxyl and carboxyl), was thus synthesized. The decrease in hydrophilicity after reduction was depicted by water contact angle measurements, showing an increase in the contact angle for the reduced composite (58.9°) in comparison to the non-reduced (21.8°) (Figure 11). The relatively still high wettability found for the reduced composite is the consequence of the residual oxygenated groups and the involvement of the more hydrophilic TiO_2 NPs, as well.

a)   b)
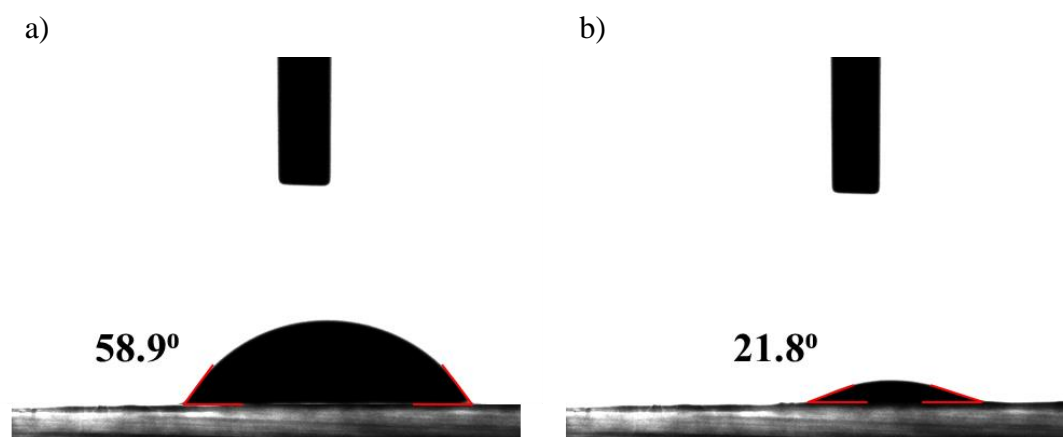
Figure 11. Contact angle measurement of: (a) $0.9Pt/TiO_2@rGO$ and $1Pt/TiO_2@GO$ composites, measured with a water droplet.

For the analyzed catalytic process, the necessity of reducing the GO support to rGO was established in a preliminary experiment in which the H_2 evolution with time was compared for similar samples either non-reduced ($1Pt/TiO_2@GO$ (2:1)) or reduced ($0.9Pt/TiO_2@rGO$ (3:1)) under similar conditions in the catalytic reactor (0.5 v/v methanol/water solution, 0.5 g_{NPs} L^{-1},

and smashed aerogel). The obtained results indicate that the reduction step was necessary to improve the efficiency of the catalyst (Figure 12a).

Indeed, the H_2 production in steady-state conditions was more than doubled for the reduced aerogel, increasing from 3280 $\mu molH_2$ h^{-1} g_{NPs}^{-1} in the 1Pt/TiO$_2$@GO (2:1) intermediate to 7070 $\mu molH_2$ h^{-1} g_{NPs}^{-1} in the 0.9Pt/TiO$_2$@rGO (3:1) aerogel. The reasons for the positive effect on the H_2 production rate of the GO reduction are two-fold. On one hand, upon the removal of the oxygenated groups on the GO surface, the graphitic structure is partially restored, although in small spots due to defect generation.[43,44] Nevertheless, rGO would own more electrical pathways than GO, enhancing the conductivity of the matrix that plays a key role in transferring the photogenerated e$^-$, thus preventing re-combination and improving H_2 production efficiency.[51] On the other hand, the more hydrophobic reduced structure favors the adsorption of the methanol sacrificial agent over water and maintains it close to the Pt/TiO$_2$ NPs to boost h$^+$ consumption, which was beneficial for production.[26]
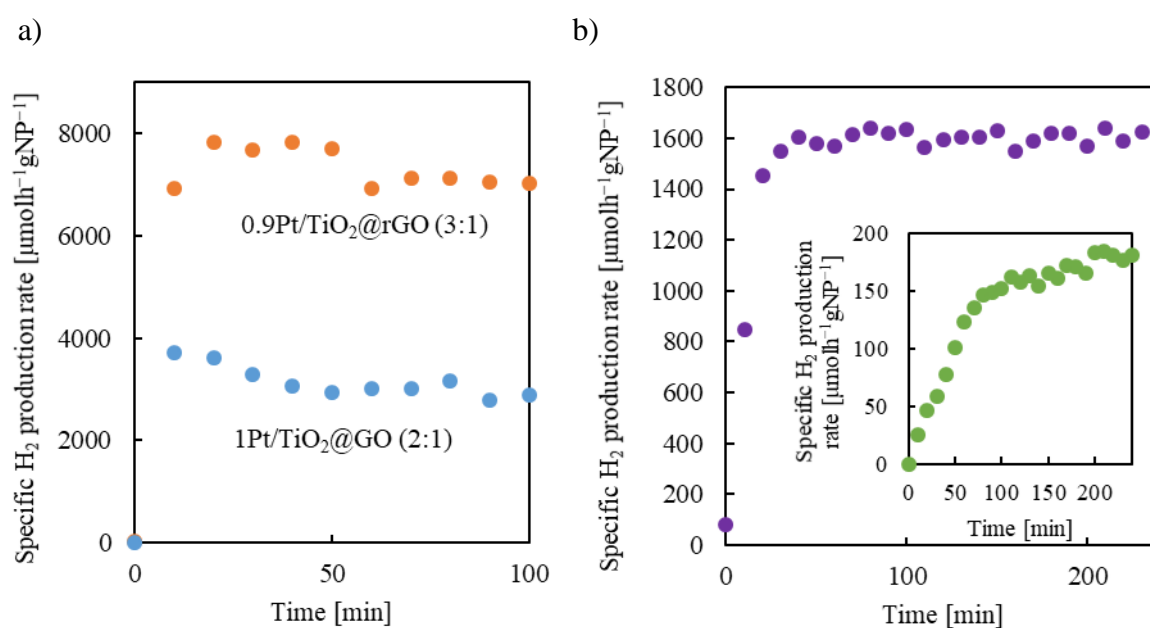
Figure 12. H_2 production rate at different experimental conditions: (a) using the non-reduced 1Pt/TiO$_2$@GO (2:1) and reduced 0.9Pt/TiO$_2$@rGO (3:1) aerogels (reaction conditions: 0.5 v/v methanol/water, 0.5 g_{NPs} L^{-1}, smashed aerogel), and (b) using the 0.9Pt/TiO$_2$@rGO aerogel as a one-piece monolith (green) and smashed (purple) (reaction conditions: 0.5 v/v methanol/water, 2_{gNPs} L^{-1}).

3.5.2. Aerogel architecture

Fabricating GO-based composite aerogels using scCO$_2$ makes possible the creation of 3D monolithic meso/macroporous architectures. Preliminary tests were performed using a set-up designed for the straight use of the monoliths (Figure 2). Four of these cylinders were simultaneously used with a total weight of *ca.* 40 mg, which represents a catalytic NPs concentration of 2 g$_{NPs}$ L^{-1} in the reactor filled with 14 mL of a 0.5 v/v methanol/water solution. Under these conditions, a specific H$_2$ production of 180 μmol h^{-1} g$_{NPs}$$^{-1}$ was reached at the steady state for the sample 0.9Pt/TiO$_2$@rGO (3:1) (Figure 12b). Compared to the literature, this value is similar to those given in some of the published works (*e.g.*, 100–400 μmol h^{-1}g$_{NPs}$$^{-1}$ using TiO$_2$/Pt/rGO composites[25]), although it is considered to be in the low range of H$_2$ production.[26,27,29,30] Definitely, the most important drawback of using monolithic one-piece aerogels in the catalytic experiment is relays in the small amount of sample exposed to light, so that during irradiation most of the Pt/TiO$_2$ NPs in the interior part of the monolith remains inactive. Moreover, a long reaction time was needed to reach the steady state, in the order of 200 min, which was related to the slow diffusion of reactants in the monolithic aerogels with low permeability due to certain densification originated by shrinkage and high tortuosity. Diffusion is further hindered in non-stirred setups such as the one used in this work for the one-piece monoliths. Agitation was not used to avoid turbulence damage to the integrity of the monoliths during the measurements. Hence, in spite of the great prospect of applying monolithic aerogels to diminish the loss of active sites during recycling,[7] the utilization of one-piece aerogel photocatalysts in liquid media appears to still face significant challenges.[52]

To improve the catalytic activity of the aerogels, a second set of experiments was performed by first dispersing the reduced monoliths in small pieces in the aqueous methanol solvent, using for that soft and short sonication. The aim of the ultrasonic treatment was not to re-exfoliate the rGO flakes but to break the monoliths into pieces. The DLS characterization of the obtained dispersion gave a bimodal pattern with peaks at *ca.* 10 and 20 μm hydrodynamic sizes, representative of the size of the broken pieces of aerogel (Figure 13).

After this treatment, the H$_2$ production rate for the sample 0.9Pt/TiO$_2$@rGO (3:1) increased to 1600 μmol h^{-1} g$_{NPs}$$^{-1}$, with the particularity that this high rate was achieved after only 40 min (Figure 12b). The shortening in the required time to reach equilibrium is related to an increase in the catalyst permeability occurring for the small pieces with shorter throughout distances than the one-piece monoliths. Hence, permeability, even having similar absolute values for the smashed and one-piece aerogels is not the key parameter limiting the catalytic activity of the micrometric samples. The setup involving small pieces has the advantage that measurements

can be performed under stirring, thus minimizing drawbacks related to reagent diffusion, adsorption, and desorption. Moreover, the small pieces of aerogel are continuously moving in the turbulences created by agitation, thus giving more chance for the catalytic NPs for being irradiated by light. All these factors lead to an enhancement in the H_2 production rate.


Figure 13. DLS analysis of the 0.9Pt/TiO$_2$@rGO (3:1) aerogel dispersed in an aqueous methanol solution (0.5 v/v). Data measured after 5 min of ultrasound treatment.

3.5.3. Methanol concentration

Concerning methanol sacrificial agent concentration in the aqueous solution, diverse, even contradictory results have been published on TiO_2-based systems used for photocatalytic H_2 production. Actually, some of them conclude that methanol contributes less than its stoichiometric ratio to the overall H_2 formation,[53] while others confirm that the overall reaction can be described as the photoconversion of exclusively methanol.[54] In fact, it is expected that an increase in the methanol concentration in the aqueous solution results in enhanced H_2 production, whether it comes either from the water/sacrificial agent or the sacrificial agent exclusively, due to the more effective scavenging of the photo-generated h^+ by the alcohol. Water is known to play an important role in the complete oxidation of alcohol to CO_2, making its presence necessary.[55] For instance, water has the ability to fasten the essential desorption of the reaction products from the catalyst surface, thus enhancing the reaction rate. As a consequence, after a certain increase in methanol concentration, the decrease in H_2 production generally occurs due to the hindered adsorption of water on the catalyst surface already occupied by alcohol molecules. To optimize this parameter for the developed catalyst, methanol was applied in increased concentrations in the aqueous solution, from 10 to 100 v% (0.01 to 1 v/v). Experiments were performed with the smashed aerogel of sample 0.9Pt/TiO$_2$@rGO (3:1) and a catalyst concentration of 2 g_{NPs} L^{-1}. The measured flow rates of the produced H_2 at the steady state, *e.g.*, at 60 min for each methanol concentration, are shown in Figure 14a.

a)

b)

Figure 14. H$_2$ production rate in steady-state conditions (60 min) for 0.9Pt/TiO$_2$@rGO (3:1) smashed aerogel: (a) influence of methanol concentration (2 g$_{NPs}$ L^{-1}), and (b) influence of NPs concentration (0.5 v/v methanol/water), in which results are expressed as the non-specific (µmolH$_2$ h^{-1}, blue) and specific (µmolH$_2$ h^{-1}g$_{NPs}$$^{-1}$, orange) production rates.
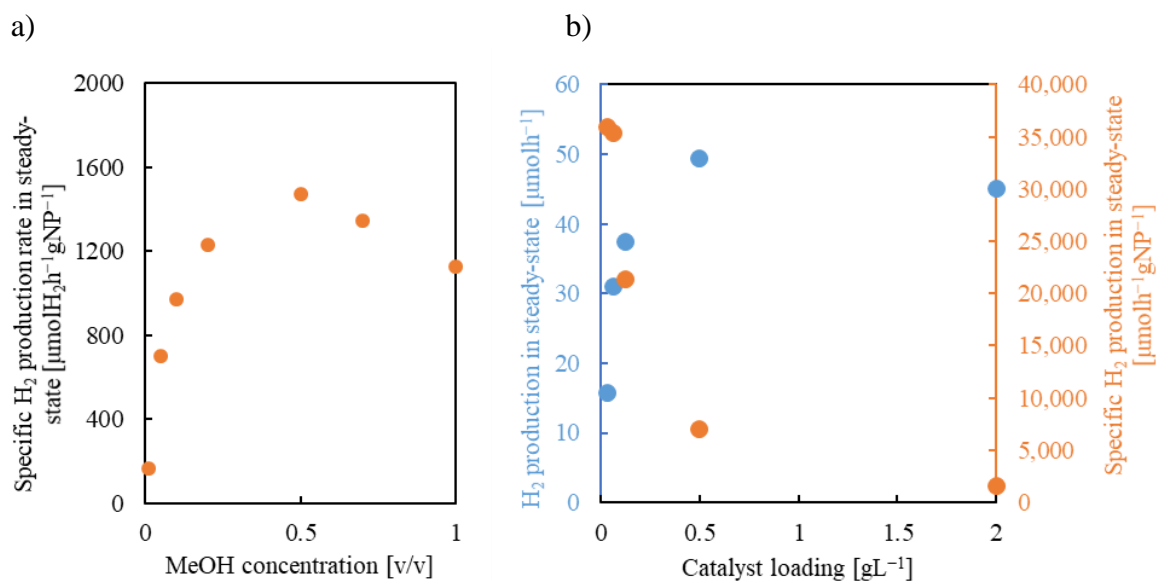
Initially, the increase in the methanol-to-water ratio favored the H$_2$ production rate up to a maximum reached at a concentration of *ca.* 0.5 v/v. Thereafter, a further increase in the alcohol concentration results in a smooth decrease in the H$_2$ evolution. Commonly, a behavior of a sharp decline in H$_2$ generation has been observed for similar catalysts.[56,57] The lack of severe decrease, caused by excess methanol on the catalytic efficiency of the studied composite, is here related to the swelling characteristics of the used rGO support. Although the photocatalytic reaction is induced by the photogenerated h$^+$ and e$^-$ on the Pt/TiO$_2$ NPs, the swelling of the rGO support is influenced by the polarity of the solvent, which affects the interaction between the dispersed active sites on the rGO surface and the reactants. Applying methanol in high concentrations would enhance the swelling of the aerogel pieces since methanol interaction with the hydrophobic graphitic regions in the rGO support would be stronger than for water.[58] The swelled structure would allow better accessibility for the reactants to the attached NPs. Hence, the above-mentioned adverse effects of the excess of methanol are somewhat compensated by aerogel swelling, and the H$_2$ production is maintained at a relatively high level in all the studied ranges of alcohol concentration.

3.5.4. Catalyst concentration

The effect of the catalyst loading, referring to the number of NPs, was investigated in the concentration interval of 0.03 to 2 g_{NPs} L^{-1} (equivalent to 0.04–2.67 $g_{aerogel}$ L^{-1}) for the 0.9Pt/TiO$_2$@rGO (3:1) smashed aerogel dispersed in 0.5 v/v water/methanol solution. The production rate of H$_2$ was measured at a steady state (60 min) (Figure 14b). In the studied interval of concentration, the H$_2$ flow rate, expressed as the specific value, *e.g.*, normalized to the catalyst NPs weight (μmolH$_2$ h^{-1} g_{NPs}^{-1}), was very high at low catalyst loading (0.03–0.125 g_{NPs} L^{-1}), and then substantially decreased at high concentrations (> 0.5 g_{NPs} L^{-1}). However, this result, which could be taken at the first instance as an indication of the benefits of working at a very low concentration of catalyst, is just a mathematical artifact since, in fact, the total amount of the produced H$_2$ can be considered as being in the low range. The representation of the catalytic data as a function of the non-specific H$_2$ production rate (μmolH$_2$ h^{-1}) indicates that the total amount of evolved H$_2$ sharply increases with the catalyst loading up to a value of *ca.* 0.5 g_{NPs} L^{-1}. Thereafter, H$_2$ production slightly decreases by increasing catalyst concentration. This decrease is likely due to light blocking by an excess of dark solid catalyst dispersion.[59]

3.5.5. Catalyst composition

Platinum content

Regarding the catalyst composition, one important parameter for regulating the photocatalytic activity in the reaction of H$_2$ production is the amount of Pt added to the TiO$_2$ NPs. The presence of Pt is necessary for suppressing the recombination of the photo-generated e$^-$ and h$^+$ in the TiO$_2$ semiconductor, thus enhancing the formation of H$_2$. Intimate Pt–TiO$_2$ contact at the interphase is also necessary to maximize the H$_2$ production efficiency.[60] To analyze this parameter, a series of experiments was performed with smashed xPt/TiO$_2$@rGO (3:1) aerogels with four different values of Pt content in the NPs: 0, 0.1, 0.5, and 1.0 wt%. In previous works involving Pt/TiO$_2$/rGO systems, the proportion of the noble metal is also within this range, typically 0.4–1%,[17,25,26,29] which facilitates data comparison. Measurements were carried out at the optimal reaction conditions previously established, *e.g.*, 0.5 v/v water/methanol and smashed catalyst with a concentration of 0.5 g_{NPs} L^{-1}. Primary tests indicated that without the addition of the noble metal (sample TiO$_2$@rGO), the H$_2$ evolution was negligible, with a value of only 60 μmolH$_2$ h^{-1} g_{NPs}^{-1}. This result corroborates previous findings pointing to the inactivity of TiO$_2$ NPs without the use of a co-catalyst.[61] In the studied range of noble metal loading, the H$_2$ production increases concomitantly with Pt content (Figure 15a). The decline

in H_2 evolution was smoother when the Pt content was decreased from 0.9 to 0.5 wt% than from 0.5 to 0.1 wt%. This observation indicates that, although the overall H_2 production was the highest with the sample of 0.9 wt% Pt content in TiO_2, the total amount of noble metal can be halved without losing significant activity. This is an important result since Pt is the most expensive component of the catalyst; therefore, the amount of noble metal incorporated into the composite would be crucial in any industrial process and must be reduced as much as possible. The design of a catalyst involving an important reduction in the use of Pt is currently an important goal targeted by the European Commission.[62]
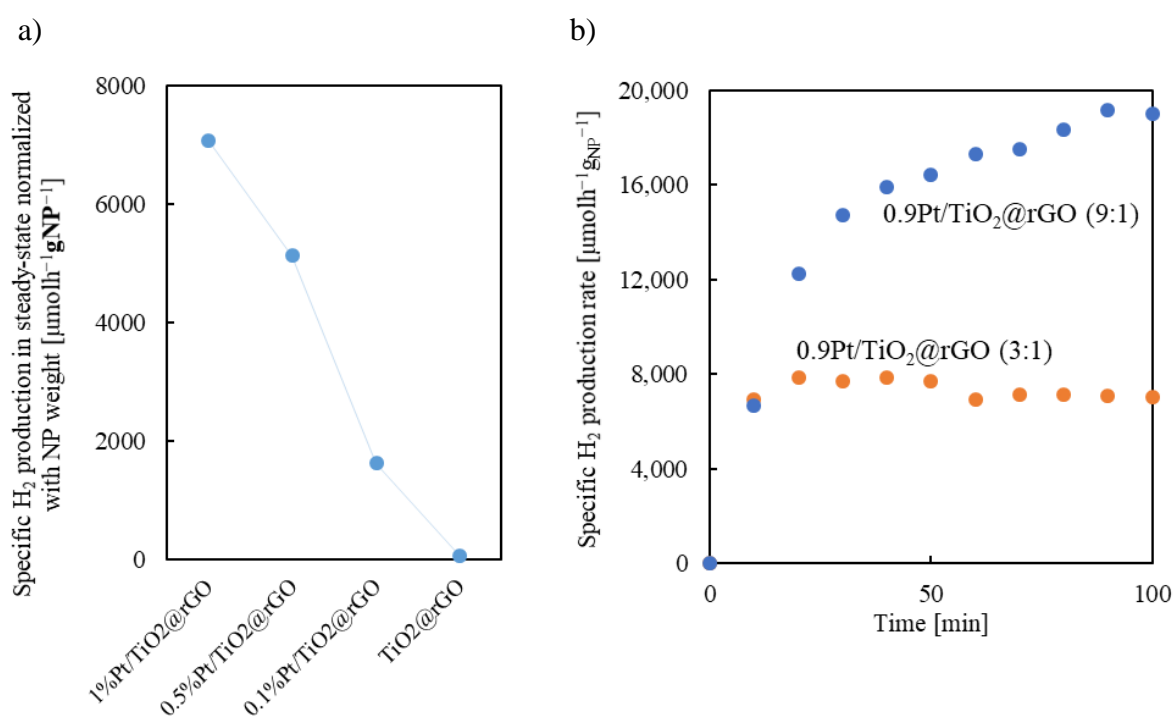
Figure 15. Specific H_2 production rate for smashed aerogel samples: (a) xPt/TiO$_2$@rGO (3:1) with different Pt content, and (b) 0.9Pt/TiO$_2$@rGO with 3:1 and 9:1 NPs:rGO ratios. Reaction conditions: 0.5 v/v methanol/water, 0.5 g$_{NPs}$ L^{-1}.

NPs:rGO ratio

The influence of modifying the NPs:rGO ratio in the 0.9Pt/TiO$_2$@rGO composite was investigated by increasing this value from 3:1 to 9:1. This modification resulted in a 2.7-fold enhancement in the H_2 production efficiency, from 7070 to 18800 µmolH_2 h^{-1}g$_{NPs}$$^{-1}$ at the steady state (Figure 15b). The foremost effect of increasing the NPs loading in the composite was to enhance the light-harvesting of the catalyst since, statistically, the probability for the UV radiation to contact active centers rises. On the contrary, the large amount of rGO in the aerogel with the lowest number of NPs shields an important portion of the active centers, hindering

overall catalyst activity.[63] Moreover, the steady state in H_2 evolution was reached at 10 and 90 min for the 3:1 and 9:1 samples, respectively. Increasing the rGO percentage in the composite should raise the hydrophobic character of the aerogel, thus improving the accessibility of the methanol vs. water in the pores. Excess amounts of methanol close to the photogenerated holes facilitate the fast h^+ trapping by the alcohol, such that in the initial phase of the reaction, the H_2 production already reaches its limit.[58] Hence, the sample with the lowest proportion of NPs has the advantage of rapidly reaching the steady state, while the sample with the higher proportion revealed the largest H_2 production rate. One point that should be underlined particularly is that the value of the H_2 production rate obtained for the $0.9Pt/TiO_2@rGO$ (9:1) catalyst exceeds *ca.* 2–10 times the values published for similar systems using aqueous methanol solutions as reaction media and involving $Pt/TiO_2/rGO$ in the catalyst.[25,29]

4. Conclusions

Three-dimensional porous $Pt/TiO_2@GO$ and $Pt/TiO_2@rGO$ composite aerogels were prepared using the one-step low-temperature green supercritical CO_2 method. The produced aerogels are intended for the photocatalytic production of H_2 from aqueous methanol solutions. For this application, optimal working operational conditions resulting in the highest H_2 production rate were settled as a 0.5 g_{NPs} L^{-1} catalyst concentration in a 0.5 v/v methanol/water reaction solution. A two-fold increase in the H_2 production was observed when the GO support was mildly reduced to rGO, an effect assigned to the generation of new electronic pathways upon the partial restoration of the graphene network, and the favored adsorption of the methanol in the reduced structure. The moderate H_2 production rate observed when a one-piece monolith was used (180 $\mu mol\ h^{-1} g_{NPs}^{-1}$) was significantly improved (*ca.* 10-fold) when the aerogels were broken into small pieces (1600 $\mu mol\ h^{-1} g_{NPs}^{-1}$), shortening also the time needed to reach the equilibrium from 200 to only 40 min. This enhancement is the result of the improved light exposure of the active sites and increased reagent and product diffusion. Increasing the NPs:rGO ratio from 3:1 to 9:1 caused a 2.7-fold increase in the H_2 evolution due to the reduced amount of shielded, and thus inactive, NPs. Regarding the catalyst composition, low Pt percentages, in the order of 0.9–0.5 wt%, can be used, still giving a high H_2 production rate. In the most favorable conditions, an H_2 production of 18800 $\mu mol\ h^{-1} g_{NPs}^{-1}$ was measured for the $0.9Pt/TiO_2@rGO$ (9:1) aerogel catalyst in aqueous methanol, which is remarkably high compared to the reported similar $Pt/TiO_2/rGO$ systems.

References

1. N.R.A. Mohd Shah, N.N. Mohamad Yunus, W.Y. Wong, K. Arifin, L. Jeffery Minggu, Current progress on 3D graphene-based photocatalysts: From synthesis to photocatalytic hydrogen production, *Int. J. Hydrogen Energy* **2021**, *46*, 9324–9340.

2. H. Nishiyama, T. Yamada, M. Nakabayashi, Y. Maehara, M. Yamaguchi, Y. Kuromiya, Y. Nagatsuma, H. Tokudome, S. Akiyama, T. Watanabe, R. Narushima, S. Okunaka, N. Shibata, T. Takata, T. Hisatomi, K. Domen, Photocatalytic solar hydrogen production from water on a 100-m^2 scale, *Nature* **2021**, *598*, 304–307.

3. S. Guo, X. Li, J. Li, B. Wei, Boosting photocatalytic hydrogen production from water by photothermally induced bi-phase systems, *Nat. Commun.* **2021**, *12*, 1–10.

4. K.C. Christoforidis, P. Fornasiero, Photocatalytic Hydrogen Production: A Rift into the Future Energy Supply. *ChemCatChem* **2017**, *9*, 1523–1544.

5. S. Zhu, D. Wang, Photocatalysis: Basic principles, diverse forms of implementations and emerging scientific opportunities, *Adv. Energy Mater.* **2017**, *7*, 1–24.

6. S. Martha, P. Chandra Sahoo, K.M. Parida, An overview on visible light responsive metal oxide based photocatalysts for hydrogen energy production, *RSC Adv*. **2015**, *5*, 61535–61553.

7. P. Kuang, M. Sayed, J. Fan, B. Cheng, J. Yu, 3D Graphene-Based H_2-Production Photocatalyst and Electrocatalyst, *Adv. Energy Mater*. **2020**, *10*, 1–53.

8. X. Chen, S. Shen, L. Guo, S.S. Mao, Semiconductor-based photocatalytic hydrogen generation, *Chem. Rev.* **2010**, *110*, 6503–6570.

9. O. Ola, M.M. Maroto-Valer, Review of material design and reactor engineering on TiO_2 photocatalysis for CO_2 reduc-tion, *J. Photochem. Photobiol. C: Photochem. Rev.* **2015**, *24*, 16–42.

10. H. Eidsvåg, S. Bentouba, P. Vajeeston, S. Yohi, D. Velauthapillai, TiO_2 as a photocatalyst for water splitting—An ex-perimental and theoretical review, *Molecules* **2021**, *26*, 1–30.

11. G.A. Blengini, C.E.L. Latunussa, U. Eynard, Study on the EU's List of Critical Raw Materials—Critical Raw Materials Factsheets; Final Report, European Comission: Brussels, Belgium, **2020**.

12. Communication from the commission to the European Parliament, the council, the European Economic and social committee and the committee of the regions, Critical Raw Materials Resilience: Charting a Path towards greater Security and Sustainability, **2020,** Available online: https://eur-lex.europa.eu/legal-content/EN/TXT/?uri=CELEX%3A52020DC0474 (accessed on 7 September 2022).

13. T.F. Yeh, J. Cihlář, C.Y. Chang, C. Cheng, H. Teng, Roles of graphene oxide in photocatalytic water splitting, *Mater. Today* **2013**, *16*, 78–84.

14. P. Solís-Fernández, M. Bissett, H. Ago, Synthesis, structure and applications of graphene-based 2D heterostructures, *Chem. Soc. Rev.* **2017**, *46*, 4572–4613.

15. X. Zhou, X. Zhang, Y. Wang, Z. Wu, 2D Graphene-TiO_2 Composite and Its Photocatalytic Application in Water Pollutants, *Front. Energy Res*. **2021**, *8*, 1–10.

16. S. Zhang, B. Li, X. Wang, G. Zhao, B. Hu, Z. Lu, T. Wen, J. Chen, X. Wang, Recent developments of two-dimensional graphene-based composites in visible-light photocatalysis for eliminating persistent organic pollutants from wastewater, *Chem. Eng. J.* **2020**, *390*, 124642.

17. P. Wang, S. Zhan, Y. Xia, S. Ma, Q. Zhou, Y. Li, The fundamental role and mechanism of reduced graphene oxide in rGO/Pt-TiO_2 nanocomposite for high-performance photocatalytic water splitting, *Appl. Catal. B* **2017**, *207*, 335–346.

18. S.S. Roy, A. Cheruvathoor Poulose, A. Bakandritsos, R.S. Varma, M. Otyepka, 2D graphene derivatives as heterogeneous catalysts to produce biofuels via esterification and trans-esterification reactions, *Appl. Mater. Today* **2021**, *23*, 101053.

19. R. Gusmão, M. Veselý, Z. Sofer, Recent Developments on the Single Atom Supported at 2D Materials beyond Graphene as Catalysts, *ACS Catal.* **2020**, *10*, 9634–9648.

20. S. Mao, G. Lu, J. Chen, Three-dimensional graphene-based composites for energy applications, *Nanoscale* **2015**, *7*, 6924–6943.

21. X. Li, J. Yu, M. Jaroniec, Hierarchical photocatalysts, *Chem. Soc. Rev.* **2016**, *45*, 2603–2636.

22. B. Bakbolat, C. Daulbayev, F. Sultanov, R. Beissenov, A. Umirzakov, A. Mereke, A. Bekbaev, I. Chuprakov, Recent developments of TiO_2-based photocatalysis in the hydrogen evolution and photodegradation: A review, *Nanomaterials* **2020**, *10*, 1–16.

23. S. Navalon, A. Dhakshinamoorthy, M. Alvaro, H. Garcia, Metal nanoparticles supported on two-dimensional graphenes as heterogeneous catalysts, *Coord. Chem. Rev.* **2016**, *312*, 99–148.

24. K.M. Yam, N. Guo, Z. Jiang, S. Li, C. Zhang, Graphene-based heterogeneous catalysis: Role of graphene, *Catalysts* **2020**, *10*, 53.

25. M.J. Rivero, O. Iglesias, P. Ribao, I. Ortiz, Kinetic performance of TiO_2/Pt/reduced graphene oxide composites in the photocatalytic hydrogen production, *Int. J. Hydrogen Energy* **2019**, *44*, 101–109.

26. P.S. Mohan, M.K. Purkait, C.T. Chang, Experimental evaluation of Pt/TiO_2/rGO as an efficient HER catalyst via artificial photosynthesis under UVB & visible irradiation, *Int. J. Hydrogen Energy* **2020**, *45*, 17174–17190.

27. P. Zeng, Q. Zhang, X. Zhang, T. Peng, Graphite oxide-TiO_2 nanocomposite and its efficient visible-light-driven photo-catalytic hydrogen production, *J. Alloys Compd.* **2012**, *516*, 85–90.

28. Z. Wang, Y. Yin, T. Williams, H.Wang, C. Sun, X. Zhang, Metal link: A strategy to combine graphene and titanium dioxide for enhanced hydrogen production, *Int. J. Hydrogen Energy* **2016**, *41*, 22034–22042.

29. R.O. Da Silva, F.J. Heiligtag, M. Karnahl, H. Junge, M. Niederberger, S. Wohlrab, Design of multicomponent aerogels and their performance in photocatalytic hydrogen production, *Catal. Today* **2015**, *246*, 101–107.

30. C.C. Lin, T.Y. Wei, K.T. Lee, S.Y. Lu, Titania and Pt/titania aerogels as superior mesoporous structures for photocatalytic water splitting, *J. Mater. Chem.* **2011**, *21*, 12668–12674.

31. A. Borrás, A. Rosado, J. Fraile, A.M. López-Periago, J. Giner Planas, A. Yazdi, C. Domingo, Meso/microporous MOF@graphene oxide composite aerogels prepared by generic supercritical CO_2 technology, *Microporous Mesoporous Mater.* **2022**, *335*, 111825.

32. A. Borrás, J. Fraile, A. Rosado, G. Marbán, G. Tobias, A.M. López-Periago, C. Domingo, Green and Solvent-Free Supercritical CO$_2$-Assisted Production of Superparamagnetic Graphene Oxide Aerogels: Application as a Superior Contrast Agent in MRI, *ACS Sustain. Chem. Eng.* **2020**, *8*, 4877–4888.

33. A. Rosado, A. Borrás, J. Fraile, J.A.R. Navarro, F. Suárez-García, K.C. Stylianou, A.M. López-Periago, J. Giner Planas, C. Domingo, A. Yazdi, HKUST-1 Metal-Organic Framework Nanoparticle/Graphene Oxide Nanocomposite Aerogels for CO$_2$ and CH$_4$ Adsorption and Separation, *ACS Appl. Nano Mater.* **2021**, *4*, 12712–12725.

34. I. Smirnova, P. Gurikov, Aerogel production: Current status, research directions, and future opportunities, *J. Supercrit. Fluids* **2018**, *134*, 228–233.

35. P. Veres, A.M. López-Periago, I. Lázár, J. Saurina, C. Domingo, Hybrid aerogel preparations as drug delivery matrices for low water-solubility drugs, *Int. J. Pharm.* **2015**, *496*, 360–370.

36. A. Borrás, G. Goncalves, G. Marbán, S. Sandoval, S. Pinto, P.A.A.P. Marques, J. Fraile, G. Tobais, A.M. López-Periago, C. Domingo, Preparation and Characterization of Graphene Oxide Aerogels: Exploring the Limits of Supercritical CO$_2$ Fabrication Methods, *Chem. A Eur. J.* **2018**, *24*, 15903–15911.

37. P. Luo, Y. Lin, Further thermal reduction of reduced graphene oxide aerogel with excellent rate performance for supercapacitors, *Appl. Sci.* **2019**, *9*, 2188.

38. N. Naffati, M.J. Sampaio, E.S. Da Silva, M.F. Nsib, Y. Arfaoui, A. Houas, J.L. Faria, C.G. Silva, Car-bon-nanotube/TiO$_2$ materials synthesized by a one-pot oxidation/hydrothermal route for the photocatalytic production of hydrogen from biomass derivatives, *Mater. Sci. Semicond. Process.* **2020**, *115*, 105098.

39. W. Liu, G. Speranza, Tuning the Oxygen Content of Reduced Graphene Oxide and Effects on Its Properties, *ACS Omega* **2021**, *6*, 6195–6205.

40. A. Litke, H. Frei, E.J.M. Hensen, J.P. Hofmann, Interfacial charge transfer in Pt-loaded TiO$_2$ P25 photocatalysts studied by in-situ diffuse reflectance FTIR spectroscopy of adsorbed CO, *J. Photochem. Photobiol. A Chem.* **2018**, *370*, 84–88.

41. P.N.O. Gillespie, N. Martsinovich, Origin of Charge Trapping in TiO$_2$/Reduced Graphene Oxide Photocatalytic Composites: Insights from Theory, *ACS Appl. Mater. Interfaces* **2019**, *11*, 31909–31922.

42. H. Saleem, M. Haneef, H.Y. Abbasi, Synthesis route of reduced graphene oxide via thermal reduction of chemically ex-foliated graphene oxide, *Mater. Chem. Phys.* **2018**, *204*, 1–7.

43. X. Díez-Betriu, S. Álvarez-García, C. Botas, P. Álvarez, J. Sánchez-Marcos, C. Prieto, R. Menéndez, A. de Andrés, Raman spectroscopy for the study of reduction mechanisms and optimization of conductivity in graphene oxide thin films, *J. Mater. Chem. C Mater.* **2013**, *1*, 6905–6912.

44. S. Stankovich, A.D. Dikin, R.D. Piner, K.A. Kohlhaas, A. Kleinhammes, Y. Jia, Y. Wu, S.T. Nguyen, R.S. Ruoff, Synthesis of graphene-based nanosheets via chemical reduction of exfoliated graphite oxide, *Carbon N. Y.* **2007**, *45*, 1558–1565.

45. D. López-Díaz, M. López Holgado, J.L. García-Fierro, M.M. Velázquez, Evolution of the Raman Spectrum with the Chemical Composition of Graphene Oxide, *J. Phys. Chem. C* **2017**, *121*, 20489–20497.

46. P. Makuła, M. Pacia, W. Macyk, How To Correctly Determine the Band Gap Energy of Modified Semiconductor Photocatalysts Based on UV-Vis Spectra, *J. Phys. Chem. Lett.* **2018**, *9*, 6814–6817.

47. P. Munk, F. Kubelka, A Contribution to the Optics of Pigments, *Z. Tech. Phys.* **1931**, *12*, 593–601.

48. Z.A. Lan, G. Zhang, X. Wang, A facile synthesis of Br-modified g-C_3N_4 semiconductors for photoredox water splitting, *Appl. Catal. B* **2016**, *192*, 116–125.

49. H. Zhang, X. Lv, Y. Li, Y. Wang, J. Li, P25-graphene composite as a high performance photocatalyst, *ACS Nano* **2010**, *4*, 380–386.

50. J. Lee, W. Choi, Photocatalytic Reactivity of Surface Platinized TiO_2: Substrate Specificity and the Effect of Pt Oxidation State, *J. Phys. Chem.* **2005**, *109*, 7399–7406.

51. W. Zeng, X. Tao, S. Lin, C. Lee, D. Shi, K. Lam, B. Huang, Q. Wang, Y. Zhao, Defect-engineered reduced graphene oxide sheets with high electric conductivity and controlled thermal conductivity for soft and flexible wearable thermoelectric generators, *Nano Energy* **2018**, *54*, 163–174.

52. W. Wan, R. Zhang, M. Ma, Y. Zhou, Monolithic aerogel photocatalysts: A review, *J. Mater. Chem. A Mater.* **2018**, *6*, 754–775.

53. F. Guzman, S.S.C. Chuang, C. Yang, Role of methanol sacrificing reagent in the photocatalytic evolution of hydrogen, *Ind. Eng. Chem. Res.* **2013**, *52*, 61–65.

54. G.N. Nomikos, P. Panagiotopoulou, D.I. Kondarides, X.E. Verykios, Kinetic and mechanistic study of the photocatalytic reforming of methanol over Pt/TiO_2 catalyst, *Appl. Catal. B* **2014**, *146*, 249–257.

55. K. Shimura, H. Yoshida, Heterogeneous photocatalytic hydrogen production from water and biomass derivatives, *Energy Environ. Sci.* **2011**, *4*, 2467–2481.

56. W.T. Chen, Y. Dong, P. Yadav, R.D. Aughterson, D. Sun-Waterhouse, G.I.N. Waterhouse, Effect of alcohol sacrificial agent on the performance of Cu/TiO_2 photocatalysts for UV-driven hydrogen production, *Appl. Catal. A Gen.* **2020**, *602*, 117703.

57. W.T. Chen, A. Chan, D. Sun-Waterhouse, J. Llorca, H. Idriss, G.I.N. Waterhouse, Performance comparison of Ni/TiO_2 and Au/TiO_2 photocatalysts for H_2 production in different alcohol-water mixtures, *J. Catal.* **2018**, *367*, 27–42.

58. F. Pendolino, G. Capurso, A. Maddalena, S. lo Russo, The structural change of graphene oxide in a methanol dispersion, *RSC Adv.* **2014**, *4*, 32914–32917.

59. J. Curcó, D. Giménez, A. Addardak, S. Cervera-March, S. Esplugas, Effects of radiation absorption and catalyst concentration on the photocatalytic degradation of pollutants, *Catal. Today* **2002**, *76*, 177–188.

60. X. Jiang, X. Fu, L. Zhang, S. Meng, S. Chen, Photocatalytic reforming of glycerol for H_2 evolution on Pt/TiO_2: Fundamental understanding the effect of co-catalyst Pt and the Pt deposition route, *J. Mater. Chem. A Mater.* **2015**, *3*, 2271–2282.

61. J. Yang, D. Wang, H. Han, C. Li, Roles of cocatalysts in photocatalysis and photoelectrocatalysis, *Acc. Chem. Res.* **2013**, *46*, 1900–1909.

62. Communication from the commission to the European Parliament, the council, the European Economic and social committee and the committee of the regions, The European Green Deal, **2019**, Available online: https://eur-lex.europa.eu/legal-content/EN/TXT/?uri=COM%3A2019%3A640%3AFIN (accessed on 7 September 2022).

63. Y. Lu, B. Ma, Y. Yang, E. Huang, Z. Ge, T. Zhang, S. Zhang, L. Li, N. Guan, Y. Ma, Y. Chen, High activity of hot electrons from bulk 3D graphene materials for efficient photocatalytic hydrogen production, *Nano Res.* **2017**, *10*, 1662–1672.

Fully supercritical CO₂ preparation of a nanostructured MOF composite with application in cutaneous drug delivery
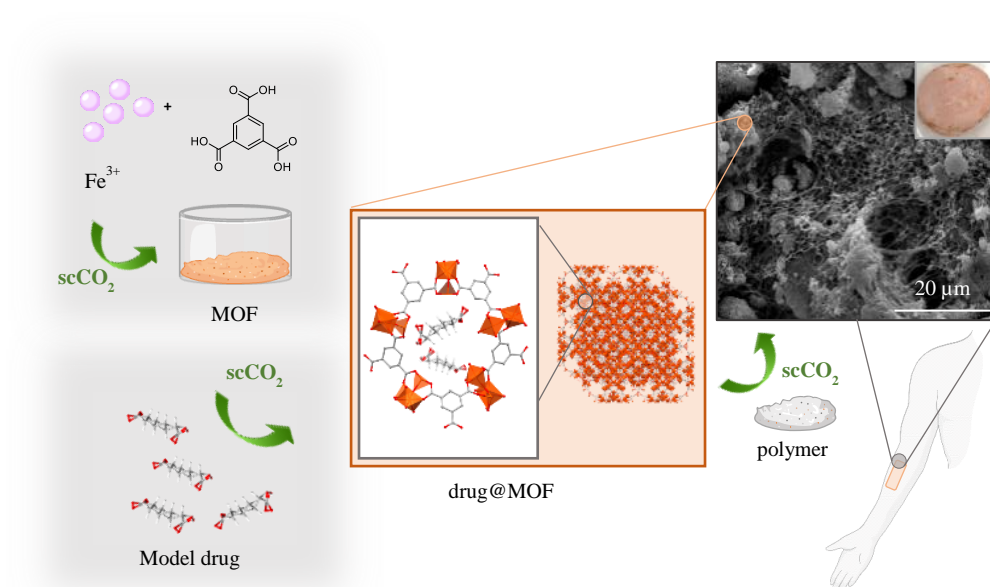
This work demonstrates a sustainable process for the fabrication of MOF-based cutaneous patches using green supercritical CO₂ in each preparation step.

This chapter is based on the following published article:

Abstract

Supercritical CO_2 (scCO_2) technology is used here as an efficient method to assist in the preparation of a cutaneous polymeric formulation based on drug containing metal-organic framework composites. The supercritical fluid is used in three steps: (*i*) as a drying agent for the nanosized mesoporous matrix, (*ii*) as the impregnation vector of a topical antibiotic drug, and (*iii*) as a plasticizing and foaming fluid to obtain dispersions of the hybrid material into a biocompatible polymer, *e.g.*, the macroporous patch. The materials were characterized using solid state technics. The drug delivery and permeation profiles of the patches were investigated using *in vitro* and *ex vivo* tests by using porcine skin. These analyses suggest that scCO_2 impregnation is an easy and fast strategy to prepare composite devices able to progressively release and diffuse the incorporated drug throughout the skin, paving the way to efficiently prepare cutaneous devices for topical or systemic therapies.

1. Introduction

Research in ordered porous materials is currently at an exciting stage in its technological evolution, mainly driven by the discovery of metal-organic frameworks (MOFs).[1] MOFs are defined as crystalline porous materials, built from metal centers connected by polytopic organic linkers. Most of the MOFs reported to date display large surface area (up to 10000 m^2g^{-1}), which is generally concomitant with pore sizes in the micropore range.[2,3] While high values of surface area are desirable for applications related to sorption and/or catalysis, such narrow pores would reduce mass diffusion rate. Additionally, these pores can result to be inaccessible for functionalization or unsuitable for hosting desired large molecules, often limiting the applications of microporous MOFs to processes involving small diameter gasses. In contrast, MOFs with cavities in the range of mesopore (> 2 nm), even having microporous apertures in the micropore range (*ca.* 0.5-1.0 nm) and presenting lower surface area values than the microporous counterparts, have the advantage of high pore volume, with tunable pore sizes, for easy accommodation of large molecules.[4-6] In particular, great progress has been made in the development of the mesoporous metal (Cr, Fe, Sc, Al, V) trimesate MIL-100 family. Among them, iron(III) trimesates, including the crystalline MIL-100(Fe) (crystallographic cages of diameters 2.5 and 2.9 nm) and its semi-amorphous analogue Fe(BTC), have attracted enormous interest for controlled drug delivery applications involving large guest molecules (*e.g.*, drugs, nucleic acids, enzymes), as they both display mesopores and biocompatible features.[7-10] However in case of the MIL-100(Fe) and Fe(BTC) the mesopores are accessible through microporous windows, the large pore volume makes them suitable for the accommodation of drugs due to the possible flexibility of the framework of MOFs and the facile diffusion of the drug inside these pores.[5]

A large variety of methodologies has been established over time to prepare iron(III) trimesates, evolving towards the development of sustainable routes entangling non-toxic solvents. Thereby, micrometric MIL-100(Fe) was first synthetized in a hydrothermal reaction involving Fe(0), fluorhydric acid and trimesic acid (H_3BTC),[11] or Fe(III) and trimesate ligand,[12] with surface areas of *ca.* 1500-2500 m^2g^{-1}; and later, by conversion in water of green rust (Fe(II)/Fe(III)) precursors at room temperature.[13] Afterwards, bench scale procedures for the synthesis of MIL-100(Fe) and Fe(BTC) nanoparticles (NPs) were developed on the basis of a soft reaction involving Fe(III) salts dissolved in water and H_3BTC.[14] In general, Fe(BTC) products have surface areas lower than MIL-100(Fe), in the order of 1000-1200 m^2g^{-1}.

Regardless of the synthetic method, crystalline and semi-amorphous compounds need extensive post-processing washing/activation to attain the mentioned values of surface area.[15] Additionally, bottom-up mass-production methods, currently used to fabricate polymer composite pharmaceuticals, have severe limitations related to high cost and reduced purity of the end product. Toxic and hazardous organic solvents are often needed. Moreover, traditional methods employed in polymer processing imply the use of high temperatures or plasticizers (*e.g.*, chlorofluorocarbons) for polymer viscosity reduction purposes.[16] By the same token, the generation of polluted aqueous waste streams in the processing of biomedical systems, together with the energy needed to remove water from products, make a significant contribution to global environmental pollution. As a consequence, major advances are required to reduce the use of both volatile/toxic organic solvents and water in the pharmaceutical and biomaterials industries. Regarding biomedical applications and sustainability, the use of CO_2, classified as a safe solvent in drugs and food manufacturing by the American and European medicine agencies, in supercritical CO_2 ($scCO_2$) technology is widely presented as a green alternative during the preparation of pharmaceutical formulations.[17,18] In this context, the objective of this work is the development of an eco-friendly, fast, and economically attractive three-steps approach based on $scCO_2$ for the development of a medical device (patch), intended for cutaneous sustained drug release. The process involves the use of $scCO_2$ in all the three steps of the cutaneous patch preparation: *(i)* synthesis of a nanoparticulate mesoporous iron(III) trimesate matrix (Fe(BTC)) in dioxane and $scCO_2$ drying, *(ii)* $scCO_2$ impregnation of the matrix with an active pharmaceutical agent (API), and *(iii)* formulation of the drug-loaded matrix with a polymer and simultaneous shaping onto a cellular pellet to obtain skin patches by $scCO_2$ foaming.

The precipitation of Fe(BTC) has previously been explored in mixtures of $scCO_2$ and ionic liquid (IL) solvents; however, the recovered product was highly contaminated with difficultly removable IL.[19] Currently, there is a long experience in eco-friendly techniques for MOFs preparation and activation involving utterly $scCO_2$.[20-22] Based on this knowledge, this work primarily addresses the design of a new, one-pot sustainable $scCO_2$ method to obtain Fe(BTC) NPs with high surface area, *i.e.*, free of adsorbed non-volatile solvents, which reduces the need of post-processing treatment, since the solvent is eliminated from the reaction medium as a gas. This multi-faceted research for green chemistry continues by using the known advantages of $scCO_2$ in the processing of MOFs-based drug delivery systems.[23] Over the past few decades, $scCO_2$ has been presented as an excellent transport vector to impregnate solid matrices, as this approach enables the elimination of the use of organic solvents and increases solute diffusivity

in narrow pores.[24,25] However, only few reports have been found describing the use of scCO$_2$ for drug loading of MOFs,[26,27] which result in an unexplored field further studied in this work. Azelaic acid (AzA), an antibacterial and anti-inflammatory active compound, normally used in the dermatological treatment of skin disorders, was here chosen as the API to analyze the scCO$_2$ impregnation of iron(III) trimesate. AzA has been previously used as a linker in a bioMOF,[28] and also incorporated within the pores of different mesoporous MOFs by using a liquid diffusion approach.[29]

Originally, this work addresses the preparation of MOFs-based skin patches obtained by applying scCO$_2$ foaming technology. Foams are defined as materials with high porosity at the microscale and low density, which are particularly attractive in tissue engineering and transdermal drug delivery, among other applications.[30] The use of cutaneous patches is a valuable solution for the administration of drugs with low oral bioavailability, as it is the case of AzA, and is alternative to reduce fluctuations in drug levels. Environment-friendly low molecular weight poly(vinyl-alcohol) (PVA) was selected as a typical biodegradable and water-soluble synthetic polymer to provide patches with suitable topical properties (*i.e.,* biocompatibility, prophylaxis against infections, lubricity, *etc.*).[16] Aside, PVA shows good mechanical strength and thermal stability, excellent film-formation qualities and commercial low-cost availability. For pharmaceutical applications, it is considered as an essential technological innovation to use environmentally friendly blowing agents for foaming instead of toxic chloro- and hydrochloro-fluorocarbons. Hence, scCO$_2$ appears again as a suitable strategy for this purpose. Actually, scCO$_2$ foaming technology has been widely used in the production of microcellular glass polymers,[31] also for the preparation of patches,[32] but never in the preparation of MOF-based cutaneous patches. Transdermal drug delivery patches are built here by composing, in a high pressure CO$_2$ atmosphere, pellets of PVA and particulate iron(III) trimesate loaded with AzA. Controlled expansion of scCO$_2$ was applied to obtain the patches with a cellular morphology, which facilitates fluids diffusion.[33] Once prepared, the drug delivery and stability of the patches were studied using *in vitro* and *ex vivo* conditions. The efficiency of the supercritically processed patches was compared with devices of similar composition made *via* a press-molding approach using previously optimized methods.[34]

The main novelty in this work relies on the fact that scCO$_2$ has been used in all the steps of the fabrication of MOF-based cutaneous patches (*i.e.,* synthesis of the porous MOF, drug impregnation and patches composing and foaming) avoiding the use of toxic solvents by combining scCO$_2$ foaming and drying processes.

2. Materials and methods

2.1. Materials

All reactants were commercially obtained and used without further purification. The used Fe(III) reagents (Merck) for the preparation of Fe(BTC) and MIL-100(Fe) were iron(III) nitrate nonahydrate ($Fe(NO_3)_3 \cdot 9H_2O$) and iron(III) chloride hexahydrate ($FeCl_3 \cdot 6H_2O$), respectively. The Fe(III) precursors were reacted, respectively, with H_3BTC, supplied by Merck, and ethyl ester 1,3,5-benzenetricarboxylic (EE-BTC, 97%), obtained from Alfa Aesar[TM]. AzA and PVA (MW 72000, 98% hydrolyzed), used for drug impregnation and patch formation, respectively, were both obtained from Merck. The solvents, compressed CO_2 (99.95 wt.%), dimethyl sulfoxide (DMSO) and 1,4-dioxane, were delivered by Carburos Metálicos S.A., Fischer Scientific and PanReac AppliChem, respectively. Ethanol (EtOH), used for the washing of the MOFs, was purchased from Scharlau. Phosphate-buffered saline (PBS) solution was obtained from Sigma Aldrich. The adhesive film (Leukoflex[®]) was purchased from a local drug store.

2.2. Methods

High pressure synthesis based on scCO₂ has been used in all the steps of the fabrication of MOF-based cutaneous patches: *(i)* synthesis of the porous MOF, *(ii)* drug impregnation and *(iii)* patches composing and foaming. Conventional synthesis methods were also applied in each step for comparison. Table 1 shows the experimental procedure used to obtain each different sample.

Table 1. Experimental procedures used to obtain the different samples showing some of their main characteristics.

Sample	Reagents	Method	Characteristics	
Iron(III) trimesate synthesis			**crystal size [nm]**	**Sa [m^2g^{-1}]**
Fe(BTC)	Fe(III)/ H$_3$BTC	scCO$_2$	10-20 (agg. 100-300)	1290
MIL-100(Fe)	Fe(III)/ H$_3$BTC	hydrothermal	300-700	1542
AzA impregnation			**AzA loading [wt%]**	**Sa [m^2g^{-1}]**
sc_AzA@Fe(BTC)	Fe(BTC)/ AzA	scCO$_2$ diffusion	17 ± 3.0	35
w_AzA@Fe(BTC)	Fe(BTC)/ AzA	water diffusion	7.9 ± 2.2	
sc_AzA@MIL-100(Fe)	MIL-100(Fe)/ AzA	scCO$_2$ diffusion	15 ± 2.0	98
w_AzA@MIL-100(Fe)	MIL-100(Fe)/ AzA	water diffusion	8.9 ± 0.4	
Patches preparation			**AzA permeability 8 h [%]**	**J 24h [$\mu gcm^{-2}h^{-1}$]**
sc@PVA	sc_AzA@MIL-100(Fe)/PVA	scCO$_2$ foaming	7.5 ± 1.6	146
pm@PVA	sc_AzA@MIL-100(Fe)/PVA	press molding	6.0 ± 0.7	60

2.2.1. Fe(III) trimesates synthesis methods

Two different methods were used for the synthesis of the two studied iron(III) trimesate phases: NPs of Fe(BTC) were precipitated by a scCO$_2$ route, while small microcrystals of MIL-100(Fe) were hydrothermally synthesized.

Synthesis of Fe(BTC) aided by scCO$_2$: The synthesis pathway is schematized in Fig. 1(a). Two vials were prepared, each with 0.20 g of H$_3$BTC (0.95 mmol) ultrasonically dispersed in 1.5 mL of dioxane. Then, 0.58 g of Fe(NO$_3$)$_3$.9H$_2$O (1.44 mmol) were added to each vial and shaken to homogenize the mixtures. A colloidal orange powder instantaneously precipitated into the vials, which rapidly gelified. One of these vials was left to partially dry under atmospheric conditions. The second vial was placed in a high-pressure reactor (TharDesign, 100 mL volume) for the supercritical processing, which was sealed and then filled with liquid CO$_2$ at 6 MPa. The reactor was heated up to 70 °C, and finally pressurized at 20 MPa. The vial was

maintained under these conditions with stirring for 48 h. Finally, system depressurization was carried out by the slow and isothermal release of CO_2, and the reactor was allowed to cool down to ambient temperature. The as-synthetized powder, from either the air-dried or supercritical-dried vial, was washed by centrifugation with water (2 x 10 mL) and EtOH (2 x 10 mL), and then dried overnight under vacuum in a desiccator. Sample Fe(BTC) was recovered with a yield of 70 wt.%, calculated with respect to the activated MOF.

Synthesis of MIL-100(Fe) by hydrothermal method: MIL-100(Fe) was synthetized following a reported method.[35] In short, 2.70 g of $FeCl_3 \cdot 6H_2O$ (10 mmol) and 2.24 g of EE-BTC (6.6 mmol) were dispersed in 50 mL of H_2O. The mixture was placed in a Teflon-lined autoclave and heated at 130 ℃ for 3 days. Then, the orange solid was recovered by filtration and washed with absolute EtOH (3 x 10 mL). The solid was then suspended in 1 L of EtOH, refluxed under stirring for 3 h, and then, the same procedure was carried out in deionized water. The solid was then suspended in a KF solution (0.1 M, 100 mL, 3 h). Finally, it was suspended in 150 mL of Milli-Q water (2 h, RT) and recovered by filtration.

2.2.2. Drug impregnation

scCO$_2$ and water diffusion impregnation methods were used to obtain drug loaded MOF systems.

Diffusion from scCO₂: in the supercritical approach (Fig. 1b), previous to drug impregnation, 0.15 g of each prepared iron(III) trimesate sample (Fe(BTC) or MIL-100(Fe)) were activated at 150 ℃ for 20 h under secondary vacuum. During the activation process, the color of the MOF changed from light orange, corresponding to the hydrated phase, to brown. The activated MOF was added to a vial, covered with paper filter, and placed in the 100 mL high-pressure reactor. In a different vial, 0.10 g of AzA were dissolved in 200 μL of DMSO. A small stirring bar was added to this vial and placed beside the first one in the reactor. During manipulation, the vials and reactor were maintained under N_2 atmosphere. The vessel was then filled with liquid CO_2 up to 6 MPa, heated at 60 ℃, and finally pressurized to 20 MPa, thus reaching supercritical conditions for the fluid, which were maintained overnight, while gently stirring the vial of the drug. Finally, the temperature was decreased to 40 ℃, the CO_2 was released, and the vessel was allowed to cool down to ambient temperature. An orange dry powder was recovered from the MOF vial, while the vial of the drug was visually empty. Drug-loaded samples were named sc_AzA@Fe(BTC) and sc_AzA@MIL-100(Fe).

Diffusion from water: for comparison purposes, drug loading was also performed using a previously described conventional water diffusion protocol.[36] In this case, the AzA aqueous solubility should be first improved by deprotonating the molecule to Az^{2-}. The deprotonated form (Az^{2-}) of the acid (pKa1 = 4.55 and pKa2 = 5.60) was prepared by dissolving AzA (0.10 g, 0.53 mmol) in 50 mL of a NaOH aqueous solution (0.02M) using a molar ratio 1:2.[37] The final pH of the solution was adjusted to 6 with HCl (0.01M). After the pH of the solution was adjusted to 6, 0.06 g of either Fe(BTC) or MIL-100(Fe) were suspended in 20 mL of the previously prepared Az^{2-} solution under stirring for 24 h at room temperature. The drug-loaded materials, named as w_AzA@Fe(BTC) and w_AzA@MIL-100(Fe), were recovered by filtration and washed with H_2O (3 x 5 mL).

2.2.3. Patches preparation

scCO$_2$ and press molding methods were used to formulate pellets of PVA, intended to be used as patches, composed of the AzA supercritically impregnated MOF.

scCO₂ approach: in the supercritical method (Fig. 1c), the pellets were prepared by adding a small amount of DMSO as a plasticizer for the polymer to overcome the foaming drawbacks of extended hydrogen bonding in PVA. In a vial, 0.10 g of the supercritically impregnated sc_AzA@MIL-100(Fe) sample were dispersed in 300 µL of DMSO. 0.10 g of PVA were then added and mixed with a spatula, obtaining a homogenous dark orange dispersion. Almost immediately, the mixture started to swell. The vial was placed in the 100 mL high-pressure reactor, which was then filled with liquid CO_2 up to 6 MPa, heated at 60 ºC, and finally pressurized to 20 MPa, maintaining these conditions for 24 h. Finally, the temperature was decreased to 40 ºC, the CO_2 was isothermally released with *ca.* 0.5 mL/min flow rate and the vessel was allowed to cool to ambient temperature. As a result, a light orange 10 mm-diameter and 2 ± 0.5 mm-thickness pellet was obtained and denoted as sc@PVA.
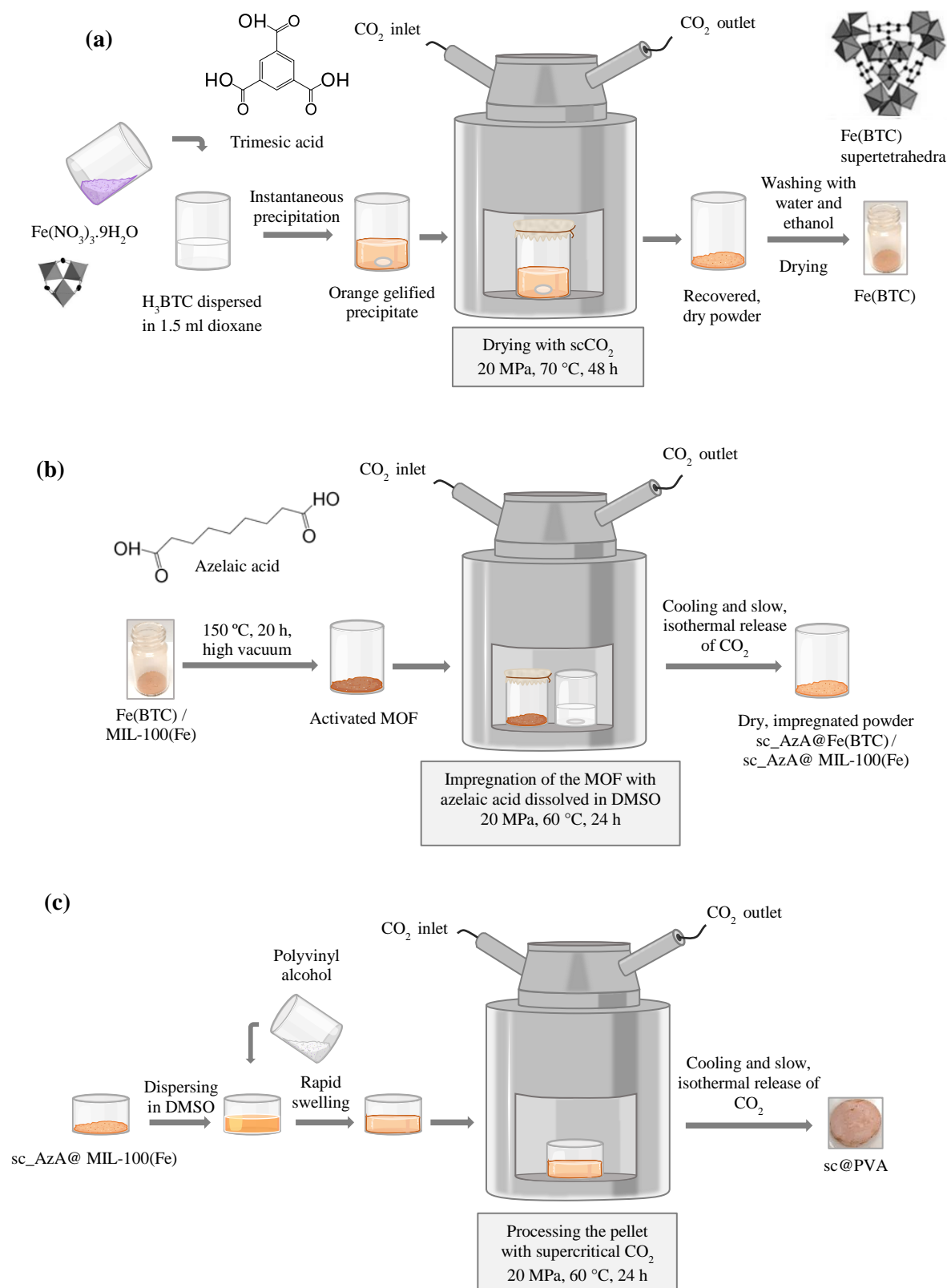
Figure 1. Schematic representation of the scCO$_2$ method used for: (a) the synthesis of Fe(BTC) NPs, (b) their impregnation, and (c) pelletization with a polymer.

Press molding: for comparison, composite patches were also prepared by an easy and rapid compression press molding approach, following a procedure described elsewhere.[29] Briefly,

0.10 g of supercritically impregnated MOF sc_AzA@MIL-100(Fe) sample and 0.10 g of PVA were mixed by manual milling. The resulting powder was readily put onto a 12 mm diameter-size wafer mold and pressed at 1 ton for 1 min, obtaining pellets of 0.6 ± 0.1 mm thickness. These samples were denoted as pm@PVA. Control patch was prepared by press molding (control@PVA) using a mixture of 0.17 g of PVA and 0.03 g of AzA, corresponding to the amount of AzA found in the sample sc_AzA@MIL-100(Fe). All these experiments were quadrupled performed.

2.3. Characterization

2.3.1. Solid state characterization

Structural characterization was performed by powder X-ray diffraction (XRD) in a Siemens D5000 using Cu Kα incident radiation, from $2\theta = 2$ to 30º with a step scan of 0.02º. Fourier transform infrared (FTIR) spectroscopy in KBr pellets was used to analyze the molecular composition of the pristine and impregnated MOFs. Dynamic light scattering (DLS, Zetasizer Nano ZS Malvern Inst.) was used to estimate particle size distribution after bath-sonication of the MOF particles dispersed in water during 1 h. The textural properties were determined by N_2 adsorption/desorption experiments at -196 ℃ using an ASAP 2020 Micromeritics Inc. MOF samples obtained before and after drug impregnation were degassed during 24 h, using temperatures of 150 ℃ for the former and only 70 ℃ for the later to avoid drug evaporation. Brunauer-Emmet-Teller (BET) surface area (Sa) was estimated in the relative pressure range of *ca.* 0.05-0.20. Morphological features of the precipitated MOF particles were examined by using scanning (SEM, Quanta FEI 200) and transmission (TEM, JEOL 1210) electron microscopes. SEM pictures of the cross-section of the foamed PVA composites were obtained after immersing the sample in liquid N_2 and breaking by impact the frozen pellets.

2.3.2. Encapsulated drug quantification

The amount of encapsulated AzA was calculated by combining thermogravimetric analysis (TGA) and high-performance liquid chromatography (HPLC). TGA was performed using a Perkin Elmer STA 6000 under an air flow of 100 mLmin^{-1} and a ramp of 5 ℃min^{-1}. The method to extract the analytes (H_3BTC and AzA) is based on a method previously described.[38] H_3BTC and AzA extraction were performed by degrading a known amount of loaded MOF (*ca.* 10 mg) with PBS (pH=7.4, 1 M, stirring 24 h). Then 10 mL of MeOH were added and the mixture was stirred for an additional hour. The samples were centrifuged (10000 rpm for 10 min) and filtered through 0.2 µm sterile syringe filter. Finally, the supernatants were evaporated, and the dry

residue was dissolved in 4 mL of MeOH and 4 mL of acetonitrile. Prior to the injection into the HPLC system, samples were diluted in the mobile phase. By HPLC, quantification of H_3BTC and AzA was performed using a reversed phase Jasco LC-4000 series system, equipped with a PDA detector MD-4015 and a multisampler AS-4150 controlled by ChromNav software (Jasco Inc., Easton, MD, USA). A purple ODS reverse-phase column (5 µm, 4.6 x 150 mm^2 Análisis Vínicos) was employed. AzA was analyzed after its derivatization to der-AzA, as it is described elsewhere.[39] For H_3BTC, the mobile phase consisted of a 50:50 solutions (v/v) of MeOH and buffer 0.04 M, pH = 2.5 (NaH_2PO_4 (2.40 g, 0.02 mol) and Na_2HPO_4 (2.84 g, 0.02 mol) dissolved in 1 L of Milli-Q water, with pH adjusted to 2.5 using H_3PO_4 (85%)). For der-AzA, the mobile phase was a 20:80 solutions (v/v) of acetonitrile and buffer 0.5 mM, pH = 4 (NH_4HCO_3 (0.39 g, 0.5 mmol) dissolved in 1 L of Milli-Q water, with pH adjusted to 4 using HCl 1 M). The injection volume was set at 30 µL with a flow rate of 1 mLmin^{-1} and the column temperature was fixed at either 25 or 40 ºC for H_3BTC or der-AzA, respectively. The standard calibration curves showed a good correlation coefficient $R^2 = 0.99$. The chromatogram of standard solutions showed a retention time (rt) of 3.51 min (identified as H_3BTC, λ_{max} at 225 nm), and 6.67 min (identified as der-AzA, λ_{max} at 255 nm). All experiments were carried out in triplicate ($n = 3$).

2.3.3. AzA *ex vivo* permeation test

Fresh porcine ears were obtained from a local slaughterhouse and after cleaning, the outer region of the ear was cut. Afterwards, the skin was dermatomed to 1.2 mm (using a Brown air Dermatome Zimmer) and stored at -20 ºC. Skin samples were placed in a simple model of Franz diffusion chambers with the inner area of the *stratum corneum* faced to the donor compartment and the dermis to the receptor one, leaving an available diffusion surface of 0.62 cm^2. The receptor compartment was filled with 5 mL of PBS (pH = 7.4), and kept at 32 ºC for 24 h. Both different formulation patches together with the control (sc@PVA, pm@PVA, and control@PVA) were readily placed on the top of the *stratum corneum* (final patches contact surface = 0.41 cm^2) and covered by an impermeable polymeric film (Leukoflex®). *Ex vivo* permeation studies were performed during 24 h, collecting 1 mL of the receptor fluid after 1, 4, 8, and 24 h, being immediately replaced with 1 mL of fresh medium at the same temperature. The obtained aliquots were analyzed by HPLC in order to quantify the AzA and H_3BTC content. The diffusion flux (J) was calculated using the following equation:

$$J = m/At$$

where *J* is the flux of a mass of compound *m* moving through a cross-sectional area *A* during *t*. It has to be noted that identical AzA content was used in all prepared patches. Finally, the patches remaining on the skin surface were removed, cleaning the skin with fresh PBS. Later, the skin was dried and cut for the AzA and H_3BTC quantification following an extraction procedure described elsewhere.[40] It should be noted that the amount of the possible ligand leached during the drug diffusion was measured in order to determine the MOF stability. 0.5 mL of sodium dodecyl sulphate (SDS, 0.01 M) and 1 mL of PBS (0.5 M, pH = 7 (NaH_2PO_4 (30 g, 0.25 mol), and Na_2HPO_4 (35.5 g, 0.25 mol)) were added to *ca.* 0.20 g of skin in an assay tube. This mixture was homogenized by grinding with a Potter-Elvehjem tissue grinder, and then sonicated for 1 h. About 15 mL of MeOH were added and the mixture was stirred for 2 h. Then, samples were centrifuged at 10000 rpm for 10 min and filtered through 0.2 μm sterile syringe filter. Finally, the supernatants were evaporated, and the dry residue was dissolved in 4 mL of MeOH and 4 mL of acetonitrile. Prior to the injection into the HPLC system, samples were diluted in the mobile phase (buffer 0.5 M, with the pH adjusted to 7 using H_3PO_4 (85%)). All the *ex vivo* studies were carried out in quadruplicate (*n* = 4) in different days. The normality of data distribution was tested by one-way ANOVA test. Data are shown as the mean and the standard deviation. A value of $p < 0.05$ was considered statistically significant.

3. Results and discussion

3.1. One-pot synthesis of Fe(BTC) aided by $scCO_2$

Associated with their large potential in relevant industrial applications (separation and catalysis, among others), many different synthetic methods have been proposed for the preparation of benchmarked iron(III) trimesate MOFs, with a clear tendency to safety and sustainability (*e.g.,* avoiding dangerous organic solvents, harsh acids and high temperatures).[41] For this reason, several methods based on water have been developed to synthetize crystalline MIL-100(Fe) or semi-amorphous Fe(BTC) materials. This work focuses on developing an alternative, based on the use of green $scCO_2$ for the straightforward preparation of Fe(BTC) with high surface area. The synthesis is carried out by mixing an Fe(III) salt (*e.g.*, $Fe(NO_3)_3$) and H_3BTC. However, none of these reagents is soluble in $scCO_2$ and, as a consequence, an aid solvent need to be used. Dioxane was selected as a cosolvent (volumetric ratio with respect to dense CO_2 of 1.5 v%), since it has two Lewis-basic oxygen atoms able to help in the deprotonation of the H_3BTC during iron(III) trimesate synthesis. Prior to the $scCO_2$ addition, the mixing of the Fe(III) salt and H_3BTC in a small amount of dioxane produced the immediate formation of a gel. XRD analysis of this gel, after drying under atmospheric conditions, and further washing and vacuum

drying, indicates that Fe(BTC) was likely already formed at this stage, as the pattern of this compound corresponded to that of the supercritically treated end compound (sample Fe(BTC) air dried in Fig. 2(a)). This observation indicates that, in the supercritical method, the main endeavor of scCO$_2$ is to dry this gel in a controlled way to obtain and improved end product. The important peak broadening in the Fe(BTC) XRD pattern indicates a high degree of structural disorder and small crystal size for this semi-amorphous solid. On the contrary, the XRD pattern of the hydrothermally formed MIL-100(Fe) is consistent with the simulated pattern from single-crystal structural data.[42]
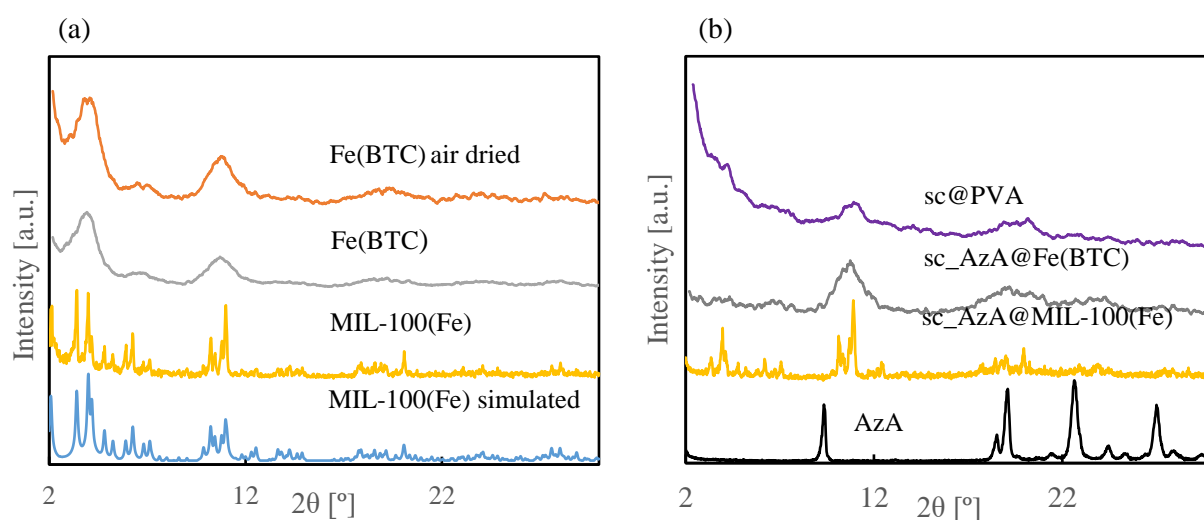

Figure 2. XRD patterns obtained for: (a) pristine iron(III) trimesate samples and simulated MIL-100(Fe), and (b) impregnated samples with AzA and composed with PVA, in both cases processed with scCO$_2$.

FTIR spectra (Fig. 3(a)) of Fe(BTC) and MIL-100(Fe) samples exhibited representative bands of Fe(III) trimesate. One of the most remarkable bands in these spectra is the C=O stretching vibration at *ca.* 1700 cm^{-1}, corresponding to free carboxylic acid, assigned to unreacted trimesic acid. It is worth to mention that the intensity ratio of the bands BTC (1625 cm^{-1})/H$_3$BTC (1700 cm^{-1}) was significantly smaller for the as-synthetized Fe(BTC) than for the as-synthetized MIL-100(Fe) (before washing procedure), and additionally an intense peak at *ca.* 1250 cm^{-1} was observed in the latter assigned to the C-H in-plane bending mode of H$_3$BTC. These observations indicate that the as-synthetized sample prepared under supercritical conditions contains less amount of residual H$_3$BTC than as-synthetized MIL-100(Fe), thus facilitating a priori their posterior purification. Thus, while the Fe(BTC) sample was washed only with water/ethanol, the MIL-100(Fe) purification required a further washing with KF (see experimental section).

After these specific washing steps, the band of the free acid was very small in the spectra of both studied samples Fe(BTC) and MIL-100(Fe), indicating low amount of residual reagent in the pores. Additionally, for the supercritical process, the elimination of dioxane cosolvent during depressurization at the end of the process was supported by the absence of C-H bands at 2800-3000 cm^{-1}. Its elimination can be justified by the CO_2-philic character of the two ether oxygen atoms in dioxane, which makes dioxane highly miscible in scCO_2.[43] This fact is extremely advantageous to reduce the toxicity risks associated to the use of dioxane in the preparation of pharmaceutical formulations.


(a)

(b)
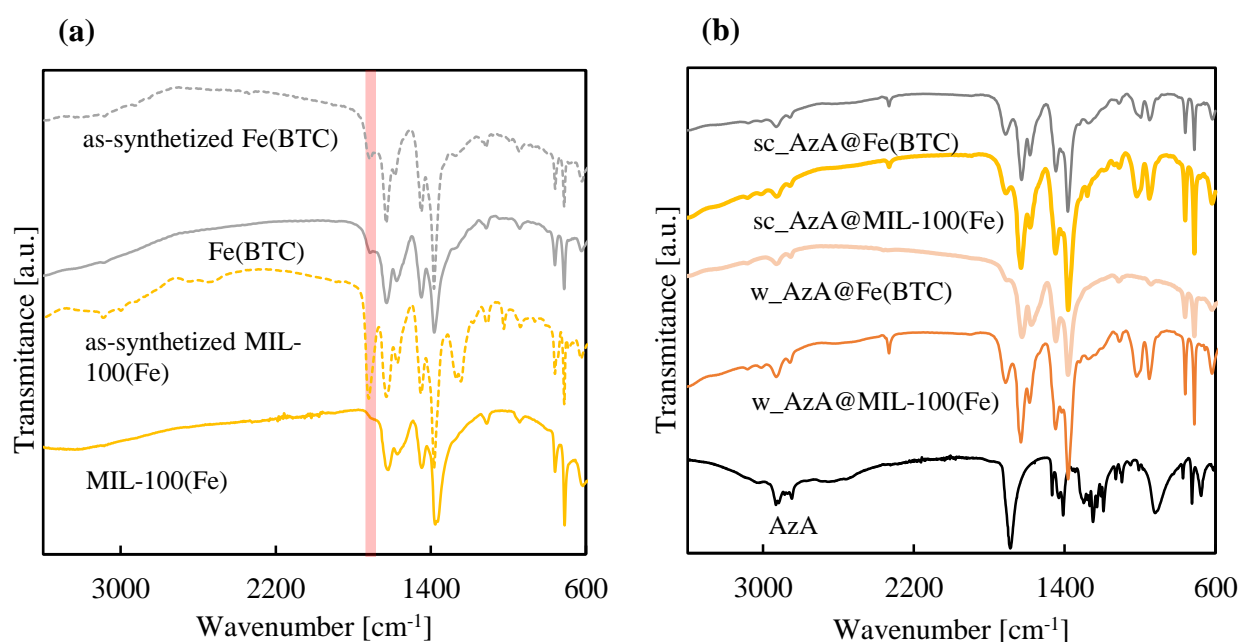
Figure 3. FTIR spectra of: (a) pristine MOFs before (as-synthetized) and after applying the washing procedure, all of them exhibiting representative carboxylate bands at 1624 cm^{-1} for C=O stretching, and at 1442 and 1371 cm^{-1} for -O-C-O- asymmetric and symmetric vibrations. C-H benzene bending vibrations were visible at 1082 and 1043 cm^{-1} (out-of-plane), and at 759 and 703 cm^{-1} (in-plane); and (b) impregnated samples with AzA.

Particles of iron(III) trimesate prepared by the supercritical and hydrothermal methods differ not only in the structure, *e.g.*, semi-amorphous and crystalline, but also in the mean particle size that was analyzed at the dry state (electronic microscopy) and suspended in water (light scattering). The morphological analysis performed by electronic microscopy evidences different habits for the precipitated samples. Compared to the relatively well-faceted submicrometric octahedral crystals (mostly below 0.5 µm) observed by SEM in the MIL-

100(Fe) sample (Fig. 4(a,b)), the near spherical NPs observed for Fe(BTC) were considerably smaller, although highly aggregated (Fig. 4(c,d)).
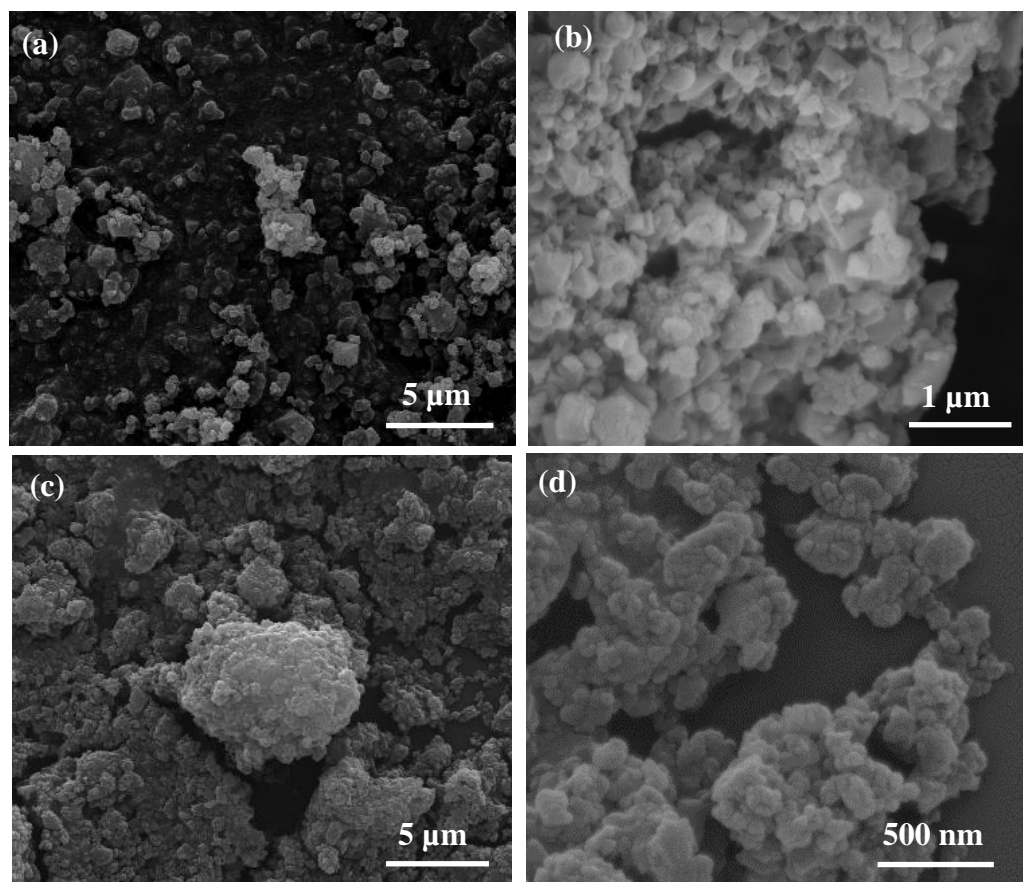

Figure 4. SEM images at different magnifications of samples: (a,b) MIL-100(Fe), and (c,d) Fe(BTC).

To estimate the size of the Fe(BTC) NPs, the use of TEM images becomes necessary (Fig. 5). Analysis of TEM images indicates the formation of very small particles of *ca.* 10-20 nm that agglomerate in structures of *ca.* 100-300 nm. For the MIL-100(Fe) hydrothermally precipitated sample, the DLS volumetric particle size distribution ranged between 300 and 700 nm with a mean hydrodynamic particle size of *ca.* 400 nm (Fig. 6). On the contrary, for the Fe(BTC)

supercritically obtained sample, the size given by DLS measurements was in the range of 200-350 nm, indicating the size of the aggregates.
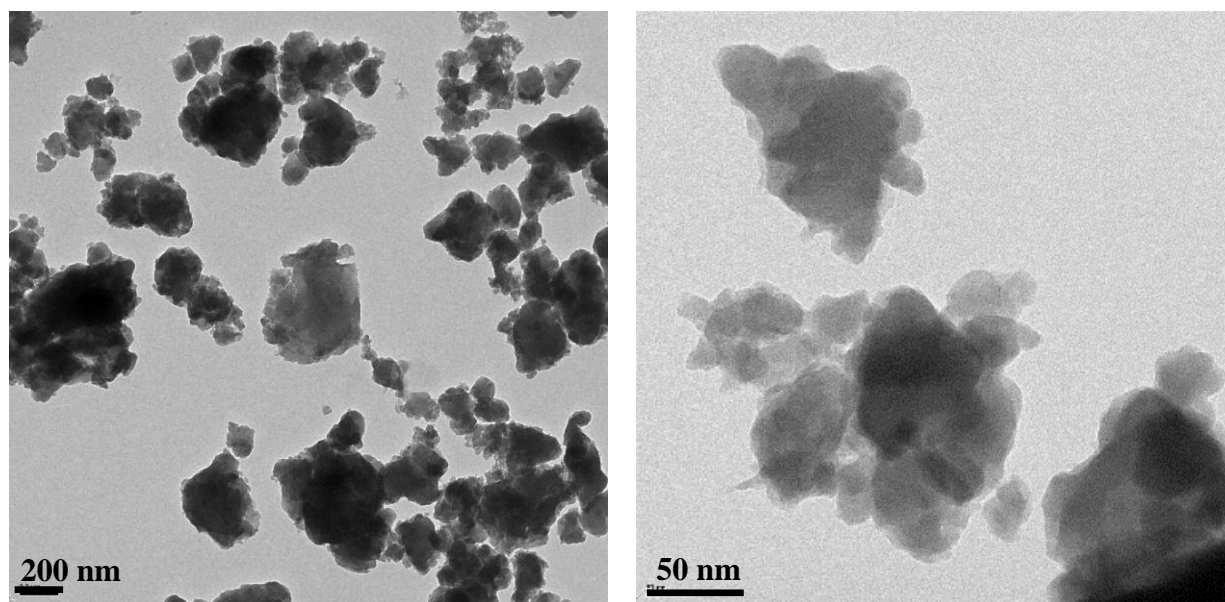

**Figure 5.** TEM images at different magnifications of sample Fe(BTC).
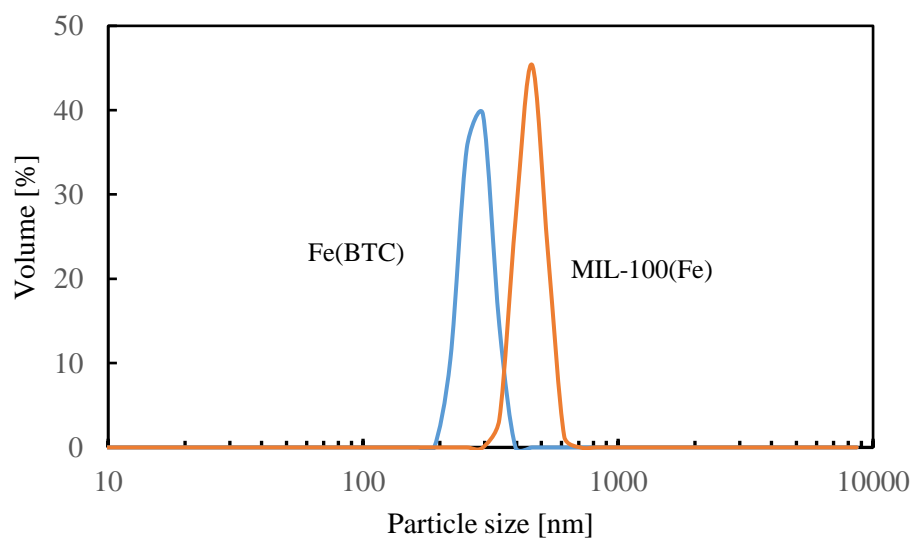
Figure 6. DLS measurements of the precipitated MOFs.

The permanent porosity of the synthetized iron(III) trimesate phases was determined by N_2 sorption measurements at low temperature (Fig. 7). MIL-100(Fe) and Fe(BTC) displayed a type I isotherm (IUPAC classification), with enhanced N_2 adsorption at low relative pressures corresponding to the filling of the small mesopores. A surface area value of 1542 m^2g^{-1} was measured for the MIL-100(Fe) microcrystals, while this parameter was slightly reduced for Fe(BTC) to a value of 1290 m^2g^{-1}. According to the BET theory, the parameter C in this equation is exponentially related to the energy of monolayer adsorption.[44] For the studied samples, the increase of the value of C from 120 in MIL-100(Fe) to 220 in Fe(BTC) is associated with adsorption on high-energy surface sites for the later caused by defects on the pore walls. Both studied iron(III) trimesate systems display some capillary condensation accompanied by hysteresis at high relative pressure, indicating mesoporosity originated from interparticle void.
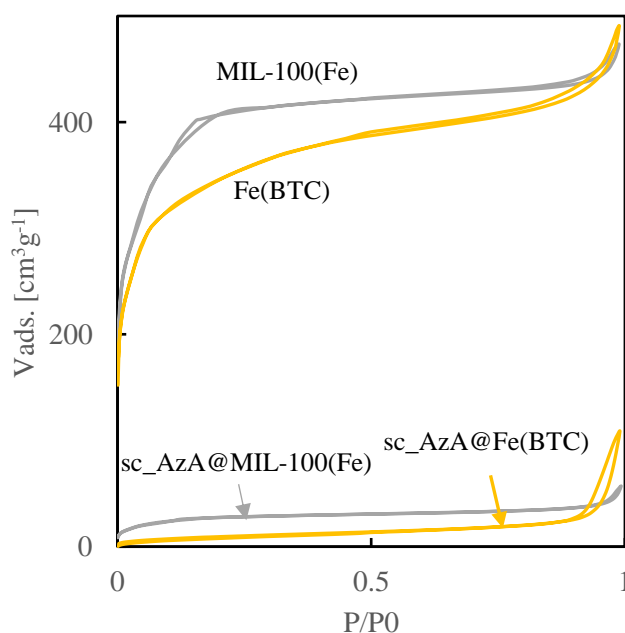

Figure 7. N_2 adsorption-desorption isotherms obtained for the pristine and scCO$_2$ impregnated MOFs.

3.2. AzA-loaded MOF formulations

AzA is loaded into the pores of iron(III) trimesate MOFs by impregnation through the diffusion of the guest from either a supercritical solution or a liquid solvent, *i.e.,* water. In the supercritical approach, a very small amount of DMSO co-solvent (0.2 v%) was added to shorten the impregnation time due to the low solubility of AzA in scCO$_2$ under working conditions (in the order of 10^{-6} mole fraction).[45] In this line, AzA is highly soluble in DMSO (*ca.* 10 mgmL^{-1}), which is a solvent widely used in the pharmaceutical industry and partially miscible with

scCO$_2$.[46] Deprotonated Az^{2-} aqueous solutions were used in the conventional liquid impregnation approach. The drug content of the different impregnated samples was determined by both TGA and HPLC methods (Table 2). Remarkably, AzA loadings using the scCO$_2$ impregnation route was around the double of the values reached using conventional liquid impregnation. This result, stressing the interest of the supercritical impregnation, could be explained by the important adsorption competition stablished between solvent and solute molecules for the substrate sorption sites in the case of water impregnation. This competition is eliminated in scCO$_2$, since supercritical fluids are essentially not adsorbed, thus allowing higher drug loadings than in conventional liquids. Further, for both impregnation solvents, AzA impregnation in Fe(BTC) was on a similar range than that obtained for the MIL-100(Fe). Therefore, we can conclude here that scCO$_2$ is the best option to attain high drug loadings.

Table 2. AzA loading (wt%) measured with different techniques, *e.g*., TGA and HPLC.

Sample	AzA loading [wt%]		Average (%)	Error (%)
	TGA	HPLC		
sc_AzA@Fe(BTC)	19	15	17	3.0
w_AzA@Fe(BTC)	8.5	7.3	7.9	0.9
sc_AzA@MIL-100(Fe)	13	16	15	2.2
w_AzA@MIL-100(Fe)	8.6	9.1	8.9	0.4

Aside from an important cargo loading, the MOFs structures were maintained, as evidenced by XRD analysis (Fig. 2(b)). However, the diffraction peaks at low angles ($< 3.8º$) observed for the pristine solids, representative of the presence of mesoporous cages, disappeared (*e.g.,* sc_AzA@Fe(BTC)) or were reduced in intensity (*e.g.*, sc_AzA@MIL-100(Fe)) due to mesopore filling effect with the organic drug. In addition, no reflections of AzA crystals were observed in the XRD patterns of the drug-loaded products, indicating that the drug was incorporated into the pores molecularly by adsorption or in an amorphous form due to small size. In agreement to this, N$_2$ adsorption isotherms after AzA entrapping indicate almost no residual porosity for these materials, with surface area values < 100 m^{2}g^{-1} (Fig. 7). Hence, likely the drug might completely fill the accessible pores blocking the entrance of N$_2$. Regarding the FTIR spectrum of AzA, it is mainly characterized by the stretching vibrations of -CH$_2$ at 2920 and 2850 cm^{-1} and of –C=O at *ca.* 1685 cm^{-1} (Fig. 3(b)). These bands were also observed in the

spectra of the impregnated samples, although for all of them the AzA carboxyl band was shifted to *ca.* 1705 cm^{-1}, indicating some definite interactions between the carboxylic groups of the drug and the walls of the mesopores in the carrier. Hence, molecular adsorption seems more plausible than amorphous NPs precipitation as the loading mechanism.

3.3. Topical AzA-containing Fe(BTC)/PVA formulations

Prior to the evaluation of these mesoporous materials in terms of AzA delivery under topical conditions, composite patches, well-adapted for cutaneous administration, were prepared with PVA using two different strategies: *(i)* scCO$_2$ foaming (sample sc@PVA) and *(ii)* press-molding (samples pm@PVA and control@PVA). The material chosen for analysis was supercritically impregnated AzA into MIL-100(Fe), because the biosafety of topical patches involving these products was previously demonstrated in human volunteers. [47,48] In these tests, intact skin without irritation, corrosion, or reddening was observed after 24 h (topical formulation are usually applied for a maximum of 8-24 h period). As previously mentioned in the introduction, the biodegradable character, biocompatibility and aqueous solubility of PVA make this polymer a proper selection to form mechanically suitable patches.[16] Often, PVA based composites are prepared by thermoplastic processing to avoid the use of toxic solvents necessary in solution methods. However, the melting temperature of PVA is very close to its thermal degradation, and moreover, it is not applicable when labile pharmaceutical compounds are involved. As an alternative, scCO$_2$ can be used of as a blowing agent, providing plasticity to the polymer at the low-temperature range, below their glass-transition temperature.[49] Plasticization decreases the viscosity of the polymer, being lower than that observed in existing molding processes. For PVA nanocomposites, plasticization with CO$_2$ must be combined with the use of a small amount of a liquid plasticizer, as the DMSO used in this work, which facilitates the initial homogeneous dispersion of the impregnated MOF particles into the polymer.[50] This way, disk-shaped test pieces (10 mm-diameter and 2 ± 0.5 mm-thickness) were first prepared *via* a general molding process in a round-bottom vial by plasticizing the mixture of the AzA-loaded MOF and the PVA powder with DMSO in the mold. Then, the system was further plasticized using scCO$_2$ at a temperature as low as 60 ℃. The controlled expansion of the compressed CO$_2$ dissolved into PVA led to the nucleation and growth of gas bubbles inside the composite, resulting in an interesting cellular morphology with interconnected pores of around 2-5 μm (Fig. 8). The crystalline structure of the MOF upon processing by supercritical foaming was still outlined in the XRD pattern (Fig. 2(b)). Besides, needle crystals of AzA were neither visible on the SEM pictures nor in the XRD pattern, indicating that AzA was not

significantly segregated from the MOF during the supercritical designed process for composite preparation.
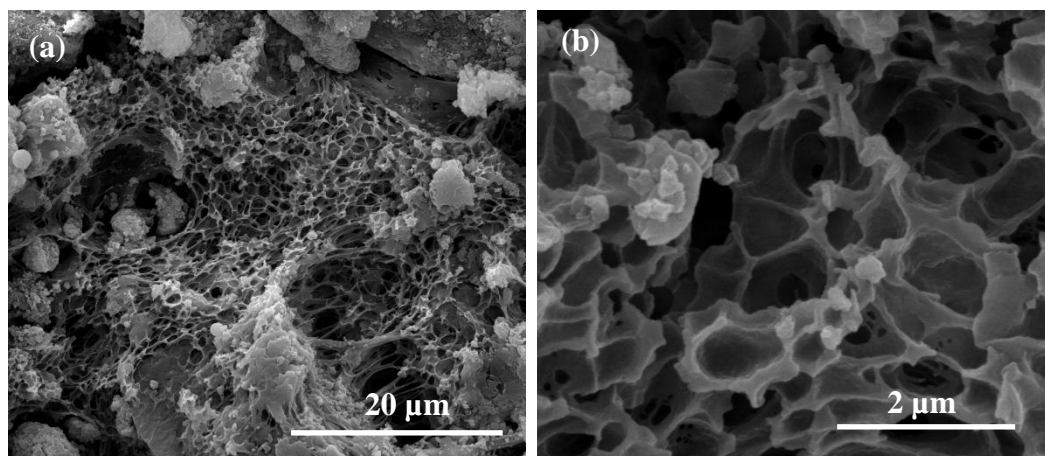
Figure 8. SEM images of the sc@PVA sample at different magnifications.

Finally, *ex vivo* permeation assays were carried out to determine the release and skin barrier crossing of AzA through Franz diffusion chambers.[51] This cell consists in two compartments (receptor and donor) separated by a skin membrane, *e.g.*, the inner region of the porcine ear, considered as a suitable model of human skin permeability. The *stratum corneum* of the skin was placed in the donor compartment in contact with the patch formulations covered by an impermeable film (Leukoflex®) to avoid dryness, and the receptor chamber was filled with PBS (pH = 7.4). The porcine skin was previously dermatomed to a thickness of *ca.* 1.2 mm, removing the fatty layer and keeping the upper layers. The amount of drug able to reach the adipose tissue and/or systemic circulation was easily quantified by HPLC within the receptor chamber (referred as diffused AzA) and expressed as the percentage with respect the total drug cargo. A progressive skin bypass was evidenced in both preparations (Fig. 9). During a typical cutaneous contact time of 8 h, AzA progressively bypasses the skin barrier from both patches preparations (7.5 ± 1.6 % or 1.2 mgcm^{-2} for sc@PVA, and 6.0 ± 0.7 % or 1.0 mgcm^{-2} for pm@PVA, being on the range of PVA control group (control@PVA) (8.3 ± 1.3 % or 1.5 mgcm^{-2}). The AzA diffusion is thus improved when compared with other reported systems, *f.i.*, ~ 4 % or 73 µgcm^{-2} for commercialized products, data corresponding to 24 h in porcine tissue.[51] Finally, no leached linker was detected in none of the samples, highlighting the stability of the formulation.
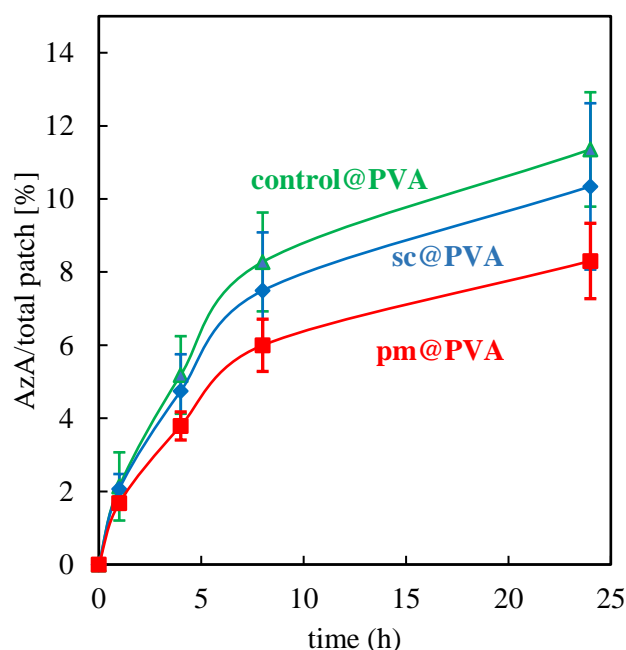
Figure 9. Amount of drugs able to reach the adipose tissue / systemic circulation quantified by HPLC within the receptor chamber (referred as diffused AzA) and expressed as the % with respect the total drug cargo.

Despite a proper drug release crossing of the tested patch formulations, an important amount of the initially loaded drug did not reach the receptor compartment. In this regard, the amount of AzA retained within the skin was estimated as the sum of the amounts of the *stratum corneum* and viable skin layered (epidermis and dermis, see Fig. 10). The AzA skin retention from sc@PVA based patches (2.60 % or 0.42 mg for both formulations) is similar or even improved when compared to other reported formulations (*e.g.,* 3.4 % or 0.13 mg of AzA in a commercial cream, 4.7% or 0.40 mg of AzA in ethanolic-based gel, and 12 % or 0.58 mg of AzA in microemulsion).[49,52] Notably, the AzA retained within the skin in the control formulation was significantly higher than that in the MOF-patches, more precisely around 2-fold higher. Again, no linker was detected in none of the samples, highlighting the stability of the formulation. The diffusion seems to be dependent on the PVA polymer since no significant ($p<0.05$) were observed for all the prepared formulations. On the contrary, the retained drug in the skin is significantly lower when using MOFs-based formulations (pm@PVA and sc@PVA) than the PVA patch. Thus, the MOF is controlling the AzA release rate, favouring a sustained drug release and the reduction of potential AzA side effects (skin irritation).[53] This result highlights the influence of the formulation on the drug biodistribution and bioavailability and could be explained by the fact that the total drug content is available in the polymer from the beginning

in the control sample, while the AzA is progressively released from the MOF to the PVA in the composite patch. The iron(III) trimesate based patches can therefore have a topical and non-systemic action by targeting the different levels of the skin (stratum corneum, epidermis and dermis), but also lead to a systemic action through a percutaneous absorption, achieving a combined effect. This is particularly important considering that the combination of these two administration routes is recommended in the treatment of some diseases (*e.g.,* eczema in children).[54]
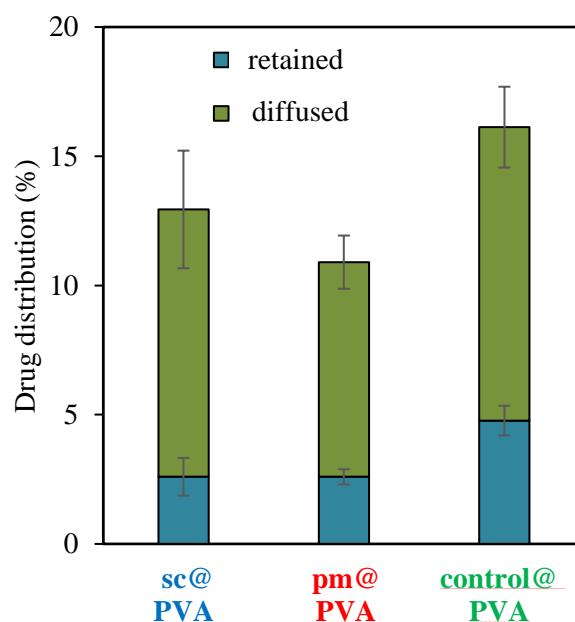

Figure 10. Amount of AzA diffused out and retained in the skin in case of the patches prepared with press-molding and scCO$_2$ approach and the control patch.

Finally, the diffusion flux (*J*) was estimated at 24 h, obtaining different values for each formulation: 146.5 µgcm^{-2}h^{-1} for sc@PVA, 60.1 µgcm^{-2}h^{-1} for pm@PVA and 175.5 µgcm^{-2}h^{-1} for control@PVA. The diffusion flux for AzA was 1.2 and 3-fold times slower from the sc@PVA and pm@PVA than from the control, respectively, indicating the progressive diffusion controlled by the drug release and extending the half-life of this drug. Note that AzA should be applied twice a day, with a topical half-life time of 12 h. In fact, it is well-know that the formulation strongly impacts on the cutaneous permeation of APIs.[55] Comparing with commercial formulations, the obtained diffusion fluxes are within the range of commercial devices (*e.g.,* 80.5 µgcm^{-2}h^{-1} for AzA-FINACEA®).[50] These findings suggest that aside from the benefits of using the scCO$_2$ strategy for MOF synthesis, AzA incorporation and patch preparation (fast, efficient, scalable, environmentally friendly), the prepared formulation lead

to a progressive release, improving the half-life time of the drug while achieving a combined (local and systemic) therapeutic effect.

4. Conclusions

The MOF synthesis, drug impregnation and device preparation can be easily performed using a simple, scalable, efficient and environmentally friendly three-steps supercritical CO_2 method. Thus, the benchmarked mesoporous iron(III) trimesate (Fe(BTC)) was first obtained as a dry and empty-pore powder at the nanoscale (10-20 nm) in a high yield (70 wt%), whilst minimizing the need of additives and organic solvents addition, or cleaning steps. Then, MOFs loading with the antibiotic AzA was carried out by diffusion from $scCO_2$ in a more efficient way than by traditional impregnation from water, attaining significantly higher drug uptake values in the former (17 ± 3 *vs* 7.9 ± 0.9 wt% for AzA in Fe(BTC)). Finally, environmentally friendly cutaneous adapted formulations with additional macroporosity were successfully prepared also by $scCO_2$ using the AzA-loaded iron(III) trimesate materials and PVA polymer, facilitating the topical delivery and skin permeation of the drug at a controlled rate within a duration compatible with topical therapies. Remarkably, the total amount of AzA diffused or retained through the skin is within the range or better (diffused) than that of current commercial formulations. The fast and easy methodology presented here (no additive one-step drug impregnation and pellet formulation) using $scCO_2$ could be potentially applied to any cutaneous soluble drug in $scCO_2$, and particularly to those unstable in solution.

References

1. S. Yuan, L. Feng, K. Wang, J. Pang, M. Bosch, C. Lollar, Y. Sun, J. Qin, X. Yang, P. Zhang, Q. Wang, L. Zou, Y. Zhang, L. Zhang, Y. Fang, J. Li, H-C. Zhou, Stable Metal–Organic Frameworks: Design, Synthesis, and Applications, *Adv. Mater.* **2018,** *30*, 1704303.

2. D. Li, L. Chen, G. Liu, Z. Yuan, B. Li, X. Zhang, J. Wei, Porous metal–organic frameworks for methane storage and capture: status and challenges, *New Carbon Mater.* **2021,** *36*, 468-496.

3. Q. Wang, D. Astruc, State of the Art and Prospects in Metal–Organic Framework (MOF)-Based and MOF-Derived Nanocatalysis, *Chem. Rev.* **2020,** *120*, 1438–1511.

4. D. Liu, D. Zou, H. Zhu, J. Zhang, Mesoporous Metal–Organic Frameworks: Synthetic Strategies and Emerging Applications, *Small*, **2018,** *14*, 1801454.

5. P. Horcajada, C. Serre, G. Maurin, N. A. Ramsahye, F. Balas, M. Vallet-Regí, M. Sebban, F. Taulelle, G. Férey, Flexible Porous Metal-Organic Frameworks for a Controlled Drug Delivery, *J. Am. Chem. Soc.* **2008,** *130*, 6774–6780.

6. J. Gordon, H. Kazemian, S. Rohani, MIL-53(Fe), MIL-101, and SBA-15 porous materials: Potential platforms for drug delivery, *Mater. Sci. Eng. C* **2015,** *47*, 172–179.

7. P. Horcajada, R. Gref, T. Baati, P.K. Allan, G.s Maurin, P. Couvreur, G. Ferey, R.E. Morris, C. Serre, Metal-Organic Frameworks in Biomedicine, *Chem. Rev.* **2012,** *112*, 1232–1268.

8. G. Zhong, D. Liu, J. Zhang, Applications of Porous Metal−Organic Framework MIL-100(M) (M =Cr, Fe, Sc, Al, V), *Cryst. Growth Des.* **2018,** *18*, 7730−7744.

9. W. Strzempek, E. Menaszek, B. Gil, Fe-MIL-100 as drug delivery system for asthma and chronic obstructive pulmonary disease treatment and diagnosis, *Microporous and Mesoporous Materials* **2019,** *280*, 264–270.

10. P. Horcajada, T. Chalati, C. Serre, B. Gillet, C. Sebrie, T. Baati, J.F. Eubank, D. Heurtaux, P. Clayette, C. Kreuz, J-S. Chang, Y.K. Hwang, V. Marsaud, P-N. Bories, L. Cynober, S. Gil, G. Férey, P. Couvreur, R. Gref, Porous metal–organic-framework nanoscale carriers as a potential platform for drug delivery and imaging, *Nat. Mater.* **2010,** *9*, 172-178.

11. P. Horcajada, S. Surble, C. Serre, D-Y. Hong, Y-K. Seo, J-S. Chang, J-M. Greneche, I. Margiolakid, G. Ferey, Synthesis and catalytic properties of MIL-100(Fe), an iron(III) carboxylate with large pores, *Chem. Commun.* **2007,** *27*, 2820–2822.

12. Y.-K. Seo, J.W. Yoon, J.S. Lee, U-H. Lee, Y.K. Hwang, C-H. Jun, P. Horcajada, C. Serre, J-S. Chang, Large scale fluorine-free synthesis of hierarchically porous iron(III) trimesate MIL-100(Fe) with a zeolite MTN topology, *Microporous Mesoporous Mater.* **2012,** *157*, 137-145.

13. G. Majano, O. Ingold, M. Yulikov, G. Jeschke, J. Pérez-Ramírez, Room-temperature synthesis of Fe–BTC from layered iron hydroxides: the influence of precursor organisation, *Cryst. Eng. Comm.* **2013,** *15*, 9885-9892.

14. A. García Márquez, A. Demessence, A.E. Platero-Prats, D. Heurtaux, P. Horcajada, C. Serre, J-S. Chang, G. Férey, V.A. de la Peña-O'Shea, C. Boissière, D. Grosso, C. Sanchez, Green Microwave Synthesis of MIL-100(Al, Cr, Fe) Nanoparticles for Thin-Film Elaboration, *Eur. J. Inorg. Chem.* **2012,** *32*, 5165-5174.

15. E. Bellido, M. Guillevic, T. Hidalgo, M. J. Santander-Ortega, C. Serre, P. Horcajada, Understanding the Colloidal Stability of the Mesoporous MIL-100(Fe) Nanoparticles in Physiological Media, *Langmuir* **2014,** *30*, 5911−5920.

16. N. Chen, L. Li, Q. Wang, New technology for thermal processing of poly(vinyl alcohol), *Plastics Rubber and Composites* **2007,** *36*, 283-290.

17.	C. Domingo, J. Saurina, An overview of the analytical characterization of nanostructured drug delivery systems: Towards green and sustainable pharmaceuticals: A review, *Analytica Chimica Acta* **2012**, *744*, 8–22.

18.	U.B. Kompella, K. Koushik, Preparation of Drug Delivery Systems Using Supercritical Fluid Technology, *Critical reviews in therapeutic drug carrier systems* **2001,** *18*, 173-199.

19.	A.M. López-Periago, P. López-Domínguez, J. Pérez Barrio, G. Tobias, C. Domingo, Binary supercritical CO_2 solvent mixtures for the synthesis of 3D metal-organic frameworks, *Microporous Mesoporous Mater.* **2016,** *234*, 155-161.

20.	A.M. López-Periago, N. Portoles-Gil, P. López-Domínguez, J. Fraile, J. Saurina, N. Aliaga-Alcalde, G. Tobias, J.A. Ayllón, C. Domingo, Metal-organic frameworks precipitated by reactive crystallization in supercritical CO_2, *Cryst. Growth Des.* **2017,** *17*, 2864-2872.

21.	P. López-Domínguez, A.M. López-Periago, F.J. Fernández-Porras, J. Fraile, G. Tobias, C. Domingo, Supercritical CO_2 for the synthesis of nanometric ZIF-8 and loading with hyperbranched aminopolymers: applications in CO_2 capture, *J. CO_2 Util.* **2017,** *18,* 147-155.

22.	K. Matsuyama, Supercritical fluid processing for metal-organic frameworks, porous coordination polymers, and covalent organic frameworks, *J. Supercrit. Fluids* **2018,** 134, 197-203.

23.	C. Domingo, P. Subra-Paternault (Eds.), Supercritical Fluid Nanotechnology: Advances and Applications in Composites and Hybrid Nanomaterials, Pan Stanford Publishing, Singapore, **2015**.

24.	A.M. López-Periago, C. Domingo, Features of supercritical CO_2 in the delicate world of the nanopores, *J. Supercrit. Fluids* **2018,** *134*, 204-213.

25.	E. Weidnera, Impregnation via supercritical CO_2–What we know and what we need to know, *J. Supercrit. Fluids* **2018**, *134*, 220–227.

26.	R. Monteagudo-Olivan, M.J. Cocero, J. Coronas, S. Rodríguez-Rojo, Supercritical CO_2 encapsulation of bioactive molecules in carboxylate based MOFs, *J. CO_2 Util.* **2019**, *30*, 38-47.

27.	K. Matsuyama, N. Hayashi, M. Yokomizo, T. Kato, K. Ohara, T. Okuyama, Supercritical carbon dioxide-assisted drug loading and release from biocompatible porous metal–organic frameworks, *J. Mater. Chem. B* **2014,** *2*, 7551-7558.

28.	C. Tamames-Tabar, E. Imbuluzqueta, N. Guillou, C. Serre, S. R. Miller, E. Elkaïm, P. Horcajada, M. J. Blanco-Prieto, A Zn azelate MOF: combining antibacterial effect, *Cryst. Eng. Comm.* **2015,** *17*, 456–462.

29.	S. Rojas, I. Colinet, D. Cunha, T. Hidalgo, F. Salles, C. Serre, N. Guillou, P. Horcajada, Toward Understanding Drug Incorporation and Delivery from Biocompatible Metal−Organic Frameworks in View of Cutaneous Administration, *ACS Omega* **2018,** *3*, 2994−3003.

30.	P. Netti (Ed.), Biomedical Foams for Tissue Engineering Applications, Woodhead Publishing, **2014**.

31.	A. Salerno, C. Domingo, Bio-based polymers, supercritical fluids and tissue engineering, *Process Biochemistry* **2015,** *50*, 826–838.

32.	R. Campardelli, P. Franco, E. Reverchon, I. De Marco, Polycaprolactone/nimesulide patches obtained by a one-step supercritical foaming + impregnation process, *The Journal of Supercritical Fluids* **2019,** *146*, 47–54.

33.	A. Salerno, S. Diéguez, L. Diaz-Gomez, J. L Gómez-Amoza, B. Magariños, A. Concheiro, C. Domingo, C. Alvarez-Lorenzo, C.A. García-González, Synthetic scaffolds with full pore

interconnectivity for bone regeneration prepared by supercritical foaming using advanced biofunctional plasticizers, *Biofabrication* **2017,** *9*, 035002.

34. A. García Márquez, T. Hidalgo, H. Lana, D. Cunha, M.J. Blanco-Prieto, C. Álvarez-Lorenzo, C. Boissiére, C. Sánchez, C. Serre, P. Horcajada, Biocompatible polymer–metal–organic framework composite patches for cutaneous administration of cosmetic molecules, *J. Mater. Chem. B* **2016,** *4*, 7031-7040.

35. P. Horcajada, S. Surblé, C. Serre, D.-Y. Hong, Y.-K. Seo, J.-S. Chang, J.-M. Grenèche, I. Margiolaki, G. Férey, Synthesis and Catalytic Properties of MIL-100(Fe), an iron(III) Carboxylate with Large Pores, *Chem. Commun.* **2007,** *27*, 2820−2822.

36. S. D. Taherzade, S. Rojas, J. Soleimannejad, P. Horcajada, Combined Cutaneous Therapy Using Biocompatible Metal-Organic Frameworks, *Nanomaterials* **2020,** *10,* 2296.

37. A. Bertuzzi, A. Gandolfi, S. Salinari, G. Mingrone, E. Arcieri-Mastromattei, E. Finotti, A.V. Greco, Pharmacokinetic Analysis of Azelaic Acid Disodium Salt: A Proposed Substrate for Total Parenteral, Nutrition, *Clin. Pharmacokinet* **1991,** *20*, 411–419.

38. T. Simon-Yarza, T. Baati, F. Neffati, L. Njim, P. Couvreur, C. Serre, R. Gref, M. Fadhel Najjar, A. Zakhama, P. Horcajada, In vivo behavior of MIL-100 nanoparticles at early times after intravenous administration, *Int. J. Pharm.* **2016,** *511*, 1042–1047.

39. E. Capristo, G. Mingrone, A. De Gaetano, G. Addolorato, A.V. Greco, G. Gasbarrini, A new HPLC method for the direct analysis of triglycerides of dicarboxylic acids in biological samples, *Clin. Chim. Acta* **1999,** *289*, 11–21.

40. T. Simon-Yarza, T. Baati, F. Neffati, L. Njim, P. Couvreur, C. Serre, R. Gref, M.F. Najjar, A. Zakhama, P. Horcajada, In vivo behavior of MIL-100 nanoparticles at early times after intravenous administration, *Int. J. Pharm.* **2016,** *511*, 1042–1047.

41. Y. Fang, Z. Yang, H. Li, L. Xinghao, MIL-100(Fe) and its derivatives: from synthesis to application for wastewater decontamination, *Environ. Sci. Pollut. Res.* **2020,** *27,* 4703–4724.

42. P. Horcajada, S. Surblé, C. Serre, D.Y. Hong, Y.K. Seo, J.S. Chang, J.M. Grenèche, I. Margiolaki, G. Férey, Synthesis and Catalytic Properties of MIL-100 (Fe), an Iron (III) Carboxylate with Large Pores, *Chem. Commun.* **2007,** *27*, 2820-2822.

43. M.B. Miller, De-Li Chen, D.R. Luebke, J.K. Johnson, R.M. Enick, Critical Assessment of CO_2 Solubility in Volatile Solvents at 298.15 K, *J. Chem. Eng. Data* **2011,** *56*, 1565–1572.

44. M. Thommes, K. Kaneko, A. Neimark, J. P. Olivier, F. Rodriguez-Reinoso, J. Rouquerol, S. W. Sing, Physisorption of gases, with special reference to the evaluation of surface area and pore size distribution (IUPAC Technical Report), *Pure Appl. Chem.* **2015,** *87*, 1051–1069.

45. D.L. Sparks, R. Hernandez, L. A. Estevez, N. Meyer, T. French, Solubility of Azelaic Acid in Supercritical Carbon Dioxide, *J. Chem. Eng. Data* **2007,** *52*, 1246-1249.

46. A.E. Andreatta, L.J. Florusse, S.B. Bottini, C.J. Peters, Phase equilibria of dimethyl sulfoxide (DMSO) + carbon dioxide, and DMSO + carbon dioxide + water mixtures, *J. of Supercritical Fluids* **2007,** *42*, 60–68.

47. K. S. Paudel, M. Milewski, C. L. Swadley, N. K. Brogden, P. Ghosh, A. L. Stinchcomb, Challenges and opportunities in dermal/transdermal delivery, *Ther. Deliv.* **2010,** *1*, 109–131.

48. M. S. Garrison, J. A. Duffy, J. J. Teal, Gentle Anti-Acne Composition, **1996**, U.S. Patent No 5,569,651.

49. E. Reverchon, S. Cardea, C. Rapuano, Formation of Poly-Vinyl-Alcohol Structures by Supercritical CO_2, *J. Appl. Polym. Sci.* **2007,** *5*, 3151-3160.

50. D. Yin, A. Xiang, Y. Li, H. Qi, H. Tian, G. Fan, Effect of Plasticizer on the Morphology and Foaming Properties of Poly(vinyl alcohol) Foams by Supercritical CO_2 Foaming Agents, Journal of Polymers and the Environment, **2019,** *27*, 2878–2885.

51. S.F. Ng, J.J. Rouse, F.D. Sanderson, V. Meidan, G.M. Eccleston, Validation of a static Franz diffusion cell system for in vitro permeation studies, *AAPS PharmSciTech* **2010,** *11,* 1432–1441.

52. H. Ma, M. Yu, F. Tan, N. Li, Improved percutaneous delivery of azelaic acid employing microemulsion as nanocarrier: Formulation optimization, in vitro and in vivo evaluation, *RSC Adv.* **2015,** *5,* 28985–28995.

53. C. J. Dannaker, J. Waterbone, Topical Compositions for the Delivery of Azelaic Acid, **2009**. Available online: https://patents.google.com/patent/US20100004296.

54. N. A. Francis, M. J. Ridd, E. Thomas-Jones, C. C. Butler, K. Hood, V. Shepherd, C. A. Marwick, C. Huang, M. Longo, M. Wootton, F. Sullivan, Oral and Topical Antibiotics for Clinically Infected Eczema in Children: A Pragmatic Randomized Controlled Trial in Ambulatory Care, *Ann. Fam. Med.* **2017,** *15*, 124-130.

55. J. Stah, M.Wohlert, M. Kietzmann, The effect of formulation vehicles on the in vitro percutaneous permeation of ibuprofen, *BMC Pharmacol.* **2011,** *11,* 12.

scCO$_2$ assisted Cu-loading on Fe(BTC) semiamorphous MOF: application in catalytic CO$_2$ hydrogenation
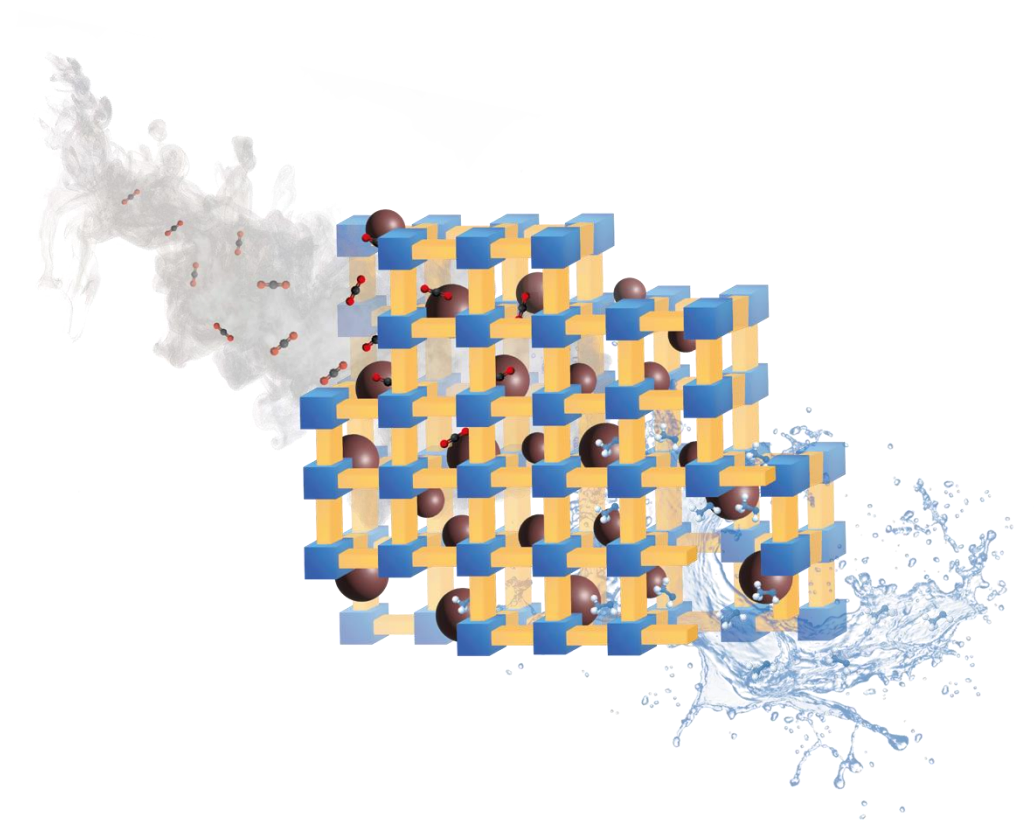
This work summarizes the preparation of a copper clusters-Fe(BTC) catalyst using supercritical CO$_2$ for the homogenous impregnation of catalytically active centers within the porous structure of the MOF. The composite was successfully applied as a catalyst for CO$_2$ hydrogenation.

Abstract

The most common issue regarding typical copper-based catalysts is the aggregation of the active metal centers and the consequent deactivation. Traditionally, in Cu-based catalyst for CO_2 hydrogenation, ZnO is used as a spacer between the copper species, so the aggregation of the copper nanoparticles is minimized. In this work, a newly developed system is presented, where iron trimesate MOF (Fe(BTC)) is serving as a mesoporous support, and the catalytic copper clusters (CuCs) are well dispersed within its pores. The growth and the aggregation of the copper clusters are hindered by the confinement of the active entities in the MOF cages. The CuCs@Fe(BTC) composite catalyst was prepared using a sustainable supercritical CO_2 method, where this media is acting as an impregnation vector to load the organometallic copper into the MOF pores. The subsequent *in-situ* H_2 reduction produces the active catalyst. The efficiency of the impregnation and the distribution of the copper phase was studied by several characterization techniques, highlighting energy dispersive spectroscopy and N_2 adsorption-desorption. The results depict important enhancement in the loading when the semiamorphous iron trimesate was used, in comparison to the crystalline counterpart (MIL-100(Fe)). The catalytic performance of the semiamorphous composite was tested in the CO_2 hydrogenation reaction at 10 bar. A significant amount of methanol was produced, actually superior to that of the traditional CuZnO catalyst (10 *vs* 3.3 $mg_{MeOH}g_{Cu}^{-1}h^{-1}$). At high temperature (T > 200 °C) important amounts of CH_4 and CO were also detected.

1. Introduction

The massive amount of CO_2 emitted to the atmosphere is currently entailing serious environmental concerns. As it is known, reducing the released quantity of CO_2 would moderate the catastrophic consequences of the greenhouse effect. One of the potential ways to relieve the pressure from carbon emission is to utilize CO_2 to produce value-added chemicals and fuels, *e.g., via* hydrogenation, which opens the way towards a circular carbon economy.[1] In this sense, CO_2 is not anymore considered only a waste that needs to be treated, but also an important C1 compound used as chemical feedstock.[2] A large variety of different products, from hydrocarbons to oxygenated carbons, such as methanol (MeOH), methane (CH_4), ethanol (EtOH), short chain olefins and aromatics, can be produced using CO_2 as the raw material. Out of these compounds, methanol and methane are often the targets for different reasons.[3,4] Methanol is of particular interest in the production of fuels due to its high energy density, and due to additional advantages related to easy storing and simple recycling of remaining CO_2.

From a stoichiometrical point of view, less H_2 is required for the formation of methanol *vs.* methane, which is a determining factor regarding cost efficiency. Nevertheless, methanation processes using waste CO_2 and renewably-sourced H_2 is recently attracting much attention, since it offers an alternative to natural gas with a low carbon footprint.[5]

Most catalytic systems for CO_2 hydrogenation involve active metal sites dispersed in a promotor and a support, all offering an immense variety of possibilities. On one hand, the metal sites/promoter pair substantially determines the reaction products. Overall, Cu/ZnO based catalysts are used for methanol production, while composites containing transition (Fe, Co, Ni) or noble (Pd, Ru, Rh) metals have been investigated in methanation reactions.[3] On the other hand, the support has the role of improving the dispersion of the active metal sites, as well as modulating metal-support interactions, thus improving the CO_2 quantitative conversion and product selectivity.[6] Metal oxides and carbides, porous zeolites and metal-organic frameworks (MOFs) or carbon based materials (activated carbon, graphene, carbon nanotubes, *etc.*) have frequently been utilized as supports. MOFs, with high structural and thermal stabilities, have lately gained attention as catalytic supports, owing to their large internal surface area, interconnected porous structure and uniformly dispersed metal nodes.[7] The archetypical microporous UiO-66, HKUST-1 and ZIF-8 MOFs, and the (near)mesoporous NU-1000, MOF-5 and the MIL-100 family have been investigated as catalysts. Active centers in MOFs can be inherent to the structure or attained in post-synthetic reactions, such as by thermal decomposition of the framework[8] or transmetalation.[9] (Fig.1a) More recently, semiamorphous

MOFs emerged into the spectrum of relevant catalysts due to their easy preparation and intrinsic structural defects, *e.g.*, metal vacancies or missed linkers, often leading to improved catalytic activity.[10,11]

a) **Pristine MOF catalyst**

Thermal decomposition

Active centers are
MOFs' metal clusters

MOF – derived
catalyst

Metal exchanged MOF

b) **Functionalized MOF catalyst**

c) **Metal@MOF composites**

Active center
coordination by linker

Active center coordination on SBU
(missing linker defects)

Active centers
deposited on MOF

Core-shell structure

d) **Our metal@MOF composite catalyst**

Confinement of active
centers in the mesopores

Figure 1. Illustration of different types of MOF and metal@MOF composite catalysts.

Functionalization of MOFs with active centers by the addition of catalytic groups to the framework during synthesis can be performed. Among these, binding of metal centers by linkers' functional groups,[12] or even coordination of active metals on free binding sites of SBUs, provided by missing linker defects have been presented.[13] (Fig. 1b) In addition, the catalytic activity in MOFs can be realized by composing them with catalytic species that are not part of the framework. Most of the developed composite systems involve the coverage of the exterior

surface of microporous MOFs with metallic nanoparticles[14] or the attainment of core-shell structures in which the MOF grow surrounding the catalyst.[15,16] (Fig. 1c) A less explored model implies the confinement of small metal clusters (MCs) into the pores, which can significantly extend the catalytic properties of the material. (Fig. 1d) These nanoscale clusters, highly efficient in catalysis, can only be stabilized thanks to the boundary and protection provided by the MOF channels. Actually, there are only few examples of this type of materials, involving clusters of Pd and Pt.[17,18] The close contact between the embedded metallic clusters and the reagents in the confined space has been considered to play an important role in the catalytic performance by facilitating charge transfer.

The main objective of this work is to advance in the fundamental understanding of the category of products designed as MCs@MOF, applied to confined heterogeneous catalysis for CO_2 hydrogenation. In this case, only MOFs with large pore size, *e.g*., extended reticular[19] and mesoporous MOFs, are susceptible of being impregnated with metal precursors and still to remain accessible for the diffusion of the reagents and products of the catalytic reaction. Well studied examples of mesoporous MOFs are chosen in this work for impregnation, the crystalline MIL-100(Fe) and the semiamorphous counterpart Fe(BTC).[20] For the semiamorphous Fe(BTC), the importance of defects in the structure has been already pointed out in acid catalyzed reactions of acetalization and epoxide ring-opening.[21,22] On the contrary, MIL-100(Fe) has demonstrated superior catalytic activity in oxidation reactions.[23] In these MOFs, the structural mesopores (and defects in the semiamorphous counterpart) are providing suitable space for confining the metallic clusters homogeneously dispersed within the structure. As a metal catalyst, copper clusters (CuCs) were loaded into the pores of the iron trimesates, since this is known to be the proper catalyst for CO_2 hydrogenation reactions.

The impregnation of MOFs with metals is usually carried out by infusion into the pores of a metal precursor or by transmetalation, both in liquid phase; followed by reduction with chemicals also dissolved in the liquid phase.[12,24] Hindered diffusion due to liquid solvent viscosity, development of capillary forces in mesopores and competition between the solvent and the solute for the substrate adsorption sites are usual drawbacks found in this synthetic route. In this study, an alternative procedure is proposed based on the use of supercritical CO_2 (scCO_2) as the solvent for the impregnation of a metal precursor into the MOF pores. scCO_2, with enhanced diffusion and mass transfer properties, is essentially not adsorbable under supercritical conditions. Hence, scCO_2 assisted impregnation has been developed as a highly efficient method for the loading of organic molecules into porous substrates and polymers.[25]

Nevertheless, the application of the scCO₂ process to metals has still unexploited potential, mainly due to the limited choice of precursors that can be solubilized in this fluid.[26,27] The organometallic copper acetylacetonate, with significant solubility in scCO₂, was here selected as the metal precursor. Further reduction with H_2 resulted on the formation of the catalyst. The reduction step turned out to be the key to design the low pressure CO_2 hydrogenation reaction studied to produce methanol in this work. Extensive solid state characterization of the synthesized catalysts, before and after catalysis, was performed. Notably, the most effective catalyst was constructed by using semiamorphous Fe(BTC) as the support.

2. Materials and methods

2.1. Materials

For the preparation of pristine and impregnated MOFs, iron nitrate monohydrate ($Fe(NO)_3.9H_2O$), iron(II) chloride ($FeCl_2$), sodium hydroxide (NaOH), trimesic acid (H_3BTC) and copper acetylacetonate ($Cu(acac)_2$), purchased from Merck, were used as reagents. Dioxane and ethanol were provided by PanReac and Scharlau, respectively. Compressed CO_2 (99.95 wt%) for impregnation, H_2 (pure) for the catalyst reduction and CO_2/H_2 mixture (molar ratio 1:3) for the catalytic experiments, were all delivered by Carburos Metálicos S.A.

2.2. Synthetic methods
2.2.1 Synthesis of Fe(BTC) and MIL-100(Fe)

The experimental procedure used for the synthesis of MIL-100(Fe) is based on a previously reported method.[28] Briefly, an aqueous basic solution (NaOH, pH *ca.* 11) of H_3BTC was added dropwise to a second aqueous solution of $FeCl_2$ to attain a mixture with a 1:5 molar ratio and pH of *ca.* 5, which was further stirred for 24 h. Orange crystals were precipitated and recovered by centrifugation. The preparation of Fe(BTC) was carried out following a scCO₂ assisted procedure described elsewhere.[29] A gel was first prepared in dioxane by mixing H_3BTC and $Fe(NO_3)_3.9H_2O$ in a molar ratio of 1:1.5. The vial was placed in a high-pressure reactor, which was sealed and filled with scCO₂ at 70 ℃ and 20 MPa under stirring. After 48 h, the system was isothermally depressurized and then cooled down to ambient temperature to recover a dry orange powder. In both cases, the as-synthesized powder was washed by centrifugation first with water and then with EtOH, and finally dried overnight under vacuum in a desiccator. The products were activated under high vacuum (*ca.* 10 Pa) at 150 ℃ during 20 h to remove residual substances from the pores, thus obtaining brown powders. Upon activation, the yield was measured giving values in the order of 70-75 wt%.

2.2.2. Synthesis of Cu(acac)₂@MOF

200 mg of each activated MOF were wrapped into a filter paper bag, while 200 mg of Cu(acac)$_2$ were added to a glass beaker with a stir bar (Fig. 2). Both compounds were placed in a 100 mL autoclave. The high pressure reactor was sealed and filled with liquid CO_2 up to 6 MPa, then heated at 80 ºC and, finally, pressurized up to 20 MPa. These conditions were maintained under stirring (200 rpm) for 72 h. After that, the system was depressurized and cooled down to room temperature, and a brown powder was recovered from the paper bag.
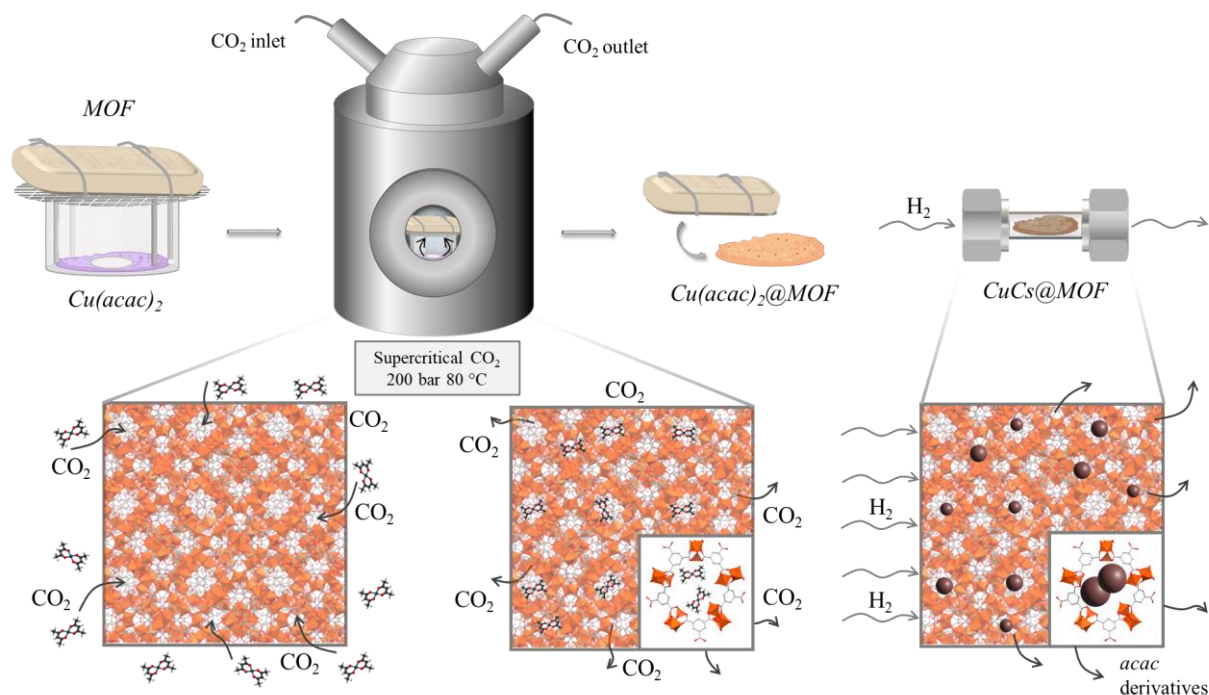
Figure 2. Scheme of CuCs@MOF composite preparation.

2.2.3. Synthesis of CuCs@MOF

The Cu(acac)$_2$@MOF samples (*ca*. 0.15 g), and the pristine MOFs (*ca*. 0.10 g) for comparison, were subjected to reduction under a pure H_2 flow (20 mLmin^{-1}) at 250 ºC, applying a heating ramp of 5 ºC min^{-1}. The process was carried out in a tubular column with the sample powder distributed over glass wool. The reduction time was of 2 h.

2.3. Structural characterization

The as-synthesized and reduced spent catalysts were characterized by solid state techniques. The structural characterization was carried out in the powder X-ray diffractometer (XRD) Siemens D5000, using Cu Kα incident radiation with a step scan of 0.01° applied in the 2θ range of 5-55°. Fourier transform infrared (FTIR) spectroscopy (Jasco 4700 Spectrophotometer) was used to ascertain the molecular composition. The textural properties

were determined by N_2 adsorption/desorption experiments at -196 ℃ performed with an ASAP 2020 Micromeritics Inc. The surface area was determined from the N_2 isotherm by using the Brunauer-Emmet-Teller (BET) equation. The Barrett-Joyner-Halenda (BJH) method was applied to estimate the pore volume from the adsorption branch in the isotherm. The morphology of the composites was investigated with a scanning electron microscope (SEM, Quanta FEI 200). Elemental mappings were recorded in a scanning/transmission (STEM, XHRSEM FEI Magellan 400 L) electron microscopes by using energy dispersive spectroscopy (EDS) in a X–Max Ultim Extreme EDX Oxford Inst. equipment, with a resolution of *ca.* 1 nm. Copper and iron content was determined in reduced composites by inductively coupled plasma mass spectrometry (ICP-MS, Agilent 7700x), after high temperature solid digestion in hydrochloric, nitric and hydrofluoric acids (3:1:0.5 v/v). *Ex situ* X-ray photoelectron spectroscopy (XPS, Specs Spectrometer) was carried out to determine the oxidation state of the copper nanoparticles and any potential modification of the iron in the MOF occurring during synthesis/reduction. For XPS, the powdered samples were compacted into disc-shaped tablets. The analysis was carried out using monochromatic Al-Kα radiation emitted from a double anode at 12 kV and 200 W. The binding energies of the resulting spectra were corrected employing the binding energy of adventitious carbon (284.6 eV) in the C1s region. The backgrounds were corrected using Shirley baselines. All the analysed regions (C1s, O1s, Cu2p and Fe2p) and Auger CuLMM were deconvoluted by means of mixed Gaussian-Lorentzian functions (90:10). The quantitative analyses were based on atomic sensitivity factors stored in the CasaXPS database (v2.3.12Dev6).

2.4. Catalytic activity tests

The described reduction process with H_2 was performed *in situ* in the fixed-bed tubular flow reactor system (Process Integral Development Engineered & Tech.). The same system was used to measure the activity of the catalyst with respect to the hydrogenation of CO_2. For that, after the reduction program, the H_2 flow was switched to the gas mixture of CO_2:H_2. The pressure was set to 10 bar, while the gas flow rate was fixed at 10 mLmin^{-1}. After the steady-state was reached (*ca.* 20 min), MeOH production was measured at the temperature range 180-240 ℃ using an online gas chromatograph (Smiadzu GC-2010) with a flame ionization detector (FID). The percentage of CO, CO_2 and CH_4 was simultaneously quantified using an Agilent Tech. 7890B GC system, with a thermal conductivity detector (TCD) and He as a carrier gas. Methanol space-time yield (STY), CO_2 conversion and selectivity between MeOH and CH_4 *vs.* CO were calculated to assess the catalytic performance.

3. Results and discussion

3.1. Synthesis of pristine MOFs

Two sustainable synthetic processes were here used to prepare MIL-100(Fe) and Fe(BTC) MOFs, the first based on the use of Fe(II) and water, and the second on the use of Fe(III) and scCO$_2$. The slow oxidation of the ferrous cations in aqueous basic media led to the straightforward precipitation of the MIL-100(Fe) crystalline phase, denoted by the development of a well-defined XRD pattern, matching the one published from single-crystal data (Fig. 3a).[20] On the contrary, by using the ferric cation, the semiamorphous character of the scCO$_2$ precipitated Fe(BTC) was reflected in strong peak widening, indicating a high degree of structural disorder for this phase (Fig. 3b). Nevertheless, the broad peaks at $2\theta = 4$ and $11°$ in the XRD pattern match the MIL-100(Fe) accumulated narrow peaks in this area, indicating structural similarities.[30]
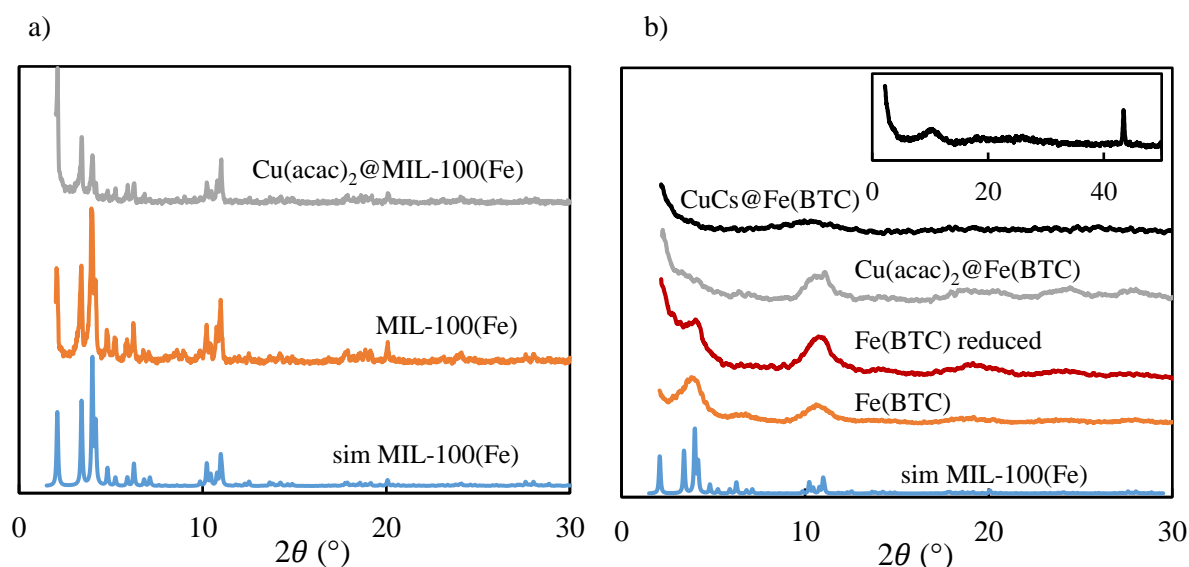
Figure 3. XRD pattern of the pristine form and the composites of the (a) crystalline MIL-100(Fe) and (b) semiamorphous Fe(BTC).

The different end products are related to the reaction mechanism stablished in each synthetic route. The crystalline character of MIL-100(Fe) is achieved through the slow formation of the solid phase in water, originated by the transformation of Fe^{2+} in Fe^{3+}, giving well-faceted micrometric octahedral crystals in the range of 0.5-1 μm (Fig. 4a). In scCO$_2$, the reaction proceed through the initial formation of a gel in dioxane, constituted by colloidal amorphous particles, which is further dried with the supercritical fluid preventing crystal growth and

leading to semiamorphous Fe(BTC) isometric nanoparticles with sizes in the order of 10-20 nm (Fig. 4b).
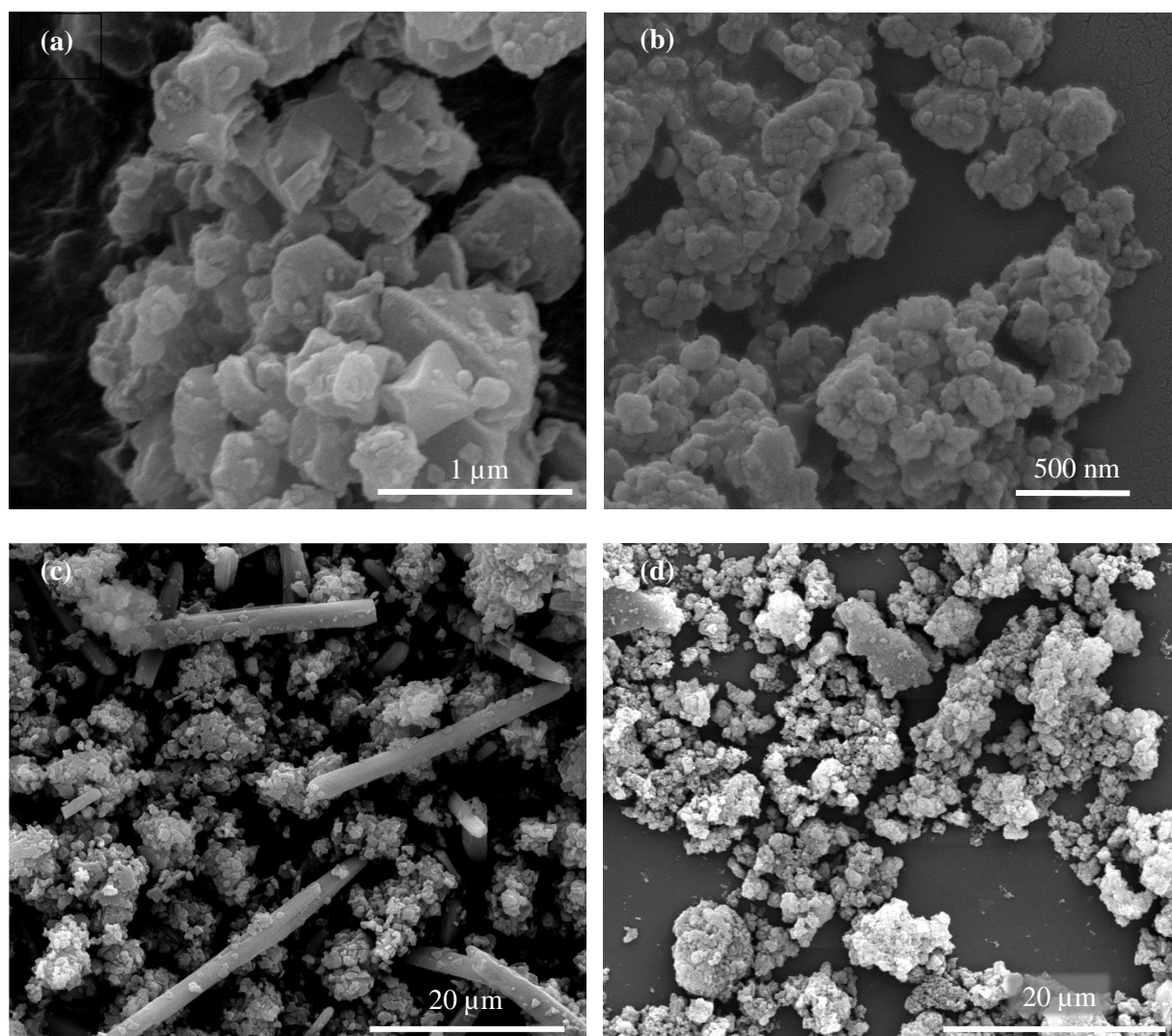

Figure 4. Morphological SEM analysis of samples: (a) MIL-100(Fe), (b) Fe(BTC), (c) Cu(acac)$_2$@MIL-100(Fe), and (d) Cu(acac)$_2$@Fe(BTC).

Regarding the N$_2$ physisorption analysis, both samples displayed a type I isotherm, with enhanced adsorption in the low pressure region. The highest intraparticle adsorption value was measured for the crystalline MIL-100(Fe) (Fig. 5a). For the semiamorphous Fe(BTC), defects on the pore walls likely generated significant blockage, thus reducing adsorption (Fig. 5b). As a consequence, a higher value of the apparent BET surface area was calculated for MIL-100(Fe) with respect to Fe(BTC) (1560 *vs.* 1074 m^{2}g^{-1}, respectively), concomitant with a decrease of the BJH pore volume observed for the later (0.56 *vs.* 0.32 cm^{3}g^{-1}, respectively). Both MOFs

displayed some hysteresis at high relative pressures due to capillary condensation in the interparticle mesopores.
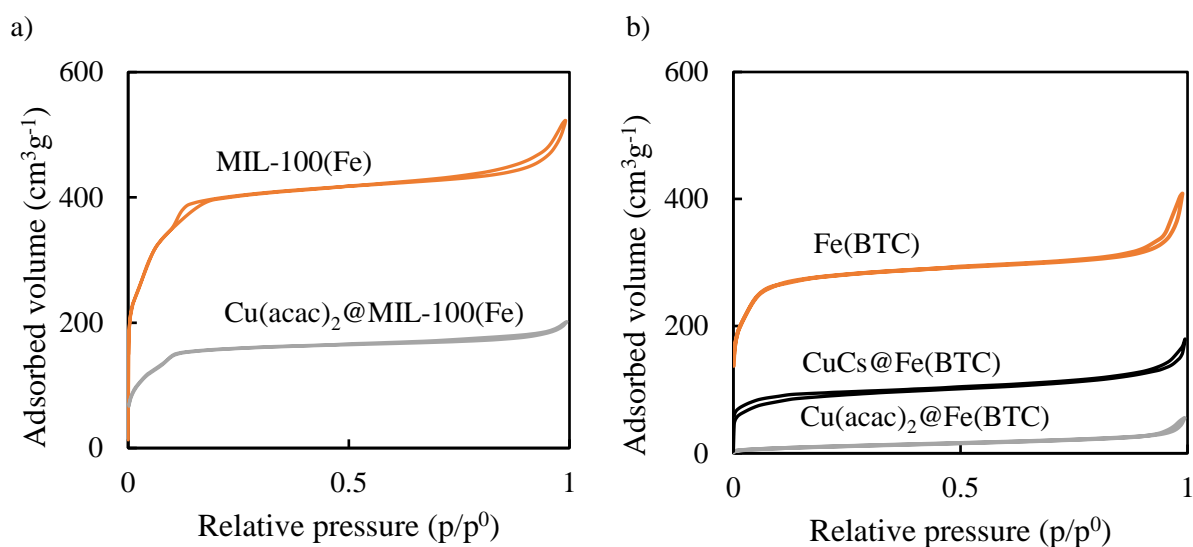

Figure 5. N_2 adsorption-desorption isotherms of the pristine form and the composites of the (a) crystalline MIL-100(Fe) and (b) semiamorphous Fe(BTC).

3.2. Impregnation of the MOFs with the catalyst precursor

The second step to generate the target catalyst involves the addition of the precursors of the catalytically active units to the MOF. Persisting in the aim of developing sustainable processes, the use of green $scCO_2$ was surveyed in this work to allow the transport of the solute precursor from the solution to the MOF pores. An essential prerequisite to achieve this goal is to attain some solubility of the precursor in the supercritical fluid under reasonable values of pressure and temperature, *e.g.*, < 250 bar and < 100 ºC. The use of low pressure values would reduce process costs, while the use of low temperatures avoid the early thermal decomposition of the precursor or support. The molecular precursor was searched among the organometallic copper family, since the typical inorganic copper salts are insoluble in $scCO_2$. In particular, the $Cu(acac)_2$ molecule was chosen. This organometallic has a reasonable solubility in supercritical CO_2, in the order of *ca.* $5 \cdot 10^{-5}$ mole fraction under working conditions.[31] Moreover, $Cu(acac)_2$ is stable in $scCO_2$ up to temperatures of 150 ºC.[32] Finally, the precursor has the proper size to diffuse along the MOF channels. Actually, the crystalline MIL-100(Fe) porous structure is defined by crystallographic cages of diameters 2.5 and 2.9 nm, while in the semiamorphous Fe(BTC) the average pore size approximates the largest cage (2.9 nm). However, the cages are only accessible through micropore windows of 0.6-0.9 nm, which must be taken into account

to analyze the molecular sieving behavior of the MOFs. The $Cu(acac)_2$ is an elongated molecule with approximated dimensions of 0.5 x 0.7 nm. Therefore, this guest molecule has a suitable size to be entrapped in the small mesopores of the iron(III) trimesate MOFs, and also to diffuse through the micrometric windows connecting those pores.

Large differences were found regarding the $Cu(acac)_2$ impregnation behavior in $scCO_2$ for the crystalline and semiamorphous studied MOFs. For the crystalline MIL-100(Fe), the impregnation into the pores was negligible. In these tests, most of the $Cu(acac)_2$ reagent was eliminated dissolved in the $scCO_2$ phase during depressurization, and only some recrystallized $Cu(acac)_2$ needles were deposited on the reactor walls and on the bulk MOF sample (Fig. 4c). The XRD pattern of the $Cu(acac)_2$@MIL-100(Fe) sample did not display the main peaks of $Cu(acac)_2$, placed at 11.3 and 11.7°. This sample still displayed a large value of surface area and pore volume, *ca.* 650 m^2g^{-1} and 0.25 cm^3g^{-1}, indicating low levels of impregnation, reached probably only on and near the exterior surface (Fig. 5a). On the other hand, using the designed set-up, the $Cu(acac)_2$@Fe(BTC) composite was recovered from the sample holder as a brown powder, not presenting the $Cu(acac)_2$ purple needles as a contaminant. SEM images depicted similar morphology for the pristine (Fig. 4b) and impregnated Fe(BTC) (Fig. 4d). In the $Cu(acac)_2$@Fe(BTC) sample, the amount of deposited guest molecules in the interior of the semiamorphous Fe(BTC) pores was quantified as 32 wt%, value obtained gravimetrically comparing pristine and impregnated samples. In the XRD pattern of this compound, again the most intense peaks of $Cu(acac)_2$ were not present (Fig. 3b) and the observed signals matched those of pristine Fe(BTC). This fact is often observed in impregnation processes in confined spaces of reduced dimensions, which is related to either molecular adsorption on the pore walls, or to the precipitation of not diffracting amorphous particles. Nevertheless, the representative peak for the mesopore cages in the Fe(BTC) at 3.9° almost disappear from the pattern.[29] The decrease in the intensity of this band can be taken as an indication of pore loading with guest molecules. The successful loading of the semiamorphous MOF was also evidenced by the massive decrease of the BET surface area and pore volume, from >1000 m^2g^{-1} and 0.30 cm^3g^{-1} in net Fe(BTC) to <100 m^2g^{-1} and 0.03 cm^3g^{-1} in $Cu(acac)_2$@Fe(BTC), thus leaving almost no residual porosity in the impregnated sample (Fig. 5b). Finally, the presence of $Cu(acac)_2$ in the pores of Fe(BTC) was confirmed by FTIR spectroscopy (Fig. 6). The spectrum of the pristine semiamorphous MOF exhibited the bands of iron(III) trimesate, represented by various sharp bands in the zone below 1300 cm^{-1}. This spectrum also corroborates the total elimination of the used dioxane in the $scCO_2$ synthetic process, since the typical C-H bands for this solvent at 2800–3000 cm^{-1} were not apparent. For the $Cu(acac)_2$@Fe(BTC) sample, the bands at 1622 and

1566 cm^{-1} and at 1444 and 1370 cm^{-1} correspond to the asymmetric and symmetric stretching vibrations, respectively, of the carboxylate groups in BTC coordinated to iron sites.[33] The composite also displayed two extra bands at 1520 and 1021 cm^{-1}, assigned to impregnated Cu(acac)$_2$, and corresponding to C=C stretching coupled to C=O and CH$_3$ rocking coupled to C=C bending, respectively.[34,35]
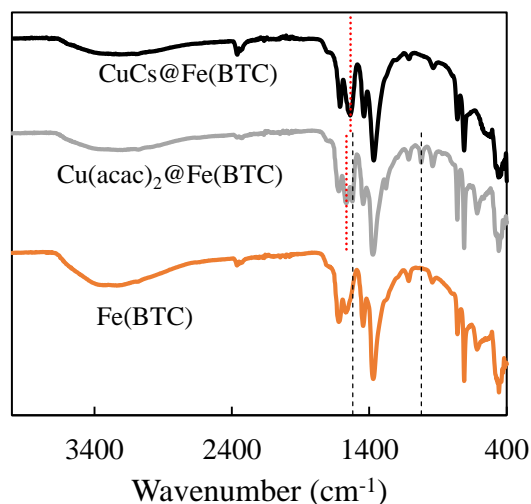

Figure 6. FTIR spectra of the the pristine Fe(BTC) and its composites. Peaks at 1520 and 1021 cm^{-1}, corresponding to impregnated Cu(acac)$_2$ is marked with dashed line, while the shift of the BTC band upon reduction is marked with red dotted line.

Different scCO$_2$ impregnation mechanisms were deduced for the crystalline and semiamorphous iron(III) trimesates, with bulky impregnation attained only into the Fe(BTC) MOF. The process of impregnation is driven by the equilibrium attained between the solubility of Cu(acac)$_2$ in scCO$_2$ and its affinity for the pore walls, the later related to the composition and number of defects on the internal surface of the MOF. This interaction can be ascertained through the analysis of the C parameter in the BET equation inferred from the N$_2$ isotherm, and exponentially related to the energy of monolayer adsorption (see in the Equipment and methodology section).[36] Fe(BTC) displayed an exceptionally high value of this parameter (315), denoting heterogeneity on the pore walls due to its semiamorphous nature conditioned by large number of defects. This value was reduced to 80 in the crystalline MIL-100(Fe) with atomically homogeneous pore walls. Hence, in amorphous Fe(BTC), strong sorption of Cu(acac)$_2$ on the high-energy defects surface sites is favored *vs.* solvation by scCO$_2$, while in the crystalline MIL-100(Fe) seems to be the other way around. Additionally, a large number of Brönsted acid sites is present in the semiamorphous MOF, which has been demonstrated to play a key role for the copper incorporation into the structure.[37] In the impregnation process, the

particle size of the host is also an important parameter to be taken into account.[38] Intraparticle transport limitations are reduced by reducing particle size. For the micrometric particles in the MIL-100(Fe), the reagents could not easily penetrate totally into the pore structure, while they certainly travel through the small nanometric entities of Fe(BTC).

3.3. Catalyst production by reduction

In the particular case of the hydrogenation reaction of CO_2 to methanol, the typical catalyst is shaped with low cost reduced copper moieties, often mixed with ZnO, used as a promotor to avoid nanoparticles aggregation and sintering, and a support to attain a suitable selectivity.[39] In this study, once the synthesis of the precursor $Cu(acac)_2$@MOF was optimized, the objective was to activate the composite to obtain the catalyst. This was achieved by reducing the precursor in a H_2 flow at 250 ºC. The chosen method was the *in situ* growth of reduced copper clusters (CuCs) into the constrained void space of the MOF pores, giving place to structures of the CuCs@MOF type. This method has the advantage of certainly avoid the formation of particles with excessive size for catalysis, and, simultaneously, circumvent the sintering of the fine catalytic entities during reduction and operation, both factors considered main drivers of catalyst deactivation. The process was analyzed for the $Cu(acac)_2$@Fe(BTC), with a significant amount of impregnated copper precursor. A weight loss of *ca.* 45 wt% occurred for the sample during reduction, which indicates the release of large amounts of acetylacetonate ligands, in the form of acetylacetonate, and smaller decomposition products (acetone, ethane, methane),[40] and likely few linkers of the MOF to complete the measured considerable weight loss. A concurrent loss of some crystallinity for the CuCs@Fe(BTC) sample was also observed, denoted by the intensity decrease of the characteristic Fe(BTC) bands (Fig. 3b). The absence of the band at 3.9º again indicates that the channels in the MOF are loaded with guests. Note that subjecting the pristine Fe(BTC) MOF to similar reduction and catalysis treatment (H_2/CO_2), the peak at 3.9º was still displayed in the XRD pattern (Fig. 3b). The relative amount of metals in the composite was quantified by ICP, giving values of 9.5 and 35 wt% of copper and iron, respectively. The elimination of acetylacetonate from the composite was reflected in the decrease of the signals at 1520 and 1021 cm^{-1} on the FTIR spectra (Fig. 6). The shift of the BTC band from 1566 cm^{-1} in Fe(BTC) to the lower frequency of 1536 cm^{-1} in the composite indicates the establishment of interactions between the linker in the MOF and the reduced copper species. By eliminating partially the organic part of the impregnated organometallic, the apparent surface area of the CuCs@Fe(BTC) increases with respect to $Cu(acac)_2$@Fe(BTC), attaining values of in the order of 330 m^{2}g^{-1} with an open pore volume of 0.22 cm^{3}g^{-1} (Fig. 5b).

The distribution of copper and iron on the reduced composite was analyzed by elemental mapping. The obtained maps indicate that both metals were well-distributed over the sample (Fig. 7).


a) b) Fe Kα1 c) Cu Kα1

500 nm
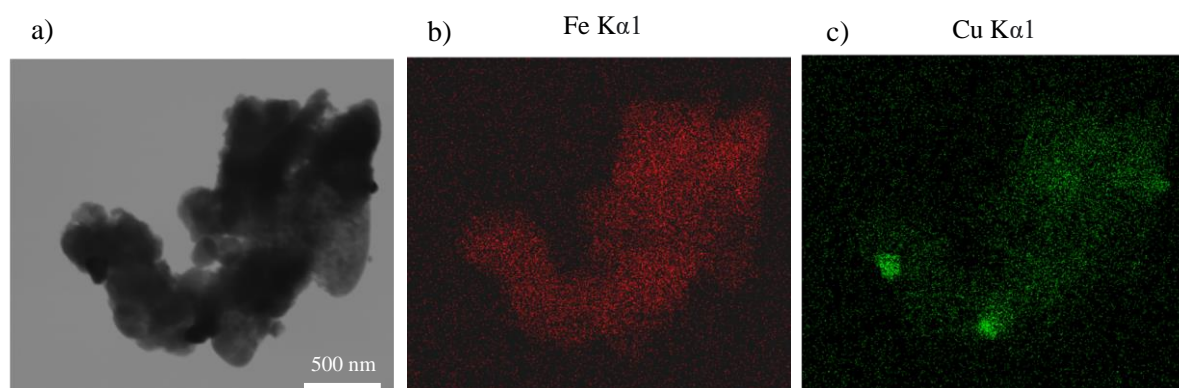
Figure 7. TEM image (a) and EDS maps of the CuCs@Fe(BTC) composite, showing the Fe (b) and the copper (c) distribution.

In the copper map, only few dense spots, assigned to large nanoparticles located outside the Fe(BTC) pores, can be discriminated. These particles are the origin of the low intensity peak at 2θ 43.3°, corresponding to metal copper observed in the XRD pattern of the CuCs@Fe(BTC) sample (Fig. 3b), since the impregnated confined copper clusters, being the predominant phase, are too small to be detected as a crystalline compound by this technique. Nevertheless, these copper particles would not be effective in any catalytic process due to both, their relatively large size and low quantity. The composite CuCs@Fe(BTC) was further studied by XPS to complete the analysis of the structure. The technique was used to determine the oxidation states of the metals in the composite. The binding energies and fractions of the recorded main XPS peaks are indicated in Table 1.

Table 1. XPS results for the different samples.

		CuCs@Fe(BTC)
Atomic ratio (XPS)	Cu/C	0.021
	Fe/C	0.080
	O/C	0.601
	Fe/Cu	3.78
B.E. shift (eV)		1.66
C1s peaks (B.E., eV)	#1	284.6
	#2	285.4
	#3	288.4
C1s peaks (fraction)	#1	0.644
	#2	0.120
	#3	0.236

O1s peaks (B.E., eV)	#1	531.7
	#2	533.3
O1s peaks (fraction)	#1	0.936
	#2	0.064
Cu2p3/2 peaks (B.E., eV)	#1	933.0
	#2	934.9
	#3 (sat)	941.1
	#4 (sat)	944.8
Cu2p3/2 peaks (Cu2p fraction)	#1	0.215
	#2	0.234
	#3 (sat)	0.283
	#4 (sat)	0.038
Fe2p3/2 peaks (B.E., eV)	#1	710.9
	#2	712.6
	#3 (sat)	716.8
Fe2p3/2 peaks (Fe2p fraction)	#1	0.234
	#2	0.161
	#3 (sat)	0.286
K.E. CuLMM (eV)		916.2
α' Cu		1849.4

For this sample, the relative amount of carbon with respect to iron (Fe/C=0.08) corresponds to an atomic ratio for Fe:C of 1:12, which is noticeably superior than the atomic ratio derived from the empirical formula of Fe(BTC) (Fe/C=0.11 in $C_9H_3FeO_6$) corresponding to 1:9. The C1s region shows the typical profile of the trimesic acid units in the Fe(BTC) MOF (Fig. 8a),[41] in which the area ratio of peaks at 285.4 and 288.4 eV, attributed to C-O and C=O groups, respectively, is *ca.* 2. The ratio expected in pure Fe(BTC) is 1, so the sample has an excess of C=O groups. In the O1s region, the area of peak at 533.3 eV, attributed to C-O, is smaller than the area of peak at 531.7 eV, attributed to C=O and coordinated metal-oxygen bonds (Fig. 8b).[42] The excess of oxygen is also observed by measuring the O/Fe atomic ratio with a value of 7.5, higher than the stoichiometric O/Fe ratio for pure Fe(BTC) (O/Fe=6). The carbon and oxygen excess are ascribed to residual acetylacetonate groups and derivatives of this moiety not totally reduced on the spent catalyst. Regarding the Fe2p region, the peaks at 710.9 and 712.6 eV (Table 1) are ascribed to Fe^{2+}/Fe^{3+} (Fe_3O_4) and Fe^{3+} (Fe_2O_3) species, respectively, whereas the presence of a satellite at 716.8 eV further confirms the existence of Fe^{3+} (Fig. 8c).[43] The peak area ratios suggest that the Fe^{3+} was slightly reduced during the H_2 treatment, *e.g.,* ~59 at% correspond to +2/+3 and 41 at% to +3. On the surface, the metallic composition stablished by XPS is *ca.* 79 at% Fe and 21 at% Cu, giving a 3.8:1 Fe:Cu atomic ratio, very close to the value measured in the bulk sample with ICP (3.6:1 Fe:Cu). These equal values prospect a homogenous distribution of the metals on the composite, the impregnation and reduction

processes minimize the amount of copper nanoparticles deposited outside the MOF pores, as already observed by elemental mapping (Fig. 7).
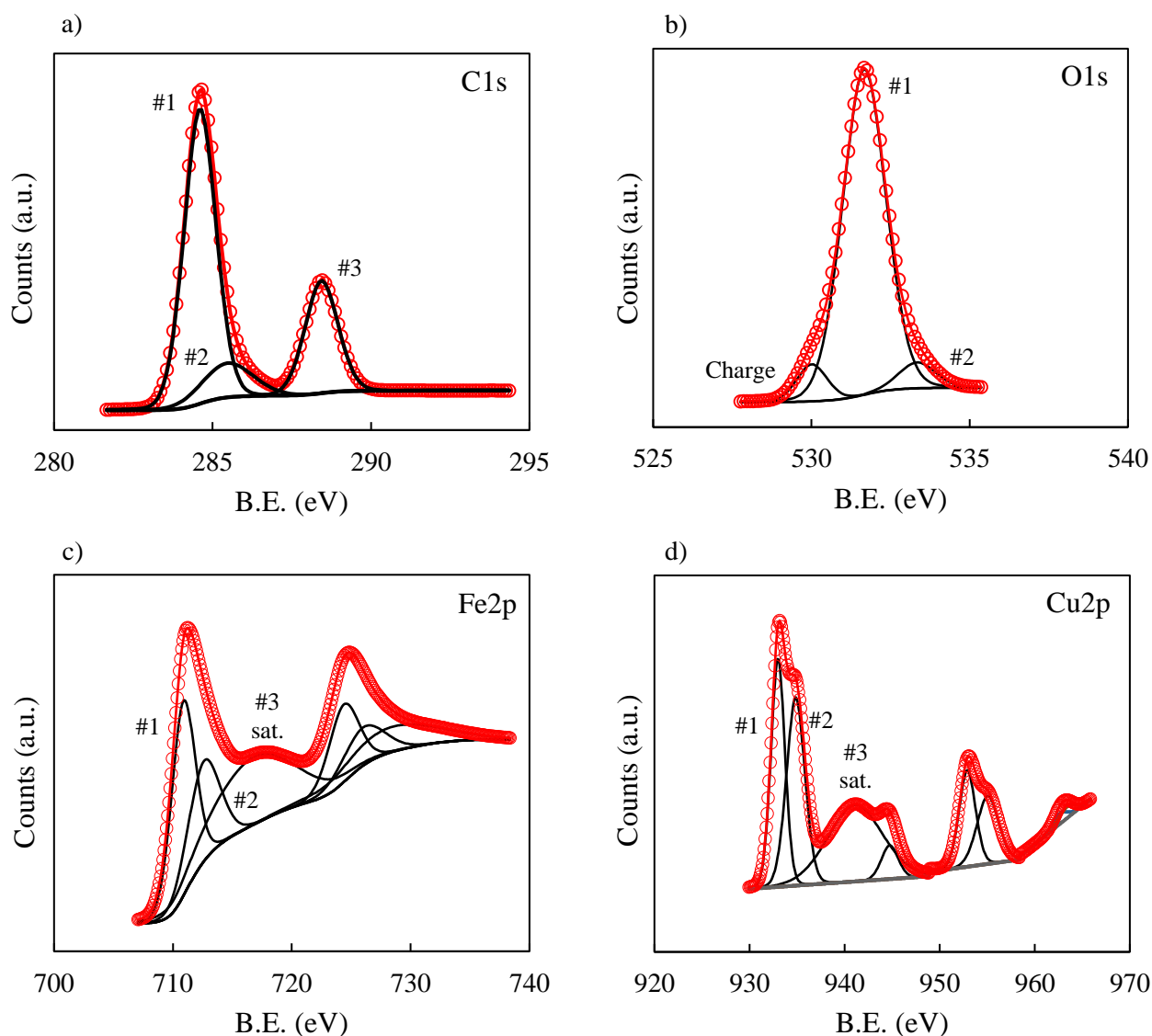

Figure 8 C1s (a), O1s (b), Fe2p (c) and Cu2p (d) region of the XPS spectra of CuCs@Fe(BTC) composite.

The Cu2p3/2 region displays four characteristic peaks. The peak at 933.0 eV might be assigned to Cu/Cu^+,[44] while the peak at 934.9 eV indicates the parallel presence of some amount of Cu^{2+}.[45] The shake-up peaks at 941.1 and 944.8 eV (Fig. 8d) confirm the latter, because these satellites do not occur on cuprous or metallic copper.[46] According to the peak area fractions, reduced copper account for around 48 at% of total copper, the rest being Cu^{2+}. The binding energy point in the copper Wagner's plot[47,48,49] for the CuCs@Fe(BTC) composite is placed

between the Cu^{2+} and Cu^+ lines, thus confirming a mixture of oxidation states in the sample (Fig. 9).
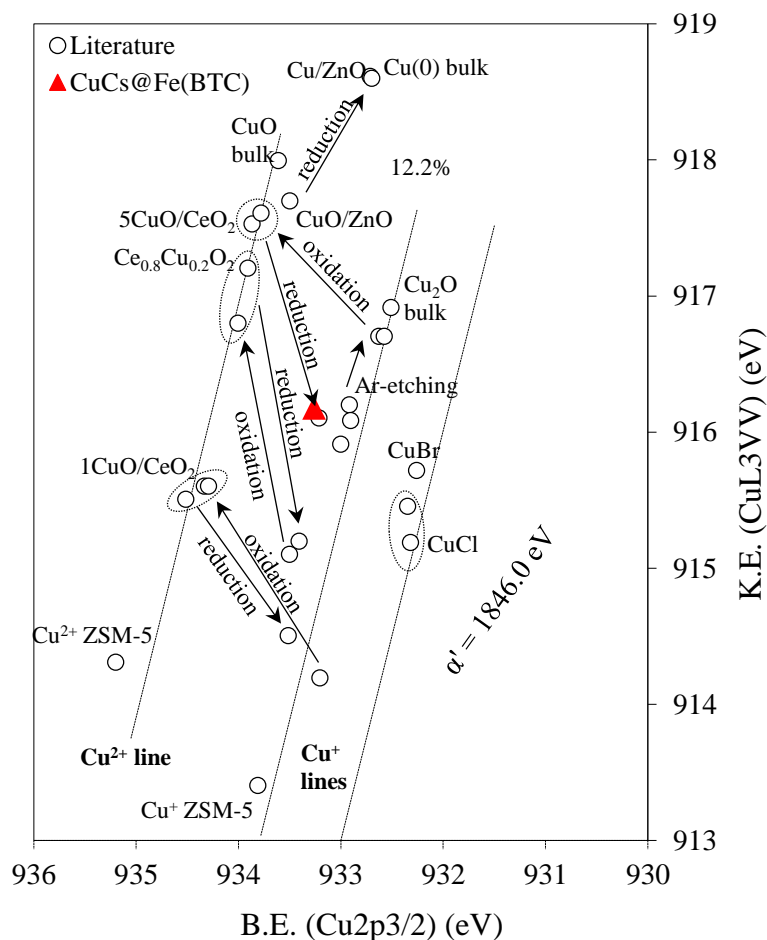

Figure 9. Copper Wagner-plot of the CuCs@Fe(BTC) composite. Empty circles correspond to data points for copper.[47,48,49]

Overall, the XPS results imply that the hydrogen treatment resulted in the partial reduction of *ca*. 50 wt% of the $Cu(acac)_2$ impregnated moieties. Moreover, the excess of C and O in the structure also indicates that the total elimination of acac moieties from the system was not achieved. It is known that the reduction of Cu(II) β-diketonates often requires the use of very strong reducing agents.[50] The sequential dissociation and reduction of $Cu(acac)_2$ in a reducing atmosphere has been described as: $Cu(acac)_2 \rightarrow Cu(acac) \rightarrow Cu$, giving different amounts of Cu^{2+}, Cu^+ and Cu end products as a function of the experimental conditions.[40] Molecular hydrogen was chosen in this work as a reducing agent because a preliminary trial showed that, under working conditions, H_2 was able to reduce net $Cu(acac)_2$ powder to metallic copper (Fig. 10).
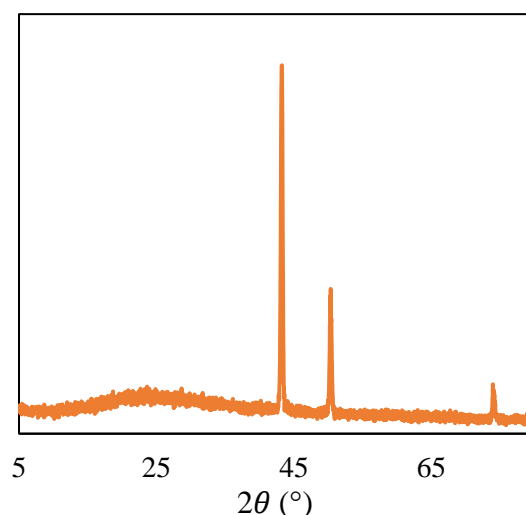
**Figure 10.** XRD spectra of the reduced net $Cu(acac)_2$ to metallic copper.

However, XPS analysis indicates that the reduction behavior of the $Cu(acac)_2$ molecules located inside the MOF pores was not equally effective. Cu and Cu^+ were simultaneously formed, with Cu^+ species as the dominant, at least on the surface. Nevertheless, the use of H_2 has relevant operational advantages, since reduction and catalysis can be performed consecutively in the same holder, without intermediate sample manipulation, simply by switching the gas. Taking into account that both Cu and Cu^+ species are described to contribute to the activity of copper-based catalysts[51,52] and that the use of H_2 as a reducing agent would simplify the design of any catalytic hydrogenation reaction, this method was considered to be the most efficient reduction approach. However, the process of reduction must be still optimized to attain a high degree of reduction. The first parameter to study is the temperature, settled here far away of the typical 350 ºC used for fully inorganic supports. Because of the organic component in the MOF, which has limited thermal stability, the reduction temperature was limited to a safety maximum of only 250 ºC. Moreover, the influence of transport limitations, and thus the reaction time on the elimination of the acac moieties from the pores during reduction in highly loaded composites should be analyzed, since it is reflected on the relatively low degree of reduction attained.

3.4. Catalytic tests

First of all, the pristine MIL-100(Fe) and Fe(BTC) MOFs were tested for their catalytic activity in the CO_2 hydrogenation reaction. These materials were *in situ* subjected to the standard reduction process with H_2 at 250 ºC used in this work. Catalysis experiments were performed at 10 bar with a 5 mLmin^{-1} flow of H_2/CO_2 in the temperature range of 180-240 ºC. The chosen H_2/CO_2 molar ratio was 3:1, stoichiometric for methanol formation. Under working conditions,

the catalytic activity of the crystalline MIL-100(Fe) was negligible. On the contrary, Fe(BTC) showed measurable activity itself, giving MeOH STY values of 0.2 $mg_{MeOH}g_{redcat}^{-1}h^{-1}$ at 240 °C with a selectivity in the order of 25 %. Such disparities on the catalytic behavior of the crystalline and semiamorphous MOFs are related to the different structural characteristics. Likely, defects in Fe(BTC) entail a large number of bare coordination sites in the Fe^{3+}/Fe^{2+} nodes, which might promote the dissociation of H_2.[53]

The effectiveness as a catalyst of using CuCs impregnated in Fe(BTC) was demonstrated in a series of CO_2 hydrogenation tests. It is worth to mention that experiments in this work were performed at low H_2/CO_2 pressure, *e.g.*, 10 bar, and not at the typical pressures > 50 bar. The absolute CO_2 conversion values were in the order of 0.5 wt%, which even being relatively low, are the expected for low pressure CO_2 hydrogenation processes.[54,55] The design and optimization of the low pressure route is necessary to make future CO_2-to-methanol processes economically attractive and energetically sustainable. Hence, even being the low pressure a detrimental factor for total CO_2 conversion, the use of low pressure is considered advantageous from an operational point of view. Hence, results could only be properly compared to those obtained using other materials under similar experimental conditions. At 240 °C, a five-fold increase in the measured MeOH STY value (0.9 $mg_{MeOH}g_{redcat}^{-1}h^{-1}$) was observed for the CuCs@Fe(BTC) sample with respect to pristine Fe(BTC). The methanol yield was compared to that produced by the typical CuZnO catalyst measured in the same equipment at 10 bar and 240 °C.[54] For proper comparison, the methanol production rate values were recalculated based on the weight of copper in the sample. STY values of 3.3 and 10 $mg_{MeOH}g_{Cu}^{-1}h^{-1}$ were measured for CuZnO and CuCs@Fe(BTC), respectively. (Fig.11a) These results are comparable with other Cu-MOF systems (0.1-12 $mg_{MeOH}g_{Cu}^{-1}h^{-1}$), although none of the previous cases used iron-based MOFs.[56]
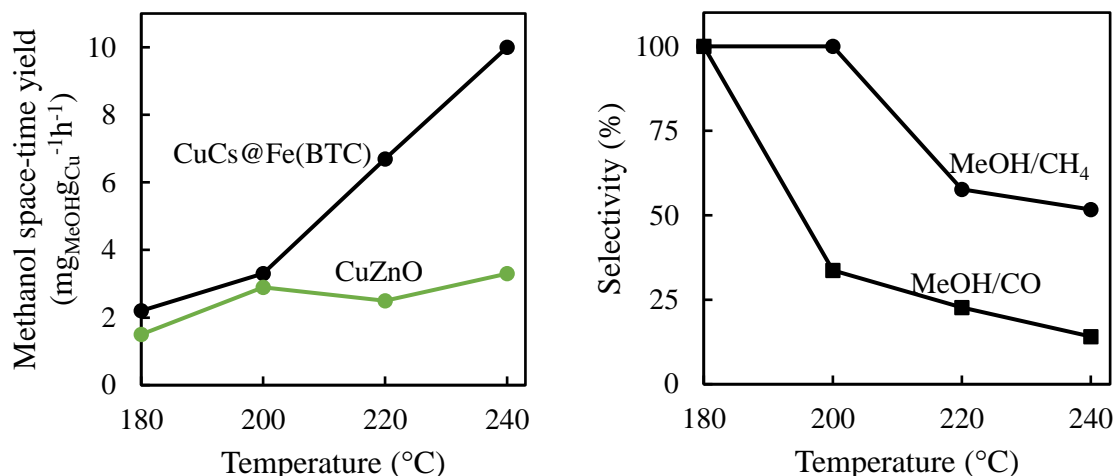
Figure 11. (a) Methanol space-time yield of the CuZnO and CuCs@Fe(BTC), related to the copper weight of the catalysts and (b) selectivity of the latter composite.

The influence of the temperature was studied in the interval of 180-240 ºC. Increasing the temperature resulted in enhanced CO_2 conversion, concomitant with a constant increase of the STY of MeOH (Fig. 11a). However, all this occurs together with a significant evolution of secondary products, including the expected CO at T>200 ºC, but also CH_4 at T>220 ºC. Considering methane and CO as sub-products, the selectivity to MeOH of the CuCs@Fe(BTC) was of 100 wt% at 180 ºC, but decreases to *ca.* of 30 wt% at 240 ºC. The CO_2 transformation to methanol and methanation reactions are expressed as in equations (1) and (2), respectively.

$$CO_2 + 3H_2 \rightarrow CH_3OH + H_2O \tag{1}$$

$$4H_2 + CO_2 \rightarrow CH_4 + 2H_2O \tag{2}$$

CO is an expected intermediate formed in the reverse water gas shift reaction (eq. (3)).

$$CO_2 + H_2 \rightarrow CO + H_2O \tag{3}$$

The origin of methane is more uncertain, since it is not commonly found when using Cu catalysts. Stoichiometrically, higher $H_2:CO_2$ ratios are required for the methanation reaction than for the formation of methanol. Actually, the experimental conditions used in this work, *e.g.*, Cu catalyst *vs.* noble metal and a feed gas mixture with a $H_2:CO_2$ 3:1 ratio, were selected for the prevalence of the hydrogenation reaction producing methanol over methane.[3] Even though the formation of a relatively high amount of methane was measured in the catalytic activity tests, together with CO and CO_2 in the gaseous fraction of the end product, mostly liquid methanol was produced. Actually, the CH_4 STY yield was of 4.9 $mg_{CH4}g_{Cu}^{-1}h^{-1}$ at 240 ºC, practically half of the MeOH yield. The reasons for the significant amount of formed methane are believed to be related to the catalyst composition. First, the blending of Cu/Cu$^+$ and

Fe^{+2}/Fe^{+3} have been described to constitute a catalyst with some efficiency in the formation of methane.[57,58] Second, the adsorption of CO_2 into the pores of Fe(BTC) can lead to the attainment of high local $H_2:CO_2$ ratios in the proximity of the catalytic centers, again favoring the formation of methane.[3] Finally, during the catalytic tests H(acac) molecules are released due to the continuous reduction of the $Cu(acac)_2$ and of the remaining Cu(acac). From this secondary product, methane molecules are easily produced through further transformation and loss of water and acetone.[¡Error! Marcador no definido.] In this study, only the mentioned three products (MeOH, CH_4 and CO) were investigated, although presumably other hydrocarbons with longer chains might also be formed, typical for Fe-based catalysts.[59]

4. Conclusions

In the search of a green approach for composite catalyst construction, $scCO_2$ was the solvent selected to carry out the synthesis. In this respect, this work aims to open the spectrum of possibilities for the $scCO_2$ synthesis of composites involving metal clusters or nanoparticles by selecting adequately the organometallic precursors. The impregnation of both, crystalline MIL-100(Fe) and semiamorphous Fe(BTC), was attempted using this technology. However, the process was only successful for the Fe(BTC) MOF, which was impregnated with $Cu(acac)_2$, and further reduced to CuCs@Fe(BTC). In the vast majority of studies, methanol production *via* CO_2 hydrogenation is realized over bifunctional catalysts, commonly Cu-ZnO interface, required to activate the CO_2 reduction. No extensive research has been found on composites of the iron trimesate type, loaded with copper species into the pores for the use as a catalyst in CO_2 hydrogenation reactions, being this study pioneer in the area. Based on the results of this study, the CuCs@Fe(BTC) sample can produce significant amounts of methanol without the incorporation of ZnO species. The most important role of ZnO is to act as a spacer among copper nanoparticles, preventing their aggregation, which is associated to the deactivation of the catalyst. In the CuCs@Fe(BTC) composite, the porous structure of the MOF is taking this role by acting as a support for dispersing the copper phase, and moreover by confining the clusters into the cages that physically hinders the growth and aggregation of the copper species. As a result, considerable amount of methanol production can be achieved without the involvement of ZnO.

References

1. A. Rafiee, K.R. Khalilpour, D. Milani, M. Panahi, Trends in CO_2 Conversion and Utilization: A Review from Process Systems Perspective, *Journal of Environmental Chemical Engineering* **2018**, *6*, 5771-5794.

2. M. Aresta, A. Dibenedetto, A. Angelini, The changing paradigm in CO_2 utilization, *Journal of CO_2 Utilization* **2013**, *3-4,* 65-73.

3. E. Furimsky, CO_2 Hydrogenation to Methanol and Methane over Carbon-Supported Catalysts, *Ind. Eng. Chem. Res*. **2020**, *59*, 15393-15423.

4. Y. Wang, K. Wang, B. Zhang, X. Peng, X. Gao, G. Yang, H. Hu, M. Wu, N. Tsubaki, Direct Conversion of CO_2 to Ethanol Boosted by Intimacy-Sensitive Multifunctional Catalysts, *ACS Catal.* **2021**, *11*, 11742-11753.

5. W. Liu, F. Wen, Y. Xue, Power-to-gas technology in energy systems: current status and prospects of potential operation strategies, *Journal of Modern Power System and Clean Energy* **2017**, *5*, 439-450.

6. Q. Zhang, S. Wang, M. Dong, W. Fan, CO_2 Hydrogenation on Metal-Organic Frameworks-Based Catalysts: A Mini Review, *Front. Chem.* **2022**, *10*, 956223.

7. D. Yang, B.C. Gates, Catalysis by Metal Organic Frameworks: Perspective and Suggestions for Future Research, *ACS Cat.* **2019**, *9*, 1779-1798.

8. J. Liu, A. Zhang, M. Liu, S. Hu, F. Ding, C. Song, X. Guo, Fe-MOF-derived highly active catalysts for carbon dioxide hydrogenation to valuable hydrocarbons, *Journal of CO_2 Utilization* **2017**, *21*, 100-107.

9. C.K. Brozek, M. Dinca, Ti^{3+}-, $V^{2+/3+}$-, $Cr^{2+/3+}$-, Mn^{2+}-, and Fe^{2+}-Substituted MOF-5 and Redox Reactivity in Cr- and Fe-MOF-5, *J.Am. Chem. Soc.* **2013**, *135*, 12886-12891.

10. J. Fonseca, T. Gong, L. Jiao, H. Jiang, Metal–organic frameworks and their catalytic applications, from this: Metal–organic frameworks (MOFs) beyond crystallinity: amorphous MOFs, MOF liquids and MOF glasses, *Journal of Material Chemistry A* **2021**, *9*, 10562.

11. Y. Liu, R.C. Klet, J. T. Hupp, O. Farha, Probing the Correlations between the Defects in Metal-Organic Frameworks and Their Catalytic Activity by an Epoxide Ring-Opening Reaction, *Chem. Commun.* **2016**, *52*, 7806−7809.

12. B. An, J. Zhang, K. Cheng, P. Ji, C. Wang, W. Lin, Confinement of ultrasmall Cu/ZnOx Nanoparticles in Metal–Organic Frameworks for Selective Methanol Synthesis from Catalytic Hydrogenation of CO2, *J. Am. Chem. Soc.* **2017**, *139*, 3834-3840.

13. Y. Zhu, J. Zhang, J. Ye, Y. Cui, K. Koh, L. Kovarik, D.M. Camaioni, J.L. Fulton, D.G. Truhlar, M. Neurock, C.J. Cramer, O.Y. Gutiérrez, J. A. Lercher, Copper-zirconia interfaces in UiO-66 enable selective catalytic hydrogenation of CO_2 to methanol, *Nature Communications* **2020**, *11*, 5849.

14. A.S. Roy, J. Mondal, B. Banerjee, P. Mondal, A. Bhaumik, Sk. M. Islam, Pd-grafted porous metal–organic framework material as an efficient and reusable heterogeneous catalyst for C–C coupling reactions in water, *Appl. Catal. A* **2014**, *469*, 320–327.

15. M. Zhao, K. Deng, L. He, Y. Liu, G. Li, H. Zhao, Z. Tang, Core–Shell Palladium Nanoparticle@Metal–Organic Frameworks as Multifunctional Catalysts for Cascade Reactions, *J. Am. Chem. Soc.* **2014**, *136*, 1738–1741.

16. B. Rungtaweevoranit, J. Baek, J.R. Araujo, B.S. Archanjo, K.M. Choi, O.M. Yaghi, G.A. Somorjai, Copper Nanocrystals Encapsulated in Zr-based Metal−Organic Frameworks for Highly Selective CO_2 Hydrogenation to Methanol, *Nano Lett.* **2016**, *16*, 7645-7649.

17. F.R. Fortea-Perez, M. Mon, J. Ferrando-Soria, M. Boronat, A. Leyva-Perez, A. Corma, J.M. Herrera, D. Osadchii, J. Gascon, D. Armentano, E. Pardo, The MOF-Driven Synthesis of Supported Palladium Clusters with Catalytic Activity for Carbene-Mediated Chemistry, *Nat. Mater.* **2017**, *16*, 760−766.

18. M. Mon, M.A. Rivero-Crespo, J. Ferrando-Soria, A. Vidal-Moya, M. Boronat, A. Leyva-Pérez, A. Corma, J.C. Hernández-Garrido, M. López-Haro, J.J. Calvino, G. Ragazzon, A. Credi, D. Armentano, E. Pardo, Synthesis of Densely Packaged, Ultrasmall Pt^0_2 Clusters within a Thioether-Functionalized MOF: Catalytic Activity in Industrial Reactions at Low Temperature, *Angew. Chem., Int. Ed.* **2018**, *57*, 6186−6191.

19. M. Eddaoudi, J. Kim, N. Rosi, D. Vodak, J. Wachter, M. O'Keeffe, O.M. Yaghi, Systematic design of pore size and functionality in isoreticular MOFs and their application in methane storage, *Science* **2002**, 295, 469.

20. P. Horcajada, S. Surblé, C. Serre, D.-Y. Hong, Y.-K. Seo, J.-S. Chang, J.-M. Grenéche, I. Margiolaki, G. Férey, Synthesis and catalytic properties of MIL-100(Fe), an iron(iii) carboxylate with large pores, *Chem. Commun.* **2007**, *27,* 2820–2822.

21. A. Dhakshinamoorthy, M. Alvero, H. Garcia, Metal–Organic Frameworks as Efficient Heterogeneous Catalysts for the Regioselective Ring Opening of Epoxides, *Chemistry – A European Journal* **2010**, *16*, 8530-8536.

22. A. Dhakshinamoorthy, M. Alvero, H. Garcia, Claisen–Schmidt Condensation Catalyzed by Metal-Organic Frameworks, *Advanced Synthesis and Catalysis* **2010**, *352*, 711-717.

23. A. Dhakshinamoorthy, M. Alvero, P. Horcajada, E. Gibson, M. Vishnuvarthan, A. Vimont, J.-M. Grenéche, C. Serre, M. Daturi, H. Garcia, Comparison of Porous Iron Trimesates Basolite F300 and MIL-100(Fe) As Heterogeneous Catalysts for Lewis Acid and Oxidation Reactions: Roles of Structural Defects and Stability, *ACS Catal.* **2012**, *2*, 2060-2065.

24. N.-N. Zhu, X.-H. Liu, T. Li, J.-G. Ma, P. Cheng, G.-M. Yang, Composite System of Ag Nanoparticles and Metal−Organic Frameworks for the Capture and Conversion of Carbon Dioxide under Mild Conditions, *Inorg. Chem.* **2017**, *56*, 3414-3420.

25. A.M. López-Periago, C. Domingo, Features of supercritical CO_2 in the delicate world of the nanopores, *The Journal of Supercritical Fluids* **2018**, *134*, 204–213.

26. E.V. Belyaeva, V.I. Isaeva, E.E. Said-Galiev, O.P. Tkachenko, S.V. Savilov, A.V. Egorov, L.M. Kozlova, V.Z. Sharf, L.M. Kustova, New method for catalyst preparation based on metalorganic framework MOF-5 for the partial hydrogenation of phenylacetylene, *Russian Chemical Bulletin* **2014**, *63*, 396-403.

27. Y. Zhao, J. Zhang, J. Song, J. Li, T. Wu, P. Zhang, B. Han, Ru nanoparticles immobilized on metal–organic framework nanorods by supercritical CO_2-methanol solution: highly efficient catalyst, *Green Chemistry* **2011**, *13*, 2078.

28. K. Guesh, C.A.D. Caiuby, Á. Mayoral, M. Díaz-García, I. Díaz, M. Sanchez-Sanchez, Sustainable preparation of MIL-100(Fe) and its photocatalytic behavior in the degradation of methyl orange in water, *Cryst. Growth Des.* **2017**, *17*, 1806-1813.

29. M. Kubovics, S. Rojas, A.M. López-Periago, J. Fraile, P. Horcajada, C. Domingo, Fully supercritical CO_2 preparation of a nanostructured MOF composite with application in cutaneous drug delivery, *The Journal of Supercritical Fluids* **2021**, *178,* 105379.

30. M. Sanchez-Sanchez, I. deAsua, K. Diaz, Direct Synthesis, Structural Features, and Enhanced Catalytic Activity of the Basolite F300-like Semiamorphous Fe-BTC Framework, *Cryst. Growth Des.* **2015**, *15*, 4498-4506.

31. W. Hui Teoh, R. Mammucari, N.R. Foster, Solubility of organometallic complexes in supercritical carbon dioxide: A review, *J. Organomet. Chem.* **2013**, *724*, 102-116.

32. S. Yoda, Y. Takebayashi, K. Sue, T. Furuya, K. Otake, Thermal decomposition of copper (II) acetylacetonate in supercritical carbon dioxide: In situ observation via UV–vis spectroscopy, *The Journal of Supercritical Fluids* **2017**, *123*, 82-91.

33. E. Rojas García, R. López Medina, M. May Lozano, I. Hernández Pérez, M. J. Valero, A.M. Maubert Franco, *Materials* **2014**, *7*, 8037-8057.

34. M. Vakili, S. Faramarz Tayyari, M. Hakimi-Tabar, A.-R. Nekoei, S. Kadjhodaei, Structure and vibrational assignment of bis(benzoylacetonato)copper(II), *Journal of Molecular Structure* **2014,** *1058*, 308-317.

35. Y. Moreno, R. Arrué, R. Saavedra, J.-Y. Pivan, O. Pena, T. Roisnell, Magnetic and structural study of unsolvated [Cu(acac)$_2$], (acac= acetylacetonate), *Journal of Chilean Chemical Society* **2013**, *58*, 2122-2124.

36. M. Thommes, K. Kaneko, A. Neimark, J.P. Olivier, F. Rodriguez-Reinoso, J. Rouquerol, S.W. Sing, Physisorption of gases, with special reference to the evaluation of surface area and pore size distribution (IUPAC Technical Report), *Pure Appl. Chem.* **2015**, *87*, 1051–1069.

37. Q. Jiang, Y. Liu, T. Dintzer, J. Luo, K. Parkhomenko, A.-C. Roger, Tuning the highly dispersed metallic Cu species via manipulating Brønsted acid sites of mesoporous aluminosilicate support for CO_2 hydrogenation reactions, *Applied Catalysis B: Environmental* **2020**, *269*, 118804.

38. C. Wang, J.L. Wang, W.B. Lin, Elucidating Molecular Iridium Water Oxidation Catalysts Using Metal-Organic Frameworks: A Comprehensive Structural, Catalytic, Spectroscopic, and Kinetic Study, *J. Am. Chem. Soc.* **2012**, *134*, 19895−19908.

39. M. Zabilskiy, V.L. Sushkevich, M.A. Newton, J.A. Van Bokhoven, Copper–Zinc Alloy-Free Synthesis of Methanol from Carbon Dioxide over Cu/ZnO/Faujasite, *ACS Catal.* **2020**, *10*, 14240–14244.

40. X. Hu, J. Schuster, S.E. Schulz, T. Gessner, Surface chemistry of copper metal and copper oxide atomic layer deposition from copper(ii) acetylacetonate: a combined first-principles and reactive molecular dynamics study, *Phys. Chem. Chem. Phys.* **2015**, 17, 26892.

41. Z. Chen, Q. Zhang, L. Huang, R. Li, W. Li, G. Xu, H. Cheng, Surface Modification of ITO Nanoparticles by Trimesic Acid: A Combined Experimental and DFT Study, *J. Phys. Chem. C*, **2014**, 118, 21244–21249.

42. K. Zhang, Y. Zhu, K. Yue, K. Zhan, P. Wang, Y. Kong, Y. Yan, X. Wang, In-situ transformed trimetallic metal-organic frameworks as an efficient pre-catalyst for electrocatalytic oxygen evolution, *Nano Res*. **2022**, 1998-0124.

43. L. Liu, W. Li, Z. Xiong, D. Xia, C. Yang, W. Wang, Y. Sun, Synergistic effect of iron and copper oxides on the formation of persistent chlorinated aromatics in iron ore sintering based on in situ XPS analysis, *J. Hazard. Mater.* **2019**, *366*, 202–209.

44. H. Zhao, M. Lin, K. Fang, J. Zhou, Y. Sun, Preparation and evaluation of Cu-Mn/Ca-Zr catalyst for methyl formate synthesis from syngas, *Applied Catalysis A: General* **2016**, *514*, 276-283.

45. D.A. Bulushev, A.L. Chuvilin, V.I. Sobolev, S.G. Stolyarova, Y.V. Shubin, I.G. Asanov, A.V. Ischenko, G. Magnani, M. Riccó, A.V. Okotrub, L.G. Bulusheva, Copper on carbon materials: stabilization by nitrogen doping, *Journal of Materials Chemistry A* **2017,** *5*, 10574.

46. H. Zhao, M. Lin, K. Fang, J. Zhou, Y. Sun, Preparation and evaluation of Cu-Mn/Ca-Zr catalyst for methyl formate synthesis from syngas, *Applied Catalysis A: General* **2016**, *514,* 276-283.

47. D. Gamarra, A. Hornés, Zs. Koppany, Z. Schay, G. Munuera, J. Soria, A. Martínez-Arias, Catalytic processes during preferential oxidation of CO in H2-rich streams over catalysts based on copper-ceria, *J. Power Sources.* **2007**, *169*, 110–116.

48. J. Agrell, M. Boutonnet, I. Melián-Cabrera, J.L.G. Fierro, Production of hydrogen from methanol over binary Cu/ZnO catalysts Part I. Catalyst preparation and characterization, *Appl. Catal. A Gen.* **2003**, *253*, 201–211.

49. M.C. Biesinger, Advanced analysis of copper X-ray photoelectron spectra, *Surf. Interface Anal.* **2017**, *49*, 1325–1334.

50. L. Wu, E. Eisenbraun, Hydrogen plasma-enhanced atomic layer deposition of copper thin films, J. Vac. Sci. Technol., B, **2007**, *25*, 2581–2585.

51. F. Studt, M. Behrens, E.L. Kunkes, N. Thomas, S. Zander, A. Tarasov, J. Schumann, E. Frei, J.B. Varley, The Mechanism of CO and CO2 Hydrogenation to Methanol over Cu-Based Catalysts *ChemCatChem* **2015**, *7*, 1105–1111.

52. X. Yuan, S. Chen, L. Li, W. Zhu, D. Zhong, Z. Zhao, J. Li, T. Wang, J. Gong, Controllable Cu^0-Cu^+ sites for electrocatalytic reduction of carbon dioxide, *Angewandte Chemie International Edition* **2021**, *60,* 15344-15347.

53. Y. Mitsuka, N. Ogiwara, M. Mukoyoshi, H. Kitagawa, T. Yamamoto, T. Toriyama, S. Matsumura, M. Haneda, S. Kawaguchi, Y. Kubota, H. Kobayashi, Fabrication of Integrated Copper-Based Nanoparticles/Amorphous Metal–Organic Framework by a Facile Spray-Drying Method: Highly Enhanced CO_2 Hydrogenation Activity for Methanol Synthesis, *Angewandte Chemie* **2021**, *133*, 22457-22462.

54. M. Kubovics, A. Trigo, A. Sánchez, G. Marbán, A. Borrás, J. Moral-Vico, A.M. López-Periago, C. Domingo, Role of graphene oxide aerogel support on the CuZnO catalytic activity: Enhancing methanol selectivity in the hydrogenation reaction of CO_2, *ChemCatChem* **2022**, *14*, e202200607.

55. A. Carrasco García, J. Moral-Vico, A. Abo Markeb, A. Sánchez, Conversion of carbon dioxide into methanol using Cu–Zn nanostructured materials as catalysts, *Nanomaterials* **2022**, *12*, 999.

56. H. Kobayashi, J.M. Taylor, Y. Mitsuka, N. Ogiwara, T. Yamamoto, T. Toriyama, S. Matsumura, H. Kitaqawa, Charge transfer dependence on CO_2 hydrogenation activity to methanol in Cu nanoparticles covered with metal-organic framework systems, *Chemical Science* **2019**, *11*.

57.   S.-F. Hung, X. Wang, F. Li, S.-H. Hsu, Y. Li, J. Wicks, E. González Cervantes, A.S. Rasouli, Y.C. Li, M. Luo, D.-H. Nam, N. Wang, T. Peng, Y. Yan, G. Lee, E.H. Sargent, A metal-supported single-atom catalytic site enables carbon dioxide hydrogenation, *Nature Communications* **2022**, 13, 819.

58.   H. Ando, Selective Alkene Production by the Hydrogenation of Carbon Dioxide over Fe-Cu Catalyst, *Energy Procedia* **2016**, *89*, 421–427.

59.   R.-P. Ye, J. Ding, W. Gong, M.D. Argyle, Q. Zhong, Y. Wang, C.K. Russel, Z. Xu, A.G. Russel, Q. Li, M. Fan, Y.-G. Yao, CO_2 hydrogenation to high-value products via heterogeneous catalysis, *Nature Communications* **2019**, *10*, 5698.

Supercritical CO₂ synthesis of porous metalloporphyrin frameworks: application in photodynamic therapy
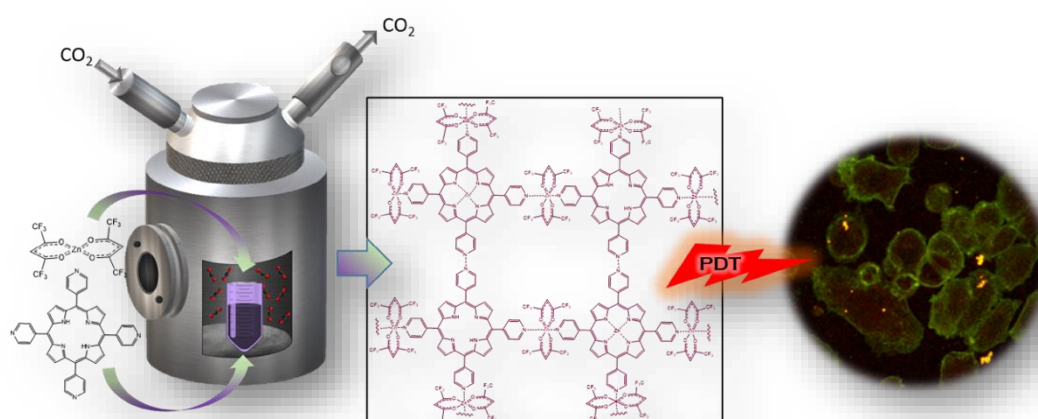
In this work a series of porous metalloporphyrin frameworks were prepared using supercritical CO₂ as solvent, involing 5,10,15,20-Tetra(4-pyridyl) porphyrin linker and four metal (Cu, Zn, Co, Ni) 1,1,1,5,5,5-hexafluoroacetylacetonate complexes. The Zn-based MOF was selected as potential photodynamic therapy showing outstanding performance.

Abstract

A series of porous metalloporphyrin frameworks prepared from the 5,10,15,20-tetra(4-pyridyl)porphyrin (H_2TPyP) linker and four metal complexes, $M(hfac)_2$ M= Cu(II), Zn(II), Co(II), Ni(II) (hfac: 1,1,1,5,5,5-hexafluoroacetylacetonate), were prepared using supercritical CO_2 (scCO_2) as a solvent. All the materials, named generically as $[M\text{-}TPyP]_n$, formed porous metal-organic frameworks (MOFs), with surface areas of ~ 450 m^2g^{-1}. All MOFs were formed through the coordination of the metal to the exocyclic pyridine moieties in the porphyrin linker. For Cu(II), Zn(II) and Co(II), incomplete metal coordination of the inner pyrrole ring throughout the structure was observed, giving place to MOFs with substitutional defects and leading to a certain level of disorder and limited crystallinity. These samples, prepared using scCO_2, were precipitated as nano to micrometric powders. Separately, a layering technique from a mixture of organic solvents was used to crystalize high quality crystals of the Co(II) based MOF, obtained with formula $[\{Co(hfac)_2\}_2H_2TPyP]_n$. The crystal structure of this MOF was elucidated by single-crystal synchrotron X-ray diffraction. The Zn(II) based MOF was selected as potential photodynamic therapy drug in the SKBR-3 tumoral cell line showing outstanding performance. This MOF resulted to be non-toxic, but after 15 min irradiation at 630 nm, using either 1 or 5 µM concentration of product, almost 70 % of tumour cell died after 72 h.

1. Introduction

Porphyrins are key building block precursors in many areas of synthetic chemistry. As an important example, the preparation of metal-organic frameworks (MOFs) containing porphyrin linkers is currently of great interest, as they can form coordination networks with multiple applications such as catalysis, sensors for molecular recognition,[1-3] or drugs for cancer treatment.[4-6] In the latter, porphyrins are the most extensively used material for photodynamic therapy (PDT).[7] The PDT procedure is based on the local application of a photosensitizer in the affected area that, by light radiation of a certain wavelength, induces the formation of reactive oxygen species (ROS)[8] able to destroy the harmful cells through either necrosis or apoptosis.[9] In this technique, the use of net porphyrins is often limited by their low bio-stability in aqueous media, self-aggregation and non-selective tumour targeting.[10] Some of these drawbacks can be significantly attenuated by building porous structures in which the porphyrins are the organic linkers located between metal-containing species, thus obtaining porphyrin based MOFs. From them, the so-called 4th generation of photosensitizers is built,[11] where the porphyrin moieties are somehow isolated and their aggregation is hindered.[12] The first report on PDT using porphyrins as building blocks in MOFs involves the use of Hf(IV)[13] and Zr(IV)[14] as metal centres for head and neck cancer and cervical cancer, respectively.

Among the most studied porphyrin MOFs are those involving Zr(IV), giving high stability and structural diversity,[15] Ti(IV), applied in photocatalysis,[16] and divalent Zn(II), Co(II), and Cu(II) cations, forming usually very stable 2D sheet-like structures.[17-19] Less common, but equally functional, are the porphyrin-based MOFs with pyridyl motifs that can form supramolecular structures through self-assembly.[20] In particular, 5,10,15,20-tetra(4-pyridyl)porphyrin (H$_2$TPyP), linker chosen in this study, which possess several potential coordination sites. The inner tetratopic unit can be coordinated by displacing the two protons of the N-H pyrrole sub-units, and the exocyclic four pyridyl groups linked to the porphyrin ring can potentially coordinate from one to four metal ions, which can greatly enrich the structure and functionality. Nevertheless, not many examples of MOF constructions are found in the literature for this type of pyridyl-based porphyrin linkers, presumably because H$_2$TPyP has an extremely low solubility in most conventional liquid solvents, which difficult enormously their processing. In fact, H$_2$TPyP is only partially soluble in chloroform, dimethylformamide and trichloroethane. Examples with total metal complexation are the coordination of Zn(II) ions with the pyridyl groups of adjacent H$_2$TPyP molecules, and the same structure but with Ag(II) coordinated to the pyrrole units forming 2D coordination polymers.[21] Two other examples of full coordination in TPyP^{2-} were

obtained using Cu(II), and consists on porous 2D coordination networks involving the paddlewheel Cu(II) tetraacetate [$Cu_2(AcO)_4$] secondary building unit[22] or the Cu(hfac)$_2$.[23] In both cases, the Cu(II) fulfilled different tasks, since it acts as a metal source to metallise the porphyrin ring by interchanging Cu(II) with the two central protons of the NH pyrrole ring, and as a neutral node maintaining the ligands AcO or hfac.

Described H_2TPyPs based MOFs have been obtained using long-lasting synthetic methods (from weeks to months), either using layering (solvent diffusion) or solvothermal approaches. These techniques produce high quality crystals proper for single crystal X-ray diffraction resolution, but in extremely small yields. Besides, these approaches can have the limitation of solvent incorporation into the pores of the MOF, which can modify the structure of the final product. Currently, the synthesis of MOFs is currently beyond the study of their fundamental framework, as in many circumstances, developing key applications do not necessarily imply having well resolved crystal structures. In fact, amorphous or semi-amorphous MOFs have also show high capability to perform certain applications, such as in drug delivery systems.[24] In this way, the search for new preparation methods involving short reaction times, low temperatures and avoiding toxic solvents, while achieving large yields is under strong surveillance, even if the quality of the crystals is partially compromised. Among the different techniques developed to synthetized MOFs and coordination polymers, those based on supercritical CO_2 (scCO_2) have proven to be excellent for precipitating materials in high yield. scCO_2 has been traditionally used for removing entrapped solvents within MOF structures. However, in the last few years, it has also been used in our research group as a solvent for the synthesis of MOFs, either by using exclusively scCO_2,[25-27] or adding a co-solvent,[28] with interesting applications in medicine (bioMOFs),[29] sensors[30] or gas adsorption after hybridized with graphene aerogels.[31] In essence, the use of the scCO_2 technology has proved excellent to prepare materials for biomedical applications.[32] In the search for new applications, and as a part of an ongoing work, we have explored here the possibilities of precipitating MOFs based on the H_2TPyPs porphyrin linker in scCO_2. Four metal hexafluoroacetylacetonate complexes (M(hfac)$_2$, M=Cu(II), Zn(II), Co(II), Ni(II)) were used to complete the MOF structure, using only scCO_2 as a solvent or adding a small amount of chloroform as a co-solvent, when necessary. In order to obtain crystals for the structural elucidation, a layering approach was attempted for all the studied products. However, this approach only allowed to attain proper crystals for the MOF involving Co(II), which was further elucidated in regard of the crystalline structure. Finally, the scCO_2 precipitated Zn(II) MOF was successfully tested as a potential photosensitizer in PDT therapy.

2. Materials and methods

2.1. Materials

The organic linker 5,10,15,20-tetra(4-pyridyl)porphyrin, the metallic units of copper, zinc, cobalt and nickel hexafluoroacetylacetonate ([Cu(hfac)$_2$]·xH$_2$O, [Zn(hfac)$_2$]·2H$_2$O, [Co(hfac)$_2$]·xH$_2$O, [Ni(hfac)$_2$]·xH$_2$O), the solvents chloroform (CHCl$_3$), methanol (MeOH) and 1,1,2-trichloroethane (Cl$_3$Et), and sodium anthracene-9,10-dipropionic acid (Na-ADPA) and perinaphthenone, used for the singlet oxygen measurement, were all purchased from Sigma Aldrich. CO$_2$ (99.995 %) was supplied by Carburos Metálicos S.A., Air Products Group (Spain).

2.2. Methods

2.2.1. Synthesis of MOFs

scCO$_2$ synthesis: [Zn-TPyP]$_n$, [Cu-TPyP]$_n$ and [Ni-TPyP]$_n$ MOFs were obtained in pure scCO$_2$. Reactions were performed in a 10 mL vial placed into a 100 mL high-pressure autoclave with two opposite sapphire windows (TharDesign). The vial was charged with 0.34 mol of the metal complex M(hfac)$_2$ and 0.11 mol of the organic linker, standardising a molar ratio of *ca.* 3.1:1 for M(II):H$_2$TPyP in all cases. A small magnetic bar was also added and the vial was finally capped with cellulose filter paper. In case of [Co-TPyP]$_n$, ~ 5 v% of CHCl$_3$ was also added as co-solvent. Experiments were performed using scCO$_2$ at 20 MPa and 60 °C, stirring the powder into the vial at 500 rpm, and for 72 h. After this running time, samples were cleaned with a flow of fresh CO$_2$ at high pressure to remove the excess of unreacted M(hfac)$_2$. Finally, the reactor was slowly depressurized and cooled down to room temperature, to recover in all cases a fine garnet coloured dry powder, in an average yield of 85 wt%.

Layering: crystallization assays using the layering approach were tried for all studied metals. However, only the one involving Co(II) successfully produced crystals available for the structural elucidation. For this experiment, H$_2$TPyP (0.025 mmol) was dissolved in 10 mL of Cl$_3$Et/MeOH (3:1) and layered with 2 mL of fresh MeOH. A solution of [Co(hfac)$_2$(H$_2$O)$_x$] (0.104 mmol) in 10 mL of MeOH was carefully layered onto the pristine MeOH layer. After several weeks at room temperature, purple needle-like crystals precipitated. The crystals were carefully filtered, rinsed with fresh MeOH and finally dried under vacuum.

2.3. Characterization

The structure of the obtained samples was analysed by powder X-ray diffraction (PXRD) with a Siemens D5000 X-ray powder diffractometer using the Cu Kα incident radiation. The diffraction patterns were recorded from 2θ=5 to 30º, with a step scan of 0.02º counting for 1 s at each step. The morphological analysis was performed using a QUANTA FEI 200 FEG-ESEM scanning electron microscope (SEM). The thermal properties of the samples were evaluated by thermogravimetric analysis (TGA, Perkin Elmer 7). Measurements were carried out under a N_2 atmosphere raising the temperature at a rate of 10 ºCmin^{-1}. Fourier transformed infrared (FTIR) spectra of the solid samples dispersed in KBr were recorded on a Perkin Elmer Spectrum apparatus. The textural properties were determined by N_2 adsorption/desorption experiments, performed at -196 ºC, using an ASAP 2020 Micromeritics Inc equipment. The samples were previously degassed at 120 ºC for 24 h. The Brunauer-Emmet-Teller (BET) surface area (S_{BET}) of the precipitated compounds was estimated in the relative pressure range of *ca.* 0.05-0.20. The micropore Langmuir surface ($S_{Langmuir}$) was also calculated, together with the micropore volume (V_{mp}) estimated by the t-method. Elemental analysis was performed with a Flash EA2000 Thermo Fisher Scientific analyser. Ultraviolet-visible (UV-Vis) absorption measurements in water were carried out in a Varian Cary 5000 apparatus with an operational range in the spectrophotometer of 190-3300 nm. Dynamic light scattering (Zetasizer Nano ZS Malvern Inst.) was used to measure the hydrodynamic size.

Single-crystal X-ray diffraction (SCXRD) experiments for [{Co(hfac)$_2$}$_2$TPyP]$_n$ were performed in the XALOC beamline at the ALBA synchrotron (Spain). Data were collected at 100 K with a 0.72931 Å wavelength using the Dectris Pilatus 6M detector placed at 120 mm from the sample. The 9-scans were performed from 0 to 360º in steps of 0.5º with a collection time of 0.15 step^{-1}. The scan was repeated at three different N angles (0, 45 and 90º), and merged afterwards to increase the completeness and redundancy when possible. Data were indexed, integrated and scaled using the XDS software.[33] The crystal structures were solved by intrinsic phasing and refined with SHELXL (version 2014/7)[34] using Olex2 as a graphical interface.[35]

2.4. Measurement of singlet oxygen ($^1O_2$) production

2.4.1. Singlet oxygen detection via fluorescence decay of ADPA

Singlet oxygen formation was detected using a Cary Eclipse spectrofluorimeter (Agilent). The process involved measuring the fluorescence decay of ADPA upon irradiation in the presence of the [Zn-TPyP]$_n$ photosensitizer.[36] For this, 100 µl Na-ADPA water solution (1.2 mM) was added to 3 mL of [Zn-TPyP]$_n$ dispersion in water (0.15 mgmL^{-1}). The mixture was irradiated at

630 nm during 15 min, using the same light source as for the photodynamic treatment (PhotoActivation Universal Light PAUL device, GenIUL). After each 5 min, the mixture was introduced to a quartz cuvette of 1 cm, and the fluorescence emission spectra of the mixture was recorded in the 380-600 nm range, using an excitation wavelength of 355 nm.

2.4.2. Singlet oxygen quantum yields (ϕ_Δ) measurement

Room-temperature singlet oxygen phosphorescence was detected at 1270 nm with a Horiba-Jobin-Ybon SPEX Nanolog spectrofluorimeter using the DSS-IGA020L detector. The use of a Schott RG 1000 filter was essential to eliminate from the infrared signal all the first harmonic contribution of sensitizer emission in the region below 850 nm. The singlet oxygen formation quantum yield was then determined by direct measurement of the phosphorescence at 1270 nm following irradiation of the aerated aqueous dispersions of the samples. Perinaphthenone in dichloromethane was used as standard reference, applying equation (1).

$$\phi_\Delta = \phi_\Delta^{ref} \frac{Emission_{1270\,nm}}{Emission_{1270\,nm}^{ref}} \quad (1)$$

being ϕ_Δ^{ref} the singlet oxygen formation quantum yield of the reference compound ($\phi_\Delta^{ref} = 0.79$).

2.5. Cell culture experimenters of [Zn-TPyP]$_n$

Biological experiments were performed using the SKBR-3 cells line, a tumorigenic human mammary epithelial cell line (ATCC, USA). Cells culture was carried out in McCoy's 5A modified medium (Gibco) supplemented with 10 % foetal bovine serum (Gibco) in a 37 °C humidified incubator set to 5 % CO_2 (standard culture conditions). For both analysis, toxicity evaluation in the dark and under irradiation (photodynamic experiments), cells were seeded in 4- or 24-well plates at a density of 3.5×10^4 cells per well. For Confocal Laser Scanning Microscopy (CLSM) experiments, cells were seeded in special confocal 35 mm dishes provided with glass coverslip bottom (µ-Dish 35 mm, high Glass Bottom, Ibidi GmbH) at a density of 1.75×10^5 cells per well. All product treatments were performed 24 h after cell seeding. Stock product dispersions were prepared in filtered distilled water to a final concentration of 1 mM. Then, stock solutions were diluted in cell media obtaining a final product concentration of 1, 5 and 10 µM.

2.5.1. Dark toxicity evaluation

The toxicity of the product in the absence of irradiation (from now on, dark toxicity) was evaluated by determining cell viability at two different time points (24 and 72 h post-incubation) by the Alamar Blue assay. Briefly, 24 h after cell seeding, cells were incubated for 24 h with different concentrations of product (0 (control), 1, 5 and 10 µM) previously treated with an ultrasonic bath. Later, cell media was removed, and cells were washed four times with Hank's Balanced Salt Solution (HBSS, BioWest) to remove any product remains, followed by fresh media addition. Viability was assessed twice, right after media addition (viability at 24 h) or after an additional 48 h incubation in standard culture conditions (viability at 72 h). Three independent experiments were performed for each condition.

2.5.2. Photodynamic treatments

Photodynamic treatments were performed following the same protocol as for the dark toxicity, but this time SKBR-3 cells were incubated with 1 or 5 µM products for 4 h. After 4 h incubation, cell media was removed, and cells were washed four times with HBSS to remove any product remains, followed by fresh medium addition. Later, cells were either kept in dark conditions (not irradiated) or irradiated for 15 min using a PhotoActivation Universal Light device (PAUL, GenIUL), in the range of 620–630 nm (red light) and with a mean intensity of 55 mWcm^{-2} (light dose of 33 Jcm^{-2}). Cell culture viability assessments were performed twice, right after irradiation (viability at 24 h) or after being incubated for an additional 48 h in standard conditions (viability at 72 h), using the Alamar Blue Assay. Three independent experiments were performed for each condition.

2.5.3. Alamar Blue assay

Cell viability was determined using the Alamar Blue cell viability reagent (Thermo Fisher Scientific). Briefly, after product incubation either during 4 or 24 h, cell media was removed, and cells were washed four times with HBSS before adding 10 % Alamar Blue in fresh medium. Cells were then incubated for 4 h in standard conditions in the dark. After incubation, media was collected, and 200 µL of the solution was transferred to a black bottom Greiner CELLSTAR® 96 well plate (Sigma Aldrich). Finally, the fluorescence of the media was measured at 590 nm wavelength, after excitation at 560 nm on a Spark multimode microplate reader (Tecan). Three independent experiments were performed for each condition.

2.5.4. Product internalisation

To visualise if there was any product internalisation, 1.75×10^5 cells were seeded on confocal 35 mm dishes provided with glass coverslip bottom. After 24 h of cell seeding, 1 µM of product was added to the culture. After product incubation (4 or 24 h) in standard conditions in the dark, cells were washed four times with HBSS to remove non internalised product and incubated with 5 µL of wheat germ agglutinin (WGA) 448 for 15 min to detect the limit of the cells. Then, images were acquired with a Leica TCS-SP5 AOBS spectral Confocal Laser Scanning Microscope (Leica Microsystems) using a PlanApochromatic 63X objective lens. WGA-Alexa Fluor 488 (plasma membrane) and product excitation was carried out using 405 and 488 nm laser lines, respectively, using a sequential mode. Different PMT devices (600-763 nm for product fluorescence emission and 500-550 nm for WGA fluorescence emission (membrane)) were used to detect each corresponding spectral range. Series of images were further analysed with Fiji software (Image J - NIH).

2.5.5. Statistical analyses

The statistical analysis was performed using GraphPad Prism version 6.01 for Windows, (GraphPad Software). Quantitative results were analysed using a two-way ANOVA with a minimal significance level set at $p \leq 0.05$. In the figures, significance is represented by an asterisk, which means that the values are significantly different from their control ($p < 0.05$).

3. Results and discussion

3.1. scCO$_2$ synthesis

It is generally recognised that when preparing MOFs, the solvent of choice is highly important, since it can affect several parameters, such as structure, morphology, crystallinity and particle size of the end product. As mentioned in the Introduction section, reported MOFs involving H$_2$TPyP as a linker have been obtained using techniques where the yield was compromised towards obtaining high quality crystals. This work explores the use of green scCO$_2$ as an efficient solvent for the preparation of new H$_2$TPyP based MOFs at a high yield and in the absence of large amounts of toxic solvents. For achieving this target, hexafluoacetylacetonate metal ligands (M(hfac)$_2$), with typical high solubility in scCO$_2$, were used. In this method, the use of neutral metallic nodes is preferred due to the limited capacity of scCO$_2$ for dissolving ionic materials. Being scCO$_2$ the solvent used in this work for product synthesis, reagents solubility in this fluid is an important parameter determining product characteristics. Reagents solubility values in this fluid were first empirically estimated by a simple visual method carried

out in the sapphire windows reactor. Weighted amounts of micronized powder were added to the reactor that was then filled with scCO$_2$ under typical reaction conditions chosen for MOFs synthesis (*e.g.*, 20 MPa, 60 ℃). The turbidity of the system, maintained under vigorous stirring, was observed for periods of several hours. Only for the H$_2$TPyP linker, the turbidity was permanent, indicating very little solubility in scCO$_2$. In regard of the metal precursors, experimentally it was observed that solubility decreases as follows: Co(hfac)$_2$ > Zn(hfac)$_2$ ~ Cu(hfac)$_2$ > Ni(hfac)$_2$. Solubility values of these substances have been compiled in the literature,[37] but they are not totally coincident with our observations, likely due to the different level of hydration of the reagents. Tests performed in this work pointed out to Ni(hfac)$_2$ having the lowest solubility value compared to the other metal precursors, concurrent with its high hydration level.

Since some of the used reagents were not highly soluble in scCO$_2$, the process was first optimized by adjusting the synthetic parameters to avoid the presence of large amounts of unreacted molecules after MOF precipitation, which can contaminate the end product. The first trial consisted in using a large excess of M(hfac)$_2$ with respect to the organic linker (molar ratio 6:1). However, no significant changes in regard of structure or purity of the end product were observed when comparing this ratio to the stoichiometric molar ratio corresponding to the addition of enough metal for reaching full complexation of all the potential binding sites in the H$_2$TPyP, *e.g.*, the four pyridine groups and the inner pyrrole ring. Accordingly, further trials were carried out using a 3.1:1 M(hfac)$_2$:porphyrin molar ratio, aiming to minimise also the presence of remaining M(hfac)$_2$ after MOF precipitation. An exception to this rule was the precipitation of the MOF of Co(II), for which whatever the experimental conditions, large amounts of unreacted H$_2$TPyP were always present in the end product. Thus, to precipitate this MOF, CH$_3$Cl co-solvent was employed to enhance linker solubility. Initial experiments were carried out lasting 3 h, but after this short period of time, mixtures of end products and unreacted H$_2$TPyP were always recovered. Hence, the influence or reaction time was studied by increasing the reaction time in steps, up to a week. The withdrawal of the diffraction peaks of the pure porphyrin linker in the PXRD patterns was chosen as the standard indication of the evolution of the H$_2$TPyP towards the end product. Analysing the results, after 72 h no further changes in the pattern were observed, thus the reaction time was standardised at this time for all of the metals to complete the reaction.

3.2. Structure of the synthetized MOFs

Several attempts were performed to synthetize high quality crystals of all the studied porphyrin-derived MOFs. Used techniques were layering and the solvothermal approach, in which the reagents were kept at 120 ºC in dimethylformamide in closed vials during 72 h. From all of the performed trials, only the layering of Co(II) and H_2TPyP in $Cl_3Et/MeOH$ resulted in crystals of the necessary quality for performing structural elucidation by SCXRD. From the rest, only fine particles were precipitated, characterised by PXRD (Figure 1) and not corresponding to the phases precipitated in $scCO_2$. The characteristics of the rest of the $scCO_2$ precipitated new compounds were determined by comparison with the PXRD pattern of the Co(II) derived porphyrin, either prepared by the $scCO_2$ method or simulated from the single-crystal structural data.
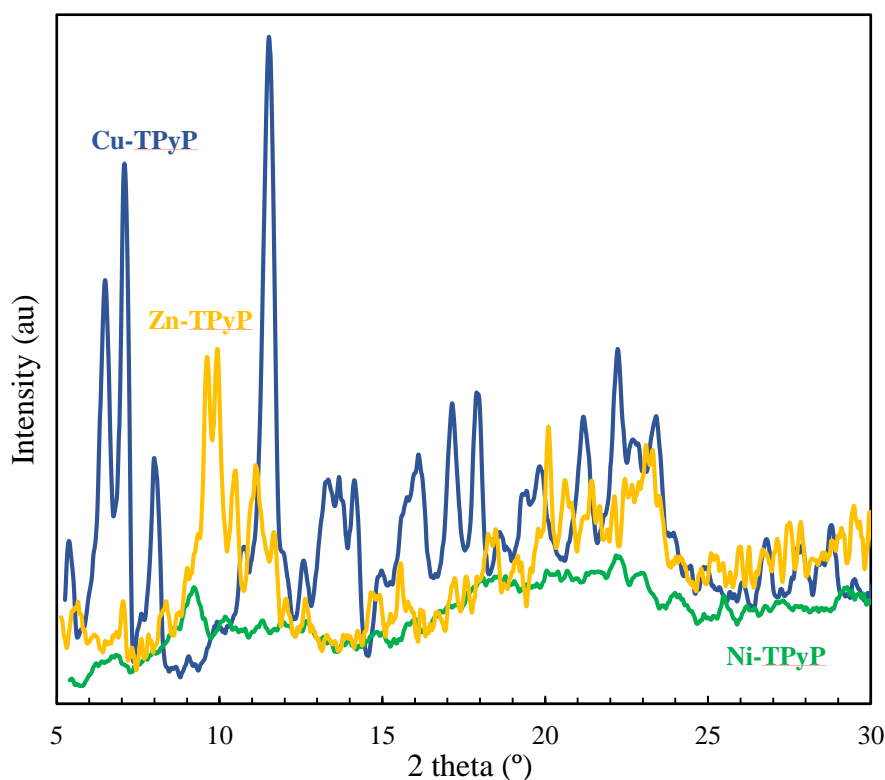
Figure 1. Capillary PXRD patterns of reaction products from the layering runs of Cu(II), Zn(II) an Ni (II) reacted with H_2TPyP.

3.2.1. [{Co(hfac)₂}₂H₂TPyP]ₙ structure

The porphyrin-derived MOF of Co(II) precipitated from layering, with formula $[\{Co(hfac)_2\}_2H_2TPyP]_n$, do not show the metal coordination in the inner porphyrin ring as shown in Figure 2(a). Crystallographic data is presented in Table 1.

Table 1. Crystallographic data for compound [{Co(hfac)$_2$}H$_2$TPyP]$_n$ determined by single crystal diffraction.

Compound	[{Co(hfac)$_2$}H$_2$TPyP]$_n$
Empirical formula	C$_{15}$H$_{7.5}$CoF$_6$N$_2$O$_2$
Formula weight	391.19
Radiation	X-rays
T (K)	100(2)
Wavelength (Å)	0.72932
System, space group	Monoclinic, *C 2/m (12)*
a (Å)	22.913(10)
b (Å)	25.721(4)
c (Å)	6.524(1)
β (°)	105.60(2)
V (Å^3)	3703.25
Z	8
*D*calc (g cm^{-3})	1.403
μ (mm^{-1})	0.597
F(000)	1560
Crystal size (mm^3)	0.100x0.060x0.040
hkl ranges	-31≤h≤31, -35≤k≤35, -8≤l≤8
2θ range (°)	1.248 to 29.967
Reflections collected/unique/[R$_{int}$]	125748/5021/[R$_{int}$ = 0.0546]
Completeness	98.6%
Refinement method	Full matrix least-squares on |F|^2
Data/restrains/parameters	5021/0/234
Goodness of fit (GOF) on |F|^2	1.134
Final *R* indices [*I*>2σ(*I*)]	R1 = 0.0483, wR2 = 0.1401
R indices (all data)	R1 = 0.0500, wR2 = 0.1416
Largest. Diff. peak and hole (e Å^{-3})	0.945 and -0.995

The four pyridines coordinated to metal clusters forming a polymeric structure. This synthesis is believed to be thermodynamically and kinetically favoured. The coordination of the pyridines is a highly favourable process because the exocyclic groups are highly exposed towards the approach of the metal clusters, and the orbital geometry of the nitrogen is also favourable. In addition, Co(hfac)$_2$ can coordinate the pyridine without the elimination of any of its hfac moieties, thus maintaining the ligands and reducing the necessary reaction energy. This addition process occurs in one-step, without the release of any component, and therefore it can occur in a fast and effective way. On the contrary, the use of large metallic clusters might sterically hinder the access of the Co(hfac)$_2$ units to the inner pyrrole ring. Furthermore, the coordination

to the pyrrolic ring would imply the substitution and elimination of the proton in the pyrrol (N-H) and the elimination of the hfac moiety as hexafluoroacetilcetone upon metal coordination. Overall, the metal coordination of the pyrrolic ring is a highly energetic process, and therefore less probable to occur in comparison to the pyridine $M(hfac)_2$ addition. Since the synthesis of the Co(II) MOF is performed at room temperature, it can be assumed that, in the apparent competing reactions pyridine-metal *vs.* pyrrole-metal, the lack of temperature as energy input is detrimental for the later *vs.* the former.

$[\{Co(hfac)_2\}_2H_2TPyP]_n$ belongs to the monoclinic crystal system, with space group C2/m (12). The asymmetric unit contains one cobalt atom, one hfac ligand and a quarter of the porphyrin linker. The crystal structure resembles to the previously described for $[\{Cu(hfac)_2\}CuTPyP \cdot 6H_2O]_n$,[23] in particular on the framework structure, space group and cell parameters. However, the Co(II) compound in this work shows three key differences: (i) it contains $Co(hfac)_2$ nodes instead of $Cu(hfac)_2$ nodes, (ii) the porphyrin is non-metallated, and (iii) the pores do not contain any solvent. The structural analysis revealed a 2D sheet coordination polymer comprising *trans* configured $Co(hfac)_2$ nodes, joined by four-connected H_2TPyP, acting as tetratopic linkers, trough the four pyridyl groups. The ensemble defines a (4,4)-net with a rhomboidal distortion from a regular square grid. The porphyrin ring system is essentially flat, although it is slightly inclined respect to the main sheet planes defined by the Co(II) positions (angle 5.67°) (Figure 2(b)). The pyridyl rings are 74.07(12)° ((76.55(8)° in the copper compound) tilted relative to the mean plane of the porphyrin macrocycle. The coordination sphere about Co(II) is essentially a distorted elongated octahedron, involving four oxygen donor atoms of the chelating hfac ligands in a plane, Co-O bond length of 2.06 Å, and the axial positions occupied by two nitrogen atoms from pyridyl groups belonging to two different H_2TPyP linkers, Co-N bond length of 2.15 Å. The bond angles about Co(II) show some deviations from the ideal 90° (values between 85 and 95°), and, besides the pyridyl ring plane, are not perpendicular to the $Co-O_4$ plane 72.27° (Figure 2(c)). The polymeric sheets are stacked, but with some offset. Therefore, the distance between main planes of adjacent sheets, 4.84 Å, is shorter than the closer Co-Co separation, 6.52 Å (Figure 2(d)).
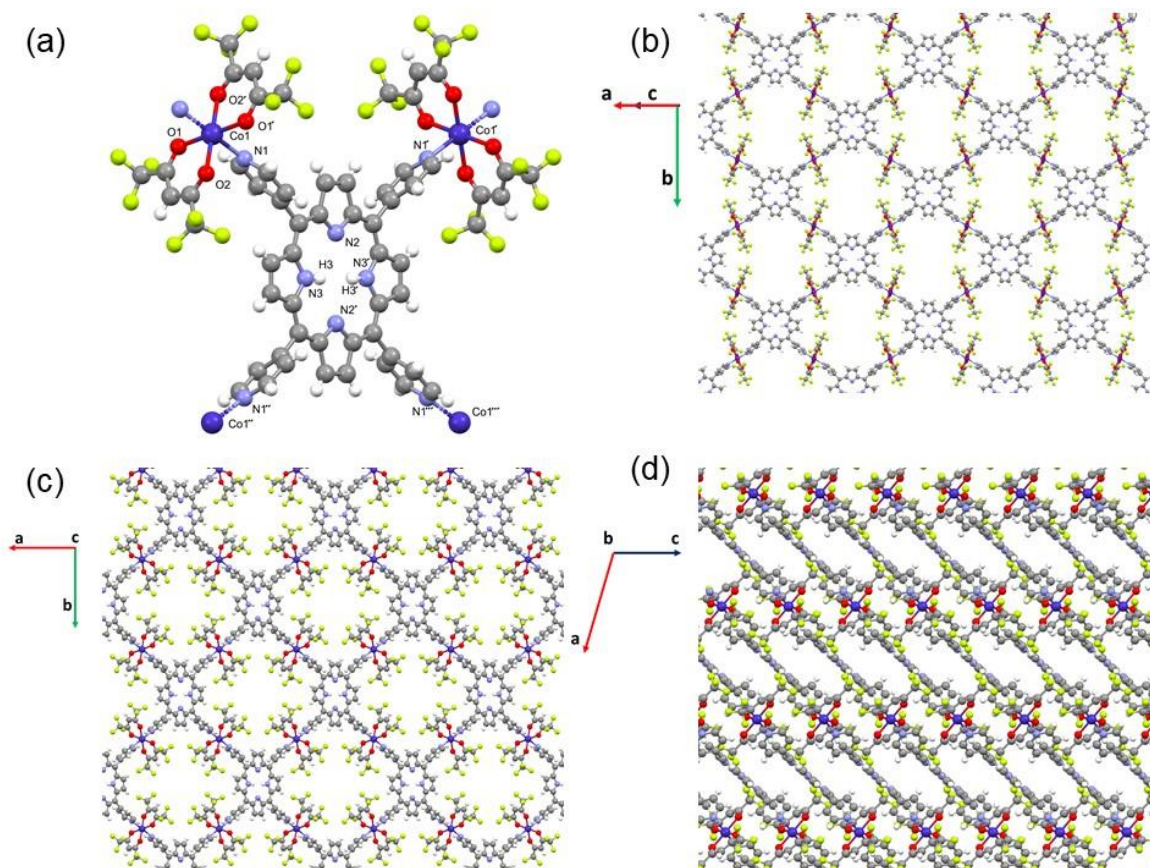
Figure 2. Plots of the crystal structure of compound [{Co(hfac)$_2$}H$_2$TPyP]$_n$: (a) numbering atoms, (b) and (c) showing different plane orientations, and (d) the stacking.

The stacking defines channels parallel to the *c*-axis. The channels have alternative protuberances in the *a* and *b* directions (Figure 3(a,b)). The estimated accessible volume is 22 v% per unit cell. Crystal are stable when subjected to humidity in air, although it is worth noting that it is very unusual for a crystal with such a high solvent accessible volume to be stable when exposed to open atmosphere. The pore size was measured along the *a*-axis, giving a value of 14 Å. Several weak interactions are established among layers, resulting in stable 3D crystals, *e.g.*, C–H···F contacts that involve the β- carbon pyrrole atom and CF$_3$ groups of neighbour layers (H13···F2 2.542 Å), interactions between the H of the pyridine rings and O from the hfac ligand, and weak F···F contacts (Figure 2(d)).
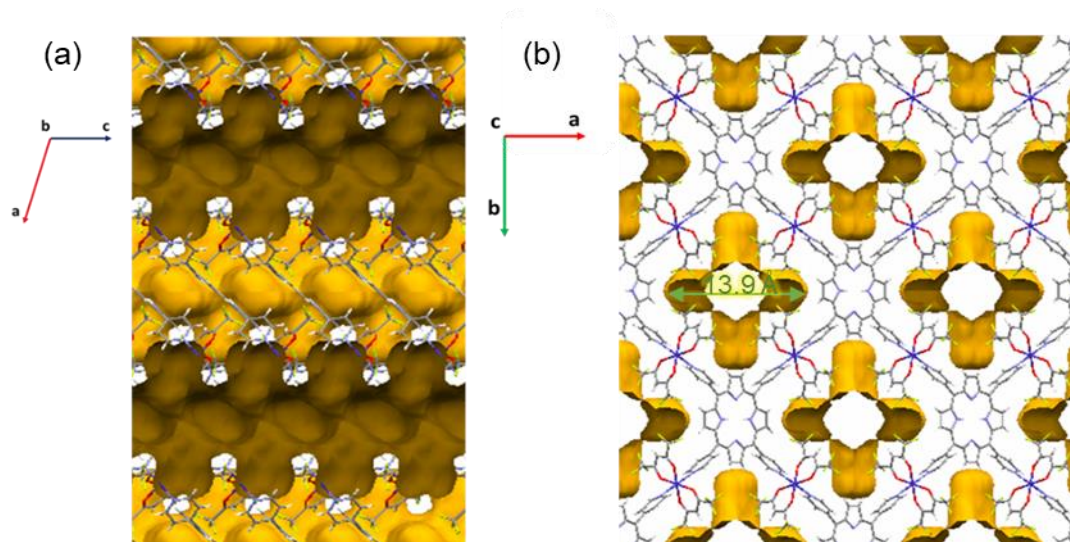
Figure 3. Plots of the crystal structure of compound $[\{Co(hfac)_2\}H_2TPyP]_n$ showing the channel voids: (a) *a*, and (b) *b* directions.

3.2.2. [M-TPyP]$_n$ MOFs prepared in scCO$_2$

scCO$_2$ was selected as the reaction media for synthesizing this type of materials as it plays many important roles within MOFs synthesis and activation. The solubility of the reagents in different solvents guides nucleation and crystal growth kinetics, while the protic/aprotic character of the solvent determines the crystallized phase. scCO$_2$ is an aprotic non-polar solvent, with a strong quadrupole moment, that has Lewis acid character. Moreover, it acts as an excellent solvent for neutral and fluorine containing metal groups, which makes it an ideal solvent for M(hfac)$_2$ metal clusters. Hence, the role of scCO$_2$ in the synthesis of the [M-TPyP]$_n$ MOFs is being a solvent for the metallic node added to the reaction media in the form of M(hfac)$_2$. The solubility of polar compounds in scCO$_2$ has historically been increased by adding small quantities of liquid co-solvents to the fluid. However, it was previously demonstrated for ZIF-8[38] and curcumin[29] 3D MOFs that these materials can also be precipitated in scCO$_2$ being only one of the reagents, *e.g.*, the metal complex, soluble in the fluid. The formation of the [M-TPyP]$_n$ MOFs is suggested to proceed in scCO$_2$ by the interaction of dissolved M(hfac)$_2$ molecules with weakly bonded H$_2$-porphyrin molecules located on the surface of the porphyrin, giving place to $[(M(hfac)_2)_x$-H$_y$TPyP]$ complexes and to MOF nuclei.

It is well known that metal coordination of the pyrrolic ring provides thermodynamic stability to the structure; however, in all of the cases presented here, there was no full coordination of the pyrrolic ring. As previously explained, the formation of [M-TPyP]$_n$ MOFs in scCO$_2$ is ruled by the reactivity between the nitrogen atoms of the pyridine and the pyrrol and the metal bonded to hfac. As scCO$_2$ is an aprotic solvent, the free nitrogen would not undergo protonation, and

therefore all the N: (the four pyridines and the inner tetrapyrrol ring) are available for bonding in this solvent. The fact that all possible N-M bonds were not completed, even adding an excess of metal, is assumed to be related to the steric hindrance of the $M(hfac)_2$ to enter the porphyrin ring, and the lack of enough energy under working conditions to break the M-hfac bond. To test which moiety reacts in preference with the metal, UV-Vis titration experiments in $CHCl_3$ were carried out taking the Zn(II) MOF as the case study (Figure 4).
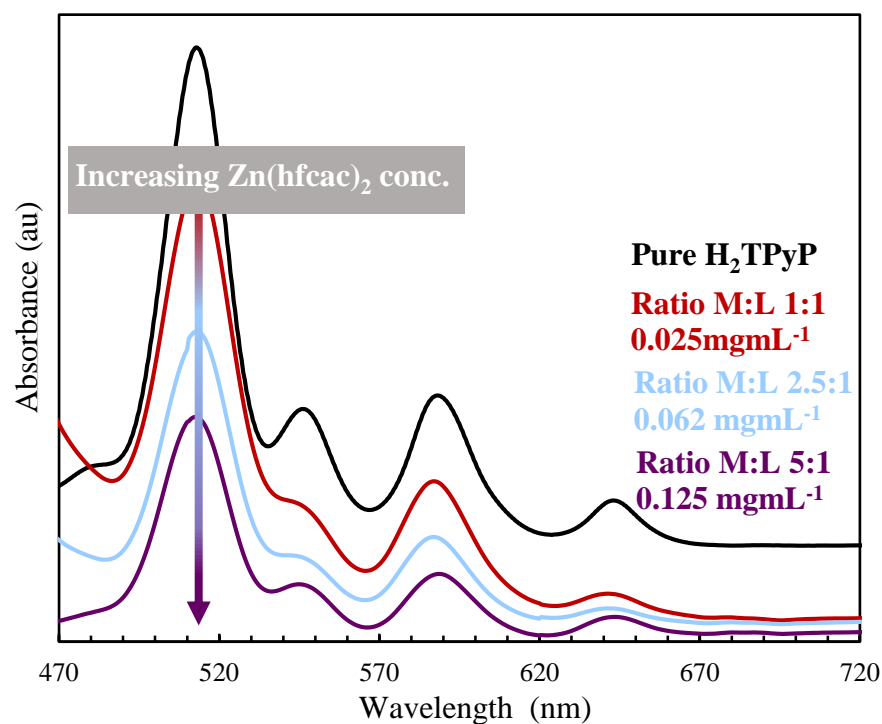
Figure 4. Titration experiments of H_2TPyP with $Zn(hfac)_2$. The porphyrin concentration was 0.025 mgmL^{-1}. The concentrations for the metal were 0.025 mgmL^{-1} (red), 0.0625 mgmL^{-1} (blue) and 0.125 mgmL^{-1} (purple).

For this, a solution of $Zn(hfac)_2$ at different concentrations was added dropwise to a solution of H_2TPyP. In all cases, even the most concentrated one, the four Q bands typical of the pyrrole ring remain present, thus indicating the lack of complexation that is exhibited by the declining to only two Q bands. The H_2TPyP porphyrin has two different ways of binding to metal: (i) the metalation of the central ring, which requires simultaneously both the deprotonation of the two pyrrole groups in the porphyrin, and the substitution of the two acetylacetonate ligands in the metal, and (ii) the coordination of the pyridine groups to the metal without the need of displacing the acetylacetonate ligands. Both reactions can enter into competition. However, it is foreseeable that the mechanism of reaction is multistage and, in any case, more complex than

the bonding of the pyridine groups necessary to form the two-dimensional network in the MOF. The obtained results in this work indicate that in $scCO_2$ the reaction produces a material with a partial degree of metalation. Hence, although both reactions compete and occur simultaneously, the bonding of the pyridine groups is favored, *e.g.*, is faster than the metalation. Probably, if a porphyrin is incorporated into the crystal lattice before being metallized in the central ring, it is highly unlike to be metallized afterwards, since the metal precursor $M(hfac)_2$ is too bulky to diffuse through the pores of the MOF. Another argument in favour of this hypothesis is derived from the nature of the $[\{Co(hfac)_2\}_2H_2TPyP]_n$ compound, obtained by slow diffusion of reagents in organic solvents, and in which the porphyrin rings are not metallized. This indicates that, under the close to equilibrium experimental conditions used for obtaining single crystals, the metallic precursor is favourably consumed to form the crystal lattice bonding to the pyridine groups than to metallize the central ring of the porphyrin. It was found that, even under rapid mixing conditions, and using an excess of metallic precursor, part of the porphyrin rings has no option of incorporating metal in the central ring, and the four characteristic Q bands of the protonated pyrrole ring are always observed (Figure 4).

3.2.3. Structural PXRD analysis

The PXRD patterns of the different samples are shown in Figure 5 in the 2θ range of 5 to 30°. For comparison, they are contrasted to the simulated PXRD pattern of $[Co(hfac)_2\}_2H_2TPyP]_n$, resolved in this work, and to the published structure of $[\{Cu(hfac)_2\}_2CuTPyP]_n$ (Nuwcak),[23] that contained six molecules of water within the structure. Both, simulated PXRD patterns show three characteristic peaks at 2θ 5.2, 6.8 and 8.0°. These peaks are also present in the $scCO_2$ prepared MOFs of Cu(II) and Zn(II), with a slight shift to lower angles attributed to the heterogeneity produced by the coordinated/uncoordinated pyrrole ring. Besides, most of the 2θ peaks between 10 and 18° found for the Co(II) resolved MOF and Cu(II) Nuwcak´s were also present in the different porphyrin samples. In short, for the $scCO_2$ synthesised Cu(II) and Zn(II) MOFs, PXRD analysis indicates similar diffraction peaks, as well as similar relative intensities, which is an indication of predominant isostructural features. By contrast, the $scCO_2$ prepared Co(II) and Ni(II) MOFs can be considered as semi-amorphous compounds when analysing their PXRD patterns. This is a clear example of a MOF, the porphyrin derived MOF of Co(II), that could be prepared as fully crystalline and semi-amorphous material. The possibility of obtaining pairs of semi-amorphous / fully-crystallized MOFs was first described for mesoporous carboxylates of Fe(III), involving the MIL-100(Fe) and Fe-BTC pair.[24] The semi-amorphous product maintains the crystallographic structure of the crystalline counterpart, as well as a

significant percentage of the porosity. It should be remarked that, for some applications, the semi-amorphous material surpasses the characteristics of the crystalline product.[39] In the scCO$_2$ synthesis, semi-amorphous MOFs were obtained when using the most (Co(II)) and less (Ni(II)) soluble metal reagents.
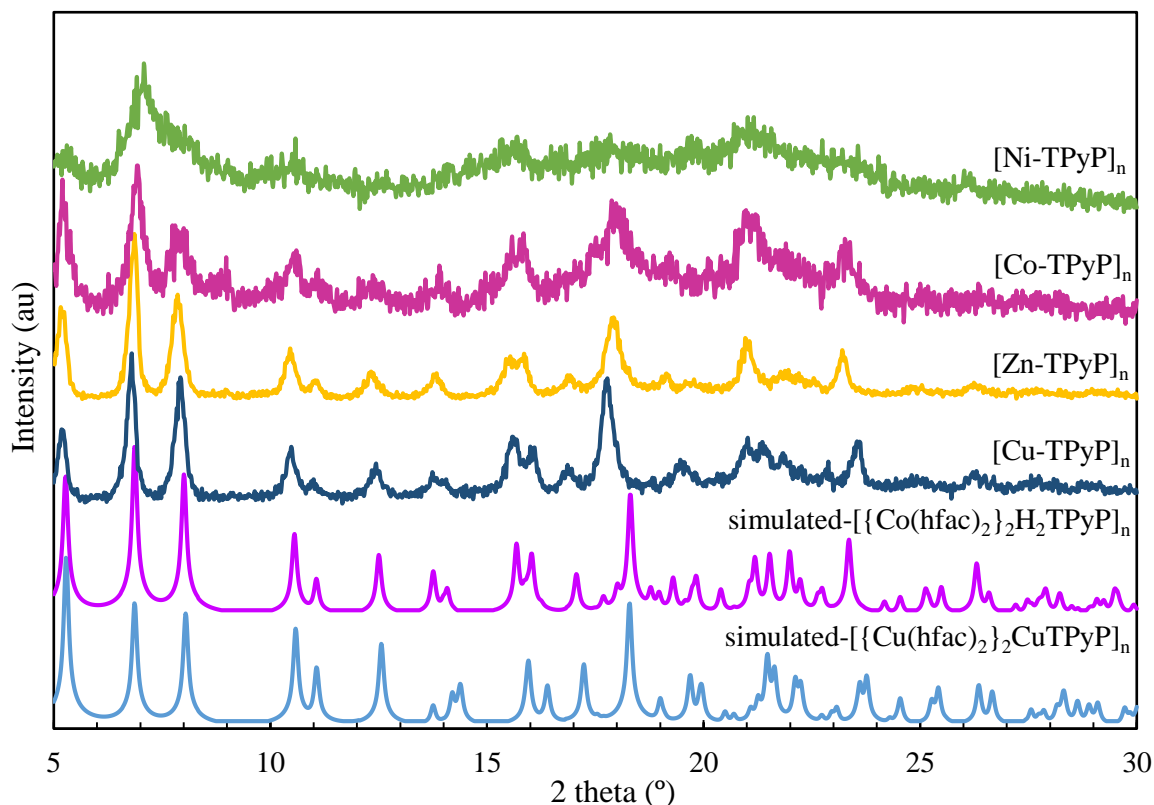

Figure 5. PXRD experimental patterns of [M-TPyP]$_n$ MOFs prepared in scCO$_2$ compared to the single-crystal simulated patterns of [{Cu(hfac)$_2$}$_2$CuTPyP$_x$6H$_2$O]$_n$ (Nuwcak)[23] and [{Co(hfac)$_2$}$_2$H$_2$TPyP]$_n$.

The published structure of Nuwcak Cu(II) MOF showed a fully metal coordinated (outer and inner ring) product, whereas the Co(II) MOF precipitated in this work does not contain any metal ion in the inner pyrrole ring. Nevertheless, both PXRD patterns, simulated from single-crystal data, were mostly similar in the number of peaks, position and relative intensities (Figure 5). This indicates that the presence or absence of the metal in the pyrrole ring hardly causes any changes in the lattice or the crystallographic structure.

3.3. Atomic and molecular composition

To further ascertain the presence or absence of the metal in the inner ring of the [M-TPyP]$_n$ MOFs synthetized in scCO$_2$, the composition was measured by performing elemental analysis

for C, H and N atoms and ICP for the metal. Analysed data indicates the precipitation of materials with intermediate atomic proportions in respect to the values expected for fully free-base or metallated porphyrin (Table 2).

Table 2. Experimentally measured C, H and N molar percentages obtained by elemental analysis, presented together with metal molar percentages by ICP for the samples precipitated in scCO$_2$.

Sample	Atom	Exp. data	Derived viable formula
[Cu-TPyP]$_n$	C	46.44	[(Cu(hfac)$_2$)$_2$Cu$_{0.32}$ (H$_2$)$_{0.67}$TPyP]$_n$
	H	1.96	1.0 % H$_2$TpyP
	N	6.99	
	Cu	9.22	
[Zn-TPyP]$_n$	C	46.74	[(Zn(hfac)$_2$)$_2$Zn$_{0.30}$(H$_2$)$_{0.70}$TPyP]$_n$
	H	1.94	
	N	7.40	
	Zn	9.31	
[Co-TPyP]$_n$	C	44.45	[(Co(hfac)$_2$)$_2$Co$_{0.70}$(H$_2$)$_{0.30}$TPyP]$_n$
	H	2.00	
	N	6.40	
	Co	9.24	
[Ni-TPyP]$_n$	C	44.64	[(Ni(hfac)$_2$)$_2$NiTPyP]$_n$
	H	1.67	3.5 % Ni(hfac)$_2$
	N	6.63	
	Ni	14.31	

Often, these results do not indicate the precipitation of a mixture of two crystallographic MOF phases, one with the pyrrole coordinated and one non-coordinated, but rather correspond to a single compound with the free-base form of porphyrin and the metalloporphyrin evenly mixed along the structure. Different results were obtained depending on the metal complex used for sample preparation. Considering that all the derived porphyrins underwent exocyclic coordination with M(hfac)$_2$ at the four pyridine moieties, the coordination of the metal inside of the ring could only be partial for Cu(II), Zn(II) and Co(II) MOFs, as it is schematized in Figure 6. For Cu(II) and Zn(II), *ca.* 30 % of the pyrrole rings was coordinated by a metal, while for the Co(II) the metalloporphyrin form reach the 70 % likely due to the high solubility of Co(hfac)$_2$ in scCO$_2$ that favours the metalation of the porphyrin. In another situation, for Ni(II), an excess of metal of *ca*. 3.5 wt% was measured in the derived porphyrin MOF, even considering full exocyclic and endocyclic coordination. Taking into account the low solubility

of Ni(hfac)$_2$ in scCO$_2$, the measured metal excess was attributed to the presence in the end product of unreacted reagent.
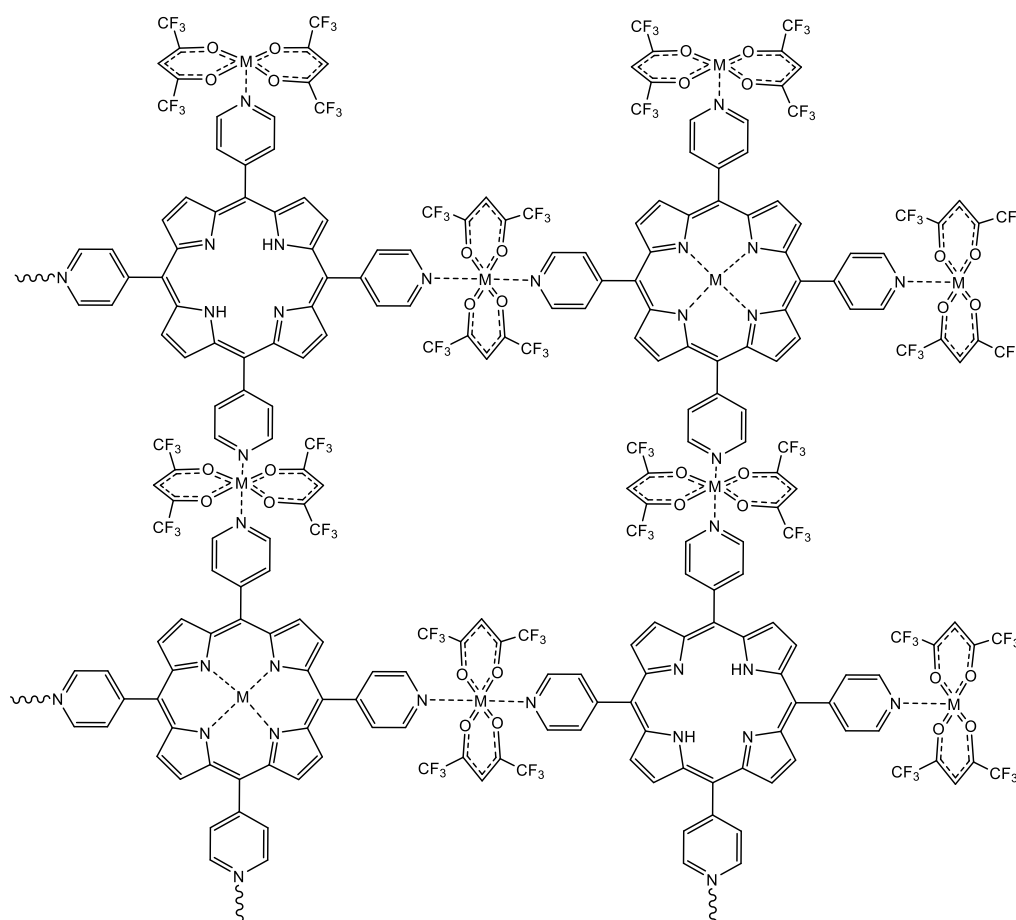
**Figure 6**. Scheme of the generic coordination of [M-TPyP]$_n$ MOFs.

The FTIR spectra of the synthetized [M-TPyP]$_n$ MOFs are shown in Figure 7. All the scCO$_2$ synthetized samples displayed similar bands. At high wavenumbers, the signal at 3300 cm^{-1} corresponds to the N-H stretching of the inner pyrrole ring. This band was highly reduced in intensity with respect to free H$_2$TPyP and shifted to higher wavelengths upon complexation with the metal. Besides, a new band emerges corresponding to the N-M bond at ~1000 cm^{-1} indicating that some metal is inserted into the porphyrin ring. The bands at 1636 and 1200 cm^{-1} were assigned to the C=O of the acetylacetonate in hfac and C=N, respectively. The bands at 1690-1540 $^{-1}$ and 1380 cm^{-1} were assigned to C=C and C-N stretching vibrations, respectively. The C=N band at 1400 cm^{-1} of the free pyridine was for the MOFs slightly shifted to higher wavelengths (*ca.* 15 cm^{-1}). The two bands at ~ 1644 and 1600 cm^{-1} are assigned to ν(CO$^-$) of the ligand, and confirm that the metal complex ligand (hfac group) was not released upon assembly of the metal to the pyridine group. The crystalline and semi-amorphous Co(II) MOFs

present slight differences in the FTIR spectra. Essentially, the signal at 1000 cm^{-1}, corresponding to the N(inner pyrrole ring)-Co bond in the semi-amorphous [Co-TPyP]$_n$, is absent in the sample obtained from layering with formula [{Co(hfac)$_2$}$_2$H$_2$TPyP]$_n$.
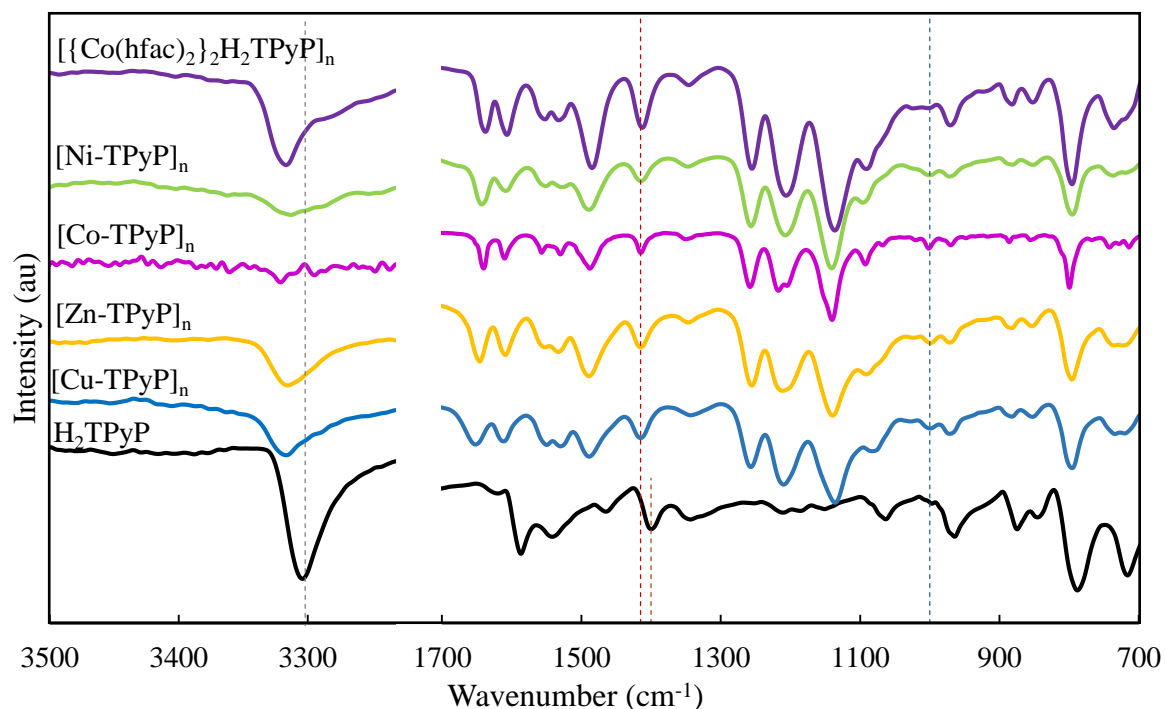

Figure 7. FTIR spectra of [M-TPyP]$_n$ MOFs compared to pure H$_2$TPyP.

3.4. Thermogravimetric analyses

The thermogravimetric decomposition curves of the different MOFs were compared to that of the free H$_2$TPyP (Figure 8). H$_2$TPyP decomposition started at an onset temperature of 450 ºC, ending at 700 ºC, with a two-stage weight loss. The first (19 wt%, 450-475 ºC) is attributed to the loss of the peripheral pyridine groups, and the second (25 wt%, 475-540 ºC) corresponds to the decomposition of the tetrapyrrol ring. The ratio of these to weight loss values is close to the theoretical values of pyridine (50 wt%) and tetrapyrrol (50 wt%) molecules in the porphyrin. The total weight loss was only of *ca.* 50 wt% up to 800 ºC. The residue has been attributed to the formation of thermal stable carbides. A comparison of the decomposition temperature of pristine H$_2$TPyP with H$_x$TPyP in the different MOFs reveals that the former has considerably more thermal stable than the corresponding metal counterparts. This behaviour has been already described for metallated Zn(II), Cu(II), Ni(II) and Co(II)) tetra(*p*-carboxylic acid phenyl)porphyrins.[6] All MOFs showed initial weight losses in the range of 125 to 190 ºC, attributed to the evaporation of the hfac. This was followed by several weight loss steps assigned to thermal decomposition, varying from metal to metal, which is attributed to the

heterogeneity of the network structures. The final residue, varying from 38 wt% in Ni(II) to 25 wt% in Cu(II) MOFs, was assigned to the formation of metal oxides. From the studied compounds, the gradation of thermal stability is Ni(II) > Co(II) > Zn(II) > Cu(II) MOFs. This behaviour has already been described for other porphyrin related materials, and related to the size of the ionic radius of the metal.[37]
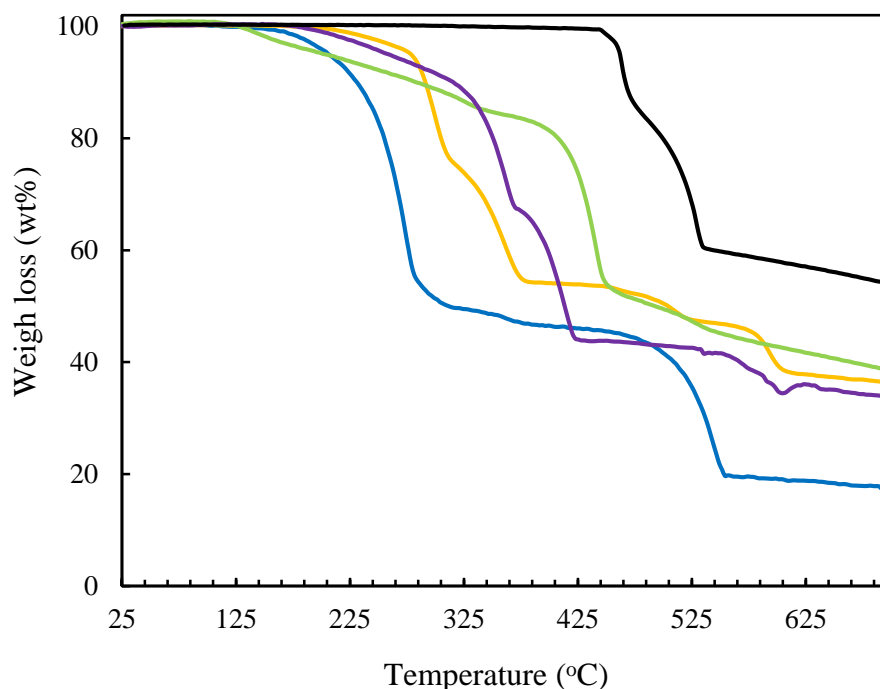

Figure 8. TGA curves of pure H_2TPyP and $[M-TPyP]_n$ MOFs.

3.5. Morphological and textural properties

The morphology of the precipitated MOFs was observed by SEM (Figure 9). For all the samples, the size of the precipitated particles was in the nano to low micrometer range. Cu(II) (Figure 9(a,b)) and Zn(II) (Figure 9(c,d)) MOFs precipitated as crystalline particles of heterogeneous diameters, from nano to micro sizes, where Cu(II) grow in an elongated way, and Zn(II) in a very well dispersed form. The hydrodynamic diameter was evaluated for the Zn(II) MOF by DLS, giving a mean value of *ca*. 140 nm (Figure 10). Crystals obtained from Co(II) (Figure 9(e,f)) precipitated with a large size, as a columnar crystals with defined edges.
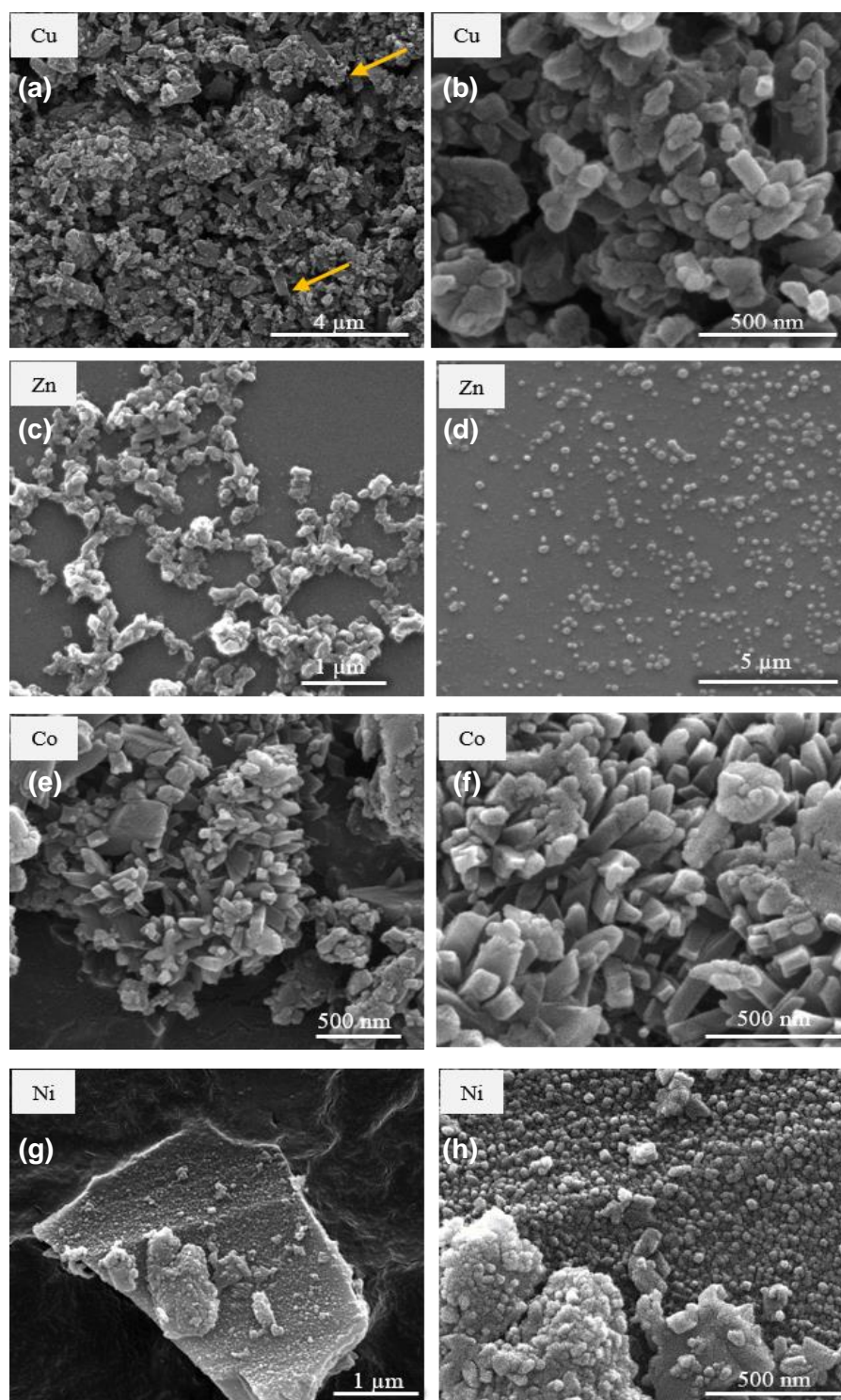
Figure 9. SEM images of [M-TPyP]$_n$ MOFs: (a,b) Cu(II), (c,d) Zn(II), (e,f) Co(II), and (g,h) Ni(II).
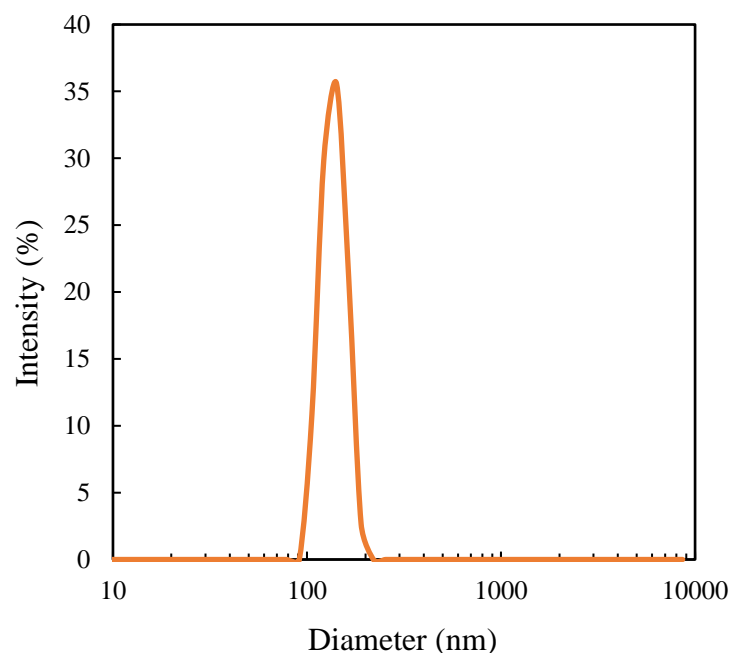
**Figure 10.** DLS measurement of [Zn-TPyP]$_n$ sample in water.

This is attributed to the enhanced solubility of Co(hfac)$_2$ in scCO$_2$ when used together with CHCl$_3$ co-solvent, which also favoured the solubility of the organic linker H$_2$TPyP and, thus, the crystal growth. A completely different scenario was observed when using Ni(hfac)$_2$ as the metal source. As it was assessed, Ni(hfac)$_2$ is the least soluble in scCO$_2$ of all the studied metal complexes, which appears to have an effect in the precipitation of the MOF. The Ni(II) based MOF contains numerous nanometric entities (Figure 9(g,h)). In this case, nucleation is clearly favoured over crystal growth. This fact is reflected in the precipitation of nanometric (< 20 nm) particles, resulting in a poorly defined PXRD (Figure 5). To improve the crystallinity of this MOF, the use of CHCl$_3$ as a co-solvent was attempted, but the final product was not suitable for characterisation, as a large amount of pyridine linker, unfeasible to be separated, remained unreacted. Only few SEM images are reported in the literature showing the morphology of similar compounds obtained in organic solvents. Well-formed structures, namely micro-lumps and micro-prims, have been described for the coordination of zinc-10,15,20-tetra(4-pyridyl)porphyrin with Cu(OAc)$_2$, but needing the use of cetyltrimethylammonium bromide for adjusting the coordination reaction and improving the crystal growth.[40]

Textural properties were obtained by measuring N$_2$ adsorption-desorption isotherms at low temperature (Table 3). Despite of the different compositional and morphological characteristics measured for the scCO$_2$ precipitated porphyrin derived MOFs, all of the compounds had a

similar N_2 adsorption behaviour, showing type I isotherms assigned to microporous products (Figure 11).

Table 3. Textural properties of the different porphyrin MOFs synthetized in $scCO_2$.

Sample	S_{BET} (m^2g^{-1})	$S_{Langmuir}$ (m^2g^{-1})	V_{mp} (cm^3g^{-1})
[Cu-TPyP]n	460	490	0.31
[Co-TPyP]n	480	520	0.36
[Zn-TPyP]n	480	520	0.34
[Ni-TPyP]n	480	535	0.32
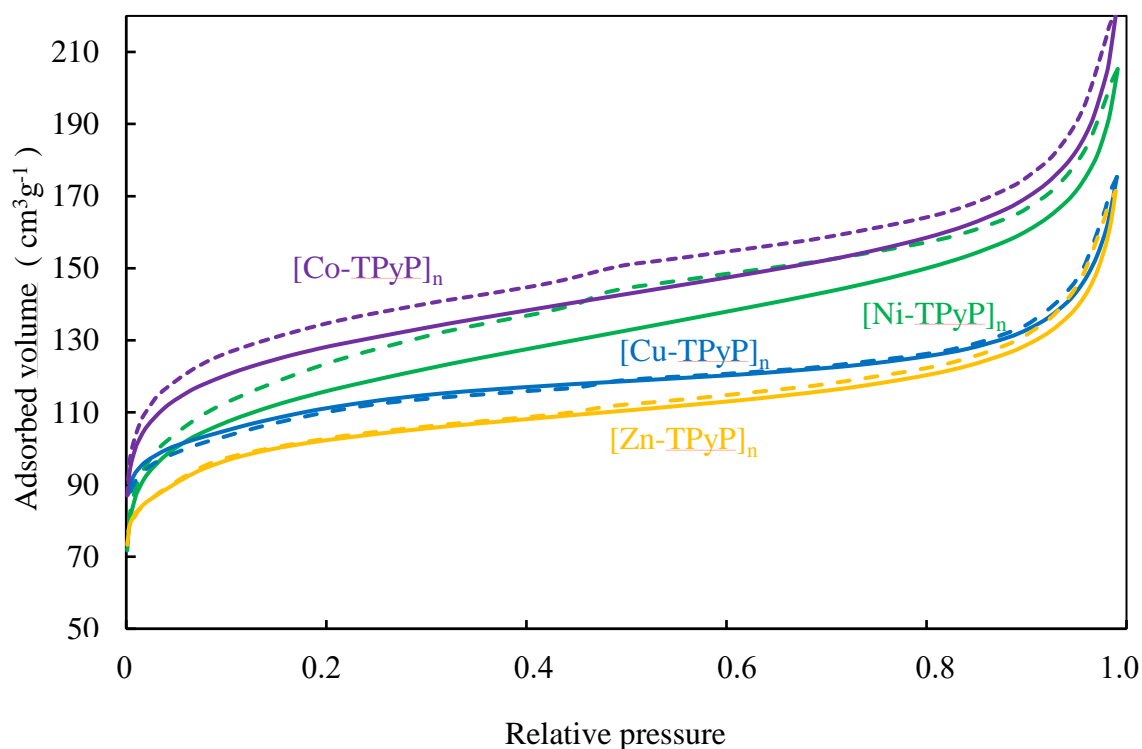
Figure 11. N_2 adsorption-desorption isotherms at -196 ºC for all samples.

For the samples prepared using $scCO_2$, theoretical surface areas could not be measured due to uncertainties in the structure definition and large number of defects in the semi-amorphous compounds. These samples were evaluated experimentally.

The BET surface area values were consistently derived at ~ 480 m^2g^{-1}, with a micropore volume of ~ 0.30-0.35 cm^3g^{-1}. This is a clear indication that, independently of the ratio of the metallized ring, the textural properties were not compromised by this fact. On the contrary, the textural

properties of the Co(II) MOF obtained from layering could not be measured due to the low amount of sample obtained using this technique. In this case, the theoretical surface area was calculated from the representation of the crystal structure taking into account void size. The pore shape was adjusted to a cylinder, using an equivalent diameter of 9.1 Å. This led to a theoretical estimated surface area of ~ 1700 m^2g^{-1}. Using this value, the calculated cell volume corresponds to 814 $Å^3$, equal to the crystallographic value. Comparing to published data for other H_2TPyP MOFs, the only value of surface area found reported was for the compound involving the paddlewheel Cu(II) tetraacetate [$Cu_2(AcO)_4$], which was in the order of 800 m^2g^{-1}.[22]

3.6. Photodynamic characterization

The [Zn-TPyP]$_n$ was tested in this work as a potential PDT compound, because Zn(II) has been reported to be highly biocompatible in metalloporphyrins.[38]

3.6.1. UV-Vis spectroscopy

UV-Vis spectroscopy is often used to understand porphyrins behaviour. However, due to the potential lability of the N-metal bond, preliminary stability studies must be carried out. For this, a sample of the Zn (II) porphyrin MOF was dispersed in water by ultra-sonication. The filtered and dried powder was analysed by PXRD (Figure 12).
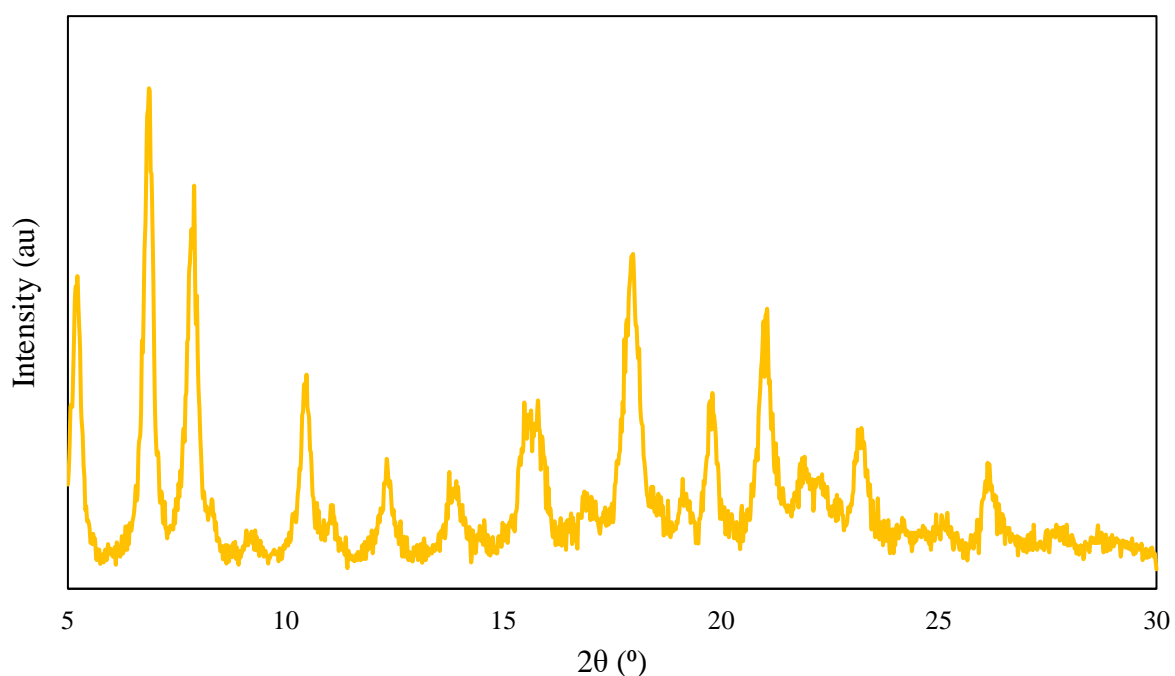

Figure 12. PXRD of the [Zn-TPyP]$_n$ sample after its dispersion in water achieved applying sonication.

Comparison with untreated samples indicates that the treated powder remained intact, demonstrating that this MOF was sufficiently stable to undergo water treatment, at least under the used experimental conditions. Red light with wavelength of 630 nm is generally used for PDT, since it corresponds to the region of the wavelength used in low-level laser therapy.[39] Hence, the first step to analyse the suitability of the material for PDT studies is to perform UV-Vis characterisation. The intensity and colour of porphyrins are derived from the highly conjugated π-electrons, giving characteristic UV-Vis spectra that consist of two distinct region in the near ultraviolet and in the visible region. Changes in the conjugation of a particular porphyrin would affect the UV-Vis absorption spectrum. In this study, the spectra of [Zn-TPyP]$_n$ and net H$_2$TPyP were compared (Figure 13). The organic linker (black line) presents the typical porphyrin broad intense Soret band at λ_{max}=437 nm. This band is present at a relative high value of absorbance, since the molecule is meso- substituted, thus corresponding to the transition from the ground state (S0) to the second excited state (S2). The second set of less intense bands are the typical four weak Q bands in the range of 500 – 700 nm with phyllo-type intensities, corresponding to the transition S0 $\rightarrow$ S1 of the free-base porphyrin.[41] Upon complexation with Zn(II) (yellow line), the Soret band shifted considerably to the blue with a λ_{max}=428 nm, which is attributed to the loss of symmetry in the porphyrin ring due to deprotonation of the central pyrrole nitrogen atoms and further metalation. In addition, the large complexation of the outer pyridyl groups with the metal can also provoke this large shift.[42] It has been described that upon fully complexation of the porphyrin with the metal in the central ring, the UV-Vis spectrum also changed with respect to the Q bands, since the four bands in H$_2$TPyP corresponding to the NH vibrational excitations, get reduced to two due to the increase on the symmetry in M-TPyP. The spectra of the Zn(II) porphyrin MOF synthetized in scCO$_2$ displayed an intermediate situation, in which the four Q bands remained in the spectrum but with modified intensities as it is observed in Figure 13. This result further indicates that, throughout the [Zn-TPyP]$_n$ MOF network, the pyrrole ring was only partially metallized. The fact that the porphyrin MOF preserves the Q bands, and specially the band at 640 nm, is of extreme importance for its study to use the material as potential PDT sensitizer.
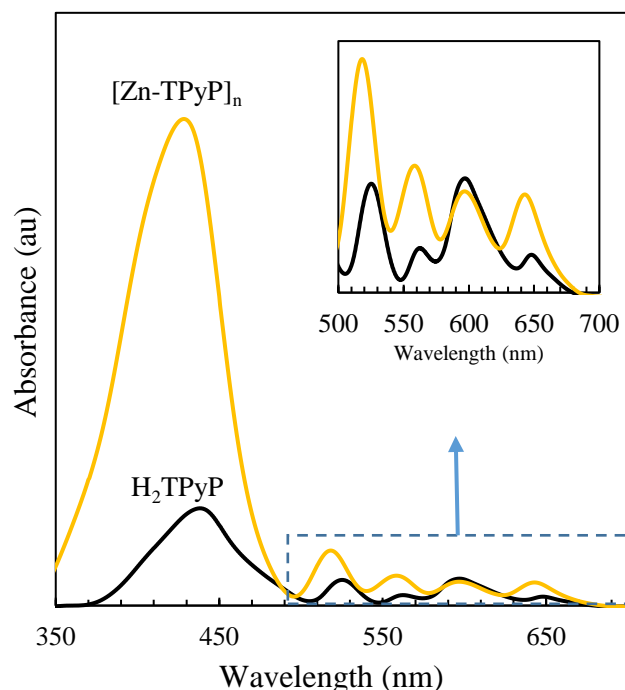
Figure 13. UV-Vis absorption spectra of H_2TPyP and $[Zn-TPyP]_n$.

3.6.2. Measurement of singlet oxygen ($^1O_2$) production

To demonstrate that the $[Zn-TPyP]_n$ MOF has the potential to be tested in PDT therapy, assessment of singlet oxygen production was carried out following two different approaches. First, the fluorescence decay caused by the photobleaching of anthracene-9,10-dipropionic acid in the presence of singlet oxygen was measured. Second, quantification was performed by determining singlet oxygen quantum yields, based on the phosphorescence of $^1O_2$ at 1270 nm. The fluorescence decay of the ADPA upon irradiation was monitored in time to detect the formation of singlet oxygen (Figure 14). The same light source, operating in the same conditions (630 nm, 55 mWcm^{-2} intensity) as in the PDT measurements, was used for irradiation. The wavelength of the irradiation closely corresponds to the typical Q-band of the porphyrin, nearest to the red region. An important decrease in the fluorescence intensity was detected already after 5 min, showing the photobleaching of the ADPA to the non-fluorescent endoperoxide[43] in the presence of the irradiated photosensitizer. After 15 min, no fluorescence signal was detected, the ADPA was irreversibly quenched. This result confirms the potential of [Zn-TPyP]n MOF to be used as photosensitizer in PDT treatment.
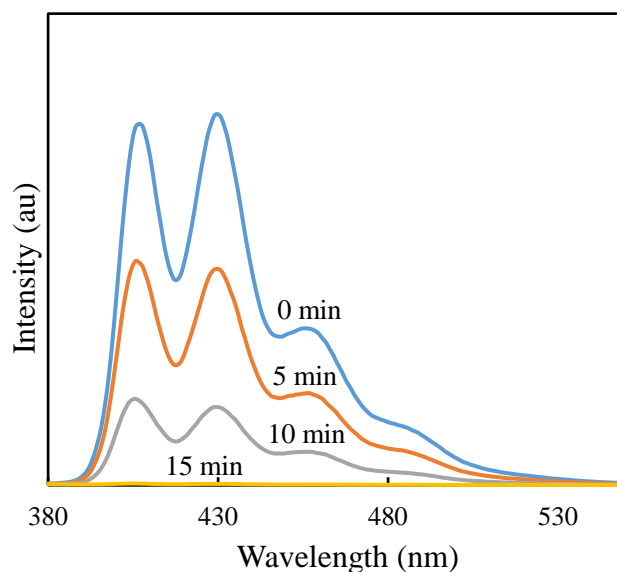
Figure 14. Fluorescence emission spectra of ADPA after irradiating for 15 min at 630 nm in the presence of [Zn-TPyP]$_n$ photosensitizer.

In a second set of experiments, the generation of singlet oxygen was performed by the direct measurement of its well-known phosphorescence at 1270 nm. Perinaphtenone was used as standard reference in order to quantify this process. As expected, similar values for the dispersion of pure porphyrin crystals ($\phi_\Delta = 2.7\%$) and the Zn(II) MOF ($\phi_\Delta = 2.3\%$) was detected, although in the first case the large H$_2$TPyP crystals do not disperse homogenously in the solvent, unlike the case of the MOF. These values found to be quite low, which is the result expected in aqueous dispersions where, in comparison with other solvents, the concentration of the dissolved O$_2$ is low.[44,45] Nevertheless, aqueous media were used in order to maintain similar conditions to the PDT experiment. Despite of the relatively low quantum yields, based on the important fluorescence decay, and the well-known photosensitizing ability of porphyrins, this experiment demonstrates that the [Zn-TPyP]$_n$ MOF is a compound with characteristics adequate to be used in PDT therapy.

3.7. Photodynamic treatments

Product toxicity in dark conditions

Once it was proved by UV-Vis that the [Zn-TPyP]$_n$ can be used in PDT therapy, the toxicity effects of the product on cell viability, in absence of light irradiation (dark toxicity), was evaluated using Alamar Blue assay at two different time-points, as the amount of fluorescence produced is proportional to the number of living cells. As it can be seen in Figure 15, none of the concentrations tested resulted cytotoxic after 24 h post-incubation, but after 72 h of incubation cell viability was significantly lower with 5 (78.6 %) and 10 μM (74.1 %)

256

concentrations. Toxicity was concentration dependent, the higher the concentration, the lower the viability.
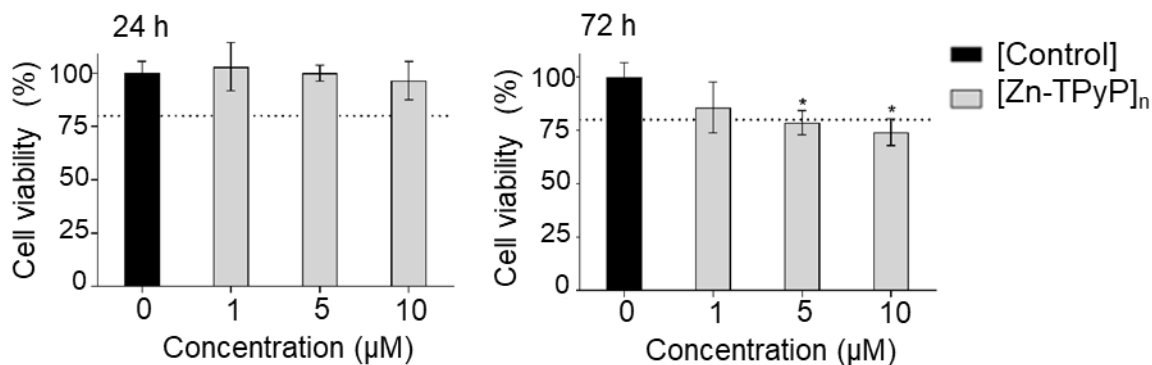

Figure 15. Dark toxicity: cell viability of SKBR-3 cells incubated for 24 h in dark conditions with different concentrations of product (1, 5, and 10 µM), and a control (0 mM) at 24 and 72 h. Asterisks indicate statistically significant differences in cell viability compared to the control at each time-point. Experiments were done in triplicates.

Cell viability after photodynamic treatments

Photodynamic treatments were performed with 1 and 5 µM concentration of products, because higher concentrations resulted toxic at 72 h post-incubation in dark conditions. Photodynamic treatments were executed in an irradiator dispositive that irradiates homogeneously all the cells. Irradiation was performed at room temperature, which can affect cell viability. For this reason, dark toxicity was also tested under these conditions. To confirm that phototoxicity was due to product internalization, the product was incubated for only 4 h followed by an exhaustive wash to eliminate all the non-internalized product (Figure 16), then cells were irradiated for 15 min. The results obtained in dark toxicity under these conditions were similar to that obtained in the first experiment, that is, product was not toxic at any time-point tested, except for 5 µM product at 72 h after product incubation (78.6 %). After 15 min irradiation, when incubating with 5 µM of product, cells showed a significant decrease in cell survival after both 24 and 72 h (69.9 and 35.7 % viability, respectively). On the other hand, incubation with 1 µM of product only led to a significant decrease in cell survival after 72 h (37.2 % viability). These results are in agreement to that obtained previously using the same SKBR-3 cell line and a porphyrin linked to Zn(II) metal complex (Na-ZnTCPP),[46] *e.g.*, using 1 µM of this product cell viability was reduced to more than a half. Other authors have also reported a reduction in cell viability using water-soluble porphyrins linked to Zn(II) metal complex.[47]
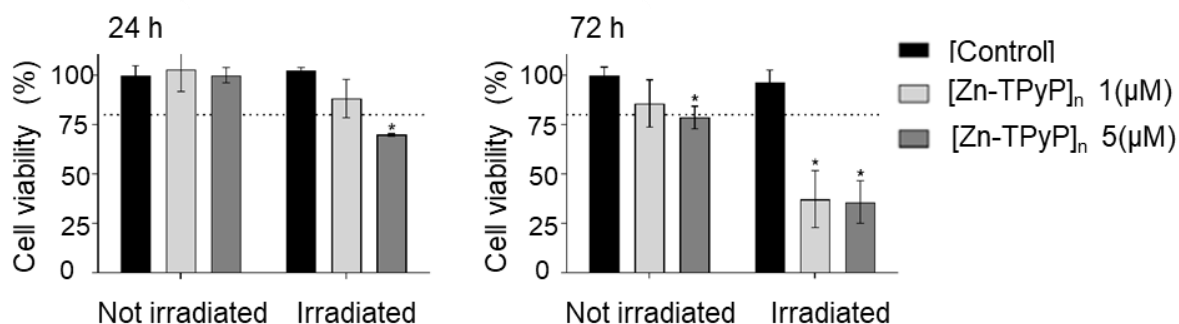
Figure 16. Photodynamic treatment effects after 15 min irradiation. Cell viability was determined by Alamar Blue for SKBR-3 cells incubated without (control) or with 1 or 5 µM of product for 4 h followed by cell wash. Cell viability was determined after incubation (24 h) either in dark conditions (not irradiated) or after 15 min irradiation at λ_{ex} 620-630 nm (irradiated) and at 72 h. Three independent experiments were performed for each set of conditions. Asterisks indicate statistically significant differences in the cell viability between control and product at each time-point and condition. Experiments were done in triplicates.

3.8. Internalisation of the photosensitisers

Internalisation of the product was analysed by confocal microscopy. SKBR-3 cells were incubated with 1 µM of product for 4 and 24 h, washed four times to eliminate all the non-internalised product and incubated with WGA-488 for 15 min to visualize the plasma membrane (limit of the cell). Consecutive optical slices throughout the cell volume were taken to obtain the 2D maximum projection (Figures 17(a,c)), whereas orthogonal sections allowed to locate the product within the limits of the cell (Figures 17(b,d)). After 4 h incubation, the product could be detected as a red background inside every single cell in the maximum projection (Figure 17(a)), but only aggregates were visible in the orthogonal projection (Figure 17(b), arrows). However, after 24 h incubation product internalisation was clearly observed in both images, maximum (Figure 17(c)) and orthogonal (Figure 17(d)) projections. Nevertheless, 4 h incubation was enough to kill more than 50 % of the cell population after 15 min irradiation. Considering that [Zn-TPyP]$_n$ has been shown to generate $^1O_2$, and that confocal studies have shown that [Zn-TPyP]$_n$ could be effectively internalized by cells, it is assumed that the reduced cell viability during light irradiation is due to the generation of ROS. [Zn-TPyP]$_n$ exhibits high phototoxicity and low dark toxicity at a concentration of 1 µM. This photosensitizer is highly efficient in inducing cell death, more than 62 % after 72 h of a tumorigenic human mammary epithelial cell line. Other authors have demonstrated the use of different photosensitizers for PDT as an anticancer therapy.[46-49]
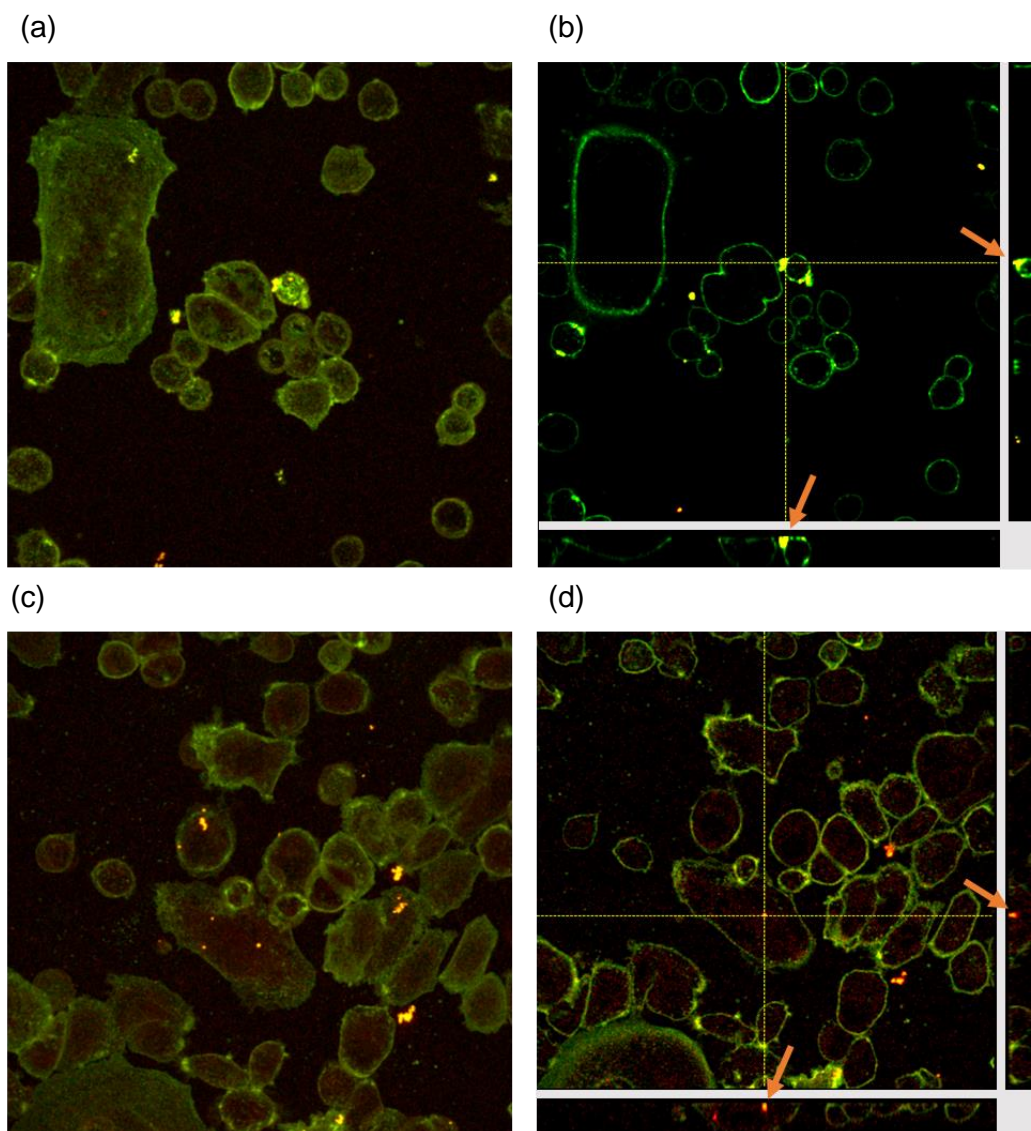
Figure 17. Live SKBR-3 cells incubated with 1 µM of product for 4 h (a,b) and 24 h (c,d) and observed under confocal microscope. To analyse the localisation of the product, fluorescence mode was used. Product fluorescence emission was detected in the range of λ 600-763 nm (orange) by exciting the cells using a λ 405 nm laser (15% of the laser power). Wheat Germ Agglutinin (WGA) fluorescence emission (membrane) was detected in the range of λ 500-550 nm (green) by exciting the cells using a λ 488 nm laser (12 1% of the laser power). Maximum projection (a and c) and orthogonal projection of z-stacks (b and d). Arrows point to some aggregates where the cross is positioned (b and d). Scale bar 20 µm.

4. Conclusions

scCO$_2$ proved to be a rapid, green and effective approach for preparing MOFs from highly insoluble organic ligands. In this way, a collection of [M-TPyP]$_n$ (M = Cu(II), Zn(II), Co(II), Ni(II)) MOFs was prepared using scCO$_2$ as reaction media using mild conditions. Elemental

analysis, PXRD patterns, FTIR and UV-Vis characterizations indicate that MOFs obtained from Cu(II), Zn(II), Ni(II) and Co(II) were obtained as porous networks, where the full coordination of all binding sites was not complete. In addition, $[\{Co(hfac)_2\}2H_2TPyP]_n$ was obtained from layering, whose structure was elucidated from SCXRD. This MOF was characterised for having a porous network from which the inner pyrrole ring remained uncoordinated. From all of the MOFs obtained, that of Zn(II) was used for PDT. The uncompleted coordination of the inner pyrrole ring gave place to the presence of a Q band at 640 nm, which was key for being targeted the MOF as a potential photosensitizer.

References

1. J. Liu, W. Zhou, J. Liu, I. Howard, G. Kilibarda, S. Schlabach, D. Coupry, M. Addicoat, S. Yoneda, Y. Tsutsui, T. Sakurai, S. Seki, Z. Wang, P. Lindemann, E. Redel, T. Heine, C. Woll, Photoinduced charge-carrier generation in epitaxial MOF thin films: High efficiency as a result of an indirect electronic band gap?, *Angew. Chem. Int. Ed*. **2015**, *54*, 7441-7445.

2. D. Micheroni, G. Lan, W. Lin, Efficient electrocatalytic proton reduction with carbon nanotube-supported metal–organic frameworks, *J. Am. Chem. Soc*. **2018**, *140*, 15591-15595.

3. G. Xu, K. Otsubo, T. Yamada, S. Sakaida, H. Kitagawa, Superprotonic conductivity in a highly oriented crystalline metal–organic framework nanofilm, *J. Am. Chem. Soc.* **2013**, *135*, 7438-7441.

4. R. Purrello, S. Gurrieri, R. Lauceri, Porphyrin assemblies as chemical sensors, *Coord. Chem. Rev*. **1999**, *190*, 683–706.

5. J. Puigmarti-Luis, W.J. Saletra, A. González, D.B. Amabilino, L. Perez-Garcia, Bottom-up assembly of a surface-anchored supramolecular rotor enabled using a mixed self-assembled monolayer and pre-complexed components, *Chem. Commun.* **2014**, *50*, 82–84.

6. K. Lang, J. Mosinger, D.M. Wagnerov, Photophysical properties of porphyrinoid sensitizers non-covalently bound to host molecules; models for photodynamic therapy, *Coord. Chem. Rev.* **2004**, *248*, 321–350.

7. J. Kou, D. Dou, L. Yang, Porphyrin photosensitizers in photodynamic therapy and its applications, *Oncotarget.* **2017**, *8*, 81591−81603.

8. M. Ethirajan, Y. Chen, P. Joshi, R.K. Pandey, The role of porphyrin chemistry in tumor imaging and photodynamic therapy*, Chem. Soc. Rev*. **2011,** *40,* 340–362.

9. S.M. Banerjee, A.J. MacRobert, C.A. Mosse, B. Periera, S.G. Bown, M.R.S. Keshtgar, Photodynamic therapy: inception to application in breast cancer, *Breast.* **2017,** *31*, 105−113.

10. J. Tian, B. Huang, M.H. Nawaz, W. Zhang, Review of porphyrin-based photodynamic therapy materials, *Coord. Chem. Rev*. **2020,** *420*, 213410-213432.

11. H. Abrahamse, M.R. Hamblin, New photosensitizers for photodynamic therapy, *Biochem J.* **2016,** *473*, 347–364.

12. S. Rodrigues-Alves, I. Rodrigo-Calori, A. Claudio-Tedesco, Photosensitizer-based metal-organic frameworks for highly effective photodynamic therapy, *Mater. Sci. Eng. C.* **2021**, *131*, 112514.

13. K. Lu, C. He, W. Lin, Nanoscale metal–organic framework for highly effective photodynamic therapy of resistant head and neck cancer, hypoxia-triggered nanoscale metal–organic frameworks for enhanced anticancer activity, *J. Am. Chem. Soc*. **2014,** *136*, 16712-16715.

14. J. Park, Q. Jiang, D. Feng, L. Mao, H.C. Zhou, Size-controlled synthesis of porphyrinic metal–organic framework and functionalization for targeted photodynamic therapy, *J. Am. Chem. Soc.* **2016**, *138*, 3518-3525.

15. D. Feng, H.L. Jiang, Y.P. Chen, Z.Y. Gu, Z. Wei, H.C. Zhou, Metal-organic frameworks based on previously unknown Zr8/Hf8 cubic clusters, *Inorg. Chem.* **2013,** *52,* 12661-12667.

16. Y. Keum, S. Park, Y.P. Chen, J. Park, Titanium-carboxylate metal-organic framework based on an unprecedented ti-oxo chain cluster, *Angew. Chem., Int. Ed. Engl.* **2018**, *57,* 14852-14856.

17. J. Li, Y. Ren, C. Qi, H. Jiang, The first porphyrin-salen based chiral metal-organic framework for asymmetric cyanosilylation of aldehydes, *Chem. Commun.* **2017,** *53*, 8223-8226.

18. E. Amayuelas, A. Fidalgo-Marijuan, B. Bazán, M.-K. Urtiaga, G. Barandika, L. Lezama, M.I. Arriortua, Cationic Mn^{2+}/H^+ exchange leading a slow solid-state transformation of a 2D porphyrinic network at ambient conditions, *J. Solid State Chem.* **2017,** *247,* 161-167.

19. P. Cai, Y. Huang, M. Smith, H. Zhou, Structural design of porphyrin-based mofs. Ch. 1 in: *P*orphyrin-based Supramolecular Architectures: From Hierarchy to Functions, **2021,** 1-58.

20. L.D. DeVries, W. Choe, Classification of structural motifs in porphyrinic coordination polymers assembled from porphyrin building units, 5,10,15,20-tetrapyridylporphyrin and its derivatives. *J. Chem Crystallogr.* **2009**, *39*, 229–24.

21. L. Carlucci, G. Ciani, D.M. Proserpio, F. Porta, Four new 2D porous polymeric frames from the self-assembly of silver triflate and silver tosylate with free-base and Zn-metallated 5,10,15,20-tetra(4-pyridyl)porphyrin. *CrystEngComm.* **2005**, *7*, 78-86.

22. T. Ohmura, A. Usuki, K. Fukumori, T. Ohta, M. Ito, K. Tatsumi, New porphyrin-based metal−organic framework with high porosity: 2-d infinite 22.2-å square-grid coordination network, *Inorg. Chem.* **2006,** 45, 7988 - 7990.

23. R.W. Seidel, I. Oppel, Assembly of a rhomboidally distorted (4,4)-net based polymeric sheet structure bearing copper(II) 5,10,15,20-tetra(4-pyridyl)porphyrin *CrystEngComm.* **2010,** *12*, 1051-1053.

24. M. Kubovics, S. Rojas, A.M. López-Periago, J. Fraile, P. Horcajada, C. Domingo, Fully supercritical CO_2 preparation of a nanostructured MOF composite with application in cutaneous drug delivery, *J. Supercrit. Fluids.* **2021**, *178*, 105379-105420.

25. A.M. López-Periago, O. Vallcorba, F. Frontera, C. Domingo, J.A. Ayllon, Exploring a novel preparation method of 1D metal organic frameworks based on supercritical CO_2, *Dalton Trans.* **2015,** *44,* 7548 – 7553.

26. N. Portoles-Gil, R. Parra-Aliana, A. Álvarez-Larena, J.A. Ayllón, A.M. López-Periago, Bottom-up approach for the preparation of hybrid nanosheets based on coordination polymers made of metal-diethyloxaloacetate complexes linked by 4,4′-bipyridine. *CrystEngComm,* **2017,** *19*, 4972–4982.

27. N. Portolés-Gil, O. Vallcorba, C. Domingo, A.M. López-Periago, J.A. Ayllón, $[Zn_2Ac_2(\mu$-$Ac)_2(bpymb)]n$ (Ac, acetate; bpymb, 1,4-bis(4-pyridylmethyl)benzene), a 2D coordination polymer obtained with a flexible N,N'-ditopic bipyridine linker, *Inorganica Chim. Acta.* **2021**, *516*, 120132-120139.

28. A.M. López-Periago, P. López-Domínguez, J. Pérez Barrio, G. Tobias, C. Domingo, Binary supercritical CO_2 solvent mixtures for the synthesis of 3D metal-organic frameworks. *Microp. Mesopor. Mat*. **2016**, *234*, 155–161.

29. N. Portolés-Gil, A. Lanza, N. Aliaga-Alcalde, J.A. Ayllón, M. Gemmi, E. Mugnailoi, A.M. López-Periago, C. Domingo, Crystalline curcumin biomof obtained by precipitation in supercritical CO_2 and structural determination by electron diffraction tomography, *ACS Sustain. Chem. Eng.* **2018**, *6*, 12309–12319.

30. N. Portolés-Gil, S. Gómez-Coca, O. Vallcorba, G. Marbán, N. Aliaga-Alcalde, A.M. López-Periago, J.A. Ayllón, C. Domingo, Single molecule magnets of cobalt and zinc homo- and heterometallic coordination polymers prepared by a one-step synthetic procedure. *RSC Adv*. **2020,** *10*, 45090–45104.

31. A. Rosado, A. Borrás, J. Fraile, J.A.R. Navarro, F. Suarez-Garcia, K.C. Stylianou, A.M. López-Periago, J. Giner-Planas, C. Domingo, A. Yazdi, HKUST-1 metal-organic framework nanoparticle/graphene oxide nanocomposite aerogels for CO_2 and CH_4 adsorption and separation. *ACS Appl. Nano Mater.* **2021**, *4,* 12712–12725.

32. P. Subra-Paternault, C. Domingo, Eds. Supercritical Fluid Nanotechnology: Advances and Applications in Composites and Hybrid Nanomaterials; Pan Stanford Publishing: Singapore, **2015.**

33. W. Kabsch, *Xds. Acta Crystallogr D Biol Crystallogr.* **2010,** *66,* 125–132.

34. G.M. Sheldrick, Crystal structure refinement with SHELXL, *Acta Crystallogr., Sect. C: Struct. Chem.* **2015**, *71*, 3–8.

35. O.V. Dolomanov, L.J. Bourhis, R.J. Gildea, J.K. Howard, H. Puschmann, H. OLEX2: a complete structure solution, refinement and analysis program, *J. Appl. Crystallogr.* **2009**, *42*, 339–341.

36. O. Penon, T. Patiño, L. Barrios, C. Nogués, D.A. Amabilino, K. Wurst, L. Pérez-García, A new porphyrin for the preparation of functionalized water-soluble gold nanoparticles with low intrinsic toxicity. *ChemistryOpen.* **2015**, *4*, 127-36.

37. R.B. Gupta, J.J. Shim, Solubility in Supercritical Carbon Dioxide, CRC Press, Taylor & Francis Group, Boca Raton, Florida.

38. P. López-Domínguez, A.M. López-Periago, F.J. Fernández-Porras, J. Fraile, G. Tobias, C. Domingo, Supercritical CO_2 for the synthesis of nanometric ZIF-8 and loading with hyperbranched aminopolymers, Applications in CO_2 capture, *J. CO₂ Util*. **2017**, *18,* 147–155.

39. B. Zhang, J. Zhang, C. Liu, X. Sang, L. Peng, X. Ma, T. Wu, B. Han, G. Yang, Solvent determines the formation and properties of metal–organic frameworks, *RSC Adv.*, **2015**, *5*, 37691-37696.

40. Z. Zhang, X. Li, Q. Zhao, J. Ke, Y. Shia, P. Ndokoye, L. Wang, Facile synthesis and characterizations of copper–zinc-10,15,20-tetra(4-pyridyl) porphyrin (Cu–ZnTPyP) coordination polymer with hexagonal micro-lump and micro-prism morphologies, *J. Colloid Interface Sci.* **2014**, *432*, 229-235.

41. L.R. Milgrom, The colours of life. An introduction to the chemistry of porphyrins and related compounds. Oxford University press **1997.**

42. X. Liu, E.K.L. Yeow, S. Velate, R.P. Steer, Photophysics and spectroscopy of the higher electronic states of zinc metalloporphyrins: A theoretical and experimental study. *Phys. Chem. Chem. Phys.* **2006,** *8*, 1298-1309.

43. K. Hubenko, S. Yefimova, T. Tkacheva, P. Maksimchuk, I. Borovoy, V. Klochkov, N. Kavok, O. Opolonin, Y. Malyukin, Reactive oxygen species generation in aqueous solutions containing $GdVO_4$:Eu^{3+} nanoparticles and their complexes with methylene blue, *Nanoscale Res. Lett.* **2018**, 13:100.

44.   M. Montalti, A. Credi, L. Prodi, M.T. Gandolfi, Handbook of Photochemistry, 3rd Ed, Taylor and Francis **2006**.

45.   A. Pinto, J.S. Ward, K. Rissanen, M. Smith, L. Rodríguez, Aggregation of gold(I) complexes: phosphorescence *vs.* singlet oxygen production, *Dalton Trans.* **2022**, 51, 8795–8803.

46.   J. Soriano, I. Mora-Espí, M.E. Alea-Reyes, L. Pérez-Gàrcia, L. Barrios, E. Ibáñez, C. Nogués, Cell Death Mechanisms in Tumoral and Non-Tumoral Human Cell Lines Triggered by Photodynamic Treatments: Apoptosis, Necrosis and Parthanatos, *Sci. Rep*. **2017,** *7*, 41340.

47.   B. Hou, W. Zhang, C. Li, X. Sun, X. Feng, J. Liu, Synthesis and in vitro biological evaluation of novel water-soluble porphyrin complexes for cancer photodynamic therapy, *Appl. Organomet. Chem.,* **2022**, *36*, 2367-2395.

48.   P. Agostinis, K. Berg, K.A. Cengel, T.H. Foster, A.W. Girotti, S.O. Gollnick, S.M. Hahn, M.R. Hamblin, A. Juzeniene, D. Kessel, M. Korbelik, J. Moan, P. Mroz, D. Nowis, J. Piette, B.C. Wilson, J. Golab, Photodynamic therapy of cancer: an update, *CA Cancer J. Clin*. **2011**, *61*, 250-281.

49.   Z. Shen, Q. Ma, X. Zhou, G. Zhang, G. Hao, Y. Sun, J. Cao, Strategies to improve photodynamic therapy efficacy by relieving the tumor hypoxia environment, *NPG Asia Mater*. **2021**, *13*, 13-39.

Conclusions

Conclusions

The focus of this thesis was built around two classes of mesoporous compounds, GO aerogels and MOFs. Both types already possess interesting properties in their pristine form, regarding surface characteristics, but by functionalizing or composing them with other materials, new properties arise, providing even greater potential for the new products. Hence, the general objective settled in this thesis was to build functional porous composites based on these materials, and to demonstrate their properties and suitability in different emerging applications. Based on that, the conclusions of this thesis are the followings:

- Various possibilities for building functional composites using $scCO_2$ technology were defined. Often, the applied preparation methodology leads to characteristics that cannot be achieved by using different traditional chemistry approaches. Indeed, many times these materials showed enhanced performance in the tested applications. Optimization of each system regarding both the preparation and the application conditions is necessary to maximize their performance. Following the same synthetic principles, infinite possibilities to build new porous functional composites can be revealed for broad scope of applications. From them, the most important supercritical CO_2 developments obtained in this thesis are listed following:

- $ScCO_2$ can be used as gelation and drying solvent to produce GO meso/macroporous aerogels composed with metal-based NPs, maintaining all the oxygenated functional groups present in the precursor material.

- $ScCO_2$ is a suitably solvent for the in situ synthesis of complex mesoporous MOFs, *e.g.*, Fe(BTC) and porphyrins involving Cu, Zn, Ni or Co. Actually, $scCO_2$ is demonstrated to be an efficient reaction solvent to prepare a series of MOFs from highly insoluble ligands, needing only the aid of a small amount of cosolvent.

- Composite materials of the type inorganic NPs@GO aerogels or NPs@MOF NPs can be efficiently synthesized using $scCO_2$ as the synthesis, gelation and drying solvent, simultaneously. The process is based on the impregnation of the inorganic NPs, either pristine or as organometallic precursors, into the pores of the mesoporous (aerogel or MOF) support.

    - $ScCO_2$ was an efficient tool to encapsulate substances into mesoporous substrates attaining high loadings. The process is demonstrated through the

impregnation of azelaic acid, a therapeutically active drug, and organometallic molecules, such as $Cu(acac)_2$ precursor of copper metal nanoparticles.

- The advantages of the non-toxic character of $scCO_2$ are used to prepare pharmaceutically active systems. In this respect, the azelaic acid@Fe(BTC) system was formulated as a macroporous composite patch by dispersing the loaded MOF in a biocompatible polymer (PVA) and using $scCO_2$ as plasticizing and foaming fluid to establish the solid foam network. This composite device was capable of progressively release and diffuse the incorporated drug throughout the skin. Additionally, the Zn-porphyrin MOF was successfully tested as photosensitizer in anticancer photodynamic therapy.

- Applying post-synthetic reduction steps to the synthesized NPs@GO or NPs@MOF systems, catalytically active composites are obtained. These systems were applied either in gas phase CO_2 hydrogenation (CuZnO@reduced GO aerogels and CuCs@Fe(BTC) nanoparticles) or in photocatalytic H_2 production form aqueous methanol solution (PtTiO$_2$@reduced GO). The mesoporous support influences the catalytic activity of the composite in multiple ways. First, it ensures the homogenous distribution of the metal-based NPs in the end product by hindering sintering and/or uncontrolled nanoparticles growth, which often results in catalytic activity loss. Second, the support can modify the characteristics attained by the catalytic NPs during reduction in different ways:

  - in the CuZnO@rGO composite, the presence of oxygenated GO in the precursor avoids the typical Cu-Zn alloy formation, thus increasing the catalytic efficiency;
  - the light harvesting properties and reagent permeation was found to be important factors influencing the H_2 production efficiency of the PtTiO$_2$@rGO composite aerogels, and
  - regarding the CuCs@Fe(BTC) composite, the MOF matrix was suitable not only to homogenously disperse the impregnated substance within the framework, but also to regulate the size of the metal species formed upon the reduction of the precursor $Cu(acac)_2$.

The dispersion and size of the active centers are crucial regarding catalytic performance, accordingly, the novel structures showed promising performance in catalytic processes. These straightforward approaches pave the way to build further metal-based NPs@GO/MOF catalysts using different active centers and synthesis conditions, adapted to the target material and application.

Personal information

Márta Kubovics

📅 23 December 1994

🛂 Hungarian

📍 Barcelona, Spain

📞 +36 70 613 6781

✉️ kubomarti@gmail.com

Education

2019-2023 Institute of Materials Science of Barcelona (ICMAB-CSIC), **PhD in Chemistry**, funded by the European Union's Horizon 2020 research and innovation program under the Marie Sklodowska-Curie grant agreement *No 754397*

2017-2019 Budapest University of Technology and Economics, Faculty of Chemical Technology and Biotechnology, **Chemical Engineer MSc,** Chemical and Process Engineering specialization

2013-2017 Budapest University of Technology and Economics, Faculty of Chemical Technology and Biotechnology, **Chemical Engineer BSc,** Chemical and Process Engineering specialization

Research/Work experience

09-11.2022 **Research Stay** in the Laboratory of Catalysis and Materials, Department of Chemical Engineering (FEUP), University of Porto, Portugal

2019 **Process Engineer** at OT Industries Engineering Co. Ltd, Budapest, Hungary

2015-2018 **Student Research work** at Budapest University of Technology and Economics, Faculty of Chemical Technology and Biotechnology, Department of Chemical and Environmental Process Engineering, Supercritical Fluid Extraction Researcher Group, Budapest, Hungary

06.2018 **Quality Assurance Intern** at Solvo Biotechnology, Szeged, Hungary

09-11.2017 **Research Internship** in the Green Technology Group of Centre for Analysis and Synthesis, Department of Chemistry at Lund University, Lund, Sweden

07-08.2016 **Chemical Engineering Internship** at Hungarian Oil and Gas Public Limited Company (MOL Group) in the department of Naphta reforming unit and hydrogen production plant, Százhalombatta, Hungary

06.2015 **Student Work** at Hungarian Oil and Gas Public Limited Company (MOL Group) in the Quality Control Laboratory, Százhalombatta, Hungary

Languages

English C1 complex language certification (2012)

German B2 complex language certification (2018)

Spanish intermediate level

Publications

<u>Márta Kubovics</u>, Oriol Careta, Oriol Vallcorba, Guillermo Romo-Islas, Laura Rodríguez, Concepción Domingo, Jose A. Ayllón, Carme Nogués, Ana M. López-Periago, Supercritical CO_2 synthesis of porous metalloporphyrine frameworks: application in photodynamic therapy, *Chemistry of Materials* **2023**

<u>Márta Kubovics</u>, Albert Trigo, Antoni Sánchez, Gregorio Marbán, Alejandro Borrás, Javier Moral-Vico, Ana M. López-Periago, Concepción Domingo, Role of Graphene Oxide Aerogel Support on the CuZnO Catalytic Activity: Enhancing Methanol Selectivity in the Hydrogenation Reaction of CO_2, *ChemCatChem* **2022**, *14*, e202200607.

<u>Márta Kubovics</u>, Cláudia G. Silva, Ana M. López-Periago, Joaquim L. Faria, Concepción Domingo, Photocatalytic hydrogen production using porous 3D graphene-based aerogels supporting Pt/TiO_2 nanoparticles, *Gels* **2022**, *8*, 719.

<u>Márta Kubovics</u>, Sara Rojas, Ana M. López-Periago, Julio Fraile, Patricia Horcajada, Concepción Domingo, Fully supercritical CO_2 preparation of a nanostructured MOF composite with application in cutaneous drug delivery, *The Journal of Supercritical Fluids* **2021**, *178*, 105379.

<u>Márta Kubovics</u>, Said Al-Hamimi, György Huszár, Kinga Komka, Charlotta Turner, Edit Székely, Preparation and analysis of polar hawthorn berry extracts, industrial application in poultry processing, *Periodica Polytechnica Chemical Engineering* **2019**, *63*, 348-356.

Conferences

05.2022   Role of reduced graphene oxide aerogel support on the CuZnO catalytic activity and enhanced methanol selectivity for the hydrogenation reaction of CO_2, **Doctoral Workshop, PhD of Chemistry,** *oral and poster presentation*, Barcelona, Spain

05.2022   Supercritical CO_2 as an efficient tool in the fabrication of Cu^0ZnO-rGO 3D aerogels for highly selective catalytic CO_2 hydrogenation, **13th International Symposium on Supercritical Fluids**, *oral presentation,* Montreal, Canada

05.2022   Light foams for emerging uses, short talk, **13th International Symposium on Supercritical Fluids**, *oral presentation,* Montreal, Canada

07.2021   Fully green preparation of nanostructured MOF composite with application in cutaneous drug delivery, **Emerging 2021 School: Functional Advanced Materials for Emerging applications**, *oral presentation,* Barcelona, Spain

05. 2021	Cu-based nanoparticle – graphene-oxide aerogels as potential solid state catalysts, **18th European Meeting on Supercritical Fluids**, *online oral presentation*
02.2021	Preparation of a metal-organic framework using supercritical carbon-dioxide for drug delivery application, **1st Greenering International Conference**, *online oral presentation*, Costa da Caparica, Portugal
09.2020	Preparation and characterization of graphene-oxide-copper composite aerogels as potential solid state platforms for CO_2 hydrogenation, **5th Scientific Meeting of PhD Students at UAB Campus (JPhD2020)**, *online flash poster presentation*, Barcelona, Spain
11.2018	Modelling supercritical extraction of hemp, optimization of the process on the basis of technological and economical aspects, **Conference of Scientific Students' Associations (TDK)**, *oral presentation,* Budapest, Hungary
05.2018	Extracting and analyzing non-polar components of hawthorn berries**, Hungarian Conference on Supercritical Fluids**, *poster presentation*, Budapest, Hungary
03.2017	Preparation and analysis of hawthorn extracts and testing the effects on the cardiovascular system, **National Conference of Scientific Students' Associations (OTDK)**, *oral presentation*, Miskolc, Hungary
11.2016	Preparation and analysis of hawthorn extracts and testing the effects on the cardiovascular system, **Conference of Scientific Students' Associations (TDK)**, *oral presentation*, Budapest, Hungary

Courses

09.2021	H_2 Summer School – Empower, Porto, Portugal
07.2021	Introducción a la caracterización de adsorbentes y catalizadores, Jarandilla de la Vera, Spain
03.2021	Leadership and Entrepreneurship for Scientists, Barcelona, Spain
02.2021	Introduction to Entrepreneurship for PhD Chemistry students, Barcelona, Spain
11.2017-03.2018	SCIndikátor Science Communication Course and Contest, Budapest, Hungary
07.2018	The European Summer School in High Pressure Technology 2018, University of Maribor and Graz University of Technology, Slovenia and Austria

Research grants